HAL
open science

Joint optical and near-infrared spectroscopic studies of stars with X-shooter : an insight into carbon stars

Anaïs Gonneau

To cite this version:

Anaïs Gonneau. Joint optical and near-infrared spectroscopic studies of stars with X-shooter : an insight into carbon stars. Solar and Stellar Astrophysics [astro-ph.SR]. Université de Strasbourg; Rijksuniversiteit te Groningen (Groningen, Nederland), 2015. English. NNT : 2015STRAE023 . tel-01332612

HAL Id: tel-01332612

https://theses.hal.science/tel-01332612

Submitted on 16 Jun 2016

HAL is a multi-disciplinary open access archive for the deposit and dissemination of scientific research documents, whether they are published or not. The documents may come from teaching and research institutions in France or abroad, or from public or private research centers.

L'archive ouverte pluridisciplinaire **HAL**, est destinée au dépôt et à la diffusion de documents scientifiques de niveau recherche, publiés ou non, émanant des établissements d'enseignement et de recherche français ou étrangers, des laboratoires publics ou privés.

Joint optical and near-infrared spectroscopic studies of stars with X-shooter

An insight into carbon stars

Anaïs Gonneau

rijksuniversiteit
groningen

Joint optical and near-infrared spectroscopic studies of stars with X-shooter

An insight into carbon stars

Proefschrift

ter verkrijging van de graad van doctor aan de
Rijksuniversiteit Groningen
op gezag van de
rector magnificus prof. dr. E. Sterken
en volgens besluit van het College voor Promoties.

De openbare verdediging zal plaatsvinden op

vrijdag 25 september 2015 om 11.00 uur

door

Anaïs Jeanine Coralie Gonneau

geboren op 5 juni 1988
te Saint-Denis, Frankrijk

Promotores
Prof. dr. A. Lançon
Prof. dr. S. C. Trager

Beoordelingscommissie
Prof. dr. P. Barthel
Dr. N. Martin
Prof. dr. J. Th. van Loon
Prof. dr. A. Zijlstra

ISBN 978-90-367-8168-8
ISBN 978-90-367-8167-1 (electronic version)

COTUTELLE

UNIVERSITÉ DE STRASBOURG
&
UNIVERSITÉ DE GRONINGEN (PAYS-BAS)

Ecole Doctorale Physique - Chimie Physique (ED 182)
Observatoire Astronomique de Strasbourg (UMR 7550)

THÈSE présentée par : **Anaïs Gonneau**
soutenue le : **25 Septembre 2015**

pour obtenir le grade de : **Docteur de l'Université de Strasbourg**
Discipline : Astrophysique

Joint optical and near-infrared spectroscopic studies of stars with X-shooter: An insight into carbon stars

THÈSE dirigée par :
Mme LANÇON Ariane, Prof. dr., Université de Strasbourg
M. TRAGER Scott, Prof. dr., Université de Groningen (Pays-Bas)

RAPORTEURS :
M. BARTHEL Peter, Prof. dr., Université de Groningen (Pays-Bas)
M. ZIJLSTRA Albert, Prof. dr., Université de Manchester (Angleterre)

AUTRES MEMBRES DU JURY :
M. MARTIN Nicolas, dr., Observatoire Astronomique de Strasbourg
M. VAN LOON Jacco, Prof. dr., Université de Keele (Angleterre)

Front cover: Seven Sisters overlooking Reunion & Mauritius Islands in a moonlit Indian Ocean, on 25 August 2013 *(credit: Karen L. Nyberg - NASA)*.

Back cover: Milky Way Over Piton de l'Eau *(credit: Luc Perrot)*.

Printed by: Ipskamp Drukkers, Enschede.

Néna des millions d'années
Ousanousava

Néna des millions d'anées ke nou lé la,
Soman komen nou larivé, sa nou koné pa.
Deux, troi i di microbe la transformé,
Na dot i di Adam et Eve envoyé par bon dié.

Kan nou mort, ousa nou sava ?
Koman nou larivé ? Sa nou koné pa.
Kan nou mort, ousa nou sava?
Koman nou larivé ? Sa nou koné pa.

A coz li lé noir, blanc, jaune, ou aime pa li.
Si li lé misèr, clochard, non ou aime pa li.
Mé kan nou lé la, nou lé la ke de passage.
Vo mieu ou essaye à faire ou hommage.

Kan nou mort, ousa nou sava ?
Koman nou larivé ? Sa nou koné pa.
Kan nou mort, ousa nou sava ?
Koman nou larivé ? Sa nou koné pa.

Kan mon monmon la mèt a moin là,
Li la pa dia moin. Si té comme sa, wo, si toute té comme sa.
Mé comme bocou dot estèr, moin lé pi dakor.
Comme in musicien, mi voudré change zaccords.

Kan nou mort, ousa nou sava?
Koman nou larivé ? Sa nou koné pa.
Kan nou mort, ousa nou sava?
Koman nou larivé ? Sa nou koné pa.

~ ~ ~ ~ ~

A toutes ces étoiles qui veillent sur moi de là-haut ...

Contents

⋆ ⋆ ⋆

1 Introduction **1**
1.1 Stellar evolution . . . 1
1.2 Stellar population synthesis . . . 4
1.2.1 Composite stellar populations . . . 5
1.2.2 Star formation history and chemical evolution . . . 5
1.2.3 Dust . . . 5
1.2.4 The Simple Stellar Population . . . 5
1.2.5 The Initial Mass Function . . . 6
1.2.6 Isochrones . . . 6
1.2.7 Stellar spectral libraries . . . 6
1.3 The X-shooter Spectral Library . . . 10
1.3.1 The instrument: X-shooter . . . 10
1.3.2 The library: XSL . . . 13
1.4 Zoom over the asymptotic giant branch . . . 13
1.4.1 Double shell-burning core . . . 13
1.4.2 Evolution of AGB stars . . . 14
1.4.3 Variability . . . 16
1.4.4 Carbon-rich stars . . . 18
1.4.5 Thermally Pulsing AGB stars in population synthesis . . . 19
1.5 Outline of this thesis . . . 20

2 Carbon stars in the X-shooter Spectral Library **23**
2.1 Introduction . . . 24
2.2 The XSL carbon star sample . . . 25
2.3 Data reduction . . . 29
2.3.1 UVB and VIS arms: extraction and flux-calibration . . . 29
2.3.2 NIR arm: extraction . . . 29
2.3.3 Telluric correction . . . 30
2.3.4 NIR telluric correction and flux-calibration . . . 32
2.3.5 Problem with the last order of NIR spectra . . . 33
2.3.6 Final steps . . . 33
2.4 The diversity of carbon star spectra . . . 34
2.4.1 Group 1 – The bluest stars: $(J-K) < 1.2$ [5 stars] . . . 34
2.4.2 Group 2 – Classical C stars : $1.2 < (J-K) < 1.6$ [7 stars] . . . 36
2.4.3 Group 3 – Redder stars: $1.6 < (J-K) < 2.2$ [13 stars] . . . 36
2.4.4 Group 4 – The reddest stars: $(J-K) > 2.2$ [9 stars] . . . 37
2.4.5 The 1.53 μm feature . . . 37

2.5 Derived spectroscopic indices for carbon stars 37
2.5.1 Broad band colors 38
2.5.2 ^{12}CO indices 39
2.5.3 ^{13}CO index 40
2.5.4 CN index 40
2.5.5 Measure of the 1.53 μm feature 41
2.5.6 C_2 indices 41
2.5.7 Measure of the high frequency structure 41
2.6 Results 45
2.6.1 Color-color plots 45
2.6.2 Molecular indices versus color 46
2.7 Comparison with the literature 48
2.7.1 Spectra from Lançon & Wood (2000) 48
2.7.2 Spectra from Groenewegen et al. (2009) 48
2.7.3 Spectra from IRTF (Rayner et al. 2009) 49
2.7.4 Results 49
2.8 Discussion 51
2.8.1 Our bluest stars 51
2.8.2 The bimodal behavior of red carbon stars 51
2.8.3 Synthetic stellar populations with carbon stars 53
2.9 Conclusions 54
Appendix 2.A The case of V CrA 55
Appendix 2.B Observed spectra of our sample of carbon stars 56
Appendix 2.C Literature properties 63
Appendix 2.D Measurements 66

3 XSL carbon star spectra: comparison with models 69
3.1 Introduction 70
3.2 Observations 71
3.3 Carbon-rich hydrostatic models 73
3.3.1 Initial grid 73
3.3.2 New grid 73
3.3.3 Examples of model spectra 74
3.3.4 Molecular indices of model spectra 76
3.4 Comparison of pseudo-observations and models 76
3.4.1 Study of pseudo-observations 76
3.4.2 Methodology 78
3.4.3 χ^2 maps and results 79
3.5 Comparison of observations and models 80
3.5.1 Color-color plot 80
3.5.2 Molecular indices 81
3.5.3 Full spectrum fits 82
3.5.4 Results 84
3.6 Conclusions 87
Appendix 3.A Comparison observations - models: best fits 87
Appendix 3.B Color-color plots 100

4 Flux calibration of X-shooter spectra 103
4.1 Introduction . . . 105
4.2 Reference spectra . . . 106
4.2.1 Sample selection . . . 106
4.2.2 Data . . . 106
4.2.3 Modelling of hot white dwarfs . . . 108
4.2.4 Selection of model spectra . . . 110
4.2.5 Correction of model spectra at short wavelengths . . . 114
4.2.6 Absolute flux calibration . . . 114
4.3 Correction of atmospheric effects . . . 116
4.3.1 Correcting the atmospheric extinction down to 300 nm . . . 116
4.3.2 Telluric absorption . . . 118
4.4 Pipeline implementation . . . 122
4.4.1 Radial velocity correction . . . 122
4.4.2 New fitting routine for response determination . . . 122
4.4.3 New reference data . . . 122
4.5 Summary . . . 124

5 Database and website 127
5.1 Introduction . . . 127
5.2 Design of the database . . . 127
5.3 Structure of the database . . . 129
5.4 Individual tables and their primary keys . . . 130
5.4.1 Table XSLstars . . . 130
5.4.2 Table XSLparam . . . 131
5.4.3 Table XSLobs . . . 132
5.4.4 Tables XSLred, XSLext and XSLflux . . . 132
5.4.5 Table XSLmerge . . . 133
5.5 Design of the XSL website . . . 133
5.5.1 Creation . . . 134
5.5.2 Further developments . . . 134

6 Conclusions 137
6.1 Data reduction . . . 138
6.2 Carbon stars . . . 139
6.3 Comparison with models . . . 140
6.4 Future perspectives . . . 141

Bibliography 145

Nederlandse samenvatting 153

English summary 161

Résumé 167

Acknowledgements / Remerciements 175

Chapter 1

Introduction

⋆ ⋆ ⋆

How do galaxies form and evolve? A century did not suffice to answer this simple question. The starting point for every thing is set 14 billion years ago with the Big Bang. From a singularity in space-time, the Universe started to expand. Immediately following the Big Bang, the primordial Universe consisted of only radiation, subatomic particles and energy. Within the first half hour that followed, the first nuclei were formed. The models for galaxy formation assume that matter and energy originally filled all of space when the Universe was young. But this distribution of matter was not perfectly uniform, with some regions slightly denser than others. This led to the formation of protogalactic clouds in less than 1 billion years. In these clouds, gravity and efficient cooling caused the gas and dust to collapse and form stars. A few million years later, these exploded as supernovae and seeded the new-born galaxies with first heavy elements. The supernovae, and probably also active galactic nuclei, heated the surrounding gas. This heating slowed star formation and the rest of the gas settled slowly into a rotating disk. In quiet environments, these disks progressively attracted more gas via gravity, and grew, forming isolated spirals in a halo mostly consisting of dark matter. In denser regions of the universe, galaxy interactions and mergers played a larger role, leading to the variety of galaxy types and sizes seen today.

1.1 Stellar evolution

The details of the previous description are still a matter of debate, and maybe a way to answer the initial question is to reverse the problem and start from the definition of a galaxy. A galaxy is a gravitationally bound system consisting of stars, stellar remnants, interstellar gas and dust, and dark matter. Therefore, understanding how stars form and evolve will help us understand the history of galaxies. This ambitious project has been a major motivation for much of the efforts devoted to stellar astrophysics over the last century. Indeed, understanding the stellar populations of galaxies requires to be able to understand and reproduce the contributions of all types of stars, at all stages of their evolution.

The common framework for stellar classification is the Hertzsprung-Russell (HR) diagram. Created in the early twentieth century by Ejnar Hertzsprung and Henry Norris Russell, the original diagram displayed the spectral type of stars on the horizontal axis and the absolute visual magnitude on the vertical axis, as shown in Figure 1.1[1].

[1] It is worth mentioning that actually the first HR diagram was published in 1910 by Hans Rosenberg, a PhD student of Karl Schwarzschild, for stars in the Pleiades. Although

The stars on the bottom-right corner are cold and faint, while the ones on the top-left corner are hot and luminous.

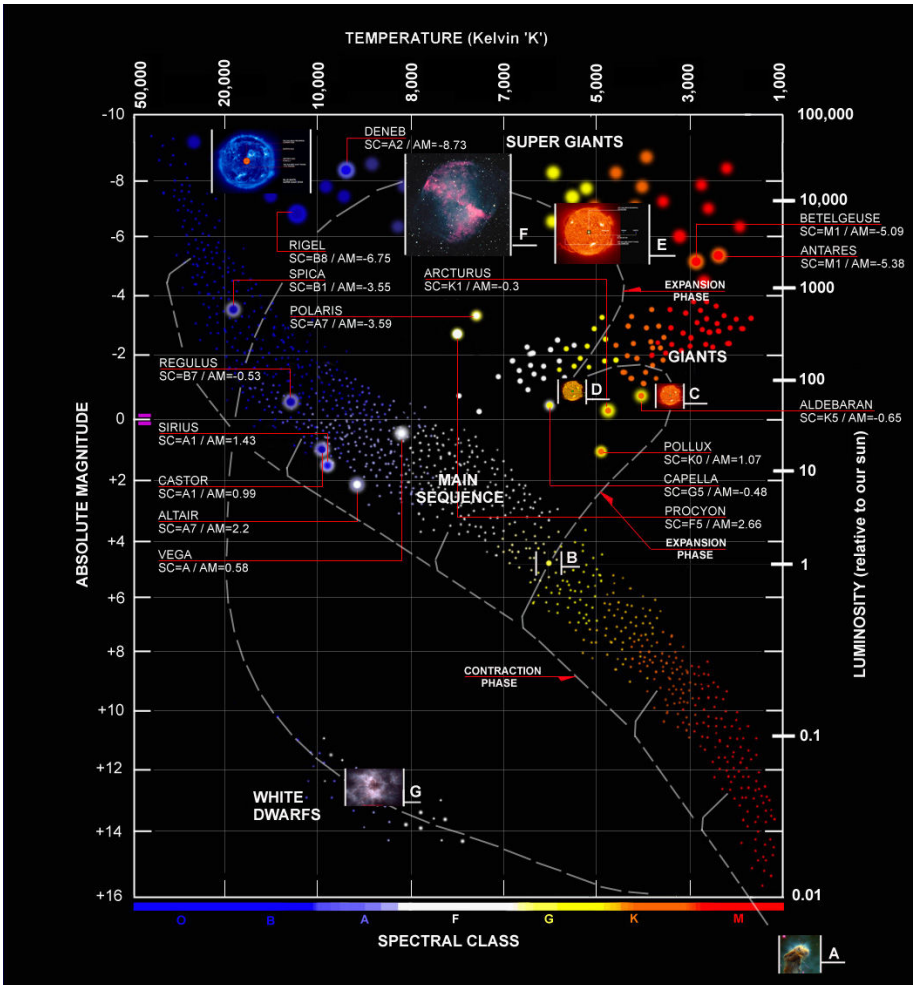

Figure 1.1: An example of a Hertzsprung-Russell diagram *(credit Cococubed)*.

All stars follow the same basic series of steps in their lives: gas cloud to main sequence to red giant to (planetary nebula or supernova) to remnant. How long a star lasts in each stage, whether a planetary nebula forms or a spectacular supernova occurs, and what type of remnant will form depends on the initial mass of the star. In the following, I describe a little bit more each step.

The stellar nurseries are called molecular clouds. These interstellar clouds are large and dense gas clouds (with dust) which are cold enough for molecules to form. These clouds are initially balanced between gravitational forces, which work

Hertzsprung had a preliminary version in 1908, his first diagram was published in 1911. Likewise, Russell published his version in 1915.

to collapse the cloud, and pressure forces (primarily from the gas) which work to keep the cloud from collapsing. When these forces fall out of balance, such as due to a supernova shock wave, the cloud begins to collapse and fragment into smaller and smaller fragments. These gas clumps compress to become protostars.

Protostars are within a cocoon of gas and dust, which make them more visible at infrared wavelengths. A famous example of protostars is the "Pillars of Creation" in the Eagle Nebula. This corresponds to image A in Figure 1.1.

A protostar continues to grow by accretion of gas and dust from the molecular cloud, becoming a pre-main-sequence star as it reaches its final mass. If the young star has sufficient mass, the collapsing gas and dust burns hotter, eventually reaching temperatures sufficient to fuse hydrogen into helium. The star turns on and becomes a main sequence star, powered by hydrogen fusion. Fusion produces an outward force that balances with the inward force caused by gravity, stabilizing the star. The star settles down to spend about 90% of its life as a main sequence star.

Eventually the hydrogen in the core is all converted to helium and the nuclear reactions stop. Gravity takes over and the core shrinks. The layers outside the core collapse too, the ones closer to the center collapse quicker than the ones near the surface. This gravitational collapse releases energy, heating concentric shells immediately outside the inert helium core.

Stars smaller than a quarter the mass of the sun collapse directly into white dwarfs (cf. image G in Figure 1.1). For larger stars, the shell layer, layer just outside the core, gets hot and dense enough for hydrogen fusion to start. This fusion is very rapid because the shell layer is still compressing and increasing in temperature. The luminosity of the star increases from its main sequence value. The energy generated in the core is so much intense that the outer layers of the star experience a larger pressure. This increased pressure cause the outer layers of the star to expand significantly. As a side effect of this expansion, the outer envelope has a lower temperature, which gives this reddish color to the star. The star is now referred as a subgiant and then a red giant (cf. image C in Figure 1.1). Massive main sequence stars will expand much further to become supergiants (cf. image E in Figure 1.1).

If the star is massive enough, gravity can compress the core enough to create high enough temperatures to start fusing helium. The energy released by helium fusion causes the core to expand, so that hydrogen fusion in the overlying layers slows and total energy generation decreases. The star contracts, although not all the way to the main sequence, and it migrates to the horizontal branch on the HR diagram, gradually shrinking in radius and increasing its surface temperature (cf. image D in Figure 1.1).

In the next-to-last stage of a star's life, the outer layers are ejected as the core shrinks to its most compact state. A large amount of mass is lost at this stage as the outer layers are returned to the interstellar medium. Massive stars explode into supernovas, while low-mass stars end up forming a planetary nebula (cf. image F in Figure 1.1).

After a star has burned out its fuel supply, its remnants can take one of three forms (white dwarfs, neutron stars or black holes), depending on the mass during its lifetime.

1.2 Stellar population synthesis

To reproduce the spectral energy distribution (SED) of galaxies, adding one star from each stage of the HR diagram is not enough. Indeed, the spectra of galaxies are shaped by almost every physical property of the system. Therefore, other properties are needed such as the stellar metallicity or the physical state and quantity of dust and gas. Over the years, tools have been developed to extract these variables from observed SEDs. This approach is called stellar population synthesis (SPS).

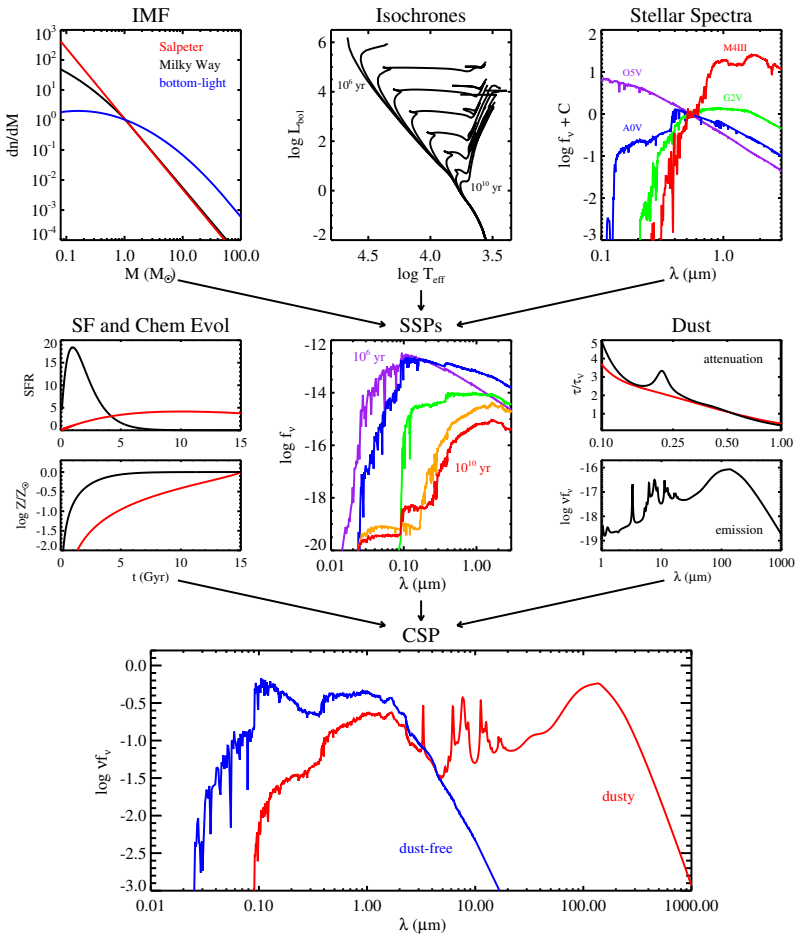

Figure 1.2: Overview of the stellar population synthesis, from Conroy (2013).

A good overview of the process is given in Figure 1.2, taken from Conroy (2013). In the following, I describe all the steps necessary to construct modelled spectra of galaxies.

1.2.1 Composite stellar populations

The final products of the stellar population synthesis process are called composite stellar populations (CSPs). They are modelled SEDs of galaxies: they contain stars with a range of ages and metalliticies and also dust. The bottom panel of Figure 1.2 shows two examples of CSPs, before (blue curve) and after (red curve) a dust model is applied. The ingredients necessary for their construction are listed in the middle panel of the same figure: from left to right, star formation histories and chemical evolution, simple stellar populations, and a model for dust attenuation and emission.

1.2.2 Star formation history and chemical evolution

To build a CSP, we need the birthrate of stars and also the chemical evolution. These two ingredients are highlighted in the left part of the middle panel of Figure 1.2.

The Star Formation Rate (SFR) depends on the amount of gas converted in stars in the galaxy. It is usually represented as an exponential: $SFR \propto e^{-t/\tau}$, where t is the age and τ is the gas depletion time scale. This form – referred as the τ-model – is derived from scenarios where the SFR depends linearly on the gas density in a closed-box model (Schmidt 1959). Some authors (e.g., Lee et al. 2010) advocate an alternative model – sometimes referred as the "delayed" or "extended" τ-model – which allows linear growth at early times followed by an exponential decline at late times. It is parametrised as follows: $SFR \propto te^{-t/\tau}$.

For the treatment of metallicity, a common simplification is to assume a single metallicity for the entire composite population.

1.2.3 Dust

Interstellar dust is a component of nearly all galaxies, especially those that are actively star-forming. Dust plays a dual role in SPS, both as an obscurer of light in the ultraviolet (UV) through near-infrared (NIR) and as an emitter of light in the infrared (IR). These two aspects are often modeled independently of one another, as they are sensitive to different properties of a galaxy (e.g., dust obscuration is highly sensitive to geometry while dust emission is more sensitive to the interstellar radiation field). These two aspects are highlighted in the right part of the middle panel of Figure 1.2.

1.2.4 The Simple Stellar Population

The key ingredients for building composite stellar populations are the simple stellar populations (SSPs). Each SSP describes the evolution in time of the SED of a single stellar population of the same age, at a single metallicity and abundance pattern. Some examples of SSPs are shown in the center part of the middle panel of Figure 1.2, and the three inputs needed to build a SSP are highlighted in the upper panel. From left to right, they are: the initial mass function, stellar evolution theory in the form of isochrones, and stellar spectral libraries, each of which may in principle be a function of metallicity and/or elemental abundance pattern.

1.2.5 The Initial Mass Function

To build a SSP, one ingredient is the initial mass function (IMF), in other words the initial distribution of stellar masses along the main sequence. This function has been quite studied over the last decades (e.g., Salpeter (1955), Kroupa (2001), Chabrier (2003)). As an example, the Salpeter IMF is defined as : $dN/dM \propto M^{-x}$ where N is the number of stars, M the mass and $x = 2.35$. Some examples of IMF are shown in the left part of the top panel of Figure 1.2.

The IMF has a small effect on the shape of the SED of single stellar populations, as the integrated light of a population of the same age is overwhelmingly dominated by stars at approximately the same mass, i.e., the turnoff mass. Still, with improving instrumentations, these small effects are becoming detectable (Spiniello et al. 2012).

1.2.6 Isochrones

The next ingredient needed to create a SSP is a set of isochrones. An isochrone is a curve on the HR diagram, representing a population of stars of the same age and metallicity. Some examples of isochrones are shown in the center part of the top panel of Figure 1.2.

Isochrones are models, constructed from stellar evolution tracks. Most of them span a wide range in ages (masses), chemical compositions, and cover most relevant evolutionary phases. Models in this category include the Padova models (Bertelli et al. 1994; Girardi et al. 2000; Marigo et al. 2008), and the BaSTI models (Pietrinferni et al. 2004; Cordier et al. 2007). The Geneva models (Schaller et al. 1992; Meynet & Maeder 2000) are tailored to follow high-mass stars through advanced evolutionary phases, including the Wolf-Rayet (WR) phase, but they do not model low mass stars. Other models have focused on the main sequence, red giant branch (RGB), and horizontal branch (HB) evolution of low-mass stars ($M < 3M_{\odot}$). Finally, there are isochrones tailored to very low-mass stars and brown dwarfs.

Implementing isochrones in an SPS model is challenging because no single set spans the necessary range of ages, metallicities and evolutionary phases. Therefore, it is common to combine them, for example by using the Padova isochrones for the bulk of the age and metallicity range and supplementing with the Geneva models at young ages. Moreover, stellar evolution calculations are subject to uncertainties. One major uncertainty is the fact that stellar models are based on one dimensional codes, and therefore approximate three dimensional processes such as convection, rotation, mass-loss, close binary interactions, and thermal pulses during AGB evolution.

1.2.7 Stellar spectral libraries

The last but not least ingredient to construct a SSP is a set of stellar spectral libraries, as shown in the right part of the top panel of Figure 1.2. Stellar libraries are used to convert the outputs of stellar evolution calculations – surface gravities and effective temperatures as a function of metallicity – into observable SEDs.

Unfortunately, there is no single spectral library that covers the entire range of parameter space necessary for constructing SPS models. Combining together various libraries, often of varying quality, is therefore necessary.

Stellar spectral libraries could be either derived from theoretical calculations or empirical. The benefits and drawbacks of these two approaches are discussed in the following.

♣ Theoretical libraries

Theoretical libraries offer everything you can dream of: a large cover in parameter space, including wavelength range and spectral resolution, and spectra which are no subject to observational issues such as flux calibration and atmospheric absorption. The side effect is that synthetic spectra are limited by the completeness of the spectral line lists and by the knowledge of line broadening parameters and numerical assumptions – e.g. plane-parallel versus spherical geometry and local thermodynamic equilibrium (LTE) versus statistical equilibrium (NLTE).

The most used set of model atmospheres currently available is the one created by Kurucz (1979). This library was extended by Lejeune et al. (1998) and Westera et al. (2002) to include spectra of M stars computed from model atmospheres from Fluks et al. (1994), Bessell et al. (1989, 1991) and Allard & Hauschildt (1995). Moreover, they calibrated the flux distribution of the synthetic spectra in order to match the colors of observed stars (BaSeL library). However, the spectral resolution of the BaSeL library is limited to the sampling of the model atmosphere grid ($\sim$ 20 Å) which is by far lower than the modern observed spectra of both individual stars and integrated stellar populations.

Other synthetic libraries exist for specific spectral types. At the high temperature end, i.e., Wolf-Rayet and O-type main sequence stars, the state-of-the-art libraries are from Smith et al. (2002) and Lanz & Hubeny (2003), while for hotter compact objects (e.g., post-AGB stars) the most up-to-date models are from Rauch (2003). For cooler temperatures, the MARCS and PHOENIX grids are the state-of-the-art because of their comprehensive molecular line lists and treatment of spherical effects on the atmospheres and spectra of cool giants. Finally, the Aringer et al. (2009) models fill out the low temperature end by providing carbon star spectra over a range of parameter space.

There are several modern spectral libraries computed by Munari et al. (2005), Martins et al. (2005), and Coelho et al. (2005) that offer fairly wide coverage in parameter space and are at high spectral resolution. More recently, Husser et al. (2013) published a new library of high-resolution synthetic spectra based on the stellar atmosphere code PHOENIX, with the idea of being useful for the analysis of spectra observed with MUSE (Bacon et al. 2010), X-shooter (Vernet et al. 2011) and CRIRES (Kaeufl et al. 2004).

♣ Empirical libraries

The strengths and weaknesses of the theoretical libraries are the weaknesses and strengths of the empirical libraries. On the one hand, empirical libraries do not suffer from issues with line lists or treatment of convection. On the other hand,

empirical spectra undergo observational constraints such as correction for atmospheric absorption, flux calibration, and limited wavelength coverage and spectral resolution.

Furthermore, the spectra cover only a limited parameter space, usually restricted to the effective temperature, the surface gravity, and the metallicity. Last but not least, empirical libraries cannot extrapolate to abundance patterns that differ from that of the library stars (Worthey et al. 1992), which are from the solar neighbourhood or, in some cases, from the Magellanic Clouds.

In the optical Table 1.1 lists some of the empirical stellar libraries in the optical and their properties.

Spectral Library Reference	Spectral range (nm)	Number of Stars	Resolving power
Lick/IDS (Worthey & Ottaviani 1997)	400 – 640	460	8 – 10 Å (FWHM)
Pickles Atlas (Pickles 1998)	115 – 2500	138	500 Å (FWHM
Lançon & Wood (2000)	500 – 2500	100	1100
ELODIE (Prugniel & Soubiran 2001)	390–680	1388	10000
UVES-POP (Bagnulo et al. 2003)	307–1030	300	80000
STELIB (Le Borgne et al. 2003)	320–930	249	2000
INDO-US (Valdes et al. 2004)	346–946	1237	5000
MILES (Sánchez-Blázquez et al. 2006)	352–750	985	2000
NGSL (Gregg et al. 2006)	167–1025	374	1000
IRTF-SpeX (Rayner et al. 2009)	800–5000	210	2000

Table 1.1: Compilation of optical stellar libraries, based on Chen et al. (2014a).

In the near-infrared Building stellar libraries in the near-infrared is more challenging. Table 1.2 lists all the NIR stellar libraries (a "library" is assumed to contain more than ten objects). The maturing of NIR spectrographs and detector arrays over the last years helps to sophisticate NIR libraries of stellar spectra. But despite this long list, we lack uniform NIR data set with high signal-to-noise ratio and resolution, covering the entire range of spectral classes, luminosity, and metallicity necessary to carry out evolutionary population synthesis in the near-infrared.

Consistency between optical and near-infrared data The consistency between optical and near-infrared data plays a key role in the study of galaxies. However, so far, there is no result showing that the studies made on both wavelength ranges agree.

For example, Lançon et al. (2008) studied the spectra of 5 massive clusters from M82 in the context of population synthesis. They obtained good fits with the near-infrared models and they estimated the near-infrared ages between 9 and 35 Myr. Studies based on optical spectra give ages between 40 and 80 Myr.

Another example is the work done by Taylor et al. (2011) with the Galaxy And Mass Assembly (GAMA) survey. While estimating stellar masses, they found that for a large fraction of galaxies the stellar population parameters inferred from the

Spectral Library Reference	Spectral range (μm)	Spectral type	Number of Stars	Resolving power
Johnson & Méndez (1970)	1.2−2.5	A−M	32	550
Kleinmann & Hall (1986)	2.0−2.5	F−M	26	2500−3100
Lambert et al. (1986)	1.5−2.5	C	30	75,000
McGregor et al. (1988)	1.0−2.5	Be, Ae	13	500
Tanaka et al. (1990)	1.5−2.5	C	33	2000
Terndrup et al. (1991)	0.45−2.45	M	32	1000
Lancon & Rocca-Volmerange (1992)	1.4−2.5	O−M	56	550
Origlia et al. (1993)	1.5−1.7	G−M	40	1500
Lazaro et al. (1994)	1.1−4.2	C	15	500
Ali et al. (1995)	2.0−2.4	F−M	33	1380
Oudmaijer et al. (1995)	2.1−2.4	post-AGB	18	400−700, ∼1500
Dallier et al. (1996)	1.57−1.64	O−M	37	1500−2000
Hanson et al. (1996)	2.0−2.4	O−B	180	800−3000
Jones et al. (1996)	1.16−1.22	M	13	1085
Morris et al. (1996)	1.45−2.4	WR, O, B, LBV	26	570−1600
Wallace & Hinkle (1996)	2.02−2.41	G−M	12	45000
Blum et al. (1997)	1.5−1.8	O−B	11	575
Figer et al. (1997)	2.0−2.4	WR	38	525
Ramirez et al. (1997)	2.19−2.34	K−M	43	1380, 4830
Wallace & Hinkle (1997)	2.0−2.4	O−M	115	3000
Joyce (1998)	1.0−4.1	C	29	∼500
Joyce et al. (1998)	1.0−1.3	M, S, C AGB	103	1100
Meyer et al. (1998)	1.5−1.7	O−M	85	3000
Pickles (1998) (compilation)	0.15−2.5	O−M	131	50-6000
Förster Schreiber (2000)	1.95−2.45	G−M	31	830, 3000
Lançon & Wood (2000)	0.5−2.5	K−M, AGB	77	1100
Wallace et al. (2000)	1.05−1.34	O−M	88	3000
Frogel et al. (2001)	2.17−2.34	RGB	129	1500
Lenorzer et al. (2002)	2.36−4.05	O−B	75	1500-2000
Malkan et al. (2002)	1.08−1.35	O−M 105	650	
Vandenbussche et al. (2002)	2.36−4.05	O−M	293	1500-2000
Wallace & Hinkle (2002)	3.3−4.2	G−M, AGB	42	3000
Ivanov et al. (2004)	1.48−2.45	G−M	218	2000-3000
Ranade et al. (2004)	1.5−1.8	O5−M3	135	1000
Cushing et al. (2005)	0.8−4.2	M, L, T	30	940-2000
Lodieu et al. (2005)	0.6−1.0	M6−L2	71	600
	1.0−2.5			
Hanson et al. (2005)	1.6−2.2	O−B	37	8000-12000
Ranada et al. (2007)	2.0−2.2	O7−M7	114	1000
Ranade et al. (2007)	1.1−1.3	O5−M8	125	1000
van Loon et al. (2008)	2.9−4.1	C, AGB, RSG	50	200-400
Venkata Raman & Anandarao (2008)	1.5−1.8	AGB	78	1000
	2.0−2.4			
Mármol-Queraltó et al. (2008)	2.1−2.4	O−M	220	2500
IRTF/SpeX (Rayner et al. 2009)	0.8−5	F−M, S, C, AGB	210	2000, 2500
CRIRES-POP (Lebzelter et al. 2012)	0.97−5.3	B, A, F, G, K, M, S, C	20	96000
APOGEE Zasowski et al. (2013)	1.5−1.7	cool stars (mainly RGB) from the Milky Way	163000	22500

Table 1.2: Compilation of near-infrared stellar libraries, based on Rayner et al. (2009).

optical-plus-NIR photometry are formally inconsistent with those inferred from the optical data alone, as shown for example in Figure 1.3. This figure shows the residuals of the stellar mass estimates, based on the Bruzual & Charlot (2003) stellar evolution models. Clearly, we see that including the NIR data degrades the quality of the optical fits.

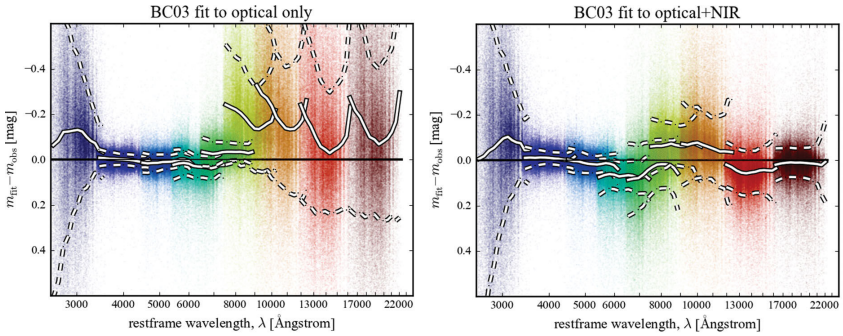

Figure 1.3: Illustrating how well the models describe the observed photometry of real galaxies, from Taylor et al. (2011). In each panel, the colors correspond to the different observed bands, the solid lines show the median and the dashed lines the 16/84 percentile residual in each band as a function of restframe wavelength. The left panel shows the fit using only optical data, while the right panel shows the result while including the near-infrared data.

1.3 The X-shooter Spectral Library

Besides the large number of stellar libraries listed before, the current spectral libraries need improvements on the following points: better calibrations, more stars, higher spectral resolution and broader wavelength coverage. With this in mind, we make use of the unique capability of the X-shooter spectrograph to build the X-shooter Spectral Library (hereafter XSL).

1.3.1 The instrument: X-shooter

X-shooter (Vernet et al. 2011) is a three-arm spectrograph mounted at the ESO Very Large Telescope (VLT) in Chile. What makes this instrument unique is the capability to collect the flux from the ultra-violet wavelength range to the near-infrared simultaneously (from 300 to 2480 nm).

A view of X-shooter, at the Cassegrain focus below the primary mirror cell of the VLT UT2, is shown in Figure 1.4. The UVB and VIS spectrographs are located at the top and bottom respectively. The NIR cryostat is visible in the center. The two boxes on the left and on the right are electronic cabinets.

X-shooter consists of a central structure (the backbone) that supports three prism-cross-dispersed échelle spectrographs optimized for the UV-Blue (UVB: 293 – 593 nm), Visible (VIS: 525 – 1048 nm) and near-infrared (NIR: 982 – 2480 nm) wavelength ranges, respectively. After the telescope focus, a series of two highly efficient dichroics reflect the UVB and VIS light to the corresponding arms and transmit longer wavelengths to the NIR arm. A functional diagram of the instrument is given in Figure 1.5. The light path runs from the top to the bottom.

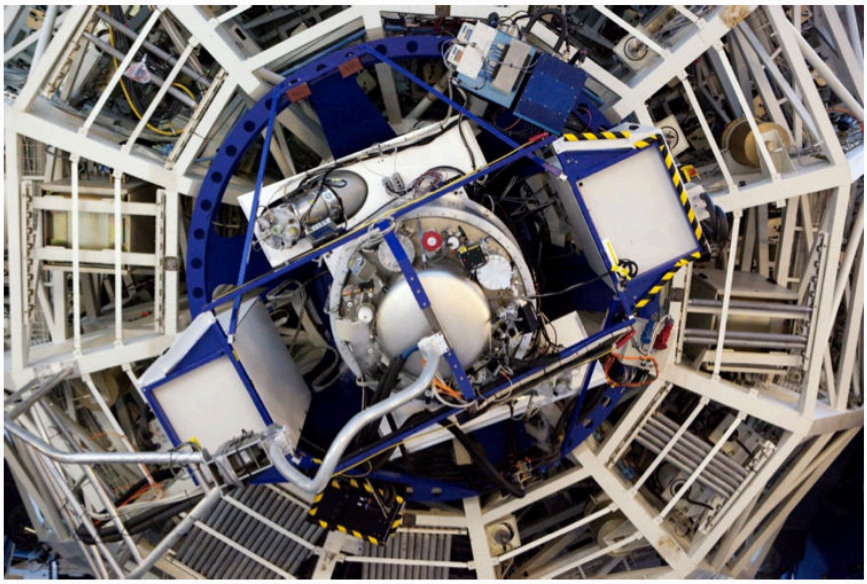

Figure 1.4: An outside view of X-shooter, from Vernet et al. (2011).

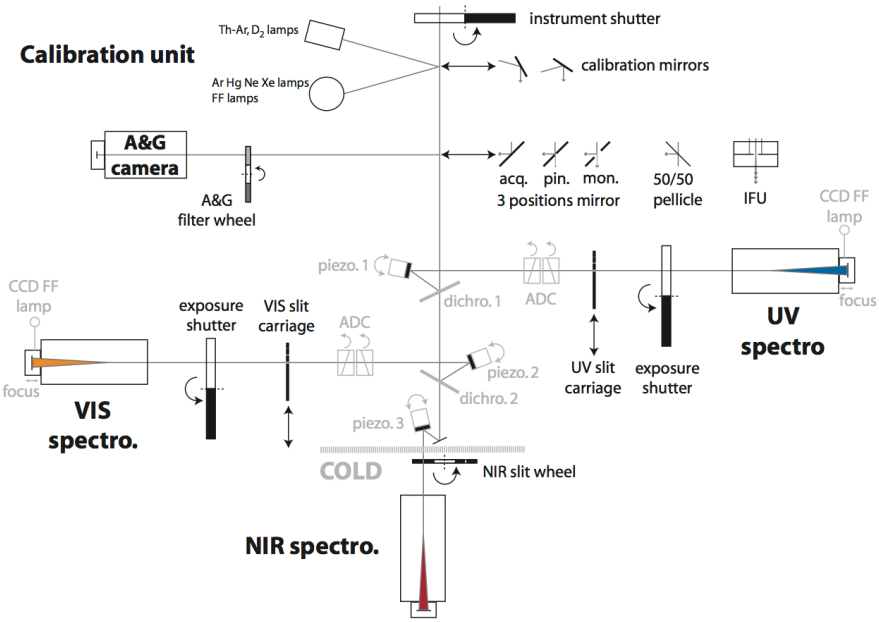

Figure 1.5: An inside representation of X-shooter, from Vernet et al. (2011).

Figure 1.6 shows an example of X-shooter raw frames, from left to right, from the UVB to the NIR arm.

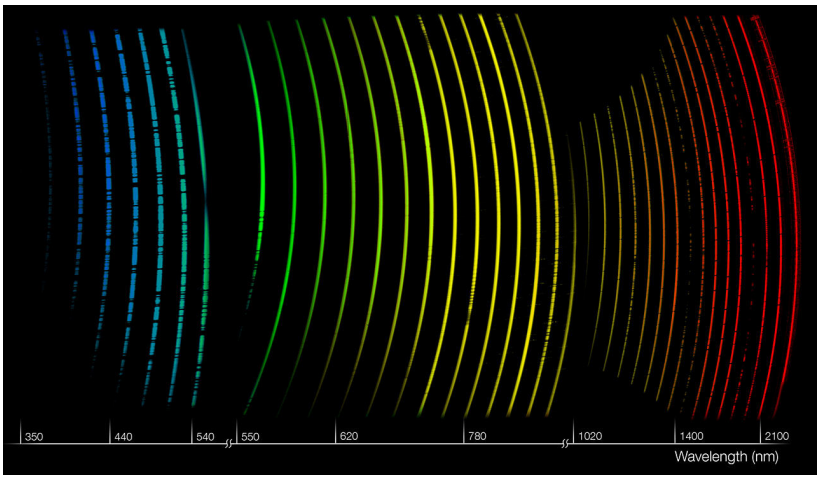

Figure 1.6: Examples of X-shooter raw frames. The rainbow of colours are meant for illustrative purpose. (*credit ESO*)

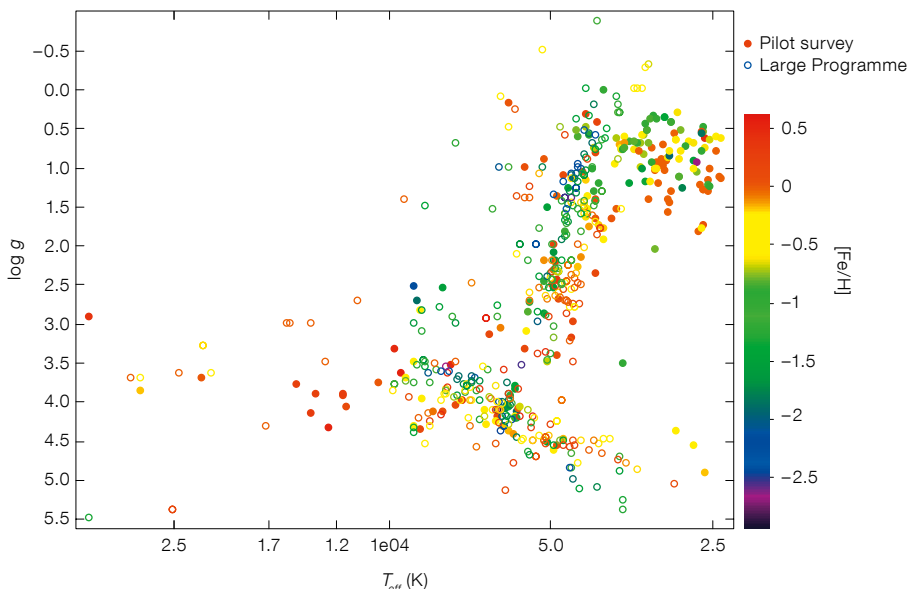

Figure 1.7: The Hertzsprung-Russell diagram of XSL stars, taken from Chen et al. (2014b) (ESO Messenger article).

1.3.2 The library: XSL

The X-shooter Spectral Library is an ESO Large Programme (P.I. S. C. Trager) designed to cover most of the HR diagram. During six semesters, we observed more than 700 stars at a mean resolving power of 10 000, from a variety of environments (from the nearby Galactic Disc to the Bulge and to the Magellanic Clouds), with a variety of chemical compositions. Figure 1.7 shows an overview of our sample in a HR diagram.

The survey was conducted in two phases: a Pilot Survey (two semesters) and a Large Programme (four semesters). For all the periods, the stars were observed with the configuration described in Table 1.3. The UVB and VIS spectra of the Pilot Survey resulted in the XSL Data Release 1 (Chen et al. 2014a). The data of both the Pilot Survey and the Large Programme are the basis of this thesis.

Wavelength range	Mode	Slit width (× 11”)	Resolution ($\lambda/d\lambda$)
UVB	NODDING	0.5”	9’200
VIS	NODDING	0.7”	11’000
NIR	NODDING	0.6”	7’700
UVB	STARE	5.0”	
VIS	STARE	5.0”	
NIR	STARE	5.0”	

Table 1.3: X-shooter configuration for XSL.

During this thesis, I could not study all the stars in detail, and therefore I focused on one important spectral type: the stars from the asymptotic giant branch.

1.4 Zoom over the asymptotic giant branch

Understanding the asymptotic giant branch (AGB) phase of stellar evolution is critical for various aspects of galaxy evolution. It affects not only the interpretation of the integrated light of distant galaxies, but also the origin of cosmic dust and the chemical enrichment of the interstellar medium.

1.4.1 Double shell-burning core

If we go back to the HR diagram, and more precisely to the horizontal branch, stars at this stage have a helium (He) burning core and a hydrogen (H) burning shell, as shown in Figure 1.8. The fusion of the helium produces carbon, which falls down deeper in the core. So, carbon builds up in the core, and the helium core grows outward on top of the new carbon core.

When the core runs out of helium, the (inert) carbon core cannot produce energy to heat up and balance the weight of the star. The core contracts, heating the layers immediately outside: helium fusion starts again.

The star expands again, following the asymptotic giant branch on the HR diagram, paralleling the original red giant evolution, but with even faster energy

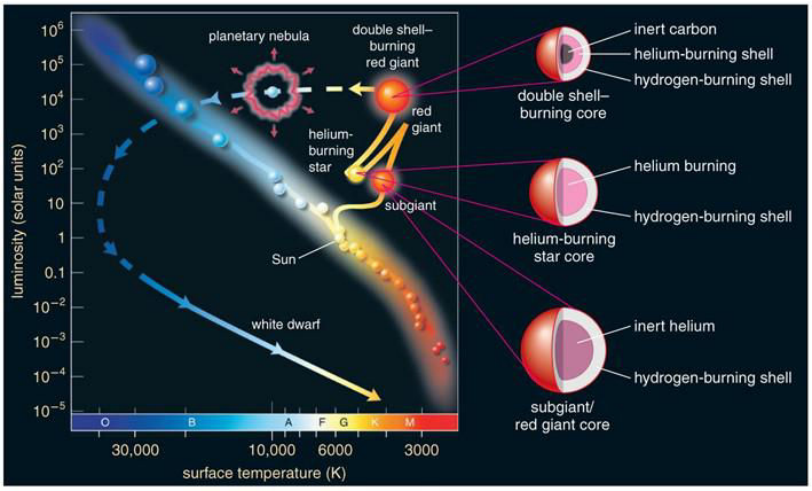

Figure 1.8: Burning shells of the red giant and asympotic giant branchs *(credit Startrail's blog).*

generation (which lasts for a shorter time). Although helium is being burnt in a shell, the majority of the energy is produced by hydrogen burning in a shell further from the core of the star.

1.4.2 Evolution of AGB stars

A star is officially on the asymptotic giant branch when it is in its double-shell burning phase. Figure 1.9 shows a representation of the central region of a AGB star.

During the initial phase – called early AGB – the stellar luminosity is provided entirely by the He-burning shell. The He shell adds mass to the carbon-oyxgen core, which becomes more degenerate. At the same time, the luminosity increases and the star expands, while the base of the convective envelope moves inwards. If the star is massive enough ($\geqslant 4M_\odot$ for solar metallicity), the convective envelope penetrates below the extinct H shell and mixes helium and other products of hydrogen burning to the surface. This is called the "second dredge-up" (as a first dredge-up already took place during the first ascent of the giant branch).

As the temperature at the He/H interface (intershell region) increases, hydrogen burning resumes. Both burning shells now start advancing at the same rate, but after a short time the He-burning shell becomes unstable. This is the start of the thermally pulsing (TP) AGB. For most of the time, the hydrogen burning shell is active while the helium burning shell is essentially dormant. Periodically, at intervals of typically $5 \times 10^4 - 10^5$ year for low mass stars, the helium ignites violently and burns up the helium produces by the hydrogen shell since the last phase of helium activity. This is known as a helium shell flash or thermal pulse. Figure 1.10 shows a schematic view of the evolution of an AGB star between two thermal pulses.

Figure 1.9: Central region of a one-solar mass AGB star *(credit Australian Telescope National Facility).*

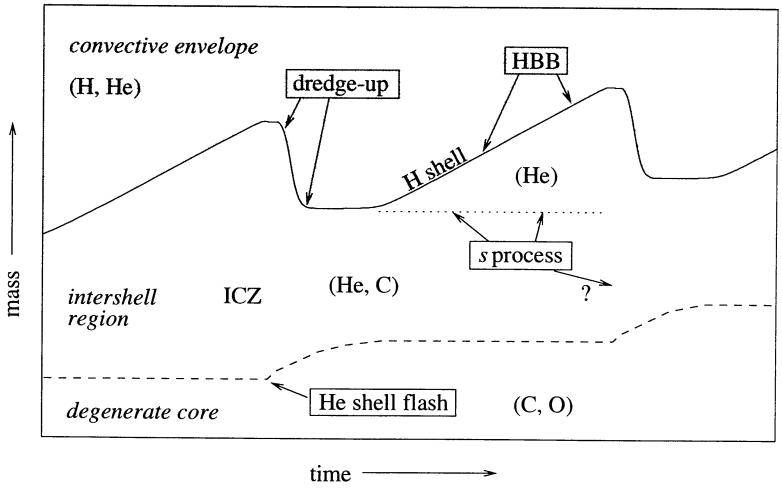

Figure 1.10: Schematic evolution of an AGB star through two thermal-pulses cycles, taken from Pols et al. (2001). The H-exhausted core mass is shown as a solid line, and the He-exhausted core mass as a dashed line. The elements in brackets indicate the main composition of each region.

As a result of the energy release, a flash-driven intershell convection zone (ICZ) forms which extends from the He shell almost up to the H burning shell. The products of helium burning (mainly ^{12}C) are mixed throughout the ICZ. As the flash dies down, the energy deposited in the intershell causes the outer layers to expand and cool, and the H-burning shell is temporarily extinguished. The base of the convective envelope reaches inward and can penetrate beyond the H/He interface and into the region enriched in carbon. Carbon can thus be mixed to the surface, in the so-called "third dredge-up" (3DU).

With each dredge-up episode, the surface ratio carbon over oxygen (C/O) increases. After a certain number of pulses it may exceed unity and the star can evolve from an oxygen-rich star (C/O < 1) to a carbon-rich star (C/O > 1).

For the most massive stars (≥ 5 M$_\odot$ for solar metallicity), the convective envelope penetrates into the top of the H-burning shell, and nucleosynthesis thus takes place in the envelope of the star. This process is known as hot bottom burning (HBB) or nowadays envelope burning. The base of the convective envelope becomes hot enough (more than $8 \times 10^7 K$) for the CN cycle to be activated and the carbon dredged-up to the envelope to be processed into nitrogen. This keeps the C/O below 1 and thus prevents the star from becoming a carbon star.

Eventually, the chemically enriched envelope is expelled into the interstellar medium through stellar winds.

1.4.3 Variability

Figure 1.11 shows a schematic view of an AGB star. In addition to thermal pulses, AGB stars have pulsating atmospheres, meaning that the stars actually increase and decrease in size periodically. This leads to changes in the brightness of the stars. The first star recognized to be variable was Omicron Ceti, later renamed Mira (the "Wonderful"). In 1596, a Dutch observer David Fabricius reported the variability (in brightness) of Mira and assumed it was a nova. But later, in 1609, he observed it again. In 1638, another Dutch observer Johannes Holwarda found that Mira disappeared and reappeared in a varying cycle of about 330 days. Prior to the observations made by Fabricius, there is some suspicion that Mira was recorded as a nova in early Chinese or Korean records. Figure 1.12 shows an image of Mira (an M7 red giant) and its binary companion (a white dwarf, according to Warner (1972)).

There are different types of pulsating variables according to their periods of pulsation and the shapes of their light curves. The long-period variable (LPV) stars have periods from tens of days to a thousand or more. There are two main types of LPV:

- Mira variables: named after the Mira star. They are characterized by long rather regular pulsation periods in the range between 80 to 1000 days and grand light variations, from 2.5 magnitudes up to 10 at optical wavelengths.

- Semiregular variables (SR): their periods lie in the range from 20 to more than 2000 days. They are characterized by small amplitude (less than 2 magnitudes) and often irregularities that makes the period determination hard. A well-known example is Betelgeuse (in the constellation of Orion).

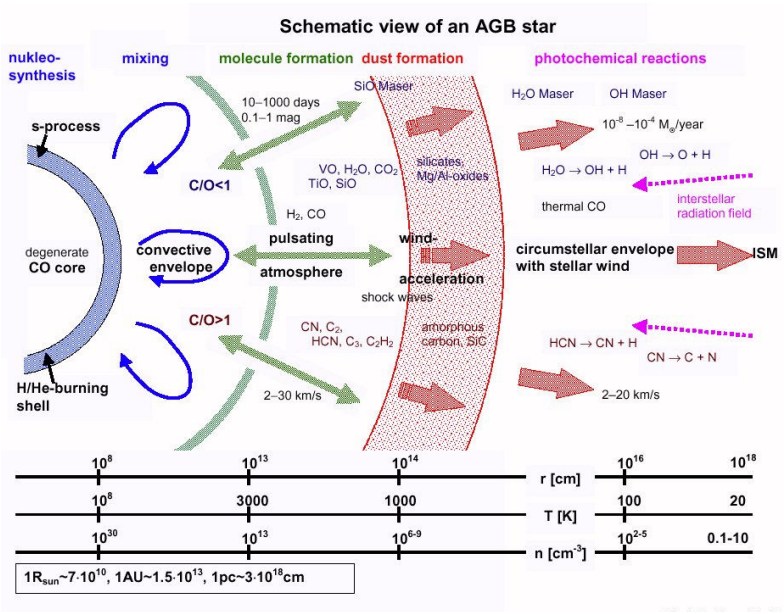

Figure 1.11: Schematic view of an AGB star *(credit dr. J. Hron)*.

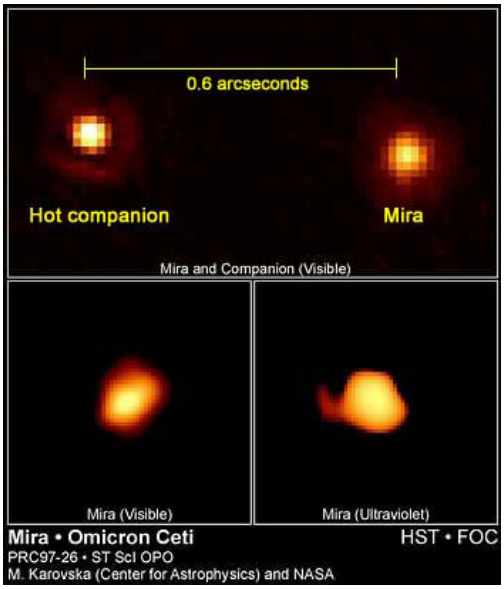

Figure 1.12: Mira and its binary companion *(credit Hubble Space Telescope)*.

1.4.4 Carbon-rich stars

Thanks to the third dredge-up, some carbon is brought up from the core to the surface. This additional material can change the chemical composition of the envelope. If the ratio of carbon over oxygen (C/O) is more than 1, the star evolves from an oxygen-rich spectral type to a carbon-rich one. Therefore, the former lines of oxides, such as TiO, VO, are replaced by CN, C_2. Figure 1.13 shows an example of a carbon star spectrum.

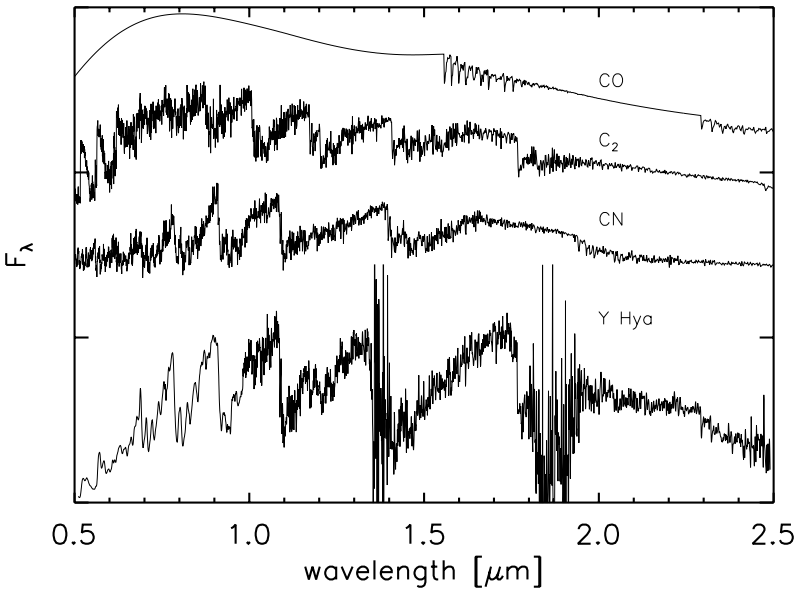

Figure 1.13: Observed spectrum of Y Hya (bottom) and the contributions of the molecules CO, C_2 and CN to a synthetic spectrum, taken from Loidl et al. (2001).

Carbon stars were discovered in the late 1860s by Father Angelo Secchi. Because of their cool surface temperatures, the molecular opacities and heavy line blanketing in the blue, their classification by temperature and luminosity remains difficult.

The Henry Draper classification system subdivided carbon stars into two types: N and R, depending on the amount of light extending into the violet region, with the implicit assumption of a temperature sequence. Later studies demonstrated that the extinction of light in the blue was more a function of carbon abundance than effective temperature.

Keenan & Morgan (1941) put aside the previous classification and decided to classify the carbon stars according to a temperature sequence with an added index for C_2 abundance.

The Revised Morgan-Keenan system (Keenan 1993) was designed to increase the accuracy of the classification and it remains the system used today. The carbon stars are classified in 5 categories, as described in Table 1.4.

Class	Criteria	Population
C-R	Strong in the blue, isotopic bands strong, Ba scarcely enhanced	Medium disk / pop I
C-N	Heavy, diffuse blue absorption, *s*-process elements enhanced over solar, weak isotopic bands	Thin disk / pop I
C-J	Very strong isotopic bands of C_2 and CN	
C-H	Very strong CH absorption	Halo / pop II
C-Hd	Hydrogen lines and CH bands weak or absent	Thin disk / pop I

Table 1.4: Spectral type of carbon stars, based on Barnbaum et al. (1996).

1.4.5 Thermally Pulsing AGB stars in population synthesis

The TP-AGB phase is difficult to model because of the physical processes which are going on. One difficulty is the fact that nuclear burning occurs in alternate hydrogen-rich and helium-rich shells. Furthermore, when the helium shell burns, it does so explosively because of the thin shell instability, which gives rise to the thermal pulses. Last but not least, mass-loss becomes catastrophic during this phase, thereby terminating the life of the star.

A few population synthesis models in the literature have accounted for the evolution of the C/O ratio along the asymptotic giant branch, a dichotomy between O-rich and C-rich spectra, and simple models for the effects of circumstellar dust (Mouhcine et al. 2002; Marigo et al. 2008). None of these can follow the cycle-dependent effects of pulsation in detail, and that is not their primary purpose. Their main aim is to predict average properties of stellar populations. Figure 1.14 shows the evolution of the isochrones for the TP-AGB over the last decade.

Intermediate mass stars become carbon-rich on the thermally pulsing asymptotic giant branch. The importance of C stars is determined by TP-AGB lifetimes and fractional TP-AGB lifetimes spent as a C star. The current trend is for TP-AGB lifetimes to be revised downwards, in particular at low metallicities and old ages (Gullieuszik et al. 2008; Girardi et al. 2010; Rosenfield et al. 2014).

TP-AGB and C star contributions are largest in populations with a significant component of intermediate age stars, such as intermediate-age star clusters ($L_{K,\mathrm{TPAGB}}/L_{K,\mathrm{total}} \sim 0.5$; Ferraro et al. 1995; Girardi et al. 2013) or galaxies with a strong post-starburst component (Lançon et al. 1999; Miner et al. 2011; but see Kriek et al. 2010 and Zibetti et al. 2013 for counter-examples). Melbourne et al. (2012) use star counts to show the contribution of TP-AGB stars reaches 17% at 1.6 μm in a sample of local galaxies, but they do not separate O-rich and C-rich stars. In near-infrared color magnitude diagrams of the Magellanic Clouds, a densely populated plume of C stars extends from $(J-K) = 1.2$ to $(J-K) = 2$ at its bright end (Nikolaev & Weinberg 2000). The corresponding contribution to the light at 2 μm amounts to 6 to 10% of the total, and is similar to that of O-rich TP-AGB stars (Melbourne & Boyer 2013).

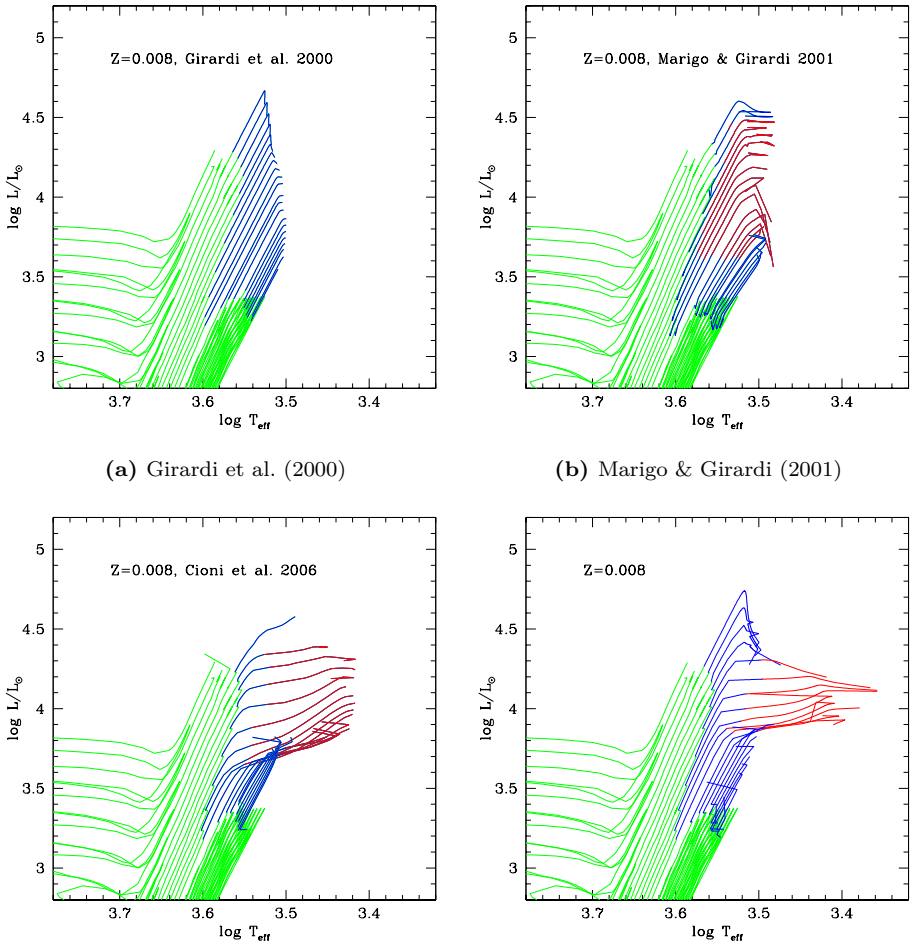

(a) Girardi et al. (2000)

(b) Marigo & Girardi (2001)

(c) Cioni et al. (2006)

(d) Marigo et al. (2008)

Figure 1.14: Evolution of the isochrones for the TP-AGB over the last decade. The pre-TP-AGB phases are drawn in green. On the TP-AGB, the O-rich surfaces are displayed in blue and the C-rich in red.

1.5 Outline of this thesis

The motivation for this thesis was to understand how the galaxies form and evolve. To answer this question, the pitch was to perform joint optical and near-infrared spectroscopic studies of stars with X-shooter.

We built a state-of-the-art stellar spectral library, XSL, which will be a benchmark library for stellar population studies in the era of James Webb Space Telescope and the European Extremely Large Telescope. A big step beforehand is to reduce the data. Although a full first-pass reduction of essentially all the XSL data was performed, only one aspect of the data reduction process is highlighted in this manuscript in *Chapter 4*. This chapter describes the computation of the response curves for X-shooter spectra. Because of the setup of the instrument and the contamination of the Earth's atmosphere, it is necessary to take both aspects into account for the flux calibration.

Our library contains more than 700 (final) stars, and at least 10 times more raw frames. Therefore, keeping track of all the frames is needed. Moreover, we want to be able to retrieve easily some basic informations such as the coordinates of the stars or to get the most up-to-date stellar parameters derived for a given star. For this purpose, we created a database and also a dedicated website to release our final spectra to the community. The description of both is done in *Chapter 5*.

Among the diversity of stars available within XSL, this thesis focuses on the carbon stars. *Chapter 2* presents our collection of carbon star spectra, which extends the range of spectra available and offers unprecedented spectral resolution ($R \sim 8000$). Our sample contains stars with a broad range of $(J - K)$ color and pulsation properties, located in the Milky Way and the Magellanic Clouds. In addition, we show that our sample becomes bimodal for $(J - K) \geq 1.6$, with the presence or absence of the absorption feature at $1.53\,\mu$m, generally associated with HCN and C_2H_2.

In *Chapter 3*, we compare those carbon-rich spectra with state-of-the-art hydrostatic models y doing so, we want to tackle the following questions: can the optical-to-near infrared SEDs be matched reasonably well, for stars with little or no evidence of circumstellar dust? In which spectral ranges can the models reproduce observed spectra at $R \sim 8000$? To what extent are parameters estimated from optical wavelengths compatible with those obtained from NIR wavelengths?

All good things come to an end, and this thesis is not an exception. The main results of this thesis are summarized in *Chapter 6*.

Chapter 2

Carbon stars in the X-shooter Spectral Library[1]

⋆ ⋆ ⋆

A. Gonneau, A. Lançon, S. C. Trager, B. Aringer, M. Lyubenova, W. Nowotny, R. F. Peletier, P. Prugniel, Y.-P. Chen, M. Dries, O. S. Choudhury, J. Falcón-Barroso, M. Koleva, S. Meneses-Goytia, P. Sánchez-Blázquez and A. Vazdekis

Submitted to Astronomy & Astrophysics

Abstract

We provide a new collection of 35 carbon star spectra that were obtained with the ESO/VLT X-shooter instrument as part of the X-shooter Spectral Library project. The spectra extend from blue optical wavelengths to 2.4 μm with a resolving power above ~ 8000. The sample contains stars with a broad range of $(J-K)$ color and pulsation properties, located in the Milky Way and the Magellanic Clouds.
We show that the distribution of spectral properties of carbon stars at a given $(J-K)$ color becomes bimodal (in our sample) when $(J-K)$ is larger than about 1.5. We describe the two families of spectra that emerge, characterized by the presence or absence of the absorption feature at 1.53 μm, generally associated with HCN and C_2H_2. Anticipating detailed comparisons with model spectra, we suggest that hot circumstellar dust emission in the near-infrared may help to explain the properties of those stars showing this feature.

[1] Based on observations collected at the European Southern Observatory, Paranal, Chile, Prog. ID 084.B-0869(A/B), 085.B-0751(A/B), 189.B-0925(A/B/C/D).

2.1 Introduction

In the 1860s, Father Angelo Secchi discovered a new type of star – Type IV – known today as the carbon stars (Secchi 1868). Carbon stars (C stars hereafter) are on the asymptotic giant branch (AGB) and have spectra that differ dramatically from those of K- or M-type giants. C stars are characterized by spectral bands of carbon compounds, such as the C_2 bands, and by the lack of bands from oxides such as TiO and H_2O. The classical distinction between carbon-rich and oxygen-rich stars is the ratio of carbon to oxygen abundance, C/O. If C/O > 1, oxygen is mostly bound to carbon in the form of carbon monoxide (CO), because this molecule has a high binding energy. As a result, little oxygen is left to form other oxides in such stellar atmospheres, whereas carbon atoms are available to form other carbon compounds.

Carbon stars are significant contributors to the near-infrared light of intermediate age stellar populations (1–3 Gyr) (e.g., Ferraro et al. 1995; Girardi & Bertelli 1998; Maraston 1998; Lançon et al. 1999; Mouhcine & Lançon 2002; Maraston 2005; Marigo & Girardi 2007). The absolute level of this contribution impacts on mass-to-light ratios and has important implications for the study of star formation in the universe. It is a matter of active research both on the theoretical side (e.g., Weiss & Ferguson 2009; Girardi et al. 2013; Marigo et al. 2013) and in the framework of extragalactic observations (e.g., Riffel et al. 2008; Kriek et al. 2010; Miner et al. 2011; Melbourne et al. 2012; Melbourne & Boyer 2013; Boyer et al. 2013; Zibetti et al. 2013). The quality of the photometric and spectroscopic predictions made by population synthesis models in this field depends on the existence of stellar spectral libraries, and to their completeness in terms of evolutionary stages and spectral types.

Carbon stars contribute significantly to the chemical enrichment and to the infrared light of galaxies, but only small collections of C-star spectra exist to represent this emission (see Lloyd Evans 2010, for a review that includes earlier observations). An extensive low-resolution optical spectral atlas (0.4–0.7 μm) was published by Barnbaum et al. (1996) as a reference for C-star classification. It contains 119 spectra. A first impression of the near-infrared (NIR) spectra of C stars was provided by Joyce (1998), again at low spectral resolution (48 spectra, with a spectral resolution of ~ 500). Repeated observations of single long-period variable (LPV) stars showed significant changes with phase, emphasizing the necessity of simultaneous observations across the spectrum. As NIR detectors improved, Lançon & Wood (2000) produced a library of 0.5–2.5 μm spectra of luminous cool stars with a resolving power $R = \lambda/\delta\lambda \simeq 1100$ in the NIR. It includes 25 spectra of seven carbon stars. Simultaneous optical spectra are available for 21 of these, but only at very low resolution ($R \simeq 200$). More recently, Rayner et al. (2009) published the IRTF Spectral Library, which includes 13 stars of spectral type S (C/O = 1) or C. Their spectra have no optical counterparts, but extend from 0.8 μm as far as 5.0 μm at a resolving power $R \sim 2000$.

The C-star collection of Lançon & Wood (2000) has been used in several population synthesis models (Lançon et al. 1999; Mouhcine & Lançon 2002; Maraston 2005; Marigo et al. 2008). Lançon & Mouhcine (2002) suggested using a near-infrared color as a first order classification parameter for the C-star spectra in

these applications, but also noted this disregards other potentially important parameters, such as the carbon over oxygen (C/O) ratio or the pulsation properties. One of the shortcomings of this data set is the narrow range of properties (Lyubenova et al. 2010, 2012). Another is that it simply contains too few stars to represent the possible variety of C-star spectra.

In the modelling of luminous cool stellar populations, two important sources of uncertainties (other than the incompleteness of spectral libraries) are the fundamental parameters assigned to the observed stars, and the effects of circumstellar dust related to pulsation and mass loss on the upper asymptotic giant branch. Estimating effective temperatures, C/O ratios and gravities requires a comparison with theoretical spectra. Loidl et al. (2001) showed that it is difficult to obtain a good theoretical representation of both the energy distribution and the spectral features, even for relatively blue C stars. Aringer et al. (2009) highlighted that static models without circumstellar dust cannot reproduce any NIR carbon star energy distribution with $(J - K) > 1.6$. Spectral energy distributions for pulsating models have been computed in small numbers and at low spectral resolution (Nowotny et al. 2011, 2013). They reproduce the global trend from optical carbon stars to dust-enshrouded sources, for which the whole spectrum is dominated by the emission from dust shells. But whether or not they reproduce the relationship between color and the depth of spectral features remains an open question. It is important to find out how dust shells may affect the optical and near-infrared spectra of C stars, especially for objects in the range $1.4 \leq (J - K) \leq 2$, in which the NIR luminosities of these AGB stars are large.

In this paper, we present 35 medium-resolution carbon star spectra that extend from the near-ultraviolet through the optical into the near-infrared (0.3–2.5 μm). Although this collection is by itself not complete, it considerably extends the range of data available, and it offers unprecedented spectral resolution. We expect it to serve both the purpose of testing theoretical models for C-star spectra (Gonneau et al., in preparation) and of improving future population synthesis models. We describe the input stellar spectral library, our sample selection and the data reduction in Sections 2.2 and 2.3. We discuss the spectra using a NIR color as a primary classification criterion in Section 2.4; in particular we discuss the appearance of a bimodal behavior of the spectral features and the global spectral energy distribution in the redder C-star spectra. We define a list of spectroscopic indices in Section 2.5 that we use in Section 2.6 to quantify the spectral behavior and in Section 2.7 to compare our spectra with existing libraries of carbon-rich stars. We discuss our results in Section 2.8 and present our conclusions in Section 2.9.

2.2 The XSL carbon star sample

With X-shooter (Vernet et al. 2011), the European Southern Observatory (ESO) made available a high throughput spectrograph allowing the simultaneous acquisition of spectra from 0.3 to 2.5 μm, using two dichroics to split the beam into three arms: ultraviolet-blue (UVB), visible (VIS) and near-infrared (NIR). This simultaneity is invaluable when observing variable stars, and many C stars are LPVs (Lloyd Evans 2010).

Table 2.1: Observational properties of our sample

Name	Coordinates (J2000)	Galaxy	ESO Run	ESO OBid	MJD	Flux note[a]	$(J-K_s)$ [mag][b]	Group [b]	1.53 μm feature [b]
Cl* NGC 121 T V8	00:26:48 −71:32:50	SMC	P89	723477	56090.41	N	0.95	1	
2MASS J00490032-7322238	00:49:00 −73:22:23	SMC	P84	389528	55110.07	N	1.43	2	
2MASS J00493262-7317523	00:49:32 −73:17:52	SMC	P84	389526	55110.09	N	1.39	2	
2MASS J00530765-7307477	00:53:07 −73:07:47	SMC	P84	389511	55116.12	N	1.35	2	
2MASS J00542265-7301057	00:54:22 −73:01:05	SMC	P84	389505	55119.07	N	1.81	3	
2MASS J00553091-7310186	00:55:30 −73:10:18	SMC	P84	389503	55119.09	N	2.02	3	
2MASS J00563906-7304529	00:56:39 −73:04:53	SMC	P84	389499	55114.12	N	1.29	2	
2MASS J00564478-7314347	00:56:44 −73:14:34	SMC	P84	389497	55119.11	N	1.69	3	
2MASS J00570070-7307505	00:57:00 −73:07:50	SMC	P84	389495	55111.07	N	1.58	2	
2MASS J00571214-7307045	00:57:12 −73:07:04	SMC	P84	389493	55111.08	N	1.47	2	
2MASS J00571648-7310527	00:57:16 −73:10:52	SMC	P84	389489	55111.11	N	1.28	2	
2MASS J01003150-7307237	01:00:31 −73:07:23	SMC	P84	389481	55111.12	N	1.32	2	
Cl* NGC 419 LE 35	01:08:17 −72:53:01	SMC	P90	804029	56213.20	V	2.04	3	
Cl* NGC 419 LE 27	01:08:20 −72:52:52	SMC	P90	804024	56213.18	V	1.92	3	
T Cae	04:47:18 −36:12:33	MW	P84	389388	55142.19	N / S	2.19	3	
SHV 0500412-684054	05:00:29 −68:36:37	LMC	P90	804254	56213.29		1.84	3	Y
SHV 0502469-692418	05:02:28 −69:20:09	LMC	P90	804257	56213.31		1.99	3	Y
SHV 0504353-712622	05:03:55 −71:22:22	LMC	P84	389445	55119.26	N	2.09	3	
SHV 0517337-725738	05:16:33 −72:54:32	LMC	P90	804263	56213.36		1.09	1	
SHV 0518222-750327	05:16:49 −75:00:22	LMC	P84	389433	55142.28	N	2.50	4	Y
SHV 0518161-683543	05:18:02 −68:32:39	LMC	P90	804266	56234.29	N	0.98	1	
SHV 0520505-705019	05:20:15 −70:47:26	LMC	P84	389428	55142.32	N	2.40	4	Y
SHV 0520427-693637	05:20:20 −69:33:44	LMC	P90	804284	56240.35		1.94	3	
SHV 0528537-695119	05:28:27 −69:49:01	LMC	P84	389414	55226.19	V / N	3.16	4	Y
SHV 0525478-690944	05:25:28 −69:07:13	LMC	P84	389421	55142.36	N	3.05	4	Y
SHV 0527072-701238	05:26:37 −70:10:11	LMC	P90	804300	56261.34		2.32	4	Y
SHV 0536139-701604	05:35:42 −70:14:16	LMC	P84	389406	55226.23	N	2.96	4	Y
[ABC89] Pup 42	08:04:57 −29:51:25	MW	P90	804003	56292.25		2.66	4	
IRAS 09484-6242	09:49:49 −62:56:09	MW	P92	998138	56617.34		1.84	3	
[W65] c2	11:22:05 −59:38:45	MW	P90	804322	56320.35		1.94	3	
[ABC89] Cir 18	13:55:26 −59:22:19	MW	P89	814763	56319.37		2.41	4	
HE 1428-1950	14:30:59 −20:03:42	MW	P91	929514	56383.33		0.72	1	
V CrA[c]	18:47:32 −38:09:32	MW	P89	723829	56144.17		-	-	
HD 202851	21:18:43 −01:32:03	MW	P89	723822	56144.31		0.65	1	

[a] The letter indicates for which X-shooter arm no absolute flux-calibration was possible: V=visible, N=near-infrared. The S letter indicates that the spectrum is saturated in the K-band.

[b] These properties are discussed in Section 2.4. The Y letter indicates the presence of the 1.53 μm absorption band.

[c] See Appendix 2.A for more details about V CrA.

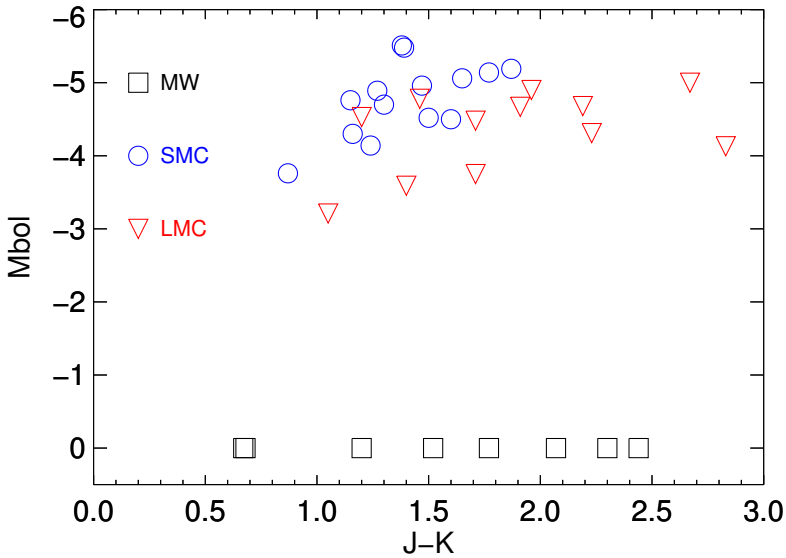

Figure 2.1: Bolometric magnitudes and literature colors of our sample stars. The LMC stars (red triangles) are taken from Hughes & Wood (1990). The SMC stars (blue circles) are derived by Cioni et al. (2003). No distances are known reliably to the MW stars (black squares) of the sample.

Our team is building a large stellar spectral library under an ESO Large Programme, the X-shooter Spectral Library (hereafter XSL, Chen et al. 2014a). It contains more than 700 stars, observed at moderate resolving power ($7\,700 \leq R \leq 11\,000$, depending on the arm) and covering a large range of stellar atmospheric parameters. The homogeneous spectroscopic extension into the near-infrared makes XSL unique among empirical libraries.

Neglecting the diversity of stars available in XSL, this paper focuses only on carbon stars. A full description of the C-star sample can be found in Table 2.1. Table 2.4 summarizes properties of these stars as available in the literature.

The sample includes stars from the Milky Way (MW) as well as from the Large and Small Magellanic Clouds (LMC, SMC). As C stars on the AGB form a relatively tight sequence in NIR color-color plots (2MASS, Skrutskie et al. 2006; DENIS, Epchtein et al. 1997; WISE, Wright et al. 2010; Whitelock et al. 2006; Nowotny et al. 2011), the primary aim of the selection was to sample an adequate range of near-infrared colors. This range was restricted to $(J - K) < 3$ to avoid stars with negligible optical flux. A few C stars with $(J-K) < 1$ are present in the sample, although these stars are considered too hot to be standard AGB objects; they are instead thought to have become carbon-rich through other processes, such as mass transfer from a companion.

While the effects of metallicity on stellar evolution tracks are large, leading to varying C star number statistics as a function of metallicity (Mouhcine et al. 2002;

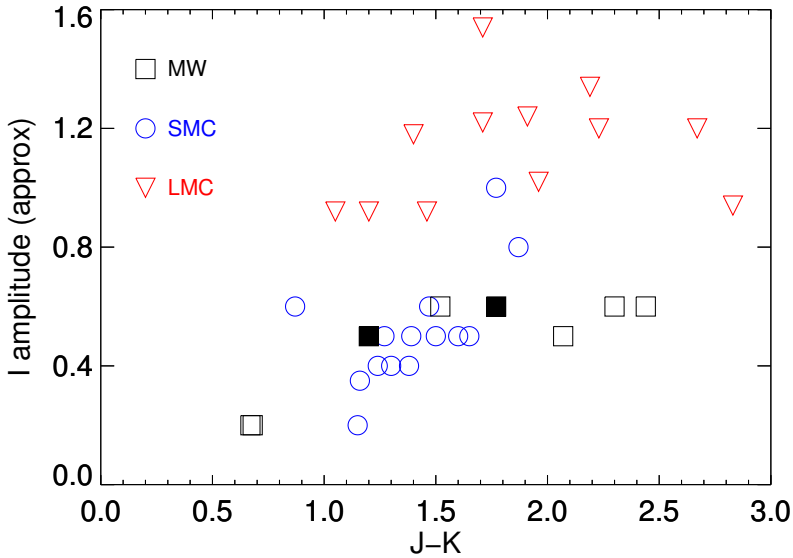

Figure 2.2: *I*-band amplitudes of our sample stars. Symbols are as in Fig. 2.1. The amplitudes are estimated peak-to-peak variations. The values for LMC stars are taken from Hughes & Wood (1990). For the SMC, we estimated amplitudes using OGLE light curves (available through the Vizier service at CDS). For the MW, we estimated amplitudes based on K-band amplitudes by Whitelock et al. (2006); a value of 0.5 was assigned when no data was available. Note that for two MW stars (highlighted as filled squares) large amplitude luminosity dips are known to occur occasionally in addition to small-amplitude variations (the R CrB phenomenon).

Mouhcine & Lançon 2003; Marigo et al. 2008; Groenewegen 2007), the effects of metallicity on the spectrum of a C star of a given color are relatively small based on static models (Loidl et al. 2001; Gonneau et al., in prep). Therefore, we initially consider all stars in the sample as one group, irrespective of the host galaxy.

A variety of LPV pulsation amplitudes and light curve shapes can be found in C stars with $1 \leq (J - K) \leq 3$. A distinct period and a clear period-luminosity relation exist for large amplitude variables (e.g., Whitelock et al. 2006), but many smaller amplitude variables found in this range have extremely irregular light curves (see Hughes & Wood 1990). As shown in Figures 2.1 and 2.2 there are systematic differences between the pulsation properties of our subsamples of C stars from the MW, the LMC and the SMC. On average, the LMC subset has a larger pulsation amplitude. And at a given color, the SMC stars tend to be brighter than their LMC counterparts (no reliable distances are available for the MW stars of the sample). These selection biases must be kept in mind when interpreting the spectra.

2.3 Data reduction

In the following section, we summarize the applied data reduction procedures. The carbon star data were acquired over ESO Periods 84, and 89 to 92 (Table 2.1). The narrow-slit widths for UVB, VIS and NIR frames were 0.5″, 0.7″, 0.6″, respectively.

2.3.1 UVB and VIS arms: extraction and flux-calibration

The UVB- and VIS-arm carbon star spectra observed in Period 84 are part of XSL Data Release I (DRI, Chen et al. 2014a) and are used here unchanged. The basic data reduction for DRI was performed with X-shooter pipeline version 1.5.0, up to the creation of rectified, wavelength-calibrated two-dimensional (2D) spectra. The extraction of one-dimensional (1D) spectra was performed outside of the pipeline with a procedure inspired by the prescription of Horne (1986). Observations of both the science targets and spectrophotometric standard stars through a wide slit (5.00″) were used to obtain absolute fluxes (see Table 2.1 for exceptions).

We reduced UVB and VIS frames from later periods with X-shooter pipeline version 2.2.0 (Modigliani et al. 2010). For the purposes of this paper, the pipeline was also used for the extraction of 1D spectra and flux calibration. The choice of pipeline version does not affect our conclusions.

2.3.2 NIR arm: extraction

All NIR frames were reduced with X-shooter pipeline version 2.2.0, up to the creation of rectified, wavelength-calibrated 2D order spectra.

The extraction of 1D spectra and flux calibration were performed outside of the pipeline with procedures of our own. A main driver for this choice was the need for more control over the rejection of bad pixels. The standard acquisition procedure for NIR spectra of point sources is a nodding mode, with observations of the target at two positions (A and B) along the spectrograph slit. By default the pipeline combines the A and B frames (flatfielded and rectified) into a single 2D image in which the central lines contain the sum of the stellar spectra of A and B, minus the sum of the skies. This cumulates the bad pixels of both the A and B positions into the bad pixel mask of the combined spectrum, sometimes leaving very few good pixels to work with. Instead, we extracted A from (A−B) and B from (B−A) and combined them subsequently. Each extraction implements a rejection of masked and outlier pixels (following Horne 1986 prescriptions), as well as a weighting scheme based on a smooth throughput profile[2] and on the local variance. After pipeline rectification, we note that the spectra in the extreme orders of the NIR arm display some residual curvature and broadening, which our profile accounts for in a satisfactory fashion. We then merged all the extracted orders to create a continuous 1D NIR spectrum.

The wide-slit observations of the program stars and of spectrophotometric standard stars, required for flux calibration, were reduced with pipeline sky subtraction switched off because residuals or negative flux levels were too frequent. The sky was estimated from both sides of the spectrum at the extraction of 1D spectra.

[2] Median boxcar (100Å) smoothing along the spectral direction.

We did not implement aperture corrections but used apertures as large as possible (considering the need to estimate the sky), sometimes at the expense of the signal-to-noise ratio of these wide-slit spectra. A number of the wide-slit observations of carbon stars lacked significant signal (especially in ESO Period P84; cf. Table 2.1), making it impossible to correct the higher resolution observations of these stars for slit losses.

The flux calibration of the NIR arm of X-shooter cannot be done without considering telluric absorption, which is discussed in Section 2.3.4.

2.3.3 Telluric correction

X-shooter is a ground-based instrument. Therefore, we must correct our spectra for extinction by the Earth's atmosphere. Standard flux calibration procedures account for continuous extinction, but not for molecular absorption lines (e.g., water vapour, molecular oxygen, carbon-dioxide, methane). We will refer to these as telluric features hereafter. Telluric absorption features particularly affect the NIR arm and the reddest part of the VIS arm of X-shooter.

Different methods exist to remove telluric absorption. Typically a telluric standard star is observed close in time and airmass to the science object, and then a telluric transmission spectrum is prepared by removing the intrinsic stellar spectrum, e.g., fitting and removing H lines and normalizing the continuum. The science spectrum is then divided by the telluric spectrum. Unfortunately, as highlighted by Chen et al. (2014a), the telluric absorption lines change strength on timescales shorter than the "long" exposure times ($\geq$ 90 seconds) of faint XSL stars and the total observational overhead time of $\sim$ 900 seconds, resulting in a noisy telluric correction. In addition, small changes in spectral resolution and wavelength zero-point occur even between successive observations. We use two different sets of telluric templates to correct telluric absorption in the VIS and NIR arms of our X-shooter spectra.

VIS FRAMES Chen et al. (2014a) built an empirical telluric library using 152 telluric standard stars with spectral types B and A from Periods 84 and 85. To do so, they separated the main telluric features in the observed telluric standard spectra from the intrinsic features of these hot stars using synthetic spectra. The original 1D spectra of the telluric standard stars were divided by the best fit set of template synthetic stellar spectra to obtain a corresponding set of 152 "raw transmission spectra". These raw transmission spectra were then cross-correlated against a high resolution model transmission spectrum to ensure that all of the empirical transmission spectra are at exactly the same wavelength. Any of the pixels in the empirical transmission spectra that deviated more than 10σ from the templates were set to unity to avoid introducing noise or artificial features into the telluric-corrected spectra.

The simplest procedure to correct the science spectra for the telluric features would be to divide a science spectrum by the temporally-closest transmission spectrum. Chen et al. improved this method by making use of the variety of telluric absorption features present in their library. They developed a method based on Principal Component Analysis (PCA) to reconstruct and remove telluric absorp-

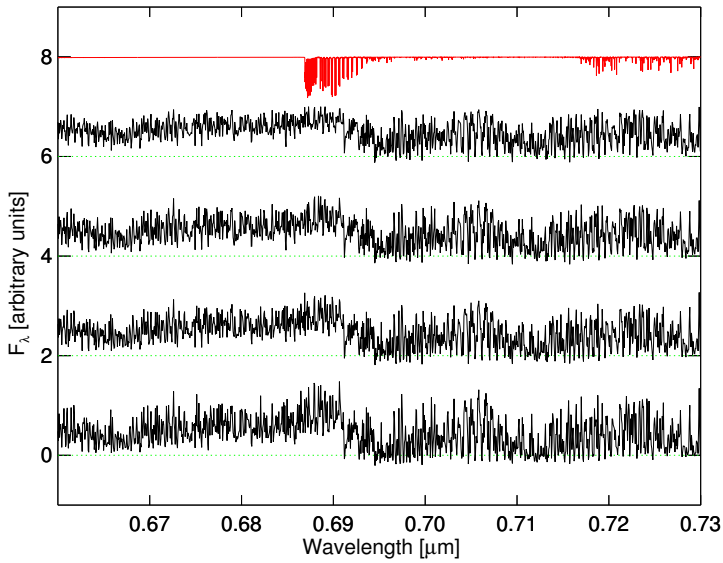

Figure 2.3: Illustrative spectra in the VIS wavelength range. The red spectrum is a telluric sky model. From top to bottom, the stars are 2MASS J01003150-7307237, 2MASS J00571648-7310527, 2MASS J00493262-7317523 and 2MASS J00571214-7307045.

tion. For cooler stars, such as carbon stars, the PCA method was not found to work well. Indeed, the accuracy of the PCA method is bound to the representation of the stellar continuum, and carbon stars have strong molecular bands, which are not easy to trace. Therefore, for the VIS carbon stars, the temporally-closest transmission spectra were used.

Figure 2.3 shows some of the spectra of the carbon stars over a small part of the visible wavelength range (0.07 μm wide). The red spectrum is a telluric model, arbitrarily chosen, shown for comparison.

NIR FRAMES For the NIR frames, we choose to use the Cerro Paranal Sky Model, a set of theoretical telluric transmission spectra provided by J. Vinther and the Innsbruck team (Noll et al. 2012; Jones et al. 2013). These models are a more complete version of the spectra that can be found on the web application SkyCalc[3,4]. We couple the telluric correction to the flux calibration process, as described in the following subsection.

[3] `http://www.eso.org/observing/etc/bin/gen/form?INS.MODE=swspectr+INS.NAME=SKYCALC`

[4] The files were computed with version 1.2 based on SM-01 Mod1 Rev.74, LBLRTM V12.2, and the line database was aer_v_3.2.

2.3.4 NIR telluric correction and flux-calibration

The need for specific procedures to account and correct for telluric absorption is common to many NIR instruments. It is exacerbated in X-shooter data by the conjunction of an unfortunate feature of the flatfield frames and of (arguable) choices made in the pipeline. In the design of the pipeline, spectral features of the flatfield exposure remain present in the (globally) normalized flatfield frames by which the data are divided and are propagated into the estimated instrument response curves. One such feature dominates over any other detector variations, a very strong and sharp bump in the K-band flatfielded spectra, with a much weaker secondary bump in the H-band (see, e.g., Fig. 9 of Moehler et al. 2014). At the altitude of the ESO Very Large Telescopes, water vapor absorption leaves broad gaps with no useable data in the NIR spectra, and only few points anywhere that are free of any telluric molecular absorption. The interpolation of estimated response curves through these gaps is a particularly poorly constrained exercise in the case of X-shooter pipeline products, because only relatively high order polynomials can match the bumps due to the flatfield. Therefore, we designed a method to evaluate the response curve that explicitely accounts for telluric absorption. Other implementations of this idea were developed in parallel by Moehler et al. (2014) and Kausch et al. (2015).

The procedure for the response curve is as follows. Because the flatfield bumps are variable in time, we ensure that the spectrophotometric standard star used to derive a response curve for a given program star is reduced with the same flatfield frames as the program star. We then fit the flatfielded spectrum of the flux standard with the product of the theoretical spectrum of this star, a telluric transmission model and the unknown response curve. Spectral regions with telluric features of intermediate depth are used to select the best-fitting telluric model within the available collection. The response curve is represented with a spline polynomial, with higher concentrations of spline nodes where required by the flatfielding bumps. We correct the response curve for continuous atmospheric extinction using the airmass of the flux standard.

For the subsequent correction of the narrow-slit spectra of carbon stars, the search of the "best" telluric model is also needed and more important than above (as we care not only about the shape but also about the lines). Here, we allow for a larger variety of telluric transmissions by combining principal components of a subset of transmission models with adequate airmasses. We perform the χ^2 minimization separately in various wavelength intervals[5]. The idea is to better target different molecules in the telluric spectra. Once the science frame is telluric corrected and divided by the response curve, we correct it for continuous atmospheric extinction using the airmass at the time of observation.

Whenever possible, the final flux-calibrated frames were absolutely flux-calibrated by using wide-slit ($5''$) observations (refer to column "Flux note" of Table 2.1 for exceptions).

Figure 2.4 shows the quality of our telluric correction process on some of our carbon stars. The red spectrum shows a telluric model for comparison.

[5] We use the following wavelength regions: 0.9–1.345 μm, 1.46–1.8 μm, 1.975–2.1 μm and 2.1–2.5 μm.

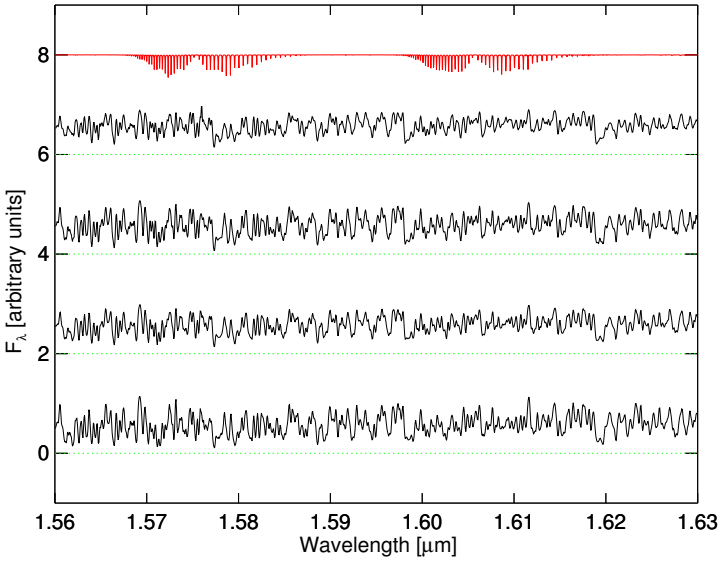

Figure 2.4: Illustrative spectra in the NIR wavelength range. The red spectrum is a telluric sky model. The stars are the same as in Fig. 2.3.

2.3.5 Problem with the last order of NIR spectra

Some of our NIR observations, once flatfielded, extracted, merged and flux-calibrated, display a step between the two reddest orders (around 2.27 μm, between orders 12 and 11). This could be related to a known vignetting problem in order 11, to the high background levels in certain exposures, or to other unidentified artifacts. Although we account for variation in the background emission along the slit in order 11, and we reduce pairs of one flux standard and one carbon star with the same flatfield, we do not eliminate the step completely. The flux level and slope within order 11 therefore remain more uncertain than in other orders. We patch this step effect by forcing the average flux level between 2.28 and 2.29 μm in order 11 to match the extrapolation of a linear fit to the spectrum between 2.150 and 2.265 μm. This choice is guided by the aspect of theoretical spectra of C stars and by published observations with other instruments. Broad band colors involving the K_s-band change by (usually much) less than 2% with this correction. The estimated extra uncertainty on measures of the ^{12}CO bandhead within order 11 remains below a few percent for weak bands, but can reach 10% for some of the stars with strong CO bands.

2.3.6 Final steps

We use theoretical models of carbon stars ($R \sim 200\,000$), computed specifically for this paper (based on the atmosphere models of Aringer et al. 2009), to shift the wavelength scale of our observed spectra to the vacuum rest-frame.

Finally, the three arms are merged to produce a complete spectrum from the near-UVB to the NIR [6]. The resolving power in the UVB, VIS and NIR ranges of the merged spectra are, respectively, $R \sim 9100$, ~ 11000 and ~ 7770.

2.4 The diversity of carbon star spectra

Our sample of carbon stars presents quite a diversity in spectral shape and absorption-line characteristics. Figures 2.21 to 2.26 show our spectra from the UVB to the NIR wavelength range. The spectra were normalized to the flux at 1.7 μm and shifted for display purposes. The grey bands in the NIR mask regions where the telluric absorption is deepest and the signal can not be recovered. It is important to note that the spectra were severely smoothed to a common resolution ($R \sim 2070$).

We group our carbon stars by $(J - K)$ values when describing them in the remainder of this Section. Figure 2.5 summarizes the spectral variety of the sample, showing representative examples of each group. The colors are used to better identify the different groups.

The vast majority of features in carbon stars spectra in this wavelength range are due to CO, CN and C_2. Some bands have sharp bandheads, but a forest of lines from various transitions are spread across the whole spectrum. Between 0.4 and 0.6 μm the C_2 Swan bands (Swan 1857) are dominant. Longward of 0.6 μm, the most prominent bandheads are due to CN. Note that the NIR CN bands, in particular the 1.1 μm bandhead, are also seen in M type giants and supergiants (Lançon et al. 2007; Davies et al. 2013). The C_2 band at 1.77 μm is one of the unambiguous characteristics of C stars in the NIR. The CO bands in the H and K window are also present with varying strengths in all the spectra.

2.4.1 Group 1 – The bluest stars: $(J - K) < 1.2$ [5 stars]

Figure 2.21 shows the five hottest C stars in our sample. The top two spectra of Fig. 2.5, displayed in blue, are representative of the two types of behaviors found in this group.

The top two stars of Fig. 2.21, HD 202851 and HE 1428-1950, have spectra similar to those of early K type giants (CN band at 0.431 μm and G band of CH of similar strength, Hβ line in absorption). But they clearly display the C_2 bands characteristic of C stars, in particular the Swan bands around 0.47 μm and 0.515 μm.

The three bottom spectra of Fig. 2.21 have spectral energy distributions (SED) that peak at longer wavelengths, but have weaker molecular features in the optical range. The CN band at 0.431 μm and the G band of CH are undetectable in two of the three stars. On the other hand, the red system of CN is slightly stronger, and the NIR C_2 bandhead (1.77 μm) and the CO bands are significantly stronger. Two of these three spectra display hydrogen emission lines, a phase-dependent signature of pulsation.

[6] The three arms overlap quite well: UVB: 0.3–0.59 μm; VIS: 0.53–1.02 μm; NIR: 0.99–2.48 μm.

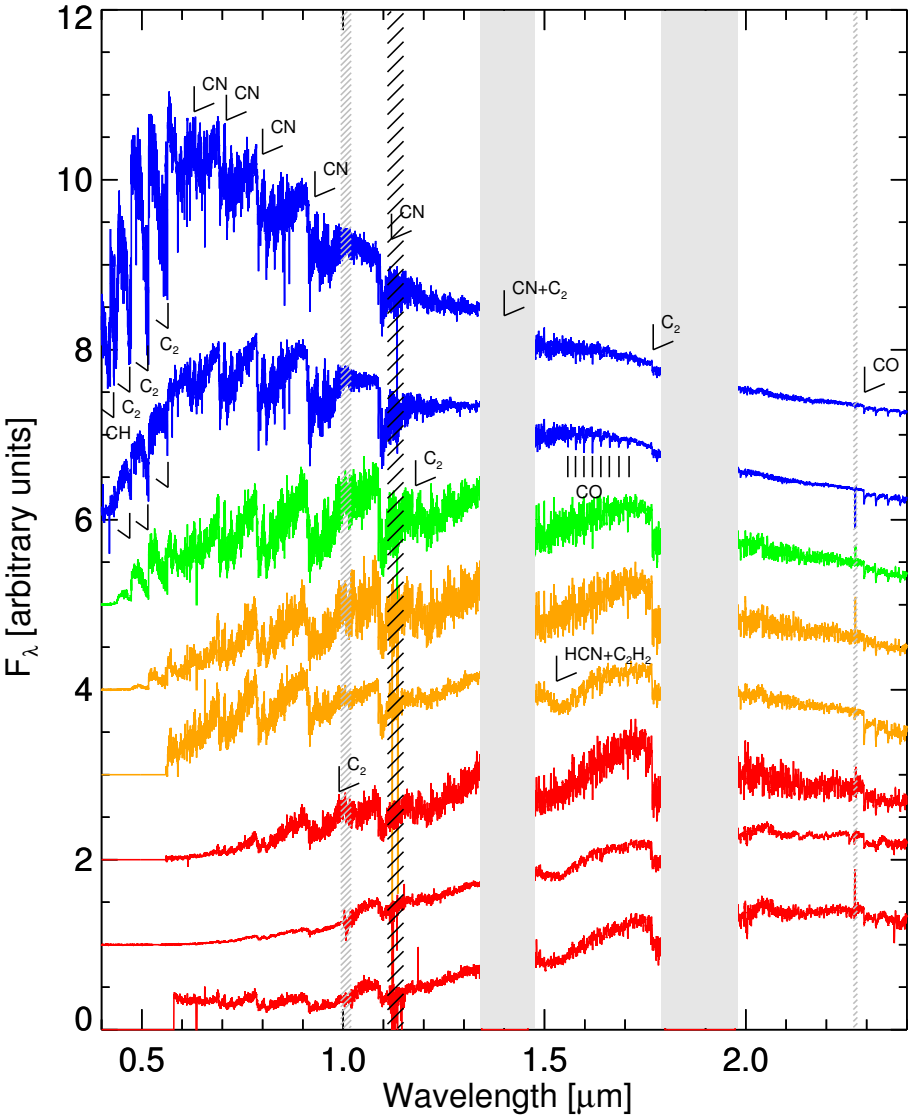

Figure 2.5: Representative spectra from our sample of carbon stars. The grey bands mask the regions where telluric absorption is strongest. The areas hatched in black are those that could not be corrected for telluric absorption in a satisfactory way. The areas hatched in grey are the merging regions between the VIS and NIR frames and between the last two orders of the NIR part. In some spectra, there is a lack of data at 0.635 μm. The spectra have been smoothed for display purposes. The colors represent the different groups of carbon stars. Blue color is for stars from Group 1, green for Group 2, orange for Group 3 and red for Group 4. The spectra in this figure are, from top to bottom, HE 1428-1950, Cl* NGC 121 T V8, 2MASS J00571214-7307045, 2MASS J00542265-7301057, SHV 0502469-692418, [ABC89] Cir 18, SHV 0525478-690944, SHV 0528537-695119.

2.4.2 Group 2 – Classical C stars : $1.2 < (J - K) < 1.6$ [7 stars]

Figure 2.22 shows classical C stars: seven stars belong to this group. The third spectrum in Fig. 2.5, displayed in green, is representative of this group. All these C stars have $1.2 < (J - K) < 1.6$. They happen to be located in the SMC, but we note that many of the Milky Way C stars of Lançon & Wood (2000) would fall in this category.

At optical wavelengths, the Swan bands are the first features to appear when C/O > 1. Compared to the first group of spectra, the spectra collected here have significantly stronger absorption bands of CN and C_2 in the NIR. C_2 absorption modifies the spectrum across the J band, and creates a strong bandhead at 1.77μm. A forest of lines of both CN and C_2 is responsible for the rugged appearance of the spectrum, which must not be mistaken as an indication of noise. CO bands in the H window appear weak, as a combined consequence of the C/O ratio and of overlap with many other features.

The SED and the H band (CO, C_2, forest of CN and C_2 lines) of the top spectrum of Fig. 2.22 seem to indicate that this star is slightly warmer, or has a lower C/O ratio, than the others. The opposite holds for the last spectrum of that figure.

2.4.3 Group 3 – Redder stars: $1.6 < (J - K) < 2.2$ [13 stars]

Figures 2.23 and 2.24 show redder stars. Thirteen stars compose this group. Group 3 is less homogeneous than Group 2: while some spectra simply seem to extend the sequence of Group 2 to redder SEDs with stronger features, others deviate from this behavior. This leads us to define two subgroups. A representative of each subgroup is included in Fig. 2.5 (see the fourth and fifth spectra, displayed in orange).

The stars that simply extend the behavior of group 2 have strong C_2 bands in the J- and H-bands and weak CO bands. In two of these stars (T Cae and [W65] c2), the CO bands are stronger, suggesting a C/O ratio closer to 1 (cf. the S/C star BH Cru in Lançon & Wood 2000). We warn however that the interpretation of ratios of CO to other band strengths in terms of abundance ratios is a non-trivial exercise, as the band strengths ratios may depend on phase (see the multiple spectra of R Lep in Lançon & Wood 2000, or those of V Cyg in Joyce 1998).

The two stars that stand out from the crowd are SHV 0500412-684054 and SHV 0502469-692418. They are characterized by an absorption band around 1.53 μm, weaker C_2 absorption, stronger CO absorption and a significantly smoother general appearance. This latter property has, to our knowledge, never been highlighted before. In hindsight, it is also noticeable in previously published spectra that display the 1.53 μm feature (Lançon & Wood 2000; Groenewegen et al. 2009; Rayner et al. 2009).

Inspection of the spectra with the 1.53 μm feature also suggests that their emission in the red part of the optical spectra is relatively strong, considering their red NIR spectra. The spectra however drop rapidly to a negligible flux in the blue.

2.4.4 Group 4 – The reddest stars: $(J - K) > 2.2$ [9 stars]

The last two figures, Figures 2.25 and 2.26, show our reddest stars. The dichotomy seen in Group 3 is very obviously present here as well. The three bottom spectra from Fig. 2.5, displayed in red, are representative of that group, composed of nine stars. The general trend in this group is that the energy peak shifts from the optical to the near-infrared, which leads to a "plateau" in the K band of the reddest objects.

It is interesting to note that at higher $(J - K)$, more stars display the 1.53 μm absorption feature. The fact that the feature appears only in very red stars (but not in all very red stars) is consistent with previous observations (Joyce 1998; Groenewegen et al. 2009). The spectra that display 1.53 μm absorption share the properties already mentioned for their counterparts in Group 3. They clearly have a smoother appearance than the others. Unfortunately, the S/N ratio is poor for some of these objects beyond 2.25 μm. Where it is good, eye inspection indicates that the CO bands in these smoother spectra have strengths similar to those in spectra with a forest of CN and C_2 lines. In three cases (SHV 0520505-705019, SHV 0527072-701238, SHV 0528537-695119), there seems to be an excess of flux in the red part of the optical spectrum, compared to other stars.

2.4.5 The 1.53 μm feature

The 1.53 μm absorption feature was first noticed in low temperature carbon stars of the Milky Way (Goebel et al. 1981; Joyce 1998). It is associated by these authors with a large amplitude variability. The underlying molecules are most likely a combination of HCN and C_2H_2 (Gautschy-Loidl et al. 2004), and the 1.53 μm band is thought to be an overtone of the strong absorption band sometimes seen around 3 μm (e.g., spectrum of R Lep in the IRTF library). However, the correlation between the depth of these features would deserve to be established more precisely (the correlation is poor according to Joyce 1998).

The 1.53 μm feature was identified in our sample of carbon stars by visual inspection. In Figures 2.14, 2.15, 2.16, 2.17 of Sections 2.6 and 2.7, these stars are identified by red circles to help identify the various spectral properties that accompany the presence of this band.

In our sample, all the spectra that display the 1.53 μm feature belong to large amplitude variables. The fact that they all happen to be in the LMC should be seen as a selection effect, since stars with this feature have previously been found both in the Milky Way and also in dwarf galaxies more metal-poor than the LMC (e.g., the Sculptor dwarf, Groenewegen et al. 2009).

2.5 Derived spectroscopic indices for carbon stars

As we obtained spectra of carbon stars over the whole X-shooter wavelength range, from the UVB to the NIR, we were able to derive spectroscopic indices from our flux-calibrated spectra to compare our sample with previous studies.

To measure the strength of any absorption band X, we use (in most cases) the following formula:

$$I(X) = -2.5 \log_{10}[F_b(X)/F_c(X)] \tag{2.1}$$

where $F_b(X)$ and $F_c(X)$ are the mean energy densities received in the wavelength bin in the absorption band region and the (pseudo-)continuum[7] of index X.

We note here that these "one-sided" indices depend on the quality of the flux calibration over moderate wavelength spans, in contrast to the classic "two-sided" Lick/IDS-type indices such as those defined by, e.g., Burstein et al. (1984), which are robust to short-wavelength flux-calibration issues. While we have confidence in our long-wavelength flux calibration, we suggest caution when considering small index differences between diffe-rent samples or even different stars. We are however confident in any strong index trend displayed below.

Table 2.2 summarizes the properties of the bandpasses used to define our spectroscopic indices, as illustrated, e.g., in Figure 2.7.

Index	Bandpass feature	λ_{min} (μm)	λ_{max} (μm)	Bandpass "continuum"	λ_{min} (μm))	λ_{max} (μm)
C2U	C2U_line	0.5087	0.5167	C2U_cont	0.5187	0.5267
CN	W110	1.0970	1.1030	W108	1.0770	1.0830
DIP153	DIP155	1.5000	1.6000	DIP149	1.4800	1.5000
COH_{52}	COH52_line	1.5974	1.6026	COH52_cont	1.5914	1.5966
COH_{63}	COH63_line	1.6174	1.6226	COH63_cont	1.6114	1.6166
C2	C2_line	1.7680	1.7820	C2_cont	1.7520	1.7620
CO12	KH86CO1	2.2931	2.2983	KH86c1	2.2873	2.2925
CO13	KH86CO3	2.3436	2.3488	KH86CO2	2.3358	2.3410

Table 2.2: Properties of our spectroscopic indices

2.5.1 Broad band colors

For each of our C star spectra, we derived magnitudes using the Bessell (1990) filters R and I and the 2MASS filters (Cohen et al. 1992) J, H and K_s. We use these magnitudes to define the colors $(R-H)$, $(R-I)$, $(I-H)$, $(I-K)$, $(J-H)$, $(H-K)$ and $(J-K_s)$.

Figure 2.6 compares our $(J-K_s)$ colors with those found in the literature. We find a good agreement for colors below $(J-K_s) < 1.6$. For colors above $(J-K_s) > 1.6$, the dispersion is larger, which is expected as the stars in this range tend to have larger pulsation amplitudes.

[7] At the resolution of our C-star spectra, the true continuum is inaccessible everywhere. What we call "pseudo-continuum" in this section is simply a reference flux level measured outside the molecular band of interest for a particular spectrophotometric index, following earlier usage by, e.g., Worthey et al. (1994).

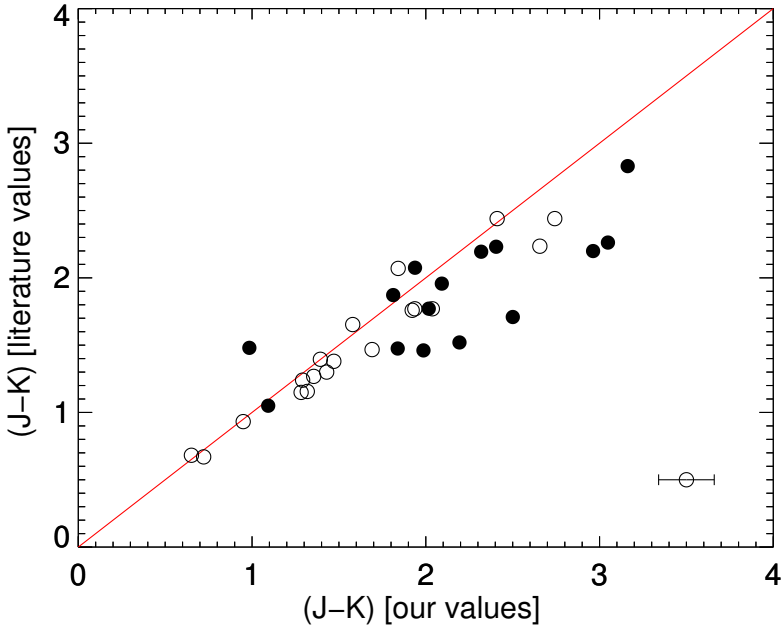

Figure 2.6: Comparison of our $(J-K_s)$ values with values found in the literature (2MASS values, Cutri et al. 2003). The red line indicates the one-to-one relation. The black points highlight the stars with large amplitude (I amplitude ≥ 0.8). The plotted error bar is based on the dispersion in the distributions of differences between our photometry and the literature (large amplitude variables excluded).

2.5.2 ^{12}CO indices

We first look at the CO bands located in the K-band. To measure the ^{12}CO(2,0) bandhead around 2.29 μm, we use the definition given by Kleinmann & Hall (1986) and call it *CO12*. Figure 2.7 shows the definition of the index with one of our spectra.

$$CO12 = (1 - KH86CO1/KH86c1) \times 52\text{Å} \tag{2.2}$$

Other CO bands can also be found in the C-star spectra. Origlia et al. (1993) studied the CO band in the H-band near 1.62 μm, corresponding to $\Delta\upsilon = 3$ ro-vibrational bands. In our spectra, this ^{12}CO(6,3) line does not always appear.

Figure 2.8 shows two examples taken from our sample where the CO(6,3) lines are seen (upper panel) or are hidden under a combination of CN and C_2 lines (lower panel). We define a new index *COH*, based on two other indices measuring the ^{12}CO lines at 1.62 μm (COH_{63}) and at 1.60 μm (COH_{52}):

$$COH = (COH_{52} + COH_{63})/2 \tag{2.3}$$

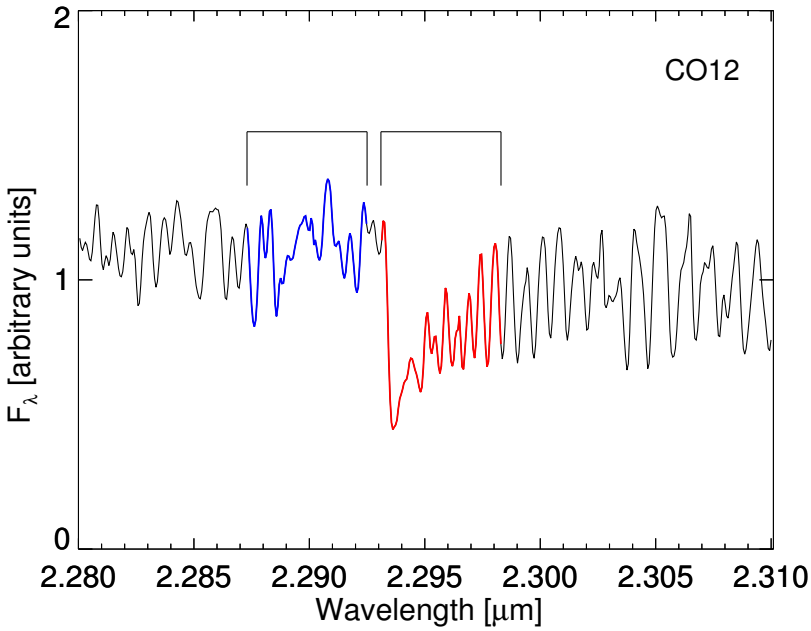

Figure 2.7: Zoom into the ^{12}CO(2,0) feature near 2.3 μm. The red line indicates the region used to calculate the KH86CO1 bandpass, while the blue line corresponds to the KH86c1 bandpass measuring the "continuum". This star is 2MASS J00571648-7310527.

2.5.3 ^{13}CO index

Another line to look at is the ^{13}CO band around 2.35 μm, corresponding to $\Delta v = 2$ ro-vibrational bands. To measure the ^{13}CO(2,0) bandhead, we use the definition of the bandpass centered on 2.3462 μm given by Kleinmann & Hall (1986) (*KH86CO3*). We do not use the same definition for the "continuum" as their bandpass is centered on 2.2899 μm and thus too far away from the absorption bandpass and more likely to be sensitive to slope effects. Therefore, we define a new bandpass for the "continuum" and create the index *CO13*. Figure 2.9 shows the definition of the bands used to define this index on one of our spectra.

2.5.4 CN index

CN is also seen in carbon star spectra. The CN bands from the red system appear beyond 0.5 μm and become stronger towards larger wavelengths. To estimate the CN in the NIR part of the spectrum, we use rectangular filters adapted from Wing (1971). Wing defines an 8-color system that can measure CN between 0.7 and 1.1 μm. We use an index *CN*, based on Wing's W110 and W108 colors, that measures the CN feature at 1.1 μm. These bandpasses are shown in Figure 2.10.

2.5.5 Measure of the 1.53 μm feature

Some of our stars exhibit the 1.53 μm feature. We interpret this feature to be caused by HCN+C_2H_2. We define an index *DIP153* to measure its depth. Figure 2.11 shows two examples taken from our sample where this feature is seen (upper panel) and absent (lower panel).

2.5.6 C_2 indices

C_2 bands can be found all over carbon star spectra. The bands between 0.4 and 0.7 μm correspond to the Swan system (Swan 1857). The C_2 bands at 0.77, 0.88, 1.02 and 1.20 μm are part of the Phillips system (Phillips 1948). The C_2 band at 1.77 μm is the Ballik-Ramsay fundamental band (Ballik & Ramsay 1963).

To measure the Ballik-Ramsay fundamental band at 1.77 μm, we use the same definition as Alvarez et al. (2000). The bandpasses used to define the *C2* index are shown in Figure 2.12.

The upper-right panel of Figure 2.13 shows the C_2 Swan system for one of our spectra. Due to low signal-to-noise for the XSL carbon stars at short wavelengths, the bands near 0.47 μm or bluer are barely seen. The band near 0.56 μm is problematic because of instrumental issues in that range (Chen et al. 2014a), and the bands above 0.6 μm are too heavily contaminated by CN. This leaves the band near 0.5165 μm as our best choice to define an index, even though this index can not be defined for all stars of our sample due to an absence of signal in the UVB/VIS parts of some of our spectra. We call this index *C2U*.

2.5.7 Measure of the high frequency structure

We also estimate the high frequency structure in the H and K bands, inspired by the smooth appearance of the NIR spectra of C stars with the 1.53 μm feature. For both windows, we first fit a straight line on the wavelength range under study: 1.66 – 1.7 μm for the H band and 2.18 – 2.23 μm for the K band. We then divide our spectrum by this fit, thus normalizing the continuum. Next, for any window X, we derive the rms from the following formula:

$$rms(X) = \sqrt{\frac{\sum_i^N (X_i - 1)^2}{N}} \tag{2.4}$$

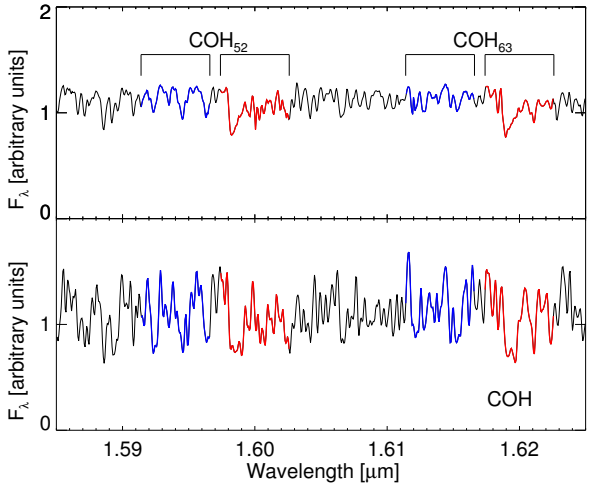

Figure 2.8: Zoom into the ^{12}CO(6,3) line near 1.62 μm. The red lines indicate the features regions, while the blue measure the "continuum". The upper panel shows an example of carbon star spectrum, Cl* NGC 121 T V8, in which the ^{12}CO(5,2) and ^{12}CO(6,3) bands are visible. The lower panel corresponds to another carbon star, 2MASS J00571214-7307045, in which the CN and C_2 lines are more prominent and overlap with the CO lines. The spectra have been normalized at 1.62 μm for display purposes.

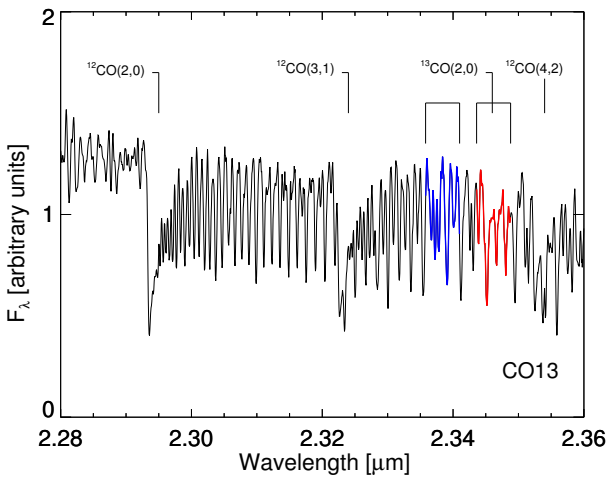

Figure 2.9: Zoom into the ^{13}CO(2,0) line near 2.35 μm. The red line indicates the region used to calculate the KH86CO3 bandpass, while the blue line corresponds to the KH86CO2 bandpass measuring the "continuum". This star is SHV 0500412-684054.

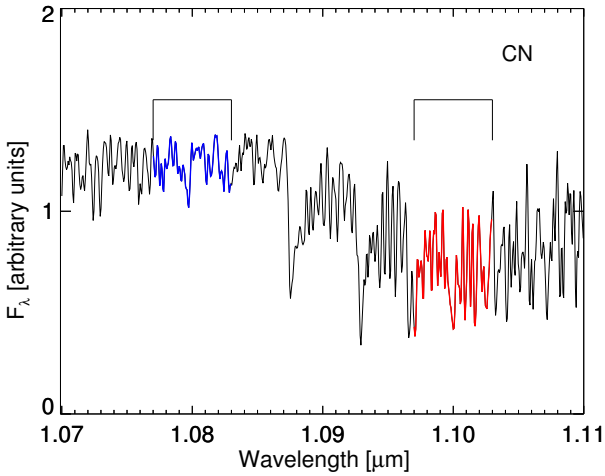

Figure 2.10: Zoom into the CN line near 1.1 μm. The red line indicates the region used to calculate the W110 bandpass, while the blue line corresponds to the W108 bandpass measuring the "continuum". This star is SHV 0502469-692418.

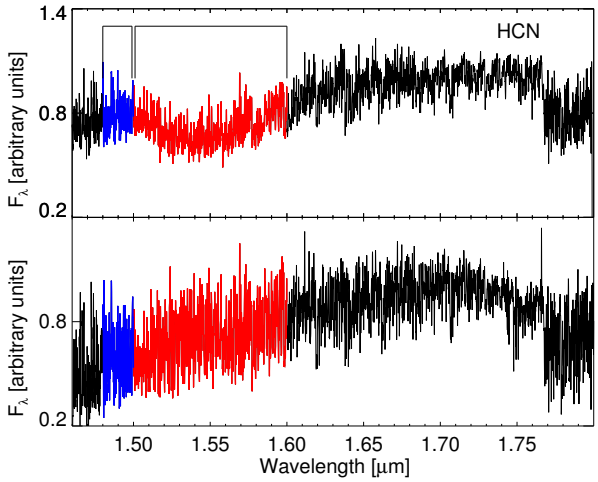

Figure 2.11: Zoom into the HCN+C_2H_2 lines around 1.53 μm. The upper panel shows an example of a carbon star, SHV 0502469-692418, in which the HCN+C_2H_2 feature is visible. The lower panel corresponds to another carbon star, T Cae, in which the feature is missing. The red line indicates the region used to calculate the absorption bandpass, while the blue line corresponds to the "continuum" bandpass.

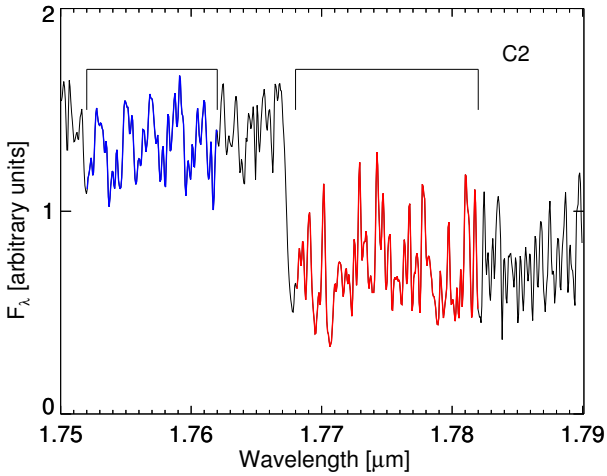

Figure 2.12: Zoom into the C_2 line around 1.77 μm. The red line indicates the region used to calculate the *C2_line* bandpass, while the blue line corresponds to the bandpass measuring the "continuum". This star is 2MASS J00563906-7304529.

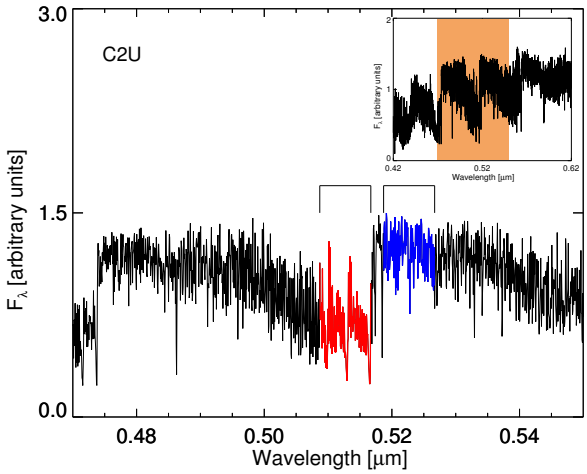

Figure 2.13: The C_2 Swan system (top panel) and a zoom into the C_2 line around 0.5165 μm. The red line indicates the region used to calculate the *C2U_line* bandpass, while the blue line corresponds to the *C2U_top* bandpass measuring the "continuum". This star is HE 1428-1950.

2.6 Results

2.6.1 Color-color plots

Figure 2.14 shows the locus of the observed carbon stars in color-color diagrams. On the whole, different colors are well correlated with each other. The dispersion along the trend is larger at redder colors.

The red circles highlight carbon stars showing the 1.53 μm feature in their spectra. A remarkable trend characterizes these stars in the color-color diagrams: at a given $(J - K_s)$, they are bluer when looking at color indices that involve R or I. We note that only panels (b), (c), (e) and (f) show colors that include the H band, which hosts the 1.53 μm feature itself. The separation between stars showing the 1.53 μm feature and normal C stars, however, is present in all the panels.

This separation into two categories of stars reflects the results of eye inspection in Sect. 2.4. Stars with the 1.53 μm feature tend to have excess flux at the red end of the optical spectrum, for a given energy distribution at further NIR wavelengths.

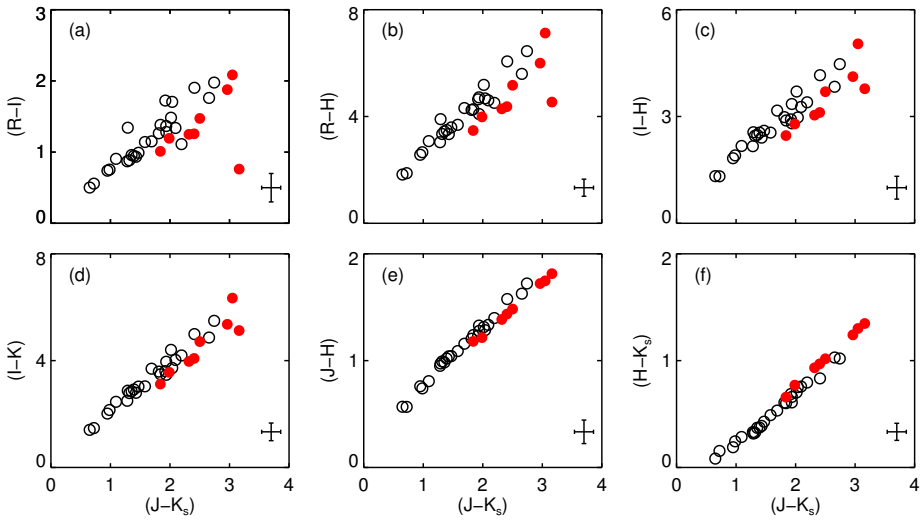

Figure 2.14: Some color-color plots derived from our sample of carbon stars. The red circles highlight carbon stars showing the 1.53 μm feature. The plotted error bars are upper limits, as they are based on the dispersion in the distributions of differences between our photometry and the literature (large amplitude variables excluded). For the R filter, we adopt some conservative values.

2.6.2 Molecular indices versus color

Figure 2.15 shows all the indices previously defined as a function of $(J - K_s)$. For each group of $(J - K_s)$ (cf. Section 2.4), we calculate the average values of each index and display them as filled symbols. The error bars indicate the 1σ standard deviations. We separate the red C stars from Groups 3 and 4 into two sub-groups: those with the 1.53 μm feature and those without.

Panels (a) to (c) in Figure 2.15 display the *CO* indices as a function of $(J-K_s)$. The data points are highly dispersed, with a marginal trend of decreasing ^{12}CO indices when $(J - K_s)$ increases.

In the H-band, the prominence of the CO bands in carbon star spectra depends on the strength of the CN and C_2 bands. These, in turn, depend on effective temperature, but also on the C/O ratio (Fig. 3 of Loidl et al. 2001). While strong in S and S/C stars (Rayner et al. 2009; Lançon & Wood 2000), the H band CO features become indistinguishable in the forest of CN and C_2 lines at large C/O. In addition, the CO band strengths anticorrelate with surface gravity (Origlia et al. 1993). In view of the many parameters that may control the amplitude of the related dispersion of COH values (our list is not exhaustive: metallicity, microturbulence, convection, and perhaps others), our sample is too small to consider the trend with $(J - K_s)$ significant.

At 2.29 μm, contamination by features other than CO is reduced but not negligible. Again, we believe the trend with $(J - K_s)$ is only marginal. Anticipating later discussions, it is interesting to note that two of the stars with the 1.53 μm feature have among the highest values of CO12.

Our measure of ^{13}CO becomes consistent with 0 above $(J - K_s) \simeq 2$ and its detection is only significant in a few relatively blue stars. To some extent, this results from contamination of the measurement bandpasses by a forest of lines from other molecules and to measurement uncertainties beyond 2.25 μm. But weak ^{13}C abundances are also a natural and well known result of the third dredge-up, which brings freshly synthesized ^{12}C to the surface (Lloyd Evans 1980; Bessell et al. 1983).

Panel (d) shows the result for the *CN* index. The behavior is not monotonic. First, the strength of the CN index increases, up to $(J - K_s) \simeq 1.6$. Then, for redder stars, the CN bandhead slowly fades.

Panels (e) and (f) display the C_2 indices. The *C2U* index is not defined for the reddest objects in the sample because of a lack of signal at the relevant short wavelengths. The strength of both C_2 indices increase with increasing $(J - K_s)$ and drop down for the reddest $(J - K_s)$ values.

Panel (g) shows the index measuring the strength of the 1.53 μm feature as a function of $(J - K_s)$. There is a clear separation between stars with the 1.53 μm feature (red points) and the others. We add a green line highlighting this separation for later comparisons.

The last two panels (h) and (i) display the results for the measure of the high frequency structure in the H- and K-bands. The contribution of observational errors to the measured rms indices is in general smaller than 0.02. As expected, the values of the rms increase with increasing $(J-K_s)$, but stars with the 1.53 μm feature follow the opposite trend. This can be seen in Figures 2.21 and following.

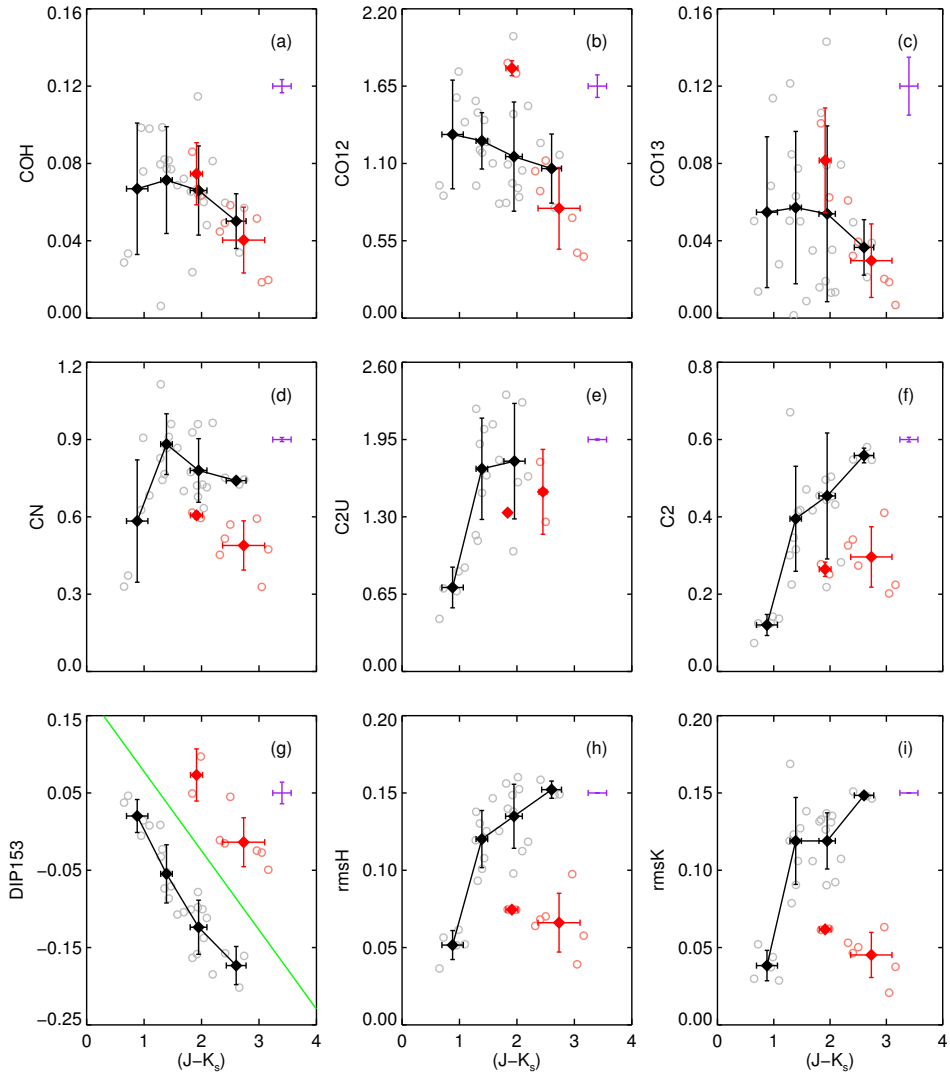

Figure 2.15: Some indices derived from our sample of carbon stars as a function of $(J - K_s)$. The red circles highlight the carbon stars with the 1.53 μm feature. The filled diamonds represent the averaged values of our indices as a function of the bin number based on $(J - K_s)$. The plotted error bars measure the dispersion within bins. The observational error bars are shown in purple. They estimate the dispersion of the response curves.

2.7 Comparison with the literature

We compare our sample of carbon stars with existing libraries in Figures 2.16 and 2.17.

2.7.1 Spectra from Lançon & Wood (2000)

One of the most comprehensive libraries containing carbon stars is the one constructed by Lançon & Wood (2000, hereafter LW2000). They built a library of spectra of luminous cool stars from 0.5 to 2.5 μm, in which 7 carbon stars are listed. In addition, their data set includes multiple observations of individual variable stars. One of their stars, R Lep, is a large amplitude variable star, which exhibits the 1.53 μm feature. The different observations of this star are highlighted as filled magenta stars in the plots.

2.7.2 Spectra from Groenewegen et al. (2009)

We also compare our sample of carbon stars with carbon stars observed by Groenewegen et al. (2009). They observed AGB stars from Fornax, Sculptor and NGC 6822. The observations were taken to cover the entire J- and H-band atmospheric windows. This sample is particularly interesting as their color-selected sample happened to contain several carbon stars with the 1.53 μm feature. Table 2.3 summarizes properties of their carbon stars: 2MASS J, H and K magnitudes and also the strength of the 1.53 μm feature. Based on this classification, stars for which this feature is "medium," "strong" or "extreme" are highlighted as filled blue triangles in the figures.

Star identifier	J 2MASS	H 2MASS	K 2MASS	Strength of the 1.53 μm feature
Fornax11	15.034	13.981	13.261	absent
Fornax13	14.485	13.377	12.618	weak
Fornax15	15.790	14.556	13.668	strong
Fornax17	14.745	13.689	13.072	weak
Fornax20	15.131	13.732	12.728	weak
Fornax21	15.424	14.122	13.182	weak
Fornax24	15.601	14.162	13.167	weak
Fornax25	14.722	13.262	12.120	weak
Fornax27	14.441	13.365	12.694	absent
Fornax31	16.052	14.483	13.315	medium
Fornax32	14.789	13.664	13.076	absent
Fornax34	16.106	14.525	12.879	extreme
Fornax-S99	14.677	13.749	13.427	absent
Fornax-S116	15.004	14.041	14.028	absent
Scl6	14.846	13.144	11.603	strong
Scl-Az1-C	14.713	14.040	13.871	weak

Table 2.3: Carbon stars from Groenewegen et al. (2009).

2.7.3 Spectra from IRTF (Rayner et al. 2009)

Finally, we compare our carbon stars with those from the IRTF Spectral Library (Rayner et al. 2009, hereafter IRTF). From the 13 S/C stars available from their collection, we only select the carbon stars, and thus remove the M and S stars. This leaves us with 8 C-star spectra from 0.8 to 5.0 μm, including R Lep. In the plots, this star is highlighted as a filled green square.

2.7.4 Results

Figure 2.16 shows the $(J-H)$–$(H-K_s)$ color–color diagram for our sample of carbon stars (circles), to which we add the C stars from LW2000 (stars), Groenewegen et al. (2009) (triangles) and IRTF (squares). The colored symbols highlight the carbon stars with the 1.53 μm feature. All the colors, except those from Groenewegen et al. (2009), were rescaled to 2MASS values for consistency in our comparison. There are clearly two close but distinct sequences: one for the "classical" carbon stars, then a turnoff around $(H-K_s) \simeq 0.7$, and another sequence with the stars showing the 1.53μm feature.

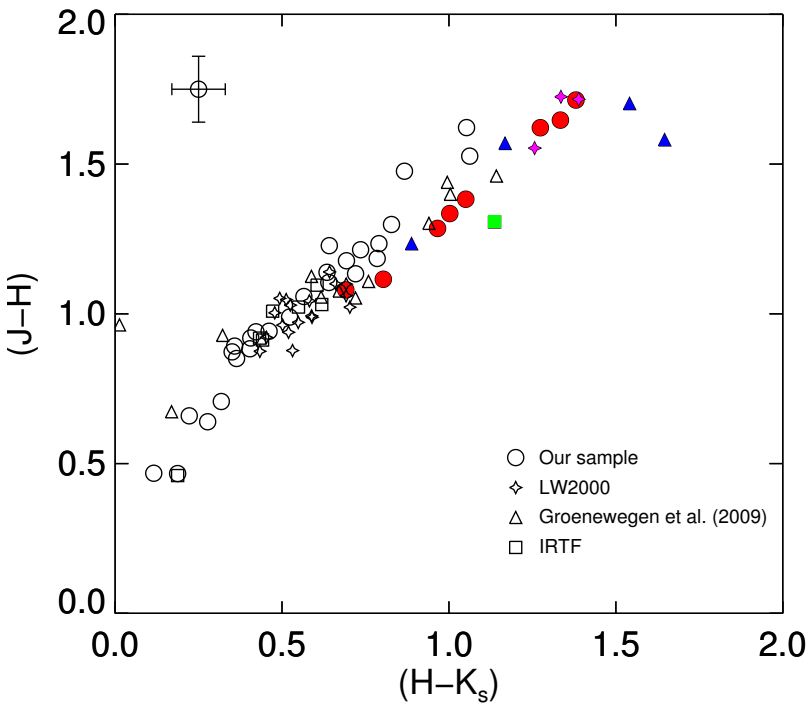

Figure 2.16: The spread of our sample of carbon stars (circles) in the $(J-H)$–$(H-K_s)$ color-color plane. The star symbols represent LW2000, the triangles represent Groenewegen et al. (2009) and the squares represent IRTF. Colored symbols highlight those carbon stars with the 1.53 μm feature.

We compute for the three samples of carbon stars under study the spectroscopic indices just like for the XSL spectra. Figure 2.17 shows six of our indices as a function of $(J-K_s)$. Not all the indices are defined for the stars from Groenewegen et al. (2009), as their spectra are confined to the J- and H-bands.

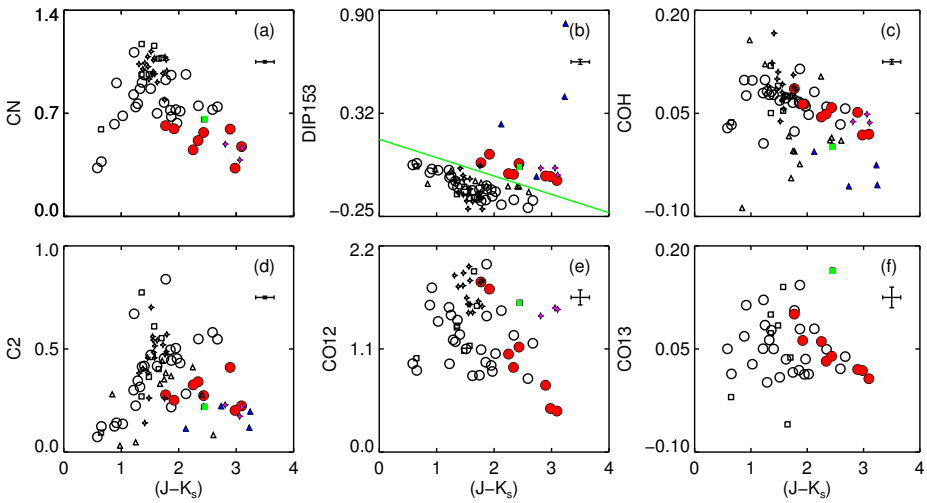

Figure 2.17: Six of our indices as functions of $(J-K_s)$. Symbols and colors are as in Figure 2.16.

Panel (a) shows the result for the *CN* index. The trend is as in Figure 2.15: an increase of the CN band up to $(J-K_s) \simeq 1.6$ and then a slow decrease at redder colors.

Panel (b) shows the result for the *DIP153* index. The green line is the same line as in panel (g) of Figure 2.15. Our criterion to identify stars with the 1.53 μm feature appears to be reasonable when applied to a larger sample. On this plot, one star identified with a star symbol and not explicitly identified as containing HCN+C_2H_2 appears clearly in the group of stars with the 1.53 μm feature. This star is the Milky Way star BH Cru and is known to have evolved from a spectral classification of SC in the early 1970s to CS recently. Figure B28 of Lançon & Wood (2000) shows spectra of this star observed at three different periods (from January 1996 to July 1996). The top spectrum in that figure was obtained close to the visual maximum (January 1996, phase 0.03), while the bottom spectrum is closest to the minimum light (July 1996, phase 0.34). It displays exceptionally strong CO bands in the H-band and these contaminate the DIP153 index. The IRAS-LRS spectrum of BH Cru implies that it is not surrounded by a lot of dust ("a hint of circumstellar emission" as mentioned by Lambert et al. 1990).

Panel (c) corresponds to the *COH* index. We still observe a decrease of the strength of the COH as $(J-K_s)$ increases.

Panel (d) shows the *C2* index. The "normal" stars seem to lay on a sequence, while the stars with this 1.53 μm feature seem to all be gathered in the lower

right-hand quarter of the plot.

Panels (e) and (f) display the *CO12* and *CO13* indices. The general trend is a decrease of those two indices as $(J - K_s)$ increases.

2.8 Discussion

2.8.1 Our bluest stars

In Section 2.4, we described the 5 hottest carbon stars of our sample (Fig. 2.21) and their differences. Only a detailed comparison with models will provide the cause for these differences. A redder SED can indicate a cooler effective temperature. Differences in the depth of the molecular bands can be the result of different metallicities and/or C/O abundance ratios. Luminosity may also play a role as the strengths of the CO and CN bands tend to increase when surface gravities drop.

Anticipating results of a future paper (Gonneau et al., in prep), we note that the shapes of standard reddening laws do not explain by themselves all the differences between the SEDs of the top two (HD 202851 and HE 1428-195) and bottom three (Cl* NGC 121 T V 8, SHV 0518161-683543 and SHV 0517337-725738) spectra in Fig. 2.21. Also, circumstellar dust is not expected to play a major role around stars this hot.

One might be tempted to consider environmental effects, as the bottom three spectra belong to stars in the Large and Small Magellanic Clouds while the top two are in the Milky Way. But one of the two top spectra belongs to a Milky Way Halo star (HE 1428-1950, Goswami et al. 2010), and is likely also of subsolar metallicity (Kennedy et al. 2011). It is unknown to which MW population the second top star belongs.

Finally, we note that two of these five spectra clearly display Hβ in absorption, and two others Hβ in emission. Hydrogen deficiency is unlikely to be an important characteristic of any of the stars in this group.

2.8.2 The bimodal behavior of red carbon stars

The previous sections have highlighted a bimodal behavior among carbon stars with relatively red near-infrared colors. The presence or absence of the 1.53 μm absorption feature, easily identified by eye, was shown to be a good separator between the two types of behavior (at least in the XSL sample).

Figure 2.18 shows two of our high-resolution C-star spectra with similar $(J - K_s)$ (of $\simeq 1.8$). The 1.53 μm feature is present in the top spectrum but not in the bottom one. In addition to the HCN+C_2H_2 feature, the top spectrum shows a smoother near-infrared spectrum than the bottom one, and excess flux at red optical wavelengths.

What might explain this bimodal behavior? Groenewegen et al. (2009) has already discussed the anti-correlation between the strength of the 1.53 μm feature and the C_2 bandhead at 1.77 μm. As the 1.53 μm feature is likely carried in part by C_2H_2, they have suggested the formation of this complex molecule occurs at the expense of C_2 when the C/O ratio and the physical conditions are appropriate.

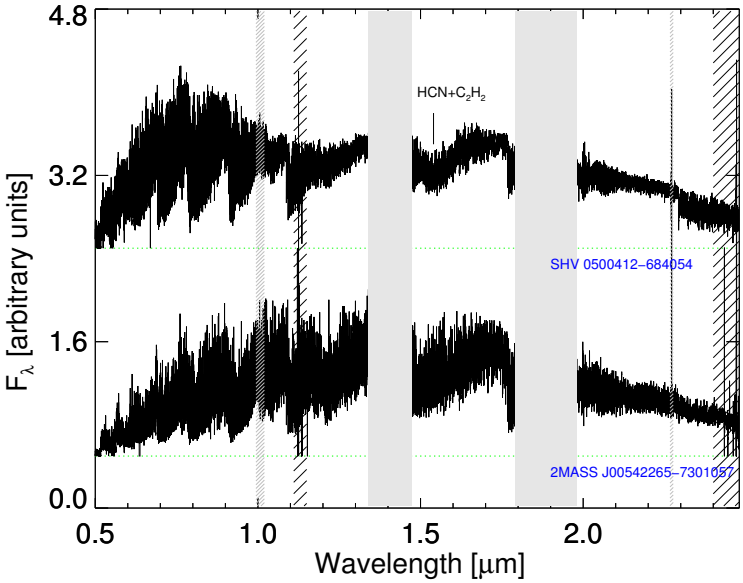

Figure 2.18: Two high-resolution C-star spectra from our sample, with similar $(J - K_s)$ values. The grey bands mask the regions where telluric absorption is strongest. The areas hatched in black are those that could not be corrected for telluric absorption in a satisfactory way. The areas hatched in grey are the merging regions between the VIS and NIR frame, and between the last two orders of the NIR part. The top spectrum exhibits the 1.53 μm feature, contrary to the bottom one.

While we have no argument against this suggestion, other parameters are needed to explain the effects we see in the global SED and the anti-correlation with the apparent strength of the forest of lines in the H- and K-bands.

Two of the main fundamental parameters of carbon star models are the effective temperature and the C/O ratio. Aringer et al. (2009) showed that dust-free hydrostatic models with these main parameters fail to reproduce stars redder than $(J - K) \geq 1.6$. Circumstellar dust is invoked to explain redder objects. At optical and NIR wavelengths, this dust is usually thought of as a cause of extinction (Lançon & Mouhcine 2002; Lloyd Evans 2010). But extinction by itself cannot explain the phenomenology we observe. All classical extinction laws are monotonic functions of wavelength through the optical and NIR range. They cannot explain that, at a given $(J - K_s)$, stars with the 1.53 μm feature have excess flux in the red part of the optical spectrum.

One natural explanation for both the SED and the apparent smoothness of the peculiar spectra in the NIR range (e.g. SHV 0500412-684054) is an additional continuous *emission* component at NIR wavelengths. This emission would, in these stars, simply extend the notorious mid-infrared emission of mass-losing asymptotic giant branch stars to shorter wavelengths. A significant additive component to the continuum weakens photospheric absorption features in the composite spectrum.

Indeed, such a dilution is seen at NIR wavelengths in some of the spectra of dusty pulsating C-star models of Nowotny et al. (2011, 2013), although this aspect was not highlighted by the authors. Furthermore the existence of dust-emission-dominated objects such as V CrA (Fig. 2.20) hints at all sorts of intermediate situations.

If we accept the idea of continuous thermal dust emission in the NIR, a new question appears: how can stars with a strong 1.53 μm feature, and with a smooth appearance, display strong CO bandheads at 2.29 μm? One possibility is that the CO molecule exists in circumstellar matter located outside the dust-emission layers. In the extended atmospheres of long period variables, the robust CO molecule is expected to exist over a broad range of radii.

For dust to emit at NIR wavelengths, it must be hot and located near the star. This is most likely to happen when the dust first forms, and to last until that dust shell is carried further out into cooler regions. At those later stages, dust emission would fade, but dust extinction can remain quite strong until the circumstellar matter is diluted in space. The effects of subsequent pulses cumulate, although atmospheric structures are predicted to vary between one pulse and the next (Bessell et al. 1996; Höfner et al. 1998; Tej et al. 2003; Ireland et al. 2011; Nowotny et al. 2013). Why the presence of dust emission seems to correlate so well with the presence of the 1.53 μm feature would remain to be explained by a renewed look at models of the chemical structures of pulsating atmospheres.

2.8.3 Synthetic stellar populations with carbon stars

This collection of carbon star spectra offers several improvements over previous collections for the simulation of spectra of intermediate age stellar populations. It extends the collection of Lançon & Wood (2000) to bluer stars and provides higher resolution at optical wavelengths. It also offers new insight into the importance of evolutionary parameters such as surface composition, pulsation properties and mass loss along the AGB.

A few population synthesis models in the literature have accounted for the evolution of the C/O ratio along the asymptotic giant branch, a dichotomy between O-rich and C-rich spectra, and simple models for the effects of circumstellar dust (Mouhcine et al. 2002; Marigo et al. 2008). None of these can follow the cycle-dependent effects of pulsation in detail, and that is not their primary purpose. Their main aim is to predict average properties of stellar populations.

Intermediate mass stars become carbon-rich on the thermally pulsing asymptotic giant branch (TP-AGB). The importance of C stars is determined by TP-AGB lifetimes and fractional TP-AGB lifetimes spent as a C star. The current trend is for TP-AGB lifetimes to be revised downwards, in particular at low metallicities and old ages (Gullieuszik et al. 2008; Girardi et al. 2010; Rosenfield et al. 2014).

TP-AGB and C star contributions are largest in populations with a significant component of intermediate age stars, such as intermediate-age star clusters ($L_{K,\mathrm{TPAGB}}/L_{K,\mathrm{total}} \sim 0.5$; Ferraro et al. 1995; Girardi et al. 2013) or galaxies with a strong post-starburst component (Lançon et al. 1999; Miner et al. 2011; but see Kriek et al. 2010 and Zibetti et al. 2013 for counter-examples).

Melbourne et al. (2012) use star counts to show the contribution of TP-AGB stars reaches 17% at 1.6 μm in a sample of local galaxies, but they do not separate O-rich and C-rich stars. In near-infrared color magnitude diagrams of the Magellanic Clouds, a densely populated plume of C stars extends from $(J - K) = 1.2$ to $(J - K) = 2$ at its bright end (Nikolaev & Weinberg 2000). The corresponding contribution to the light at 2 μm amounts to 6 to 10% of the total, and is similar to that of O-rich TP-AGB stars (Melbourne & Boyer 2013).

Many of the C stars detected in the above populations are in the range of colors for which we have found bimodal spectral properties. It will be necessary to evaluate proportions of C stars of the two types in the future, based on models and on observations. However, considering the above assessments of the weight of C stars in galaxy spectra, approximate proportions will be sufficient for many purposes. Demand for precision will come, for instance, when next generations of extremely large telescopes will produce detailed near-infrared observations of star clusters in samples of remote galaxies.

In the short term, the spectra of this paper will be compared with stellar models, with the double purpose of validating those models and of constraining the location of the observed stars along stellar evolution tracks. The X-shooter archive contains additional C star spectra that should be added to the XSL collection in the future. O-rich stars on the AGB are also included in XSL. They should be compared with those of LW2000 and included in the TP-AGB modelling procedures.

2.9 Conclusions

We have presented in this paper a new collection of carbon star spectra, observed at medium resolution and covering wavelengths from the near-ultraviolet to the near-infrared. Our sample displays quite a diversity which will contribute to the improvement of stellar population synthesis models.

To use these spectra in studies of stellar populations, it is necessary to relate them to fundamental stellar parameters such as surface gravities, effective temperatures. One way to do so is to compare the collection of spectra with theoretical models. This will be done in a forthcoming paper.

Among the diversity of our spectra, we highlighted a bimodal behavior of the carbon stars, with the presence of the absorption feature at 1.53 μm, associated with a smoother appearance. A comparison with dynamical models will be needed to confirm that hot circumstellar dust emission in the near-infrared helps to explain these properties.

Appendix 2.A The case of V CrA

V CrA is a well-known variable star of type R Coronae Borealis (R CrB). As discussed by Lloyd Evans (2010), the characteristic feature of this star is the occasional occurrence of drops in brightness of up to 9 magnitudes, with a rapid drop and a usually slower recovery which may extend over several years. The common explanation is that the star ejects clouds of carbon dust which obstruct the light of the star until they dissipate. Figure 2.19 shows the light curve for V CrA over the last 20 years.

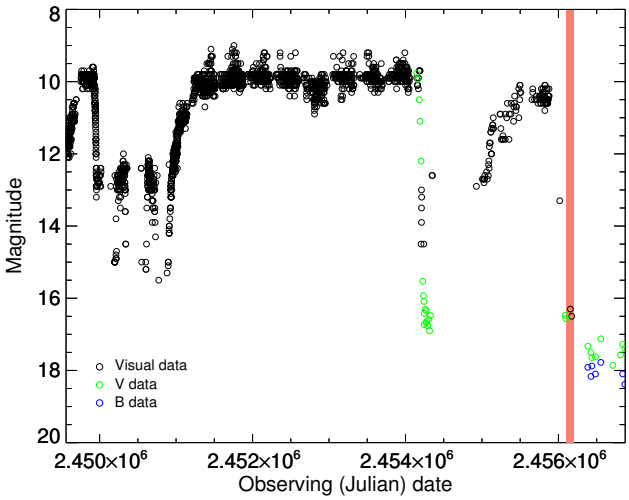

Figure 2.19: Light curve of V CrA, based on AAVSO data. The time range is from 01/08/1994 to 29/07/2014. Our observing time is highlighted by the red marker, so clearly during a drop in brightness of the star.

We observed V CrA during one of these fading events. Indeed, in its spectrum, displayed in Figure 2.20, we are not able anymore to see the stellar photospheric absorption lines and we only have an emission spectrum. Because this star is ongoing an extreme phase, it is not considered further in this paper.

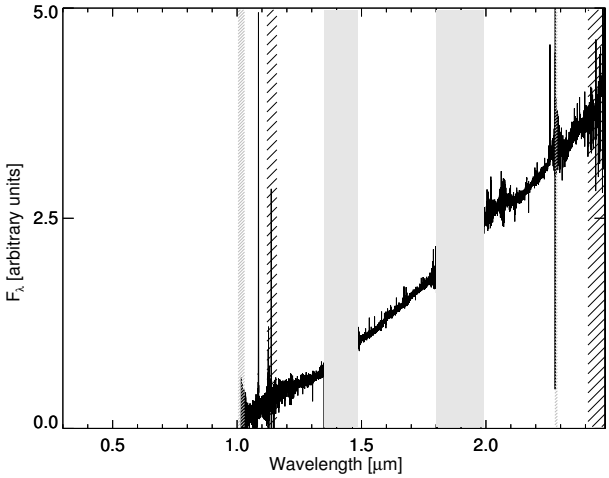

Figure 2.20: Spectrum of V CrA, from the UVB to NIR. The grey bands mask the regions where telluric absorption is strongest. The areas hatched in black are those that could not be corrected for telluric absorption in a satisfactory way. The area hatched in grey is the merging region between the last two orders of the NIR part.

Appendix 2.B Observed spectra of our sample of carbon stars

Figures 2.21 to 2.26 show the entire UVB–VIS–NIR spectra for our sample of carbon stars.

In the following figures, the grey bands mask the regions where telluric absorption is strongest. The areas hatched in black are those that could not be corrected for telluric absorption in a satisfactory way. The areas hatched in grey are the merging regions between the VIS and NIR frames and between the last two orders of the NIR part. In some spectra, there is a lack of data at 0.635 μm. The spectra were normalized around 1.7 μm and smoothed by the same factor for display purposes.

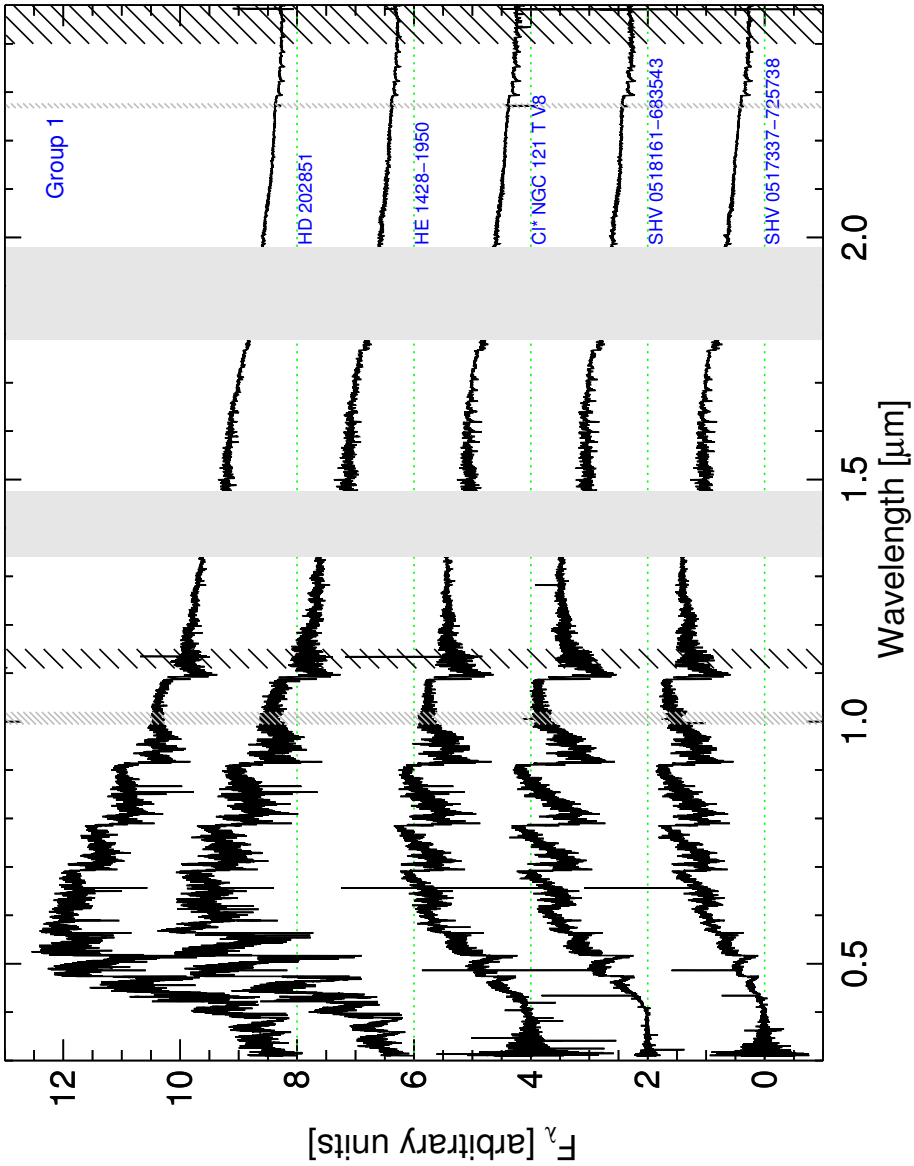

Figure 2.21: Spectra of our sample of carbon stars.

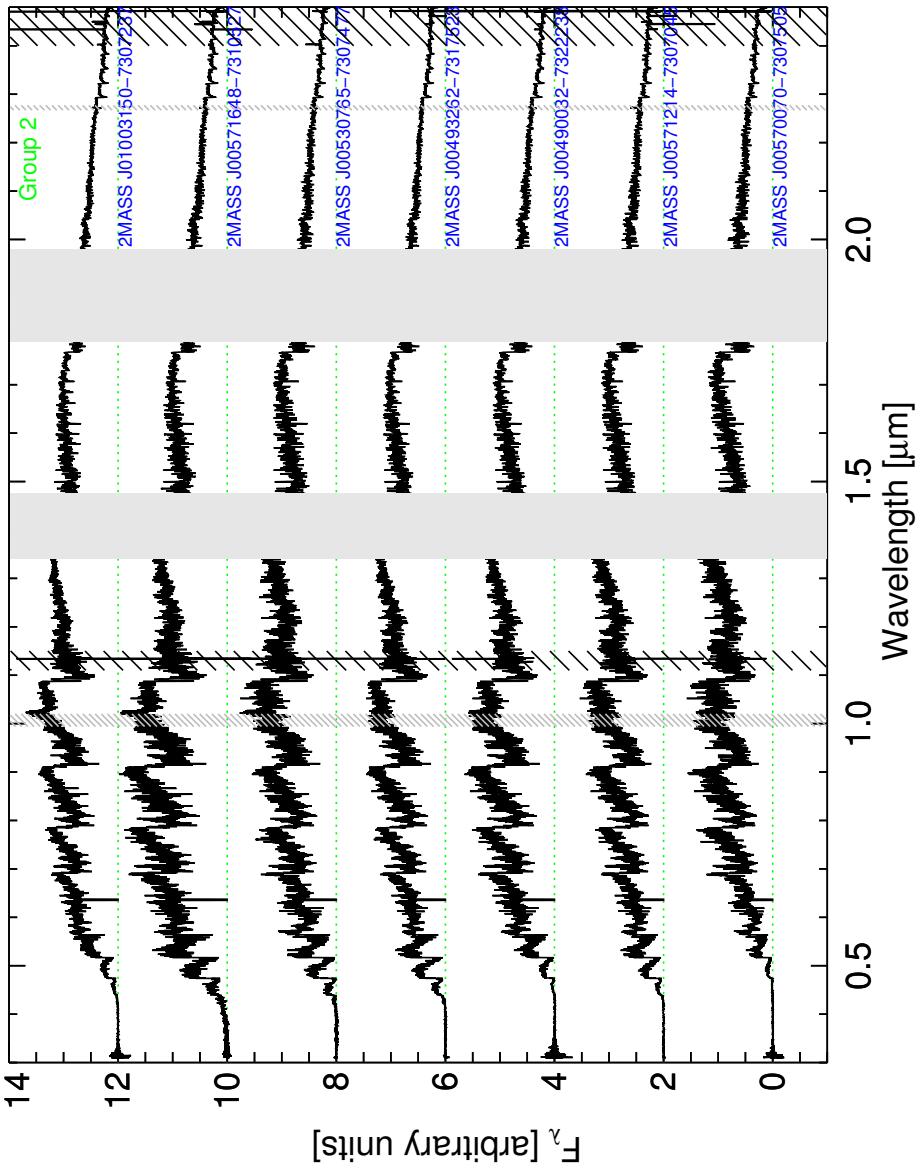

Figure 2.22: As for Fig. 2.21.

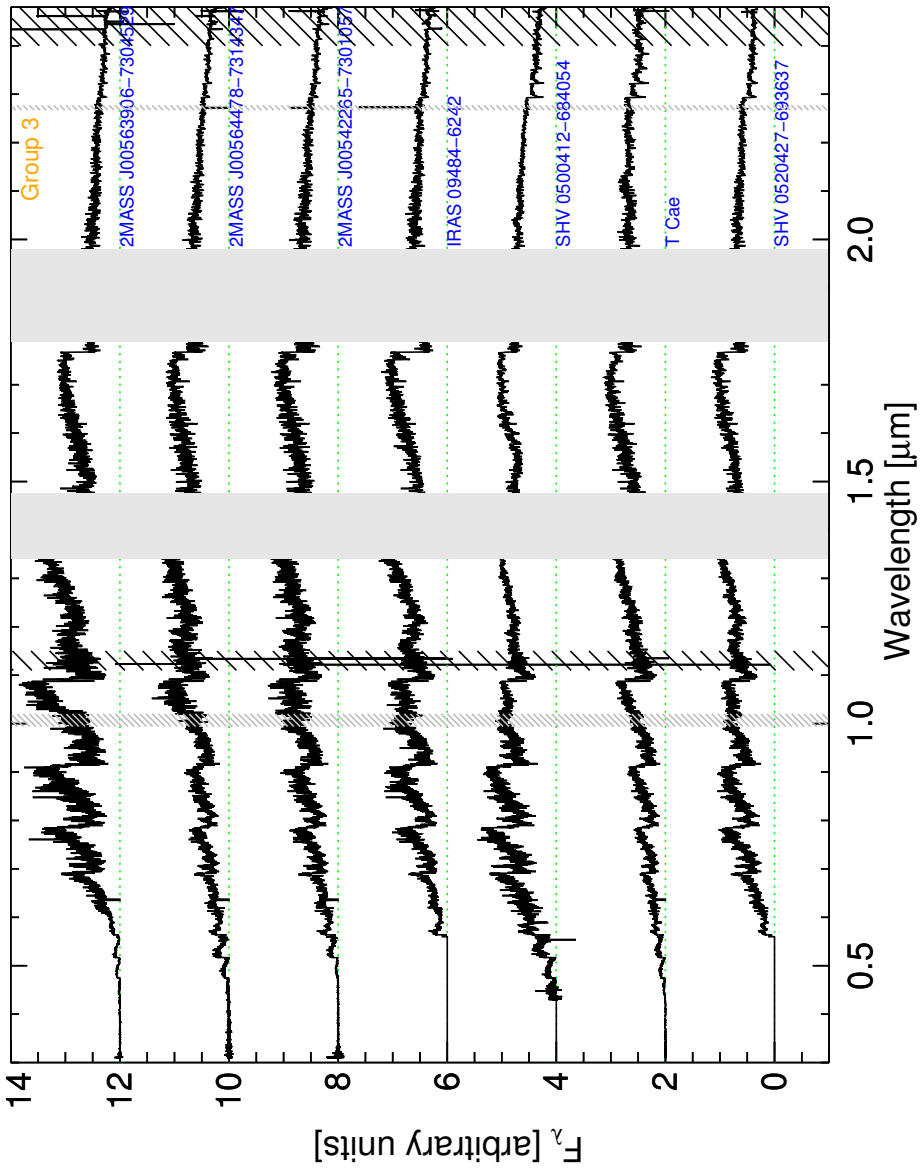

Figure 2.23: As for Fig. 2.21.

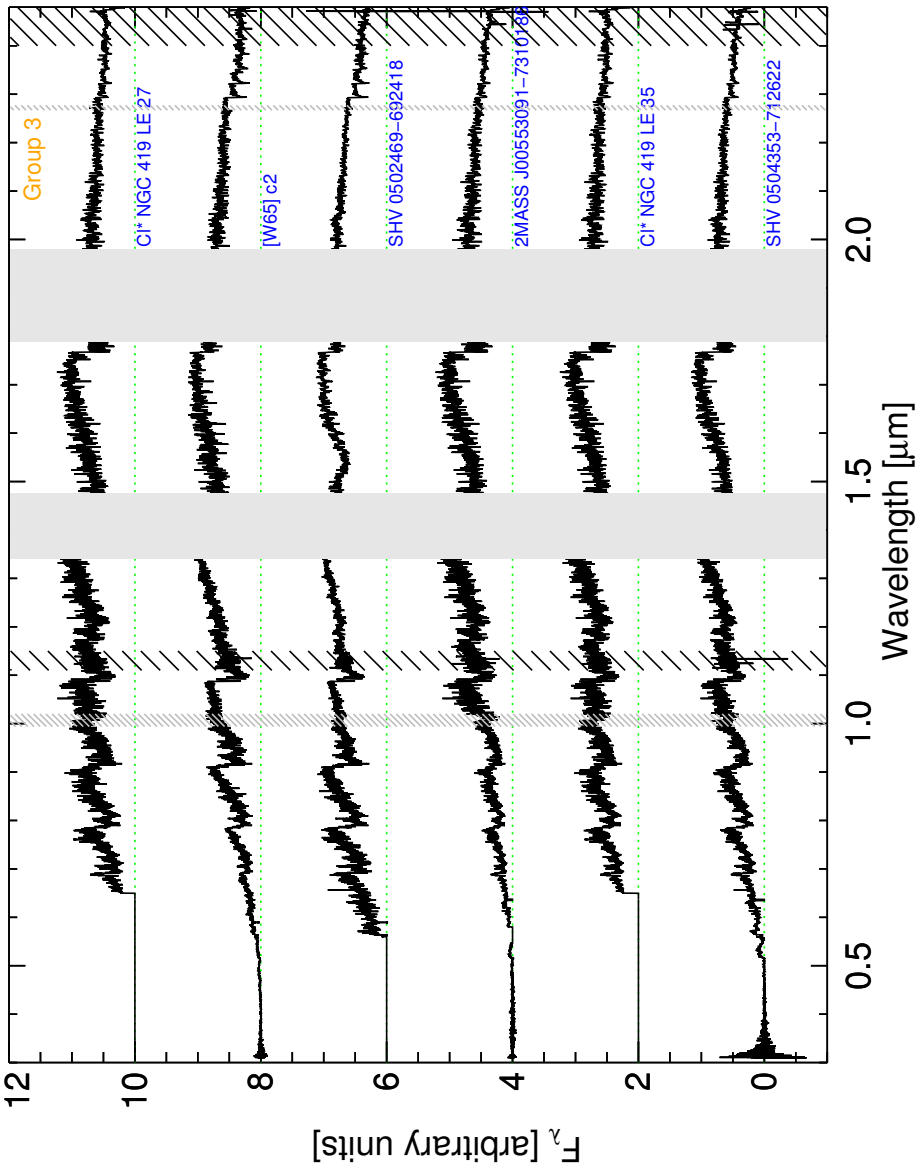

Figure 2.24: As for Fig. 2.21.

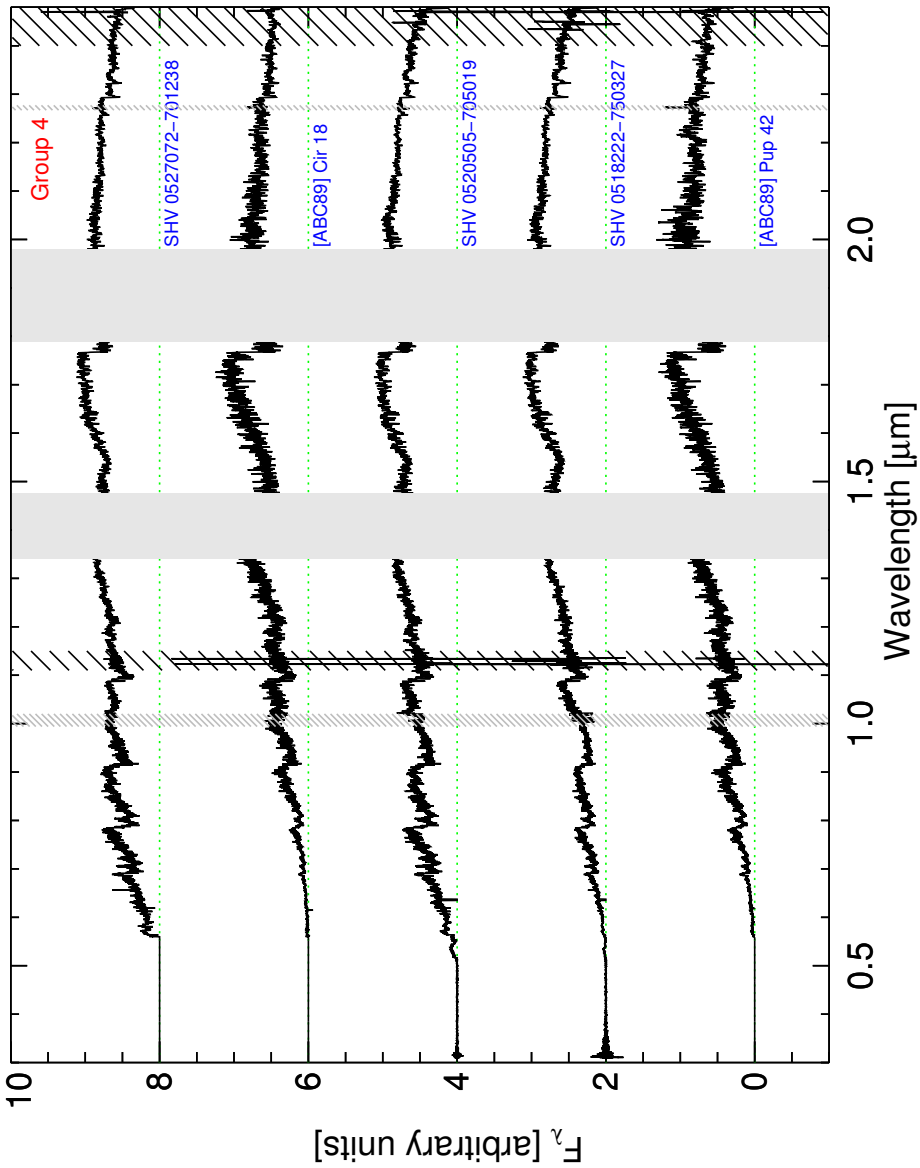

Figure 2.25: As for Fig. 2.21.

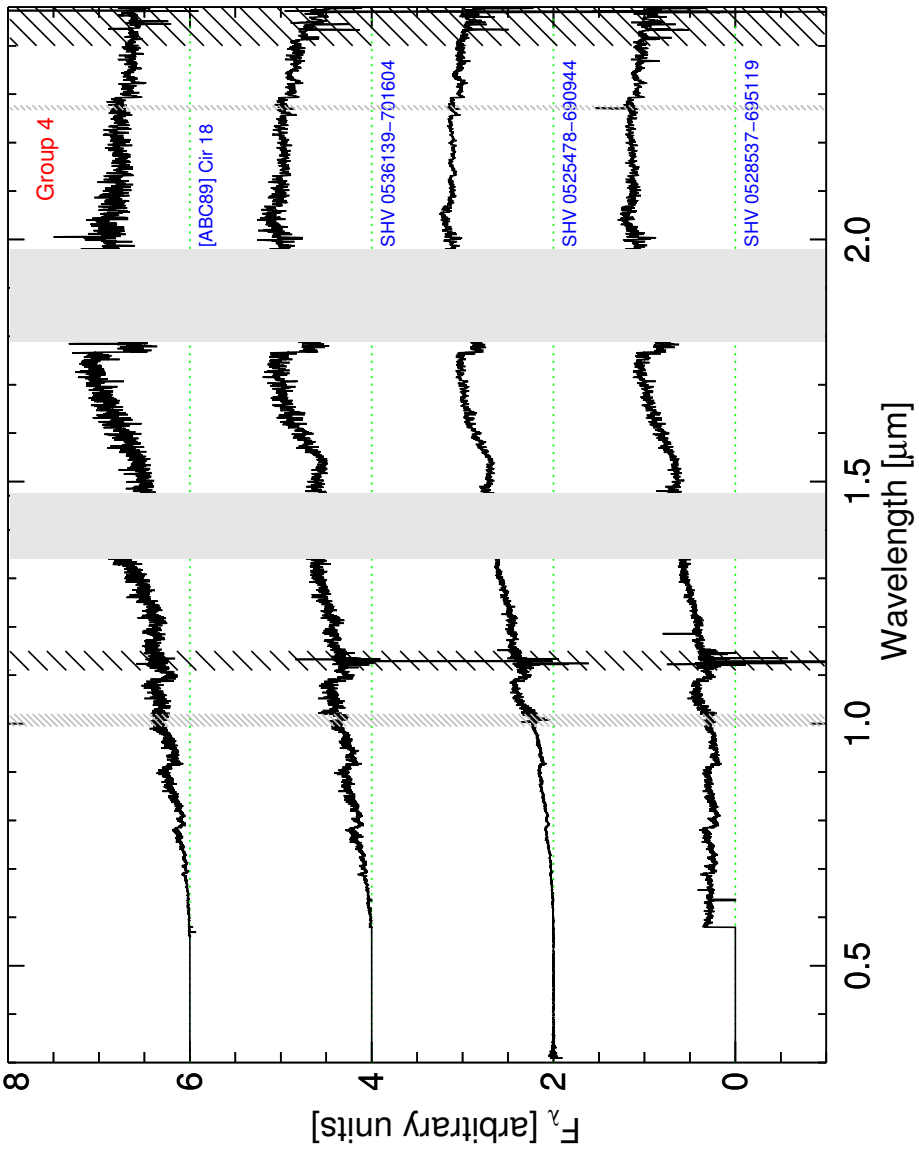

Figure 2.26: As for Fig. 2.21.

Appendix 2.C Literature properties

To facilitate future usage of the X-shooter spectra, we summarize some of the properties of the C-stars observed, as found in the literature or derived therefrom.

In Table 2.4, the stars are sorted by RA with horizontal lines facilitating the separation between SMC, LMC and Milky Way sources. The names in Col. (1) are understood by standard interpreters such as those of CDS (Centre de Données astronomiques de Strasbourg). Col. (2) provides the reference of the input catalog used in the initial construction of the X-shooter sample. Our systematic searches of the literature for known stellar properties were made using the generic search through the Vizier catalog database at CDS, as made available via a search link on the Simbad pages of individual objects. Information from other sources was added on a best-effort basis.

Spectral type information was found for only a few of the program stars. The N star T Cae (Alksnis et al. 2001) is labelled C6.4 by Sanford (1944) and C5II by Egret (1980). Alksnis et al. (2001) assign type R0 to the R CrB star V CrA (in its non-obscured phases) and to HD 202851, and type R to IRAS 09484-6242. In the LMC, the Mira variable SHV0504353-712622 was of type C7.5 when observed by van Loon et al. (2005).

Columns (3) to (8) of Tab. 2.4 provide pulsation information. The periods and amplitudes in columns (3) and (4) are from I band light curves when found, otherwise as specified in Col. (5). Periods followed by a colon are highly uncertain, as the corresponding light curves are very irregular (for most of these stars, a detailed literature search produces half a dozen of very different periods depending on passband, method, and time of observation). The amplitudes given are representative of the peak-to-peak variations over long time spans rather than single-period fits of sine functions (for V CrA, the amplitude given does not include the deep obscuration events). The SR and M variability types in Col. (6) is (as is common practice) based on amplitude, not on the shape of the light curve. A comment in Col. (8) summarizes our eye inspection of the available light curves.

The K magnitude and the $(J-K)$ color taken from 2MASS (Cutri et al. 2003) are listed in Col. (9) and (10).

The bolometric magnitudes in Col. (11) are apparent when in parentheses, absolute otherwise. For LMC stars, they are taken from Hughes & Wood (1990), who use the bolometric corrections of Wood et al. (1983) and a distance modulus of 18.5. For SMC stars, we list the values of Cioni et al. (2003) when available. They are based on energy distributions from the I band to 12 μm and we assumed a distance modulus of 18.9 to the SMC. We adopted (m-M)=18.5 for SMC cluster NGC 419 and (m-M)=19.06 for NGC 121 (Glatt et al. 2008). For these stars, we use the apparent bolometric magnitudes of Frogel et al. (1990), which are based on the bolometric corrections of Frogel et al. (1980). A more modern compilation of bolometric corrections BC(K) as a function of $(J-K)$ is shown in Nowotny et al. (2013). The spread between authors in that data set amounts to about 0.4 mag. The relations of Wood et al. (1983) and of Frogel et al. (1980) lie near the average of the newer compilation. Re-presentative errors on these are therefore of the order of 0.2 mag.

We have not found distances to the Milky Way stars that we consider reliable,

and hence we provide only apparent bolometric magnitudes, based on K, $(J-K)$ and bolometric as above.

NOTES to Tab. 2.4:

Light curve descriptions in Col. (8): irr = irregular; irr.d = irregular with marked dips in brightness; irr.a = irregular with marked changes in amplitude; reg = mostly regular; reg.d1 = mostly regular with one dip near the end of the available time series; reg.at = mostly regular with variations in amplitude and mean magnitude comparable to half the mean amplitude ; reg.atV = same as reg.at but with larger variations in the OGLE V light curve; reg.t = mostly regular short period pattern, but long term trends in the mean that are comparable or larger than the amplitude (possibly associated with a secondary long period).

References:
(a) Hughes & Wood (1990). **(b)** Bergeat et al. (2002). Stars found non-variable by these authors based on Hipparcos satellite photometry are labelled nv in Col. (6).
(c) Lançon & Wood (2000). **(e)** Christlieb et al. (2001). **(f)** Whitelock et al. (2006).
(g) Cioni et al. (2003) with updates from Raimondo et al. (2005). **(h)** 2MASS (Cutri et al. 2003).
(i) Frogel et al. (1990) with the distance moduli to SMC clusters from (Glatt et al. 2008).
(k) General Catalog of Variable Stars (GCVS) (Samus et al. 2007-2012).
(n) Alksnis et al. (2001): General Catalog of galactic Carbon Stars.
(o) Egret (1980).
(p) OGLE LMC data in V and I (Soszyński et al. 2009, via Vizier)
(q) OGLE SMC data in V and I (Soszyński et al. 2011, via Vizier)
(r) EROS data in B and R (Kim et al. 2014)
(s) MACHO data in B and R (Alcock et al. 1996, 2001 version via Vizier)
(t) DIRBE data in J and K (Price et al. 2010, via Vizier)
(u) Association Française des Observateurs d'Etoiles Variables (AFOEV)
(v) American Association of Variable Star Observers (AAVSO)
(w) ASAS data in V (Pojmanski 2002, via Vizier)
(z) Our estimate based on $(J-K)$ and Nowotny et al. (2013) (see text). When in parentheses, the values are apparent magnitudes.

NOTES on individual stars:
HE 1428-1950 is a high galactic latitude star, which might be metal-poor and higher gravity than a typical AGB star (Placco et al. 2011).
HD 202851 was assigned an approximate bolometric luminosity of -1.9 by Bergeat et al. (2002), which is lower than the expected luminosity of intrinsic C-stars on the thermally pulsing AGB.
[W65] c2: Whitelock et al. (2006) note that Aaronson et al. (1988) find K =7.21, $(J-K)$ =1.95, while Aaronson & Mould (1985) had values consistent with 2MASS and themselves. This star may have obscuration events.

Table 2.4: Properties of the observed stars *(adapted from the literature).*

Name (1)	Input cat (2)	Period [d] (3)	Ampl. [mag] (4)	Band & Ref. (5)	Var. type (6)	LC ref. (7)	LC desc. (8)	K [mag] (9)	$J-K$ [mag] (10)	M_{bol} [mag] (11)	M_{bol} ref. (12)
Cl* NGC 121 T V8	i							12.73	0.93	-3.76	i
2MASS J00490032-7322238	g	235:	0.40	I, g, q	SR	q	irr	11.37	1.30	-4.70	z
2MASS J00493262-7317523	g	175:	0.50	I, g, q	SR	q	irr	10.66	1.39	-5.48	g
2MASS J00530765-7307477	g	948:	0.50	I, g, q	SR	q	irr.d	11.19	1.27	-4.89	g
2MASS J00542265-7301057	g	1328:	0.80	I, g, q	SR	q	irr	10.68	1.87	-5.19	g
2MASS J00553091-7310186	g	216:	1.00	I, g, q	M	q	irr.a	10.56	1.77	-5.14	g
2MASS J00563906-7304529	g	809:	0.40	I, g, q	SR	q	irr	11.91	1.24	-4.14	g
2MASS J00564478-7314347	g	304:	0.60	I, g, q	SR	q	irr.a	10.89	1.47	-4.96	g
2MASS J00570070-7307505	g	1397:	0.50	I, g, q	SR	q	irr	10.63	1.65	-5.06	g
2MASS J00571214-7307045	g	306:	0.40	I, g, q	SR	q	irr	10.31	1.38	-5.51	g
2MASS J00571648-7310527	g	913:	0.20	I, g, q	SR	q	irr	11.38	1.15	-4.76	g
2MASS J01003150-7307237	g	168:	0.35	I, g, q	SR	q	irr.a	11.86	1.16	-4.30	z
Cl* NGC 419 LE 35	i		0.50	I, q				10.75	1.77	-4.52	i
Cl* NGC 419 LE 27	i		0.50	I, q				11.00	1.76	-4.55	i
T Cae	c	156:	1.08	V, k	SR	v, t, u	irr	2.24	1.52	(5.29)	z
SHV 0500412-684054	a	224	0.92	I, a	M	p, s, r	reg	11.59	1.47	-4.53	a
SHV 0502469-692418	a	310	0.92	I, a	M	p, r	reg	10.65	1.46	-4.78	a
SHV 0504353-712622	a	364:	1.02	I, a	M	r	reg.d1	10.41	1.96	-4.90	a
SHV 0517337-725738	a	152	0.92	I, a	M			12.00	1.05	-3.21	a
SHV 0518222-750327	a	338	1.54	I, a	M			10.79	1.71	-4.48	a
SHV 0518161-683543	a	193	1.22	I, a	M	p, r	reg	11.64	1.71	-3.75	a
SHV 0520505-705019	a	298	1.20	I, a	M	p, s, r	reg.at	10.99	2.23	-4.31	a
SHV 0520427-693637	a	317	1.18	I, a	M	p, s, r	reg.atV	10.77	2.07	-3.59	a
SHV 0528537-695119	a	353	0.94	I, a	M	p	reg.t	10.85	2.83	-4.13	a
SHV 0525478-690944	a	398	1.20	I, a	M	p, r	reg.t	10.17	2.83	-5.00	a
SHV 0527072-701238	a	312	1.24	I, a	M	p, r	reg.atV	10.77	2.19	-4.67	a
SHV 0536139-701604	a	460	1.34	I, a	M	p, r	irr	19.73	2.19	-4.68	a
[ABC89] Pup 42	f		∼0.14	K, f	SR			6.10	2.30	(9.40)	z
IRAS 09484-6242	f		∼0.08	K, f	SR			5.56	2.07	(8.80)	z
[W65] c2	f		< 0.40+dips?	K, f	SR			6.22	1.70	(9.30)	z
[ABC89] Cir 18	f		< 0.40	K, f	SR			7.21	2.44	(10.50)	z
HE 1428-1950	e							9.32	0.67	(11.10)	z
V CrA	b		0.3+dips	V,w	R CrB	v, w		7.49	1.20	(10.20)	z
HD 202851	b				nv	b		7.02	0.68	(8.80)	z

Appendix 2.D Measurements

Tables 2.5 and 2.6 display the color and index measurements associated with Figures 2.14 and 2.15.

Name	$(R-I)$ [mag]	$(R-H)$ [mag]	$(I-H)$ [mag]	$(I-K_s)$ [mag]	$(J-H)$ [mag]	$(H-K_s)$ [mag]	$(J-K_s)$ [mag]
HD 202851	0.50	1.83	1.32	1.41	0.57	0.08	0.65
HE 1428-1950	0.56	1.88	1.32	1.47	0.57	0.15	0.72
Cl* NGC 121 T V8	0.74	2.57	1.83	2.02	0.76	0.19	0.95
SHV 0518161-683543	0.75	2.66	1.91	2.15	0.74	0.24	0.98
SHV 0517337-725738	0.91	3.08	2.17	2.46	0.81	0.29	1.09
2MASS J00571648-7310527	0.87	3.04	2.17	2.50	0.95	0.33	1.28
2MASS J00563906-7304529	1.34	3.90	2.56	2.88	0.97	0.32	1.29
2MASS J01003150-7307237	0.89	3.35	2.46	2.78	0.99	0.33	1.32
2MASS J00530765-7307477	0.96	3.44	2.48	2.85	0.98	0.37	1.35
2MASS J00493262-7317523	0.95	3.49	2.55	2.92	1.02	0.37	1.39
2MASS J00490032-7322238	0.93	3.34	2.41	2.80	1.04	0.39	1.43
2MASS J00571214-7307045	0.99	3.59	2.60	3.03	1.04	0.43	1.47
2MASS J00570070-7307505	1.14	3.69	2.55	3.04	1.09	0.49	1.58
2MASS J00564478-7314347	1.15	4.32	3.17	3.70	1.16	0.53	1.69
2MASS J00542265-7301057	1.26	4.25	2.98	3.59	1.21	0.61	1.81
SHV 0500412-684054	1.01	3.47	2.46	3.12	1.18	0.66	1.84
IRAS 09484-6242	1.38	4.27	2.89	3.49	1.24	0.60	1.84
Cl* NGC 419 LE 27	1.72	4.64	2.92	3.61	1.23	0.69	1.92
SHV 0520427-693637	1.37	4.72	3.35	3.96	1.33	0.61	1.94
[W65] c2	1.28	4.09	2.81	3.47	1.28	0.66	1.94
SHV 0502469-692418	1.19	3.98	2.79	3.56	1.22	0.77	1.99
2MASS J00553091-7310186	1.48	5.18	3.70	4.40	1.31	0.70	2.02
Cl* NGC 419 LE 35	1.71	4.68	2.97	3.72	1.29	0.75	2.04
SHV 0504353-712622	1.34	4.61	3.27	4.03	1.33	0.76	2.09
T Cae	1.11	4.51	3.40	4.19	1.40	0.80	2.19
SHV 0527072-701238	1.25	4.29	3.04	3.97	1.39	0.93	2.32
SHV 0520505-705019	1.26	4.37	3.11	4.08	1.44	0.97	2.40
[ABC89] Cir 18	1.90	6.06	4.16	4.99	1.58	0.83	2.41
SHV 0518222-750327	1.47	5.17	3.70	4.71	1.48	1.02	2.50
[ABC89] Pup 42	1.76	5.60	3.84	4.86	1.63	1.03	2.66
[ABC89] Cir 18	1.98	6.45	4.47	5.49	1.72	1.02	2.74
SHV 0536139-701604	1.88	6.00	4.12	5.36	1.72	1.24	2.96
SHV 0525478-690944	2.08	7.12	5.04	6.34	1.75	1.30	3.05
SHV 0528537-695119	0.76	4.54	3.78	5.13	1.81	1.35	3.16

Table 2.5: Color measurement

Table 2.6: Index measurement

Name	$(J-K_s)$ [mag]	COH	$CO12$	$CO13$	CN	$C2U$	$C2$	$DIP153$	$rmsH$	$rmsK$
HD 202851	0.65	0.03	0.94	0.05	0.33	0.44	0.07	0.04	0.04	0.03
HE 1428-1950	0.72	0.03	0.87	0.01	0.37	0.70	0.12	0.05	0.06	0.05
Cl* NGC 121 T V8	0.95	0.10	1.57	0.07	0.63	0.67	0.12	−0.01	0.05	0.04
SHV 0518161-683543	0.98	0.08	1.75	0.11	0.91	0.84	0.14	0.01	0.06	0.04
SHV 0517337-725738	1.09	0.10	1.39	0.03	0.68	0.87	0.14	0.01	0.05	0.03
2MASS J00571648-7310527	1.28	0.08	1.54	0.05	0.83	1.15	0.30	0.01	0.12	0.12
2MASS J00563906-7304529	1.29	0.01	0.94	0.12	1.11	2.21	0.67	−0.03	0.14	0.17
2MASS J01003150-7307237	1.32	0.10	1.46	0.08	0.74	1.10	0.22	−0.02	0.09	0.08
2MASS J00530765-7307477	1.35	0.08	1.20	0.00	0.77	1.91	0.35	−0.07	0.13	0.12
2MASS J00493262-7317523	1.39	0.08	1.18	0.06	0.87	1.50	0.32	−0.05	0.10	0.09
2MASS J00490032-7322238	1.43	0.08	1.41	0.08	0.91	2.04	0.41	−0.09	0.11	0.11
2MASS J00571214-7307045	1.47	0.08	1.25	0.05	0.96	1.65	0.42	−0.07	0.13	0.13
2MASS J00570070-7307505	1.58	0.07	1.10	0.01	0.87	2.08	0.47	−0.11	0.15	0.14
2MASS J00564478-7314347	1.69	0.07	0.81	0.03	0.70	1.78	0.42	−0.10	0.13	0.11
2MASS J00542265-7301057	1.81	0.07	0.82	0.02	0.77	2.33	0.45	−0.10	0.16	0.13
SHV 0500412-684054	1.84	0.09	1.81	0.10	0.62	1.34	0.28	0.05	0.07	0.06
IRAS 09484-6242	1.84	0.02	1.09	0.11	0.93	-	0.84	−0.16	0.14	0.13
Cl* NGC 419 LE 27	1.92	0.07	0.96	0.02	0.72	-	0.50	−0.16	0.15	0.13
SHV 0520427-693637	1.94	0.11	2.01	0.14	0.96	1.01	0.22	−0.10	0.14	0.14
[W65] c2	1.94	0.06	1.45	0.08	0.68	-	0.44	−0.08	0.10	0.09
SHV 0502469-692418	1.99	0.06	1.74	0.06	0.60	-	0.25	0.10	0.07	0.06
2MASS J00553091-7310186	2.02	0.06	0.92	0.01	0.73	1.59	0.50	−0.10	0.16	0.13
Cl* NGC 419 LE 35	2.04	0.06	0.86	0.04	0.63	-	0.45	−0.14	0.15	0.14
SHV 0504353-712622	2.09	0.05	1.05	0.01	0.71	2.26	0.43	−0.11	0.11	0.09
T Cae	2.19	0.08	1.51	0.08	0.96	1.64	0.28	−0.18	0.12	0.11
SHV 0527072-701238	2.32	0.04	1.05	0.06	0.45	-	0.33	−0.01	0.06	0.05
SHV 0520505-705019	2.40	0.05	0.90	0.03	0.52	1.76	0.34	−0.02	0.07	0.05
[ABC89] Cir 18	2.41	0.06	1.25	0.05	0.75	-	0.55	−0.16	0.16	0.15
SHV 0518222-750327	2.50	0.06	1.12	0.04	0.57	1.26	0.27	0.05	0.07	0.05
[ABC89] Pup 42	2.66	0.03	0.78	0.02	0.73	-	0.58	−0.20	0.15	0.15
[ABC89] Cir 18	2.74	0.06	1.16	0.04	0.74	-	0.55	−0.16	0.15	0.15
SHV 0536139-701604	2.96	0.05	0.71	0.02	0.59	-	0.41	−0.02	0.10	0.06
SHV 0525478-690944	3.05	0.02	0.46	0.02	0.33	-	0.20	−0.03	0.04	0.02
SHV 0528537-695119	3.16	0.02	0.44	0.01	0.47	-	0.22	−0.05	0.06	0.04

Chapter 3

XSL carbon star spectra between 0.4 and 2.4 μm: comparison with models [1]

⋆ ⋆ ⋆

A. Gonneau, A. Lançon, S. C. Trager, B. Aringer, W. Nowotny

To be submitted to Astronomy & Astrophysics

Abstract

We make use of a collection of carbon star spectra, obtained as part of the X-shooter Spectral Library, to infer some carbon-rich models. The observed spectra span from 0.4 to 2.4 μm and present quite a variety in $(J-K)$, chemical enrichment and pulsation properties. Because of the bimodal behaviour of our sample, highlighted by the presence of an absorption band at 1.53 μm, the comparison with the hydrostatic models is not straightforward.

[1] Based on observations collected at the European Southern Observatory, Paranal, Chile, Prog. ID 084.B-0869(A/B), 085.B-0751(A/B), 189.B-0925(A/B/C/D).

3.1 Introduction

Modelling the spectra of luminous red stars, such as red supergiants or luminous asymptotic giant branch stars, remains an immense challenge. These stars have hugely extended atmospheres which host molecules and sometimes dust. Their heavy element abundance ratios are non-solar as the result of dredge-up episodes in their previous evolutionary history. This is particularly true for carbon stars (C stars), whose atmospheres have carbon-to-oxygen abundance ratios larger than 1. Many, if not all, luminous red stars are variable due to pulsation (Wood 2015), and pulsation sends shock waves through the atmospheres. In addition, interferometric observations have demonstrated significant departures from spherical symmetry in some of these objects, that have been interpreted as the signatures of large scale convective cells. In the case of red supergiants, these inhomogeneities have been identified as a plausible cause of differences between the stellar effective temperatures estimated from optical molecular bands on one hand, or from the spectral energy distribution on the other (Davies et al. 2013). Qualitatively similar inhomogeneities have been discovered in asymptotic giant branch stars (van Belle et al. 2013).

However, luminous red stars can be observed at very large distances, and they contribute significantly to the light of certain galaxies especially at red and near-infrared (NIR) wavelengths. Their relative numbers are predicted to be sensitive functions of age and initial metallicity. Their importance in studies of the stellar populations of local and remote galaxies justifies the continuous efforts devoted both to their empirical characterization and to their modelling.

In a previous article (Gonneau et al. 2015, hereafter *Chapter 2*), we have described new spectroscopic observations of carbon stars (C stars) obtained with the ESO/VLT/X-shooter instrument as part of the XSL project (X-shooter Spectral Library, PI. S. C. Trager). This collection is the first to provide simultaneous optical and NIR observations at a resolving power $R = \lambda/\delta\lambda \sim 8000$. Hence it offers a unique possibility to test state-of-the art synthetic spectra of C stars. For stars that can be reproduced in a satisfactory fashion, estimates of the stellar fundamental parameters may be derived. These estimates are essential if the empirical spectra are to be used as templates in future studies of the stellar populations of galaxies.

A recent series of four articles has provided the largest current collection of model atmospheres and low-resolution theoretical spectra for C stars (Aringer et al. (2009), Nowotny et al. (2011, 2013), Eriksson et al. (2014) – respectively referred to as Papers T1 to T4 hereafter). These papers demonstrate that only the energy distributions of relatively blue asymptotic giant branch C stars (in that case, $J-K \leq 1.5$) can be matched with hydrostatic models. The energy distributions of redder objects result from the combination of photospheric emission and radiative transfer through the dusty circumstellar material, that is produced naturally as a result of pulsation. The dynamic models of these series are able to reproduce the location of C stars in a number of color-magnitude and color-color diagrams, and also reproduce typical properties of the mass loss and wind velocities.

In this article, we focus on the hydrostatic models of T1. Early synthetic spectra based on these models were used by Paladini et al. (2011) to analyse low-resolution spectra ($400 < R < 1800$) of C stars with no circumstellar dust in the near-infrared ($0.9 < \lambda < 4.2\,\mu$m), together with interferometric observations. It allowed the authors to select prefered line lists for C_2. They concluded that the C_2H_2 feature at $3.1\,\mu$m was the spectral signature most sensitive to effective temperature. A large grid of new high-resolution theoretical spectra based on the hydrostatic models of T1 has been computed for the present article. High-resolution theoretical spectra for the pulsating models of T2, T3, T4 are not yet available. The following questions guide our comparisons with the X-shooter observations. Can the optical-to-near infrared spectra be matched reasonably well, for stars with little or no evidence of circumstellar dust? To what extent are parameters estimated from optical wavelengths compatible with those obtained from NIR wavelengths?

The paper is organized as follows. Section 3.2 describes the input carbon-rich spectra and Section 3.3 presents the theoretical grid of models. Section 3.4 shows the first part of the study: a comparison between models. In Section 3.5, we use the result from Section 3.4 and compare our observations with the previous models. In Section 3.6, we discuss the results and conclude the paper.

3.2 Observations

Our sample of carbon stars is composed of 35 medium-resolution spectra, observed with the European Southern Observatory (ESO/VLT) spectrograph X-shooter (Vernet et al. 2011). The beauty of this instrument lies in the fact that it allows simultaneous acquisition of spectra from 0.3 to $2.5\,\mu$m, using two dichroics to split the beam into three arms, respectively ultraviolet-blue (UVB), visible (VIS), and near-infrared (NIR).

The C-star spectra were acquired as part of the X-shooter Spectral Library (hereafter XSL, Chen et al. 2014a), through an ESO Large Programme. This empirical library contains about 700 stars, observed at a moderate resolving power ($7\,700 \leq R \leq 11\,000$ depending on the arm) and covering a large range of stellar atmospheric parameters.

Our sample of carbon stars includes stars from the Milky Way (MW) and the Large and Small Magellanic Clouds (LMC, SMC). Details about the star selection and the data reduction can be found in *Chapter 2* Here, we only briefly recall the properties of the resulting spectra.

Our sample presents quite a diversity in spectral shape and absorption-line characteristics. The highlight of our previous paper was a bimodal behaviour among carbon stars with relatively red near-infrared colors. Some of our carbon stars with $(J - K) > 1.6$ display an absorption band at $1.53\,\mu$m, which is usually associated to HCN+C_2H_2 (Gautschy-Loidl et al. 2004). In our sample, the $1.53\,\mu$m feature was also associated to a smoother near-infrared spectrum and an energy distribution with two components, one peaking at red optical wavelengths, the other at long wavelengths.

In the following, our sample will be divided in four groups, which can be different from the groups described in *Chapter 2*. The first group (A) will gather the bluest C stars from our sample, with $(J-K) < 1.2$. It remains the same as Group 1. The second group (B) will gather the classical C stars with $1.2 < (J-K) < 1.6$, as Group 2. The two last groups will gather all the carbon stars with $(J-K) > 1.6$. The dichotomy between the stars displaying or not the 1.53 μm absorption will be used to separate the stars into two groups. The stars from the former Groups 3 and 4 without this absorption feature will be in Group C. All the other stars, thus with the absorption feature, will be gathered in Group D.

Name	Galaxy	$(J-K_s)$ [mag]	Gr. I	Gr. II
HD 202851	MW	0.65	1	A
HE 1428-1950	MW	0.72	1	A
Cl* NGC 121 T V8	SMC	0.95	1	A
SHV 0518161-683543	LMC	0.98	1	A
SHV 0517337-725738	LMC	1.09	1	A
2MASS J00571648-7310527	SMC	1.28	2	B
2MASS J00563906-7304529	SMC	1.29	2	B
2MASS J01003150-7307237	SMC	1.32	2	B
2MASS J00530765-7307477	SMC	1.35	2	B
2MASS J00493262-7317523	SMC	1.39	2	B
2MASS J00490032-7322238	SMC	1.43	2	B
2MASS J00571214-7307045	SMC	1.47	2	B
2MASS J00570070-7307505	SMC	1.58	2	B
2MASS J00564478-7314347	SMC	1.69	3	C
2MASS J00542265-7301057	SMC	1.81	3	C
IRAS 09484-6242	MW	1.84	3	C
Cl* NGC 419 LE 27	SMC	1.92	3	C
[W65] c2	MW	1.94	3	C
SHV 0520427-693637	LMC	1.94	3	C
2MASS J00553091-7310186	SMC	2.02	3	C
Cl* NGC 419 LE 35	SMC	2.04	3	C
SHV 0504353-712622	LMC	2.09	3	C
T Cae	MW	2.19	3	C
[ABC89] Cir 18	MW	2.41	4	C
[ABC89] Pup 42	MW	2.66	4	C
[ABC89] Cir 18	MW	2.74	4	C
SHV 0500412-684054	LMC	1.84	3	D
SHV 0502469-692418	LMC	1.99	3	D
SHV 0527072-701238	LMC	2.32	4	D
SHV 0520505-705019	LMC	2.40	4	D
SHV 0518222-750327	LMC	2.50	4	D
SHV 0536139-701604	LMC	2.96	4	D
SHV 0525478-690944	LMC	3.05	4	D
SHV 0528537-695119	LMC	3.16	4	D

Table 3.1: Main properties of our observed carbon stars

Table 3.1 lists the observed carbon stars used in this paper. All spectra are plotted in the appendix of *Chapter 2*. In the following, we will not discuss the case of V CrA, a star of type R Coronae Borealis (R CrB) that was undergoing an obscuration event at the time of observation. Its spectrum is dominated by circumstellar emission and shows no photospheric features.

3.3 Carbon-rich hydrostatic models

We use a grid of theoretical models atmospheres computed specifically for this project, in the framework of Aringer et al. (2009). These models are hydrostatic dust-free carbon-rich models, based on spherically symmetric COMARCS atmospheres.

3.3.1 Initial grid

The original series of models covers a wide range of parameters in effective temperatures, surface gravities and carbon over oxygen ratios. In addition, sub-grids with various metallicities were computed, in order to reproduce the population from the Milky Way and the Magellanic Clouds, and also various masses.

For the microturbulent velocity, a value of $\xi = 2.5$ km s^{-1} was adopted. The models were calculated in the range $\tau_{Rosseland} = 10^2$ to 10^{-5} with a constant logarithmic step size of 0.1.

The hydrostatic COMARCS atmospheres were then used to compute synthetic opa-city sampling spectra covering the range between 0.444 to 25.0 μm with a resolution of R = 10000. Due to the statistical nature of the opacity sampling, only the average over a large number of wavelength points (usually 20 to 100) gives a realistic representation of the observed stellar spectra. Thus, the resolution was reduced to R = 200 by convolving their spectra with a Gaussian function defined by the corresponding half width. No additional broadening caused for example by a macroturbulent velocity was assumed.

3.3.2 New grid

Due to the resolution of the X-shooter spectra ($\simeq$ 10000), the actual resolution of the models was not sufficient to perform high resolution comparisons. A new grid of models was computed with a resolution of R = 200000, that we smoothed afterwards to match the resolution of our spectra. These models were computed for solar abundances and for M = 1.0 $M_{\odot}$. The effective temperature of the models spans from 2500 to 4000 K, with a step of 100 K. The surface gravity takes the following values: -0.4, 0 and 2. The ratio of carbon over oxygen is sampled as follows: 1.01, 1.05, 1.10, 1.40 and 2.0. A second set of models with $[Fe/H] = -0.5$ was also computed. Figure 3.1 shows a schematic representation of all the models available, as a function of the parameters listed before.

It is important to keep in mind that although this grid is a good starting point, it does not vary all the relevant parameters. We know from red supergiants that at least the turbulent velocity parameters and the nitrogen abundance will affect the relative strengths of molecular bands.

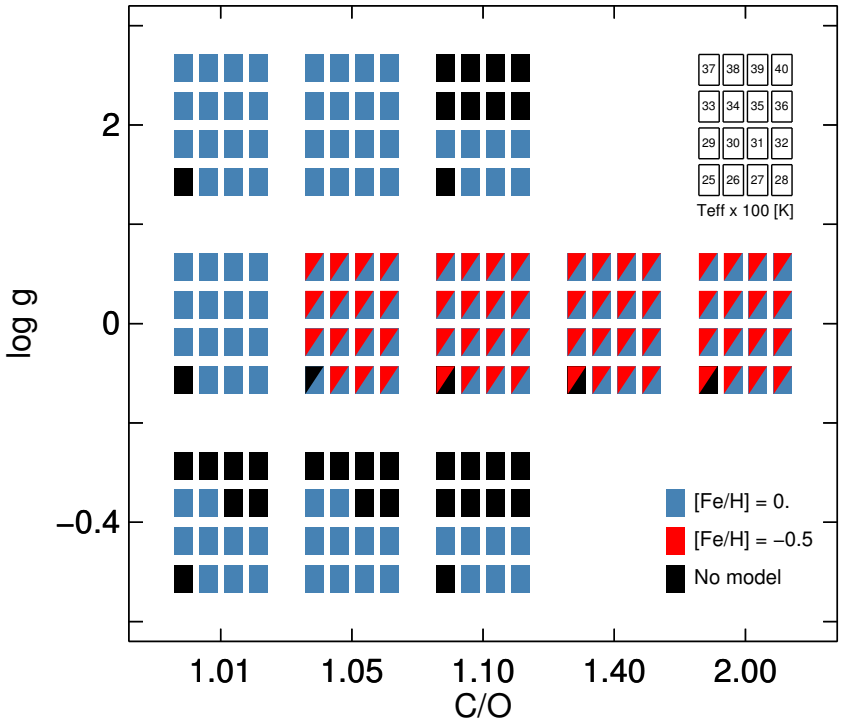

Figure 3.1: Schematic overview showing our grid of models.

3.3.3 Examples of model spectra

Figure 3.2 shows an example of a model spectrum at high resolution (R = 200000) as a black curve and its smoothed version (R $\simeq$ 10000) as a red curve. The parameters of the model used are listed on the top-right corner of the figure. By smoothing the high resolution model spectra we loose the information of the continuum.

Figure 3.3 shows three hydrostatic models which share the same properties except the temperature. The temperature decreases from the top to the bottom. The peak of the SED slowly shifts from the blue to the red, when the spectra get cooler. The strongest bandheads and the ragged aspect of the spectra are due mostly to numerous lines from CN and C_2, which tend to increase with decreasing temperature. The signatures with a weaker dependence on T_{eff} over the plotted range, such as those of CO around 1.65 and 2.3 μ, are progressively masked into a forest of other features when T_{eff} decreases.

The effects of the fundamental parameters on the spectra are not obvious to the eye in plots of the whole spectrum. They are more efficiently summarized by index measurements, as shown below.

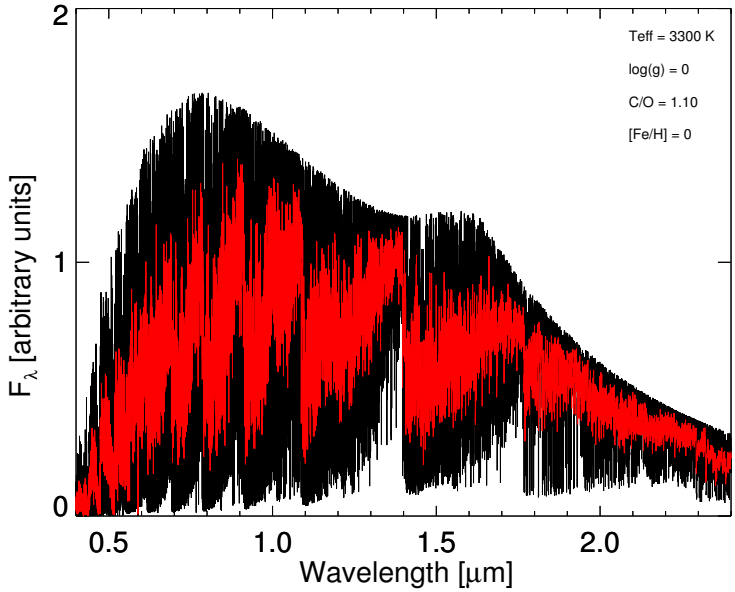

Figure 3.2: Example of a model spectrum at high resolution (black curve) and smoothed to XSL resolution (red curve).

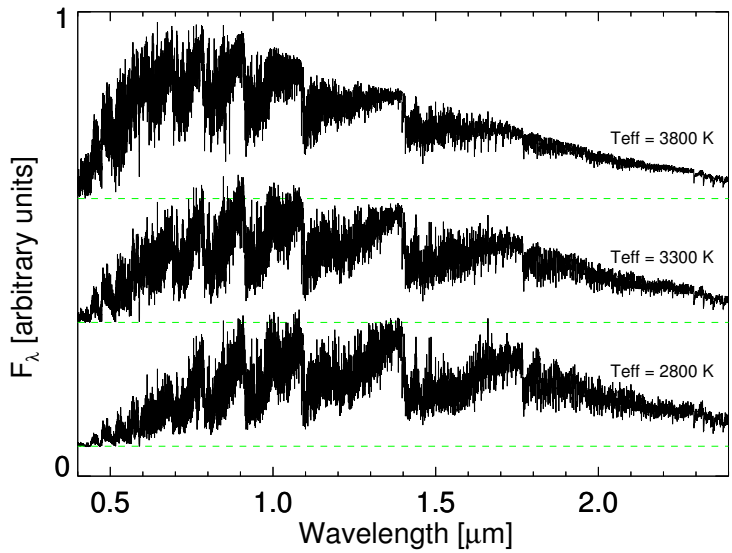

Figure 3.3: Examples of synthetic spectra of C-rich giants with different temperatures ($\log(g)$ =0, C/O = 1.10 and [Fe/H] = 0). The spectra are normalized around 1.35 μm for display purposes.

3.3.4 Molecular indices of model spectra

In *Chapter 2*, we defined spectroscopic indices for carbon stars. We calculated the values of these indices for the grid of models. We define a new version of the index $DIP153$, based on the clear separation, shown in *Chapter 2*, between the stars with and without the 1.53 μm absorption feature. To do so, we fit the averaged values of the $DIP153$ index (as a function of $(J - K_S)$) for our (observed) stars without the 1.53 μm feature, and subtract these values to the values of the $DIP153$ index.

$$DIP153b = DIP153 - \text{fit} = DIP153 - 0.123 * (1 - (J - K_S)) \qquad (3.1)$$

Figure 3.4 shows the values of four representative near-infrared indices as a function of the effective temperature of the models. In addition to $DIP153b$, we plot CN, which measures the strength of the CN molecule at 1.11 μm, $C2$, which measures the bandhead of the C_2 molecule at 1.77 μm, and $CO12$, which measures the first overtone ro-vibrational band of CO at 2.3 μm. The symbol sizes represent model C/O ratios in the upper panels, model surface gravities in the lower panels.

As a general trend, molecular bandhead strengths increase with decreasing temperatures. This is the case for CN, C_2 and CO. At the lowest temperatures, contamination of the index passbands by lines from other molecules (or other bands of the same molecule) weakens the index values.

At a given T_{eff}, the bands of CN and C_2 increase with C/O, while CO decreases. For the surface gravity, the strengths of the bands increase with decreasing $\log(g)$. For $T_{eff} < 3000$ K, the high-gravity models ($\log(g)$=2) really contrast with the other models.

From the plots showing $DIP153b$ versus temperature, it is clear that some of the cool models ($T_{eff} < 3000$ K) display the 1.53 μm absorption band.

3.4 Comparison of pseudo-observations and models

3.4.1 Study of pseudo-observations

Before comparing our observations to the grid of models, it is important to evaluate the amount of information present in the models themselves. If the models were perfect representations of the reality, with what uncertainties could we estimate the values of the fundamental parameters, such as T_{eff}, $\log(g)$, C/O? To answer that question, we select a subset of models that we analyse with the full model grid as if they were observations. We refer to the subset as pseudo-observations. Table 3.2 summarizes the parameters of the pseudo-observations.

Before analysis, the pseudo-observations are smoothed to a resolving power comparable to X-shooter spectra, R $\sim$ 10000 and resampled. Artificial gaussian noise is added, to reach a signal-to-noise ratio of 75 per pixel. Because these models are hydrostatic and thus dust-free, we redden them artificially with $A_V = 1$, using the extinction law of Cardelli et al. (1989).

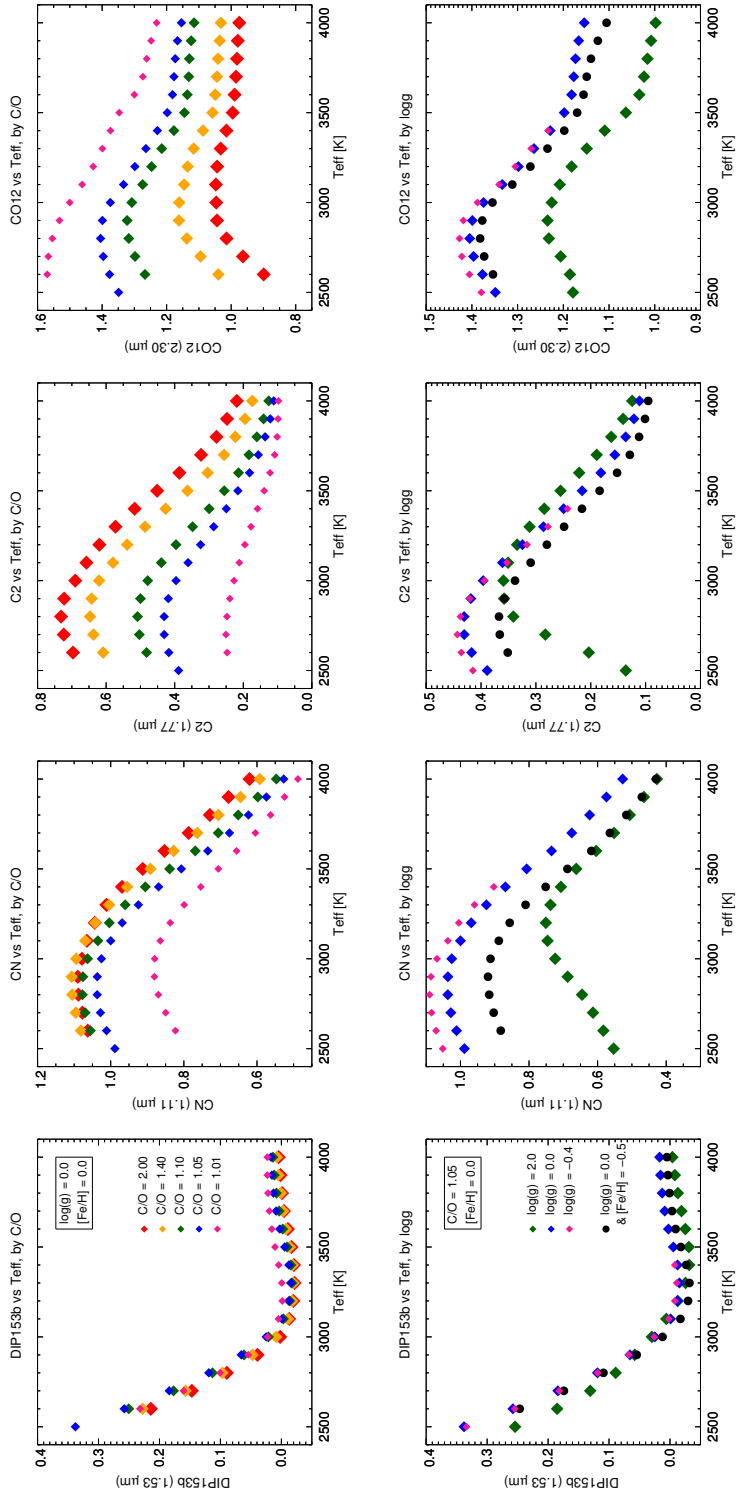

Figure 3.4: Molecular indices vs T_{eff} for a representative set of models. The symbols are for C/O in the upper panels and for log(g) in the lower panels. More indices are shown in Fig. 3.8.

Input parameters	Values
T_{eff} [K]	2600 - 3300 - 3800
$\log(g$ [cm/s^2])	0.0
C/O	1.05 - 1.40
[Fe/H]	0.0
A_V	1

Table 3.2: Properties of the subset of models selected as pseudo-observations

3.4.2 Methodology

To compare our pseudo-observations to the models, we perform a χ^2 minimization in a four-dimensional space. The grid of models spans four dimensions which are T_{eff}, $\log(g)$, (C/O) and [Fe/H].

To absorb any residual flux calibration errors in the observed data, a multiplicative spline polynomial is used instead of a standard extinction law to reshape the energy distribution. For consistency, it is important to note that this can only mimic multiplicative effects of circumstellar dust such as extinction, and not additive effects such as any continuous emission by dust.

In order to avoid unphysical dereddening of the models, we exclude any models intrinsically redder than the fitted observed spectrum, based on $(R - I)$ for the UVB/VIS range or $(J - K)$ for the NIR. A tolerance of 10% on these colors is implemented as an allowance for spectrophotometric errors in the data.

The reduced χ^2 is calculated as follows:

$$\chi^2_{red} = \frac{1}{N} \sum_{i=1}^{M} W(i) \times \frac{(F_{obs}(i) - polynomial \times F_{mod}(i))^2}{\sigma^2_{F_{obs}}(i)}, \tag{3.2}$$

with: F the observed or theoretical flux, σ the noise spectrum of the observation and W the weights assigned to each pixel. The weights take values of 0 in the regions of strong telluric absorption[2], and 1 elsewhere. M is the total number of pixels and N is defined as the sum of the weights.

As the wavelength range of our observations spans from 0.4 to 2.4 μm, we decide to perform for each observation two comparisons: one over the visible (VIS) wavelength range (0.4–1.0 μm) and one over the near-infrared (NIR) wavelength range (1.0–2.4 μm). The aim is to determine which wavelength range sets the strongest constraints on the various stellar parameters. When applied to observations, these separate studies will allow us to explore whether the parameters derived from optical and near-infrared wavelength using hydrostatic models are consistent with each other.

[2] In the empirical spectra, these regions are frequently affected by residual telluric absorption (even after correction). We set the weights to 0 in the following regions: 0.758–0.768 μm, 0.93–0.97 μm, 0.994–1.02 μm, 1.11–1.15 μm, 1.34–1.475 μm, 1.8–1.98 μm, 2.26–2.28 μm.

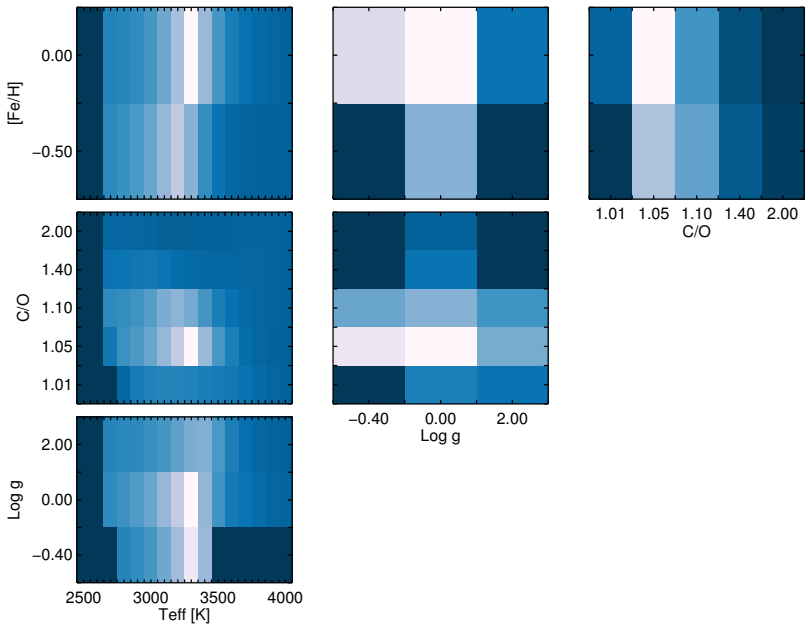

Figure 3.5: Example of χ^2 maps for one of our pseudo-observations ($T_{eff} = 3300$ K, $\log(g) = 0$, C/O = 1.05, [Fe/H] = 0) for the VIS wavelength range. The whiter colors stand for the lower χ^2 values.

3.4.3 χ^2 maps and results

For each pseudo-observation, we can compute a χ^2 map showing the distribution of the best models in the parameter space of the models. Figures 3.5 and 3.6 show an example of χ^2 maps for the fit of a pseudo-observation respectively over the VIS and NIR wavelength ranges. The best models, which correspond to the lowest value of the χ^2, are represented in white. The columns are from left to right: T_{eff}, $\log(g)$ and C/O. The rows are from bottom to top: $\log(g)$, C/O and [Fe/H]. The best values (i.e., the ones that minimize the χ^2 calculation) are represented in white.

In certain regimes, a degeneracy is seen between C/O and T_{eff} . The direction of the degeneracy depends on the wavelength range used. At NIR wavelengths, a higher estimated T_{eff} is associated with a higher estimated C/O ratio, while the opposite is found in the VIS (when the VIS shows any degeneracy).

Another more classical degeneracy is seen between [Fe/H] and T_{eff}: at higher T_{eff}, larger [Fe/H] are needed to produce strong features.

The peaked aspect of the maps shows that, within our limited grid of models, $\log(g)$ and [Fe/H] are relatively well constrained at all temperatures, the VIS constraints being significantly tighter than the NIR constraints. Of course, this may be different if the models are compared to real observations.

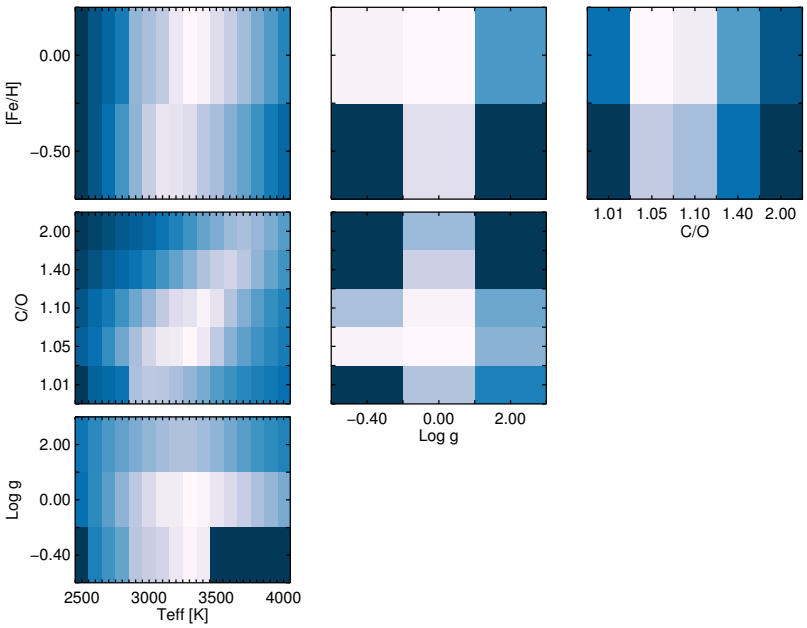

Figure 3.6: Example of χ^2 maps for one of our pseudo-observations ($T_{eff} = 3300$ K, $\log(g) = 0$, C/O = 1.05, [Fe/H] = 0) for the NIR wavelength range. The whiter colors stand for the lower χ^2 values.

3.5 Comparison of observations and models

3.5.1 Color-color plot

We compute synthetic photometry through the 2MASS near-infrared filters (Cohen et al. 1992) and standard R and I filters (Bessell 1990). The results are displayed in Fig. 3.7 and in Appendix 3.42. The solid line in Fig. 3.7 shows the effect of a simple reddening screen (Cardelli et al. 1989). The colors of neither the reddest nor the bluest XSL spectra can be reproduced with the hydrostatic models and this extinction law.

A comparison of the colors of the XSL targets and those of models provides a sanity test on the energy distributions as well as information on effects of dust. At all but the lowest temperatures, color indices involving a near-infrared passband are good first order indicators of effective temperature, with a low sensitivity to other fundamental parameters. In that regime, only dust may have a strong effect on the colors.

The error bars are upper limits, as they are based on the dispersion in the distributions of differences between our photometry and the literature values (large amplitude variables excluded).

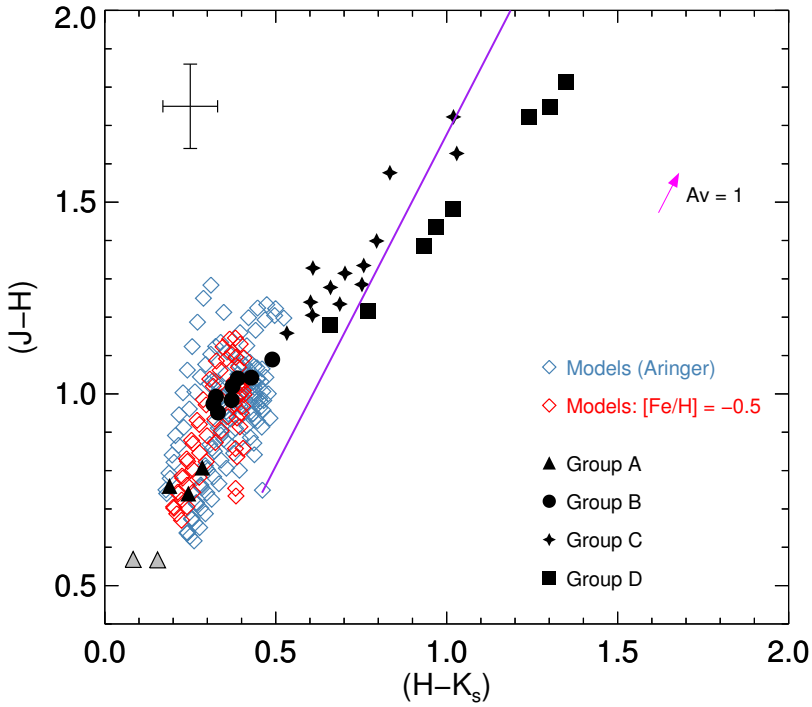

Figure 3.7: Colors (no correction for interstellar reddening) for our sample of carbon stars (filled symbols), using the 2MASS J, H and K_s filters. The synthetic colors (open diamonds) of our grid of hydrostatic models are overplotted for comparison. The plotted error bars are based on the dispersion in the distributions of differences between our photometry and the literature values (large amplitude variables excluded).

Group A gathers the bluest stars of our sample, represented as filled triangles in Figure 3.7. From this Figure, we clearly see that two of our stars, HD 202851 and HE 1428-1950, represented as grey triangles, are out of the parameter space of the models, and thus can not be reproduced with our current grid of models. Therefore, they are not considered in the comparison with the models.

Group D gathers all the stars with the absorption band at 1.53 μm (attributed to HCN+C_2H_2). Although a small number of hydrostatic models contains this feature, the current grid combined with simple extinction does not reach values of $(H - K_s)$ red enough to explain all the observations.

3.5.2 Molecular indices

Figure 3.8 shows the values of the spectroscopic indices designed for carbon stars in *Chapter 2*. In addition, we also plot the values for the $DIP153b$ index defined in Section 3.3.4. The filled symbols stand for our observations (the triangles are

for stars from Group A, the circles for Group B, the stars for Group C and the squares for Group D), while the open diamonds represent the models (in red we highlight the models with [Fe/H] = -0.5).

Error bars account for the noise per resolved element and uncertainties in the shape of the spectrograph's response curve in the scale of molecular features. The latter component is usually dominant because the signal-to-noise ratio of the spectra is of order 10^2. Uncertainties in the response curve on the relevant scales are due to a large part to imperfect modelling of the telluric absorption that affects spectro-photometric standard star observations.

Spectrophotometric indices provide a synthetic view of the models with respect to the XSL data, at a somewhat higher resolution than broad band colors. For brevity, we only discuss the loci in the bins of $(J-K_s)$, as already done in *Chapter 2*.

In general, the model loci agree well with the locus of the observations of our sample with $(J-K_s) < 1.8$. This is true in particular for the CN bands. The CO bands in the H window tend to be too strong in the models compared to the data. These features are sensitive to surface gravity at a given effective temperature. The relative strengths of the first and second overtone CO bands (measured by CO12 and COH) are also sensitive to the microturbulent velocity (Origlia et al. 1997; Lançon & Hauschildt 2010). It is as yet unclear what the predominant cause of the systematic difference should be. Like the data, the model indices present a large dispersion within color bins.

Some of the models display the 1.53 μm feature (panels d and g). However, these models do not display damped line forests in the H and K window, as seen in the corresponding observations (panes h and i). In *Chapter 2*, the damping of the high frequency structure in spectra with the 1.53 μm feature was interpreted as veiling by circumstellar dust. The index plots for the dust-free static models are consistent with this picture.

3.5.3 Full spectrum fits

For a direct comparison between the empirical and the model spectra, we use a methodology similar to Sect. 3.4.2. The differences are the following:

- The noise spectra of our observations are the ones that come out of the X-shooter reduction pipeline and we propagate them throughout all the reduction process, including the correction of the telluric features and the flux calibration.

- We degrade the resolution of the XSL spectra to $R \sim 2000$. The velocity resolution of the XSL data amounts $\sim$ 30 km/s. In Mira-type long period variables, velocity discontinuities with amplitudes larger than 10 km/s are expected as shocks propagate through the atmospheres (Nowotny et al. 2005). They produce significant wavelengths shifts that may differ for various molecular bands. We postpone the study of these high resolution effects to a future article.

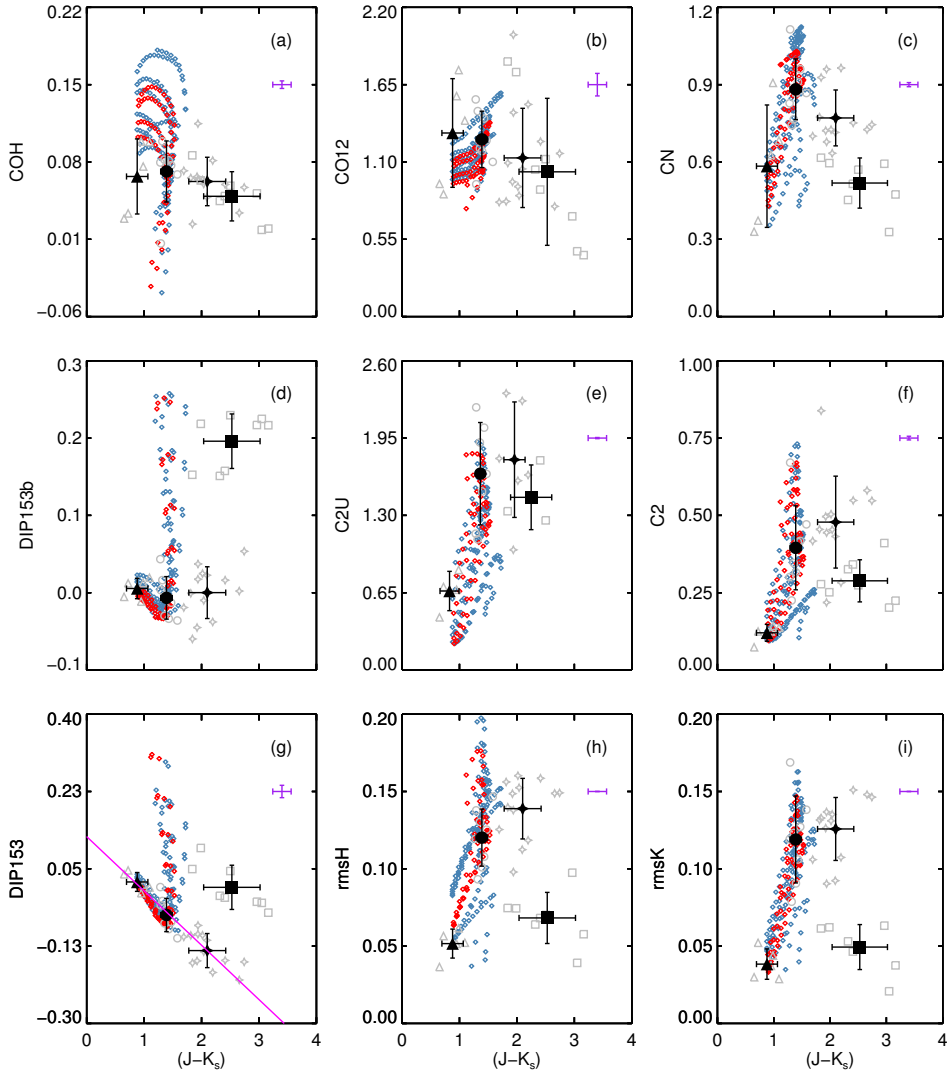

Figure 3.8: Some indices derived from our sample of carbon stars (black symbols) and the grid of models (color symbols) as a function of $(J - K_s)$. The triangles are for stars from Group A, the circles for Group B, the stars for Group C and the squares for Group D. The filled symbols represent the averaged values of our indices in the groups. The open diamonds represent the models at solar (in blue) and sub-solar metalliticity (red). The plotted error bars measure the dispersion within bins. The observational error bars are shown in purple.

3.5.4 Results

For each observation, the best model found is the one which minimizes the χ^2 calculation. We derive the range of acceptable parameters around the best models found over the VIS and the NIR wavelength ranges by setting the limit of χ^2/χ^2_{min} to 1.1.

Tables 3.3 to 3.6 show the range of values of the best models found while comparing our observations to the grid of models. The V letter indicates the values found over the VIS wavelength range, the N letter stands for near-infrared. As said before, what we call the visible wavelength range in this paper runs in principle from 0.4 μm to 1.0 μm, which covers in practice the UVB and VIS parts of X-shooter. But in practice, for some of the coolest stars, we do not have the full visible wavelength range. For each parameter (T_{eff}, log(g), C/O, [Fe/H]), the first column gives the value of the best model (i.e. the one that minimizes the χ^2 calculation), the second column gives the weighted best value and the third and fourth columns give the extreme values. The weighted value is calculated as follows:

$$param_weighted = \frac{\sum_i param(i) \times exp(-(\chi^2_i/\chi^2_{min})/2)}{\sum_i exp(-(\chi^2_i/2 \times \chi^2_{min}))} \tag{3.3}$$

As a general comment for all our observations, the favoured surface gravity is log(g) = 0, and a metallicity of -0.5. These values are satisfactory for TP-AGB stars, and for a sample consisting mostly of LMC, SMC and Milky Way halo stars.

The best fits are shown in Appendix 3.A. For each observation, the upper panel shows the star spectrum as a black curve and the best model times the polynomial as a red curve. The weights applied for the χ^2 minimization are displayed in orange. The middle panel shows the residuals (in green), while the bottom panel shows the difference between the best model and a smoothed version of itself (in blue). In addition, a small insert shows the output χ^2/χ^2_{min} values as a function of the temperatures of the input models.

Figure 3.9 compares the values of the effective temperatures found while fitting the VIS and NIR wavelength range. The dashed line indicates the one-to-one relation. The symbols indicate the values for the different groups. The temperatures derived from our fits tend to be in general warmer in the VIS than in the NIR.

Group A The parameters listed in Table 3.3 agree quite well between the VIS and the NIR wavelength ranges. The best fits are shown from Figures 3.10 to 3.12. Effective temperatures in Group A are above 3750 K.

Two of the three stars in Group A display hydrogen lines in emission. They are large amplitude variables (*Chapter 2*) and the lines are interpreted as signatures of shocks that propagate through the atmosphere. For one of the stars, the model fit is not quite as good as for the others. But overall it is remarkable how well hydrostatic models reproduce the medium resolution spectral features of these warm pulsators.

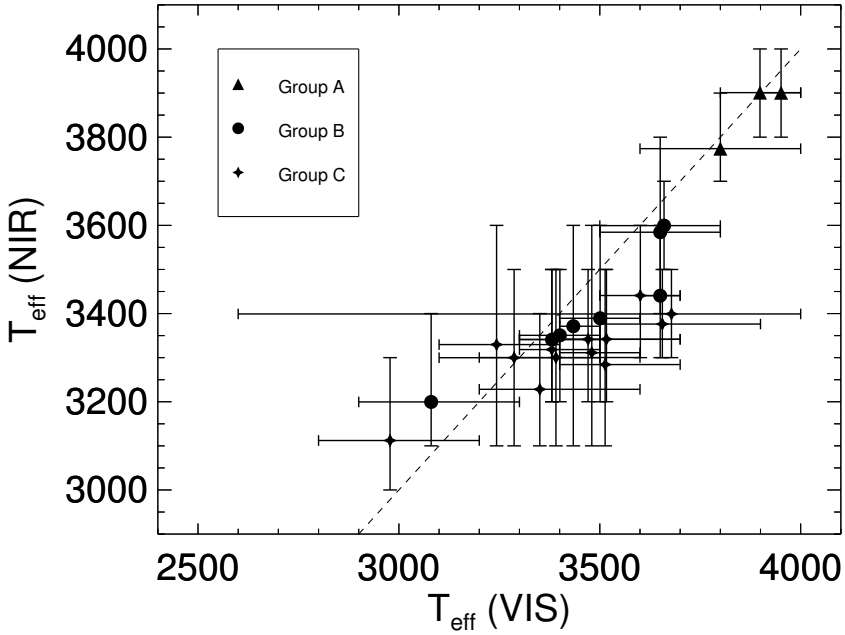

Figure 3.9: Comparison of the best values found for the effective temperature for both wavelength range (VIS and NIR), for Groups A, B and C. The dashed line indicates the one-to-one relation.

Group B Stars from Group B are the most likely to be reproduced by the grid of models, according to Fig. 3.7. The fits are good indeed, and the curves of χ^2 versus model T_{eff} are well behaved with narrow minima. The best values are summarized in Table 3.4. In all but one case (Fig. 3.14), the T_{eff} range derived from the VIS spectrum is narrower than the range accepted based on the NIR data, in agreement with expectations from Sec. 3.4. The temperatures within Group B are spread between 3100 and 3700 K.

In general, a slightly higher temperature in the VIS is compensated by a higher C/O ratio.

From Figures 3.13 to 3.20, some small discrepancies progressively appear. Some are probably instrumental, as the lack of data around 0.63 μm (due to a bad column). A real systematic difference in the shape and depth of the C_2 band at 1.77 μm becomes apparent for $(J - K) \geq 1.4$. This will be discussed further in Group C below.

Group C Table 3.5 summarizes the properties of the best models found for the stars of Group C. Stars from Group C are stars with $(J - K) \geq 1.6$ and they begin to be more affected by the pulsation than stars from the previous groups. Therefore, we are closer to the limits of what can be done with hydrostatic models. The best fits are shown from Figures 3.21 to 3.33.

The range of temperatures found in Group C is similar to that in Group B, despite the redder colors in Group C. The favour C/O value is 2. The effect of C/O on color, at a given T_{eff} (above 3000 K), is very small and hence C/O does not explain the redder colors of Group C. The difference in color between Groups B and C is mainly driven by circumstellar extinction.

Group D Table 3.6 summarizes the results for the stars from Group D, i.e the stars that display the 1.53 μm absorption feature. This subset is the one most affected by the effects of pulsation. It contains only large amplitude variables (cf. *Chapter 2*), and the use of hydrostatic models is a clear limitation. The fits are shown from Figures 3.34 to 3.41.

While the χ^2 distributions as a function of effective temperature remain relatively well behaved for most of the VIS spectra, the distributions for the NIR are very flat. A flat distribution means that the fits provide no or only weak constraints on the temperature. The NIR X-shooter spectra in Group D have a relatively smooth appearance, compared to Groups C and B, as was highlighted in *Chapter 2*. As a consequence, the best fit models tend to have relatively high temperatures (sometimes > 3500 K), and they favour $\log(g)$=2 over $\log(g)$=0. Can we trust any of these? A hot temperature is difficult to reconcile with the presence of the 1.53 μm feature, and indeed high temperature fits fail to reproduce this (e.g. Fig. 3.40 and 3.41). A gravity as high as $\log(g)$=2 is difficult to reconcile with the expected location of large amplitude C-rich variables on the asymptotic giant branch. Our favoured interpretation is that these stars have normal AGB gravities and are not as warm as the NIR fits at $\log(g)$=2 may indicate. Instead, their spectra are profoundly modified by dust that produces both extinction and emission (the combination is known as veiling). The (additive) emission component attenuates the equivalent widths of molecular absorption features produced in the photosphere, and both extinction and emission affect the energy distribution. The parameters given in Table 3.6 based on the NIR spectra should not be relied on.

In principle, the parameters derived in the VIS should be more reliable than those based on the NIR, as dust emission is stronger at longer wavelengths and dust absorption does not modify molecular absorption equivalent widths. However, the useful part of the VIS spectrum of highly reddened objects contains almost exclusively signatures of CN, and one should keep in mind that unexplored parameters such as the Nitrogen abundance could affect these.

Finally, we emphasize two systematic spectral misfits. The C_2 feature at 1.77 μm is never matched correctly. And the 1.53 μm feature present in the coolest hydrostatic models does not have the shape of its observed counterpart (e.g. Fig. 3.35). The line lists for the main carriers (C_2 on one hand, HCN and C_2H_2 on the other) may need revision.

3.6 Conclusions

We have compared optical and near-infrared spectra of carbon stars with hydrostatic models at a spectral resolving power of $\sim$ 2000. The models provide impressive matches to most of the features in the optical and NIR range, but it remains difficult to fit all features simultaneously with a single model, when only extinction is allowed to alter the energy distribution.

In defining a goodness-of-fit criterion, choices can be made that focus either on the high frequency structure within the bands, or on the low resolution energy distribution. In this paper, we have emphasized the latter. XSL spectra contain a wealth of high frequency information, that will be exploited more completely in the future. A main difficulty encountered at the native resolution of the XSL data, R $\sim$ 10000 in the VIS and 8000 in the NIR, is an effect of pulsation. Shocks that travel through the atmospheres of Long Period Variables (LPV) create velocity discontinuities with amplitudes above 10 km/s, which will affect the location and shape of lines at the resolution of XSL. Smoothing to $R \sim 2000$ allows us to avoid this difficulty. Nevertheless, the residuals of the fits show that it remains difficult to fit all the spectral features even at low resolution, and even when a multiplicative polynomial mimicking extinction and flux calibration corrections is allowed to modify the energy distribution.

Quantitative criteria show it becomes progressively more difficult to obtain reasonable matches of the data for redder observed spectra. This is due to a combination of a more complex forest of molecular lines (that is only matched in detail in small parts of the spectra), and to the effects of circumstellar material on the energy distribution (that a simple extinction law cannot reproduce). Relaxing the assumptions on the energy distribution by allowing for an arbitrary polynomial in the fit will provide a complementary view on the respective roles of high and low resolution properties.

Effective temperature ranges derived from optical and NIR fits usually overlap when good fits are found, with a tendency for optical ranges to be narrower than NIR ranges. However, the ranges obtained with our current threshold are very broad.

The fits show that the R $\sim$ 2000 features in the models are not perfect representations of the data. This justifies the use of empirical spectra as templates for C stars in the universe. At this stage however, it is not possible to assign an evolutionary stage precisely to individual stars in the collection based on their spectra alone. When using the C-star observations as templates, it will probably be necessary to continue to use averages, as done for instance by Lançon & Mouhcine (2002) for O-rich and C-rich LPVs.

Appendix 3.A Comparison observations - mo-dels: best fits

Tables 3.3 to 3.6 show the range of parameters of the best models. Figures 3.10 to 3.41 show the best fits of our observations. For each figure, the upper panel shows the observation (black curve), the best model times the polynomial (red

curve) and the weights used for the χ^2 minimization (orange). The middle panel shows the residuals (in green), while the bottom panel shows the difference between the best model and a smoothed version of itself (in blue).

		T_{eff}				log(g)				C/O				[Fe/H]			
Name	Waves	Best	Wei	Min	Max	Best	Wei	Min	Max	Best	Wei	Min	Max	Best	Wei	Min	Max
Cl* NGC 121 T V8	V	4000	3951	3900	4000	0.0	0.0	0.0	0.0	1.40	1.40	1.40	1.40	−0.5	−0.5	−0.5	−0.5
	N	3900	3900	3800	4000	0.0	0.3	0.0	2.0	1.10	1.13	1.05	1.40	−0.5	−0.4	−0.5	0.0
SHV 0518161−683543	V	3900	3800	3600	4000	0.0	0.0	0.0	0.0	1.40	1.28	1.10	1.40	−0.5	−0.5	−0.5	−0.5
	N	3700	3773	3700	3900	0.0	0.0	0.0	0.0	1.10	1.16	1.05	1.40	−0.5	−0.5	−0.5	−0.5
SHV 0517337−725738	V	3800	3898	3800	4000	0.0	0.0	0.0	0.0	1.40	1.60	1.40	2.00	−0.5	−0.5	−0.5	−0.5
	N	4000	3900	3800	4000	0.0	0.0	0.0	0.0	1.40	1.30	1.10	1.40	−0.5	−0.5	−0.5	−0.5

Table 3.3: Range of parameters for the best fits for the stars from Group A

		T_{eff}				log(g)				C/O				[Fe/H]			
Name	Waves	Best	Wei	Min	Max	Best	Wei	Min	Max	Best	Wei	Min	Max	Best	Wei	Min	Max
2MASS J00571648-7310527	V	3700	3650	3600	3700	0.0	0.0	0.0	0.0	2.00	1.70	1.40	2.00	−0.5	−0.5	−0.5	−0.5
	N	3400	3440	3300	3600	0.0	0.8	0.0	2.0	1.10	1.13	1.05	1.40	−0.5	−0.3	−0.5	0.0
2MASS J00563906-7304529	V	3100	3080	2900	3300	−0.4	−0.1	−0.4	0.0	1.10	1.24	1.05	1.40	0.0	−0.1	−0.5	0.0
	N	3200	3199	3100	3400	0.0	0.0	0.0	0.0	2.00	1.78	1.40	2.00	−0.5	−0.2	−0.5	0.0
2MASS J01003150-7307237	V	3700	3650	3500	3800	0.0	0.0	0.0	0.0	1.40	1.39	1.05	2.00	−0.5	−0.5	−0.5	−0.5
	N	3600	3584	3400	3800	0.0	0.0	0.0	0.0	1.10	1.18	1.05	1.40	−0.5	−0.5	−0.5	−0.5
2MASS J00530765−7307477	V	3600	3659	3500	3800	0.0	0.0	0.0	0.0	2.00	2.00	2.00	2.00	−0.5	−0.3	−0.5	0.0
	N	3600	3599	3500	3700	0.0	0.0	0.0	0.0	2.00	1.80	1.40	2.00	−0.5	−0.5	−0.5	−0.5
2MASS J00493262-7317523	V	3500	3500	3400	3600	0.0	0.0	0.0	0.0	1.40	1.60	1.40	2.00	−0.5	−0.5	−0.5	−0.5
	N	3400	3389	3200	3600	0.0	0.7	0.0	2.0	1.10	1.14	1.05	1.40	−0.5	−0.3	−0.5	0.0
2MASS J00490032-7322238	V	3500	3434	3400	3500	0.0	0.0	0.0	0.0	2.00	1.80	1.40	2.00	−0.5	−0.5	−0.5	−0.5
	N	3400	3371	3100	3600	0.0	0.0	0.0	0.0	1.40	1.44	1.10	2.00	−0.5	−0.5	−0.5	−0.5
2MASS J00571214-7307045	V	3500	3400	3300	3500	0.0	0.0	0.0	0.0	2.00	1.70	1.40	2.00	−0.5	−0.5	−0.5	−0.5
	N	3400	3350	3200	3500	0.0	0.0	0.0	0.0	1.40	1.48	1.10	2.00	−0.5	−0.5	−0.5	−0.5
2MASS J00570070-7307505	V	3400	3381	3300	3500	0.0	0.0	0.0	0.0	2.00	1.77	1.40	2.00	−0.5	−0.5	−0.5	−0.5
	N	3400	3340	3200	3500	0.0	0.0	0.0	0.0	2.00	1.76	1.40	2.00	−0.5	−0.5	−0.5	−0.5

Table 3.4: Range of parameters for the best fits for the stars from Group B

		T_{eff}				log(g)				C/O				[Fe/H]			
Name	Waves	Best	Wei	Min	Max	Best	Wei	Min	Max	Best	Wei	Min	Max	Best	Wei	Min	Max
2MASS J00564478-7314347	V	3600	3600	3500	3700	0.0	0.0	0.0	0.0	2.00	2.00	2.00	2.00	−0.5	−0.5	−0.5	−0.5
	N	3500	3440	3300	3600	0.0	0.0	0.0	0.0	2.00	1.76	1.40	2.00	−0.5	−0.5	−0.5	−0.5
2MASS J00542265-7301057	V	3500	3516	3400	3700	0.0	0.0	0.0	0.0	2.00	1.80	1.40	2.00	−0.5	−0.5	−0.5	−0.5
	N	3400	3341	3200	3500	0.0	0.0	0.0	0.0	2.00	1.76	1.40	2.00	−0.5	−0.5	−0.5	−0.5
IRAS 09484-6242	V	3000	2977	2800	3200	0.0	0.0	0.0	0.0	2.00	1.74	1.40	2.00	−0.5	−0.5	−0.5	−0.5
	N	3100	3112	3000	3300	0.0	0.0	0.0	0.0	2.00	1.93	1.40	2.00	−0.5	−0.2	−0.5	0.0
Cl* NGC 419 LE 27	V	3600	3470	3300	3700	0.0	0.0	0.0	0.0	2.00	1.55	1.05	2.00	−0.5	−0.5	−0.5	−0.5
	N	3400	3341	3200	3500	0.0	0.0	0.0	0.0	2.00	1.77	1.40	2.00	−0.5	−0.5	−0.5	−0.5
[W65] c2	V	3900	3678	2600	4000	0.0	0.2	0.0	2.0	2.00	1.70	1.10	2.00	−0.5	−0.4	−0.5	0.0
	N	3400	3399	3300	3500	0.0	0.0	0.0	0.0	1.05	1.07	1.05	1.10	−0.5	−0.5	−0.5	−0.5
SHV 0520427-693637	V	3500	3480	3400	3600	0.0	0.0	0.0	0.0	2.00	1.76	1.40	2.00	−0.5	−0.5	−0.5	−0.5
	N	3200	3311	3100	3600	2.0	0.9	0.0	2.0	1.10	1.46	1.05	2.00	0.0	−0.3	−0.5	0.0
2MASS J00553091-7310186	V	3600	3513	3400	3700	0.0	0.0	0.0	0.0	2.00	1.67	1.10	2.00	−0.5	−0.5	−0.5	−0.5
	N	3300	3284	3100	3500	0.0	0.0	0.0	0.0	2.00	1.80	1.40	2.00	−0.5	−0.5	−0.5	−0.5
Cl* NGC 419 LE 35	V	3800	3655	3500	3900	0.0	0.4	0.0	2.0	2.00	1.42	1.05	2.00	−0.5	−0.4	−0.5	0.0
	N	3400	3376	3300	3500	0.0	0.0	0.0	0.0	2.00	1.85	1.40	2.00	−0.5	−0.5	−0.5	−0.5
SHV 0504353−712622	V	3400	3380	3300	3500	0.0	0.0	0.0	0.0	2.00	1.76	1.40	2.00	−0.5	−0.5	−0.5	−0.5
	N	3500	3318	3200	3500	0.0	0.3	0.0	2.0	2.00	1.65	1.10	2.00	−0.5	−0.4	−0.5	0.0
T Cae	V	3300	3243	3100	3400	0.0	0.0	0.0	0.0	1.40	1.23	1.10	1.40	−0.5	−0.3	−0.5	0.0
	N	3300	3329	3100	3600	0.0	0.4	0.0	2.0	1.10	1.13	1.05	1.40	−0.5	−0.4	−0.5	0.0
[ABC89] Cir 18	V	3500	3350	3200	3600	0.0	0.2	0.0	2.0	2.00	1.47	1.05	2.00	−0.5	−0.5	−0.5	0.0
	N	3200	3228	3100	3400	0.0	0.0	0.0	0.0	2.00	1.83	1.40	2.00	−0.5	−0.4	−0.5	0.0
[ABC89] Pup 42	V	3500	3390	3200	3600	0.0	0.0	0.0	0.0	2.00	1.45	1.05	2.00	−0.5	−0.5	−0.5	−0.5
	N	3300	3300	3100	3500	0.0	0.0	0.0	0.0	2.00	1.80	1.40	2.00	−0.5	−0.4	−0.5	0.0
[ABC89] Cir 18	V	3400	3286	3100	3500	0.0	0.1	0.0	2.0	2.00	1.37	1.05	2.00	−0.5	−0.5	−0.5	0.0
	N	3300	3299	3100	3500	0.0	0.0	0.0	0.0	2.00	1.78	1.40	2.00	−0.5	−0.4	−0.5	0.0

Table 3.5: Range of parameters for the best fits for the stars from Group C

		T_{eff}				log(g)				C/O				[Fe/H]			
Name	Waves	Best	Wei	Min	Max	Best	Wei	Min	Max	Best	Wei	Min	Max	Best	Wei	Min	Max
SHV 0500412-684054	V	3600	3550	3500	3600	0.0	0.0	0.0	0.0	2.00	1.70	1.40	2.00	−0.5	−0.5	−0.5	−0.5
	N	3400	3407	2700	3800	2.0	1.1	0.0	2.0	1.05	1.33	1.05	2.00	0.0	−0.2	−0.5	0.0
SHV 0502469-692418	V	3300	3349	3200	3500	0.0	0.0	0.0	0.0	1.10	1.18	1.05	1.40	−0.5	−0.5	−0.5	−0.5
	N	2700	–	–	–	2.0	–	–	–	1.05	–	–	–	0.0	–	–	–
SHV 0527072-701238	V	3500	3658	3500	3800	2.0	0.8	0.0	2.0	1.05	1.50	1.05	2.00	0.0	−0.3	−0.5	0.0
	N	3500	3380	2700	4000	2.0	1.3	0.0	2.0	1.05	1.37	1.05	2.00	0.0	−0.2	−0.5	0.0
SHV 0520505-705019	V	3700	3699	3600	3800	0.0	0.0	0.0	0.0	2.00	2.00	2.00	2.00	−0.5	−0.5	−0.5	−0.5
	N	3300	3326	3000	3700	2.0	1.5	0.0	2.0	1.05	1.26	1.05	2.00	0.0	−0.1	−0.5	0.0
SHV 0518222-750327	V	3600	3599	3500	3700	0.0	0.0	0.0	0.0	2.00	1.70	1.40	2.00	−0.5	−0.5	−0.5	−0.5
	N	3400	3422	3000	3800	2.0	1.2	0.0	2.0	1.05	1.33	1.05	2.00	0.0	−0.2	−0.5	0.0
SHV 0536139-701604	V	3500	3614	3400	3900	2.0	0.4	0.0	2.0	1.05	1.41	1.05	2.00	0.0	−0.4	−0.5	0.0
	N	3200	3246	3000	3600	2.0	0.9	0.0	2.0	1.10	1.41	1.05	2.00	0.0	−0.3	−0.5	0.0
SHV 0525478-690944	V	3800	3808	3500	4000	2.0	1.5	0.0	2.0	1.05	1.15	1.01	2.00	0.0	−0.1	−0.5	0.0
	N	4000	3802	3600	4000	0.0	0.8	0.0	2.0	2.00	1.63	1.05	2.00	−0.5	−0.3	−0.5	0.0
SHV 0528537-695119	V	4000	3883	3700	4000	0.0	0.7	0.0	2.0	2.00	1.49	1.05	2.00	−0.5	−0.3	−0.5	0.0
	N	3900	3700	3400	4000	0.0	0.9	0.0	2.0	2.00	1.51	1.05	2.00	−0.5	−0.3	−0.5	0.0

Table 3.6: Range of parameters for the best fits for the stars from Group D

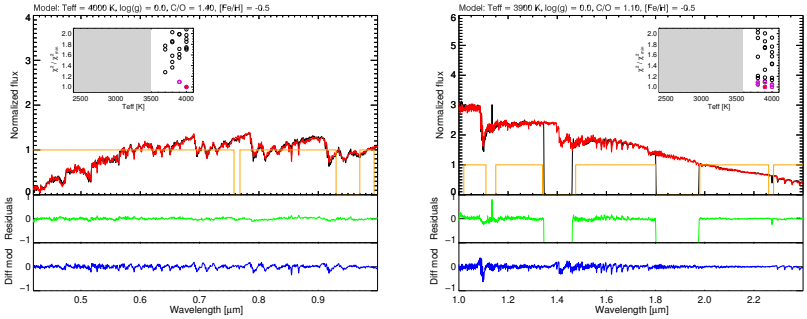

(a) VIS **(b)** NIR

Figure 3.10: Best fit for Cl* NGC 121 T V8 (Group A).

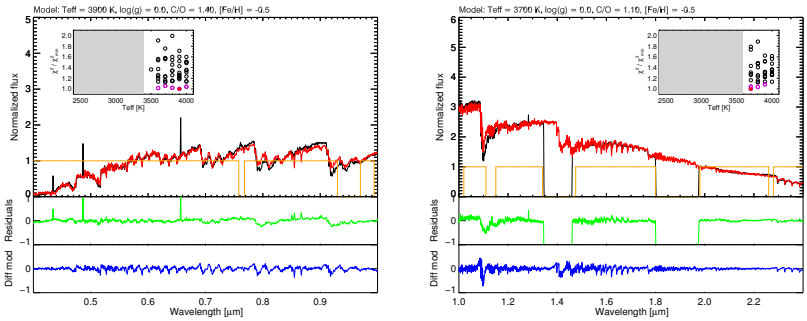

(a) VIS **(b)** NIR

Figure 3.11: Best fit for SHV 0518161-683543 (Group A).

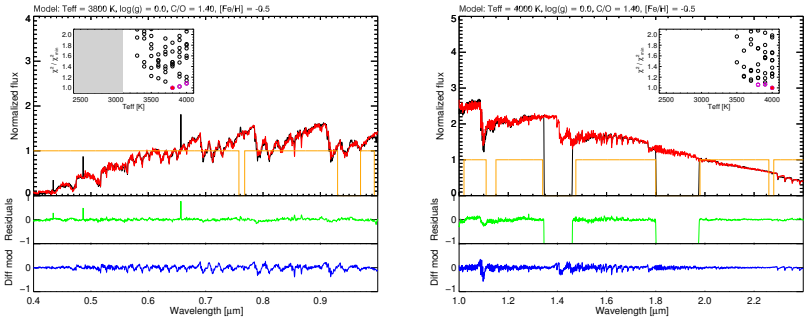

(a) VIS **(b)** NIR

Figure 3.12: Best fit for SHV 0517337-725738 (Group A).

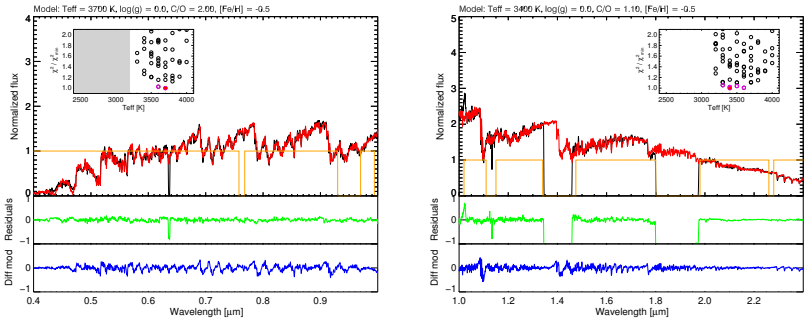

(a) VIS **(b)** NIR

Figure 3.13: Best fit for 2MASS J00571648-7310527 (Group B).

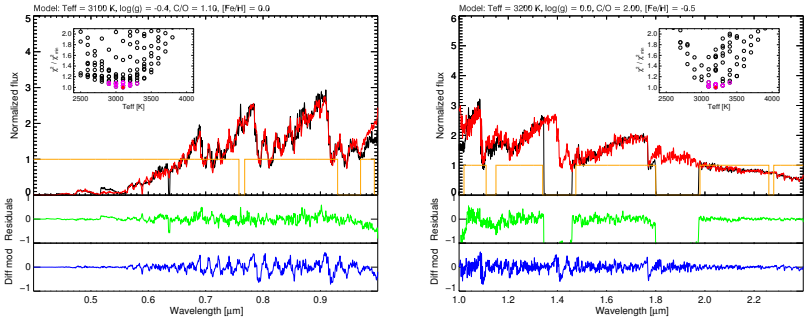

(a) VIS **(b)** NIR

Figure 3.14: Best fit for 2MASS J00563906-7304529 (Group B).

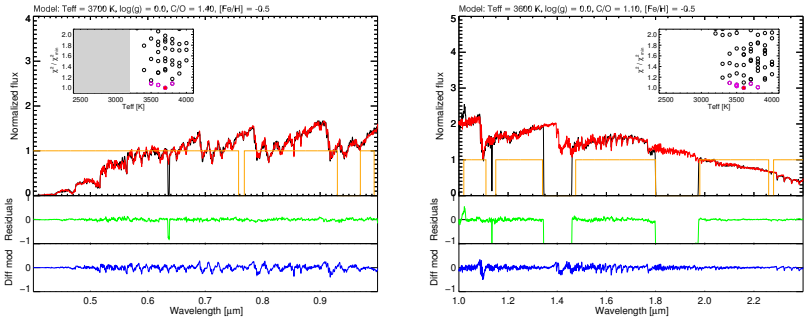

(a) VIS **(b)** NIR

Figure 3.15: Best fit for 2MASS J01003150-7307237 (Group B).

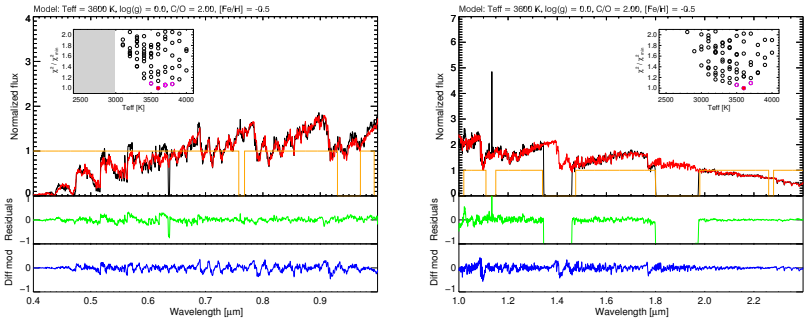

(a) VIS **(b)** NIR

Figure 3.16: Best fit for 2MASS J00530765-7307477 (Group B).

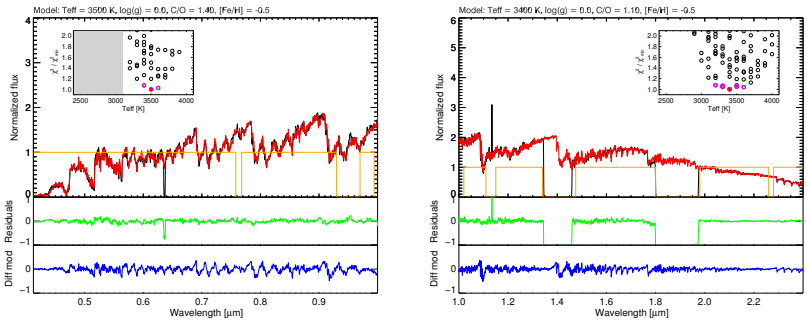

(a) VIS **(b)** NIR

Figure 3.17: Best fit for 2MASS J00493262-7317523 (Group B).

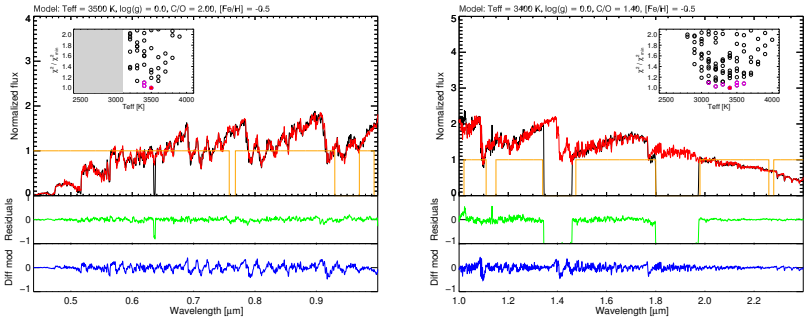

(a) VIS **(b)** NIR

Figure 3.18: Best fit for 2MASS J00490032-7322238 (Group B).

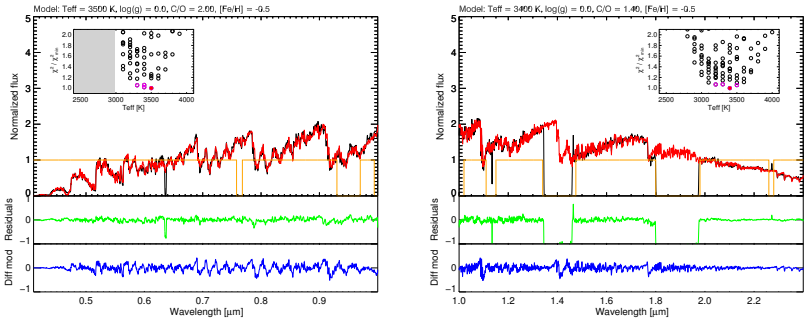

(a) VIS **(b)** NIR

Figure 3.19: Best fit for 2MASS J00571214-7307045 (Group B).

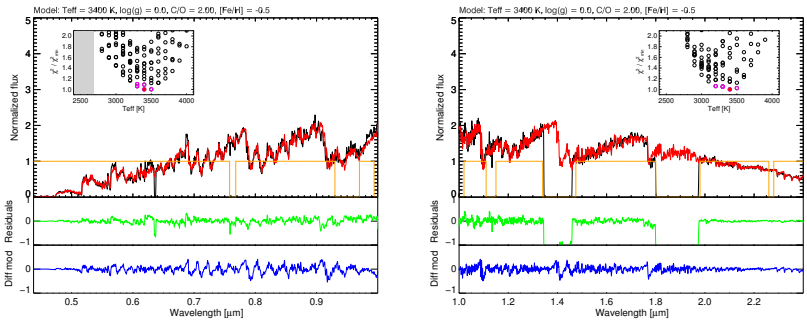

(a) VIS **(b)** NIR

Figure 3.20: Best fit for 2MASS J00570070-7307505 (Group B).

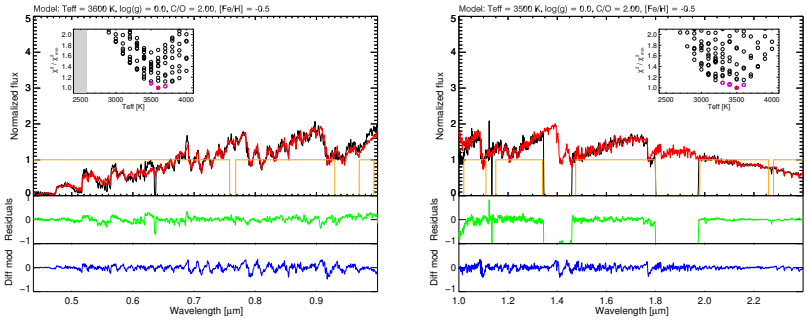

(a) VIS **(b)** NIR

Figure 3.21: Best fit for 2MASS J00564478-7314347 (Group C).

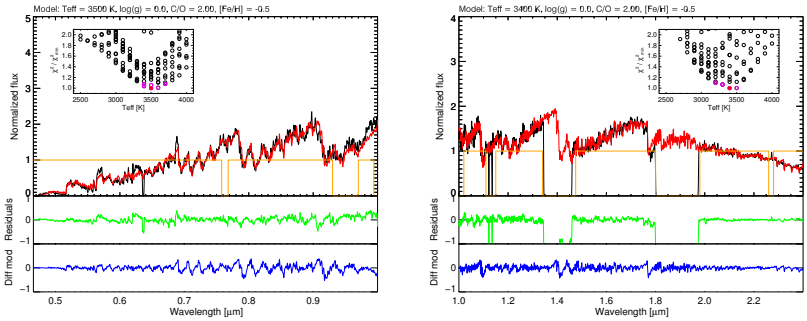

(a) VIS **(b)** NIR

Figure 3.22: Best fit for 2MASS J00542265-7301057 (Group C).

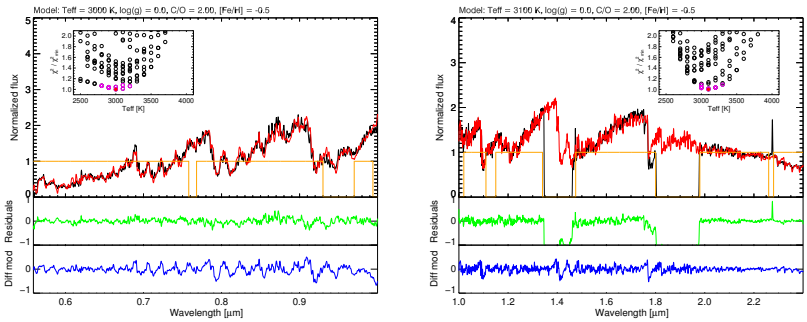

(a) VIS **(b)** NIR

Figure 3.23: Best fit for IRAS 09484-6242 (Group C).

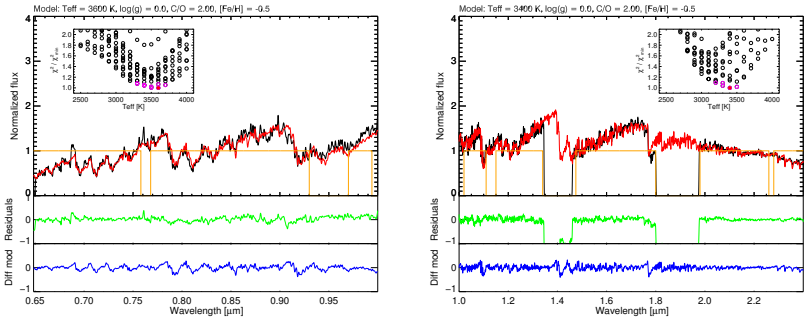

(a) VIS **(b)** NIR

Figure 3.24: Best fit for Cl* NGC 419 LE 27 (Group C).

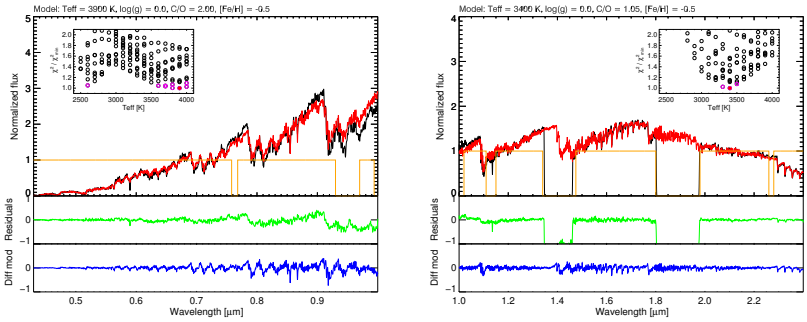

(a) VIS **(b)** NIR

Figure 3.25: Best fit for [W65] c2 (Group C).

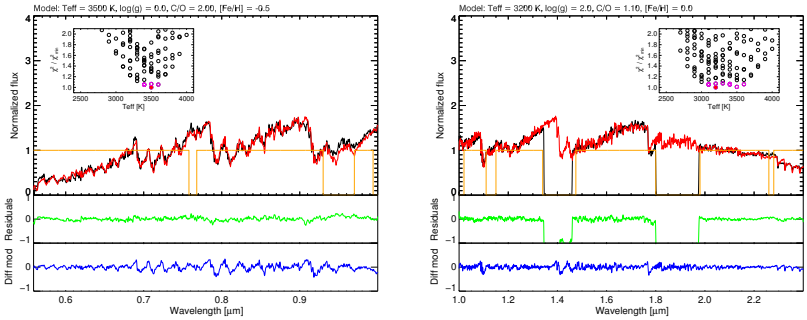

(a) VIS **(b)** NIR

Figure 3.26: Best fit for SHV 0520427-693637 (Group C).

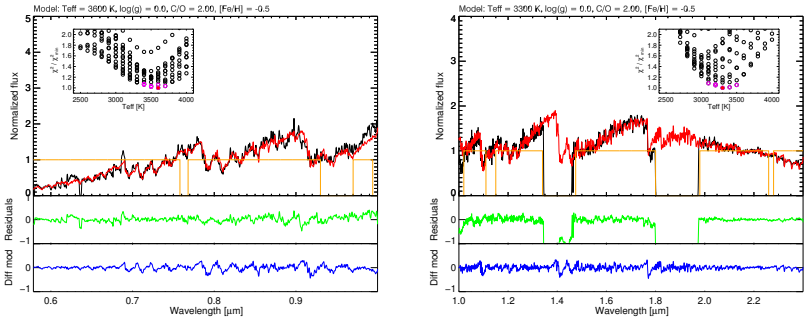

(a) VIS **(b)** NIR

Figure 3.27: Best fit for 2MASS J00553091-7310186 (Group C).

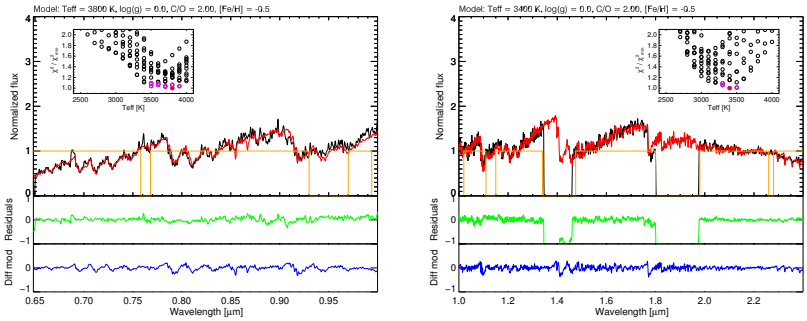

(a) VIS **(b)** NIR

Figure 3.28: Best fit for Cl* NGC 419 LE 35 (Group C).

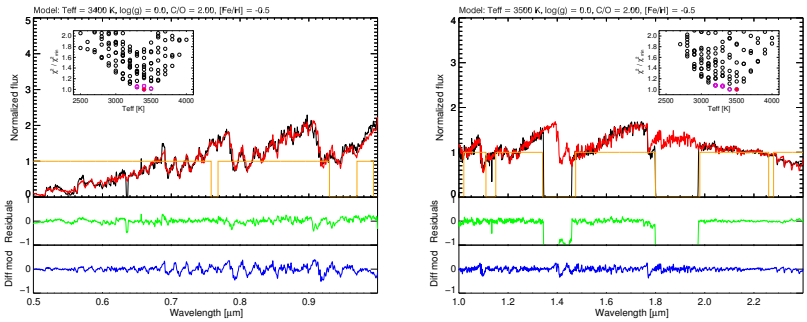

(a) VIS **(b)** NIR

Figure 3.29: Best fit for SHV 0504353-712622 (Group C).

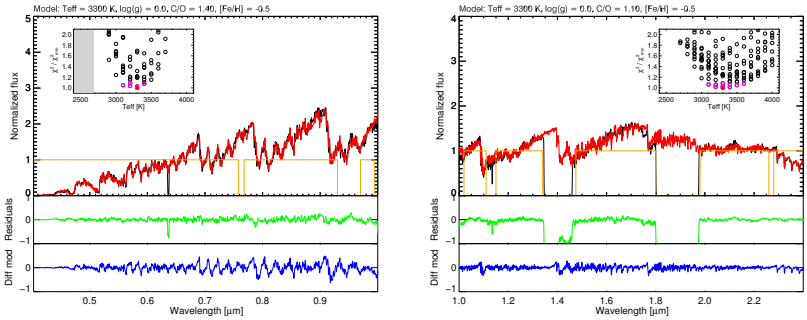

(a) VIS **(b)** NIR

Figure 3.30: Best fit for T Cae (Group C).

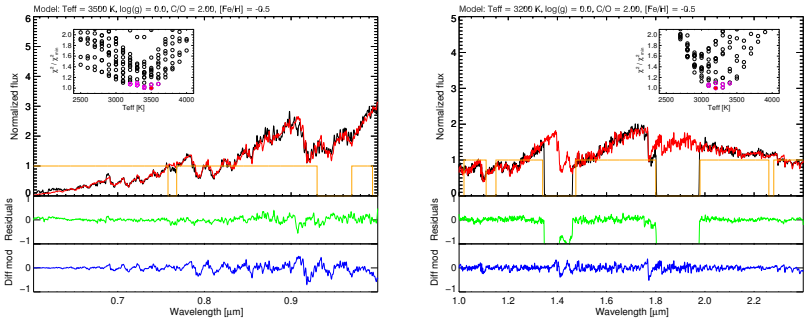

(a) VIS **(b)** NIR

Figure 3.31: Best fit for [ABC89] Cir 18 (Group C).

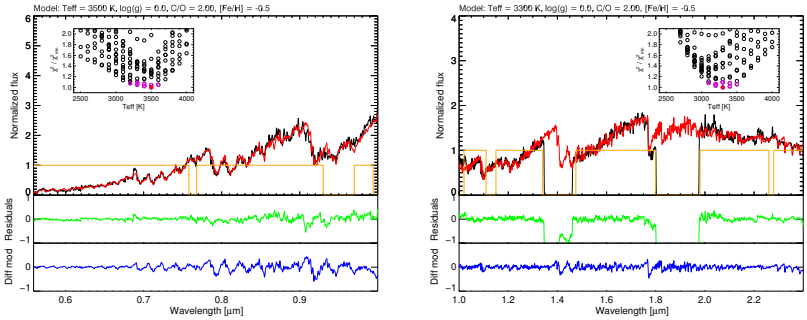

(a) VIS **(b)** NIR

Figure 3.32: Best fit for [ABC89] Pup 42 (Group C).

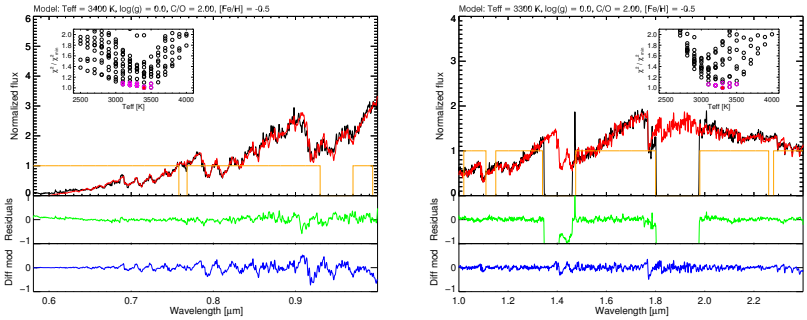

(a) VIS **(b)** NIR

Figure 3.33: Best fit for [ABC89] Cir 18 (Group C).

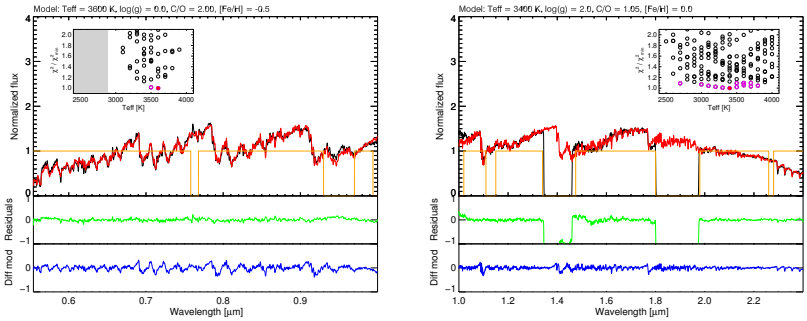

(a) VIS **(b)** NIR

Figure 3.34: Best fit for SHV 0500412-684054 (Group D).

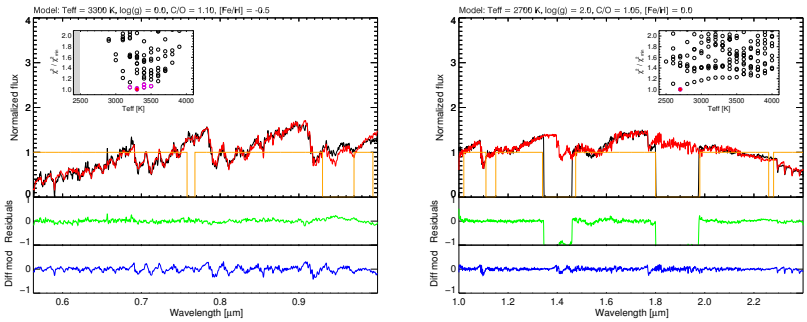

(a) VIS **(b)** NIR

Figure 3.35: Best fit for SHV 0502469-692418 (Group D).

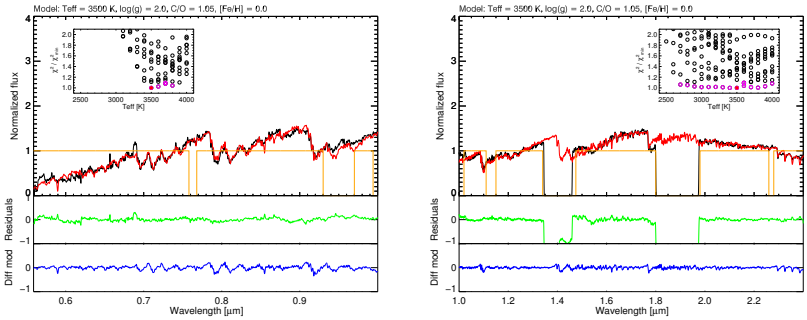

(a) VIS **(b)** NIR

Figure 3.36: Best fit for SHV 0527072-701238 (Group D).

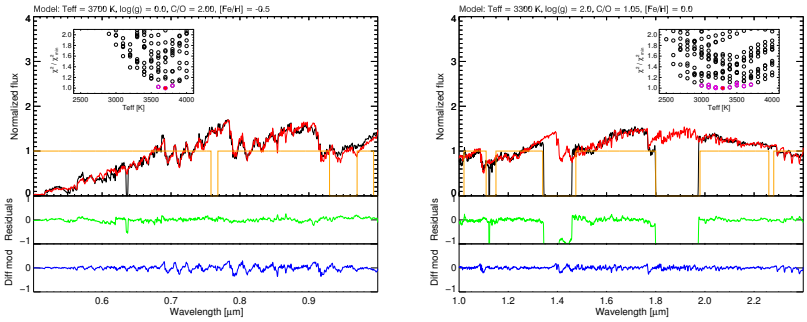

(a) VIS **(b)** NIR

Figure 3.37: Best fit for SHV 0520505-705019 (Group D).

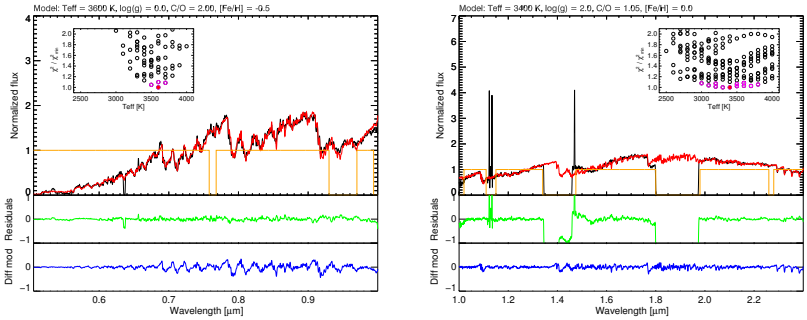

(a) VIS **(b)** NIR

Figure 3.38: Best fit for SHV 0518222-750327 (Group D).

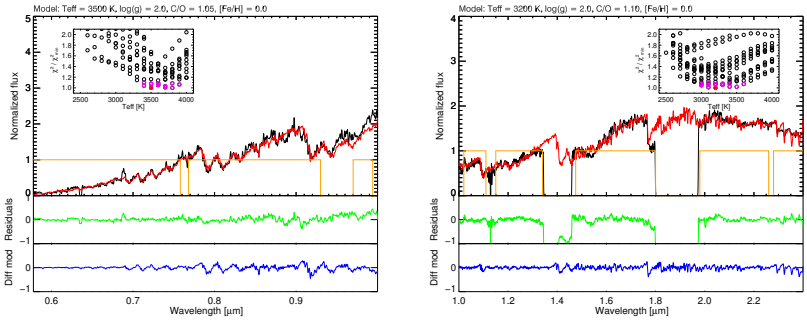

(a) VIS **(b)** NIR

Figure 3.39: Best fit for SHV 0536139-701604 (Group D).

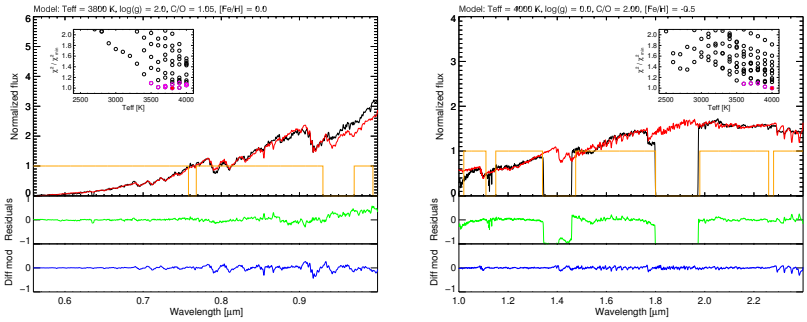

(a) VIS **(b)** NIR

Figure 3.40: Best fit for SHV 0525478-690944 (Group D).

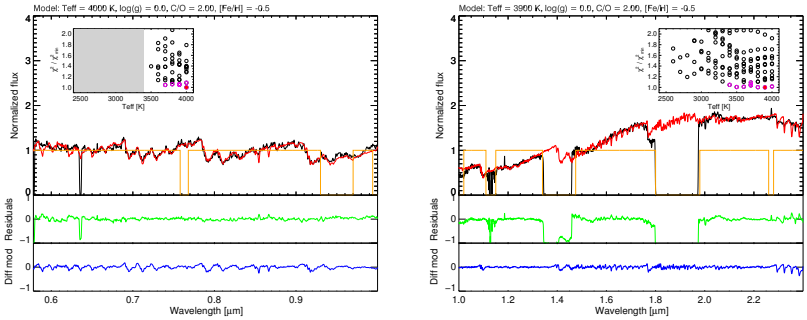

(a) VIS **(b)** NIR

Figure 3.41: Best fit for SHV 0528537-695119 (Group D).

Appendix 3.B Color-color plots

Figure 3.42 shows the color-color plot for our observations and the grid of models.

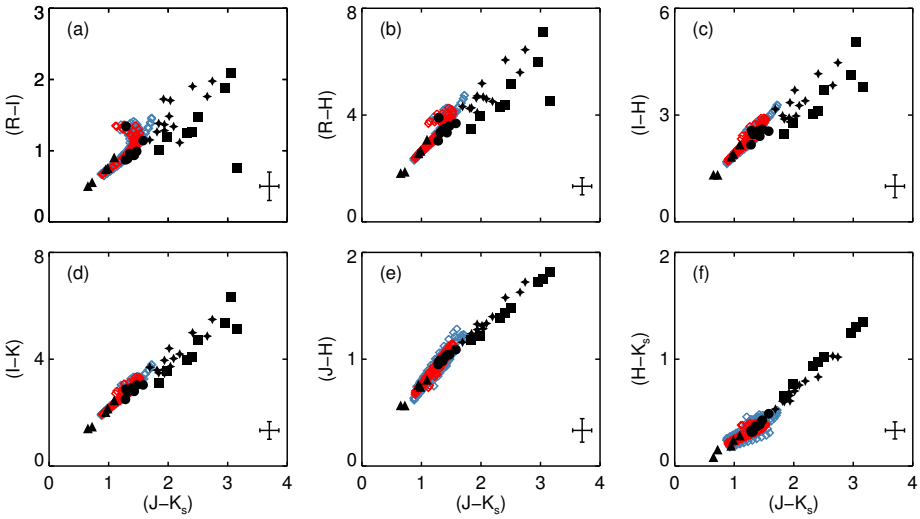

Figure 3.42: Some color-color plots derived from our sample of carbon stars (filled symbols) and the models (open diamonds). The triangles are for stars from Group A, the circles for Group B, the stars for Group C and the squares for Group D. The open diamonds represent the models at solar (in blue) and sub-solar metalliticity (red). The plotted error bars are upper limits, as they are based on the dispersion in the distributions of differences between our photometry and the literature (large amplitude variables excluded).

Chapter 4

Flux calibration of X-shooter spectra: Model reference spectra and telluric correction

⋆ ⋆ ⋆

The X-shooter Spectral Library is a state-of-the-art stellar library wich contains $\sim$ 750 stars. Several hundred observations of spectrophotometric standard stars and telluric standard stars were also acquired over the time of the survey. This represents a huge amount of raw data. Indeed, a given star is observed in three arms (UVB, VIS and NIR) and in two observing modes: NODDING (at least 2 raw frames) and STARE (at least 1 raw frame). Therefore, for a given star, we end up with (at least) 9 raw frames. Thus, multiplying by 10 the number of observed stars gives a rough idea of the number of raw frames: of the order of 10^4. To deal with such a number of raw frames, automatic procedures have been developed (mainly using bash scripts). All the programs written are available to the collaboration on a git server.

The survey was conducted in two phases: a two-semester pilot survey and a Large Programme (LP, four semesters). The UVB and VIS frames of the pilot survey were reduced by Yanping Chen and resulted in XSL Data Release 1 (DR1; Chen et al. 2014a). To reduce around 230 star spectra, she used the X-shooter pipeline (version 1.5.0) for the first steps of the data reduction, up to the creation of rectified, wavelength-calibrated two-dimensional (2D) spectra. The extraction of one-dimensional (1D) spectra was performed outside of the pipeline with a procedure inspired by the prescription of Horne (1986). Observations of both the science targets and spectrophotometric standard stars through a wide slit ($5.00''$) were used to obtain absolute fluxes. Because X-shooter is a ground-based instrument, we must correct our spectra for extinction by the Earth's atmosphere, usually referred to as telluric features. Telluric absorption features particularly affect the NIR arm and the reddest part of the VIS arm of X-shooter. For the VIS, Chen et al. (2014a) built an empirical telluric library using 152 telluric standard stars with spectral types B and A from the two first semesters.

During my thesis, I was first responsible for the data reduction of the NIR frames of the pilot survey. In the end, I also performed the first pass reduction

of all the arms for the Large Programme. The UVB and VIS frames from the LP were reduced entirely with the X-shooter pipeline. But before doing so, a big step implies to build the so-called Set-Of-Frames (sof), which lists all the files (either science files or calibration files) needed for a given recipe. For the NIR frames, no matter the periods, we use the pipeline for the basic reduction steps, up to the creation of rectified, wavelength-calibrated 2D order spectra. Then, we extract the 2D orders, with a procedure of our own inspired by Horne (1986), and merge them into a continuous 1D spectrum. Because of the telluric contamination, we couple the telluric correction and the flux calibration.

Prior to the flux calibration, we derived the response curves from the flux standard frames. In the NIR, it was necessary to develop a new procedure for this step, which combined the determination of the response curve with an adjustment of all the telluric absorption features. The need for such a combined procedure is explained in Sect. 3.4 of Gonneau et al. 2015 (Chapter 2 of this thesis). We developed this original idea and shared it with colleagues from ESO who visited us at Strasbourg Observatory. They provided access to theoretical models for the telluric features. The following paper gives an overview of an implementation similar to ours, that resulted from these discussions.

***

S. Moehler, A. Modigliani, W. Freudling, N. Giammichele, A. Gianninas, A. Gonneau, W. Kausch, A. Lançon, S. Noll, T. Rauch and J. Vinther

Adapted from Moehler et al. 2014 (2014,A&A,568,9)

Abstract

While the near-infrared wavelength regime is becoming more and more important for astrophysics there is a marked lack of spectrophotometric standard star data that would allow the flux calibration of such data. Furthermore, flux calibrating medium- to high-resolution échelle spectroscopy data is challenging even in the optical wavelength range, because the available flux standard data are often too coarsely sampled. We will provide standard star reference data that allow users to derive response curves from 300 nm to 2 500 nm for spectroscopic data of medium to high resolution, including those taken with échelle spectrographs. In addition we describe a method to correct for moderate telluric absorption without the need of observing telluric standard stars. As reference data for the flux standard stars we use theoretical spectra derived from stellar model atmospheres. We verify that they provide an appropriate description of the observed standard star spectra by checking for residuals in line cores and line overlap regions in the ratios of observed (X-shooter) spectra to model spectra. The finally selected model spectra are then corrected for remaining mismatches and photometrically calibrated using independent observations. The correction of telluric absorption is performed with the help of telluric model spectra. We provide new, finely sampled reference spectra without telluric absorption for six southern flux standard stars that allow the users to flux calibrate their data from 300 nm to 2 500 nm, and a method to correct for telluric absorption using atmospheric models.

4.1 Introduction

Accurate flux calibration of astronomical spectra remains a significant challenge. Spectral flux calibration requires flux calibrators with known absolute fluxes that are accessible with the same spectrograph that also takes the spectra of the science targets. With the arrival of new generations of spectrographs that cover wide wavelength ranges and produce relatively high-resolution spectra, known and well-tested spectrophotometric standard star catalogues as listed by Oke (1990) and Hamuy et al. (1992, 1994) are no longer adequate for spectral flux calibration because they do not extend to the near-infrared (NIR) and/or are too coarsely sampled to permit the flux calibration of high-resolution spectra. For example, the European Southern Observatory's (ESO) X-shooter instrument covers, in a single exposure, the spectral range from 300 nm to 2500 nm and operates at intermediate spectral resolution ($R \approx$4000–17 000, depending on wavelength and slit width) with fixed échelle spectral format in three optimized arms (UVB: 300 nm–550 nm, VIS: 550 nm–1000 nm, NIR: 1000 nm–2500 nm; see Vernet et al. 2011 for more details). In this paper we present a new set of calibrated model spectra for flux standard stars covering the wavelength range from 300 nm to 2 500 nm. These spectra are useful for deriving consistent instrumental response curves over this wide range of wavelengths with a spectral resolving power of up to 40 000 and possibly more. We also describe in detail how to use the spectra in this manner.

Our approach to obtain fully calibrated model spectra was as follows. First, we selected a set of flux standard stars observable from the southern hemisphere that cover the full right ascension range, whose spectra can be modelled accurately, and for which X-shooter spectra exist (Sects. 4.2.1, 4.2.2, and 4.2.3). We then used X-shooter observations of these stars to compute the ratio of the observed spectra to the model spectra, i.e. the instrumental response (see Sect. 4.2.4). If the model spectra perfectly described the spectra of all stars, response curves derived from different stars observed with the same instrumental setup should only differ by signatures imposed by the atmosphere (e.g. telluric absorption, varying atmospheric transmission). However, due to small deficiencies in the model spectra, for most of the stars such ratios show star-specific features in regions dominated by overlapping lines (see Fig. 4.3). To be able to identify and fit such deficiencies we observed a star that does not show any lines within the X-shooter spectral range and whose spectrum can be modelled accurately. We used the ratio between model and observations of that star together with the observed spectra of all our stars to derive corrections to their model spectra (Sect. 4.2.5). Finally, we use the available (spectro-)photometric data for the stars to compute the absolute flux scale of the corrected model spectra (see Sect. 4.2.6). The result is a self-consistent new set of fully flux calibrated spectrophotometric standards for the southern hemisphere.

In order to compute response curves for an instrument from observed spectra and the models, the effect of the Earth's atmosphere must be removed from the observed spectra. In Sect. 4.3, we describe a method for such a correction that we used for X-shooter spectra. This includes a fast and efficient removal of the telluric absorption feature, that is sufficiently accurate for the intended purpose of deriving response curves and can be adapted for any other instrument providing spectra of

sufficient resolution between 600 nm and 2 500 nm. Finally, in Sect. 4.4, we describe in detail the full procedure of our approach to compute response curves for the X-shooter instrument, i.e. medium-resolution échelle spectra covering a very wide wavelength range.

4.2 Reference spectra

4.2.1 Sample selection

Spectral flux calibration utilizes as reference either well-calibrated observations or a spectral model of a standard star. The advantage of using a model is that it is noiseless, and does not include features imposed by the terrestrial atmosphere. The process of flux calibration requires computing the ratio of an observed spectrum with the model, and such a ratio is less sensitive to errors in the wavelength scale if the spectrum is smooth and featureless. Therefore, the ideal star to be used as a spectral flux standard has a smooth and featureless spectrum that can be accurately modelled with a minimum number of parameters. Since spectral models in most cases cannot predict the absolute scaling of the spectrum, the model must be accompanied by accurate absolutely calibrated (spectro-)photometric observations at some wavelengths within the wavelength range covered by the spectrum. Unfortunately, only few available standards satisfy all criteria simultaneously. However, it should be noted that the model of a star can be used to derive the *shape* of the response curve of an instrument even if no absolute spectral calibration is available. Such a spectrum can therefore be used to test and improve the model spectra of other stars.

For the current work, we searched for stars with the following criteria. In order to be able to model the spectra, we limited our search to hot white dwarfs and hot subdwarfs. As a first step, we limited our search to stars in the southern hemisphere, and to stars with available flux information from Hamuy et al. (1992, 1994) or the Hubble Space Telescope[1] and X-shooter spectra in the ESO archive. This selection resulted in six standard stars, namely EG 274, GD 71, GD 153, LTT 3218, LTT 7987 (all hot DA white dwarfs), and Feige 110 (a hot subdwarf). We then extended our search to include at least one star in the southern hemisphere that has a spectrum free of absorption lines between 300 nm and 2 500 nm, regardless of whether X-shooter observations existed, and found L97-3 (a white dwarf with a featureless spectrum in the X-shooter wavelength range).

4.2.2 Data

The six standard stars are routinely observed with X-shooter as part of its regular cali-bration plan. We selected X-shooter spectra of these flux standard stars observed in NODDING[2] mode between June 1, 2011 and July 5, 2012 (always referring to the beginning of the night), which resulted in 203 spectra per arm, observed on 185 nights. We used data from nights of any photometric quality as

[1] `http://www.stsci.edu/hst/observatory/crds/calspec.html/`

[2] This observation mode permits a good sky correction because it involves a series of short exposures with the object at different positions along the slit.

we are interested in the shape of the response curves and not in their absolute level.

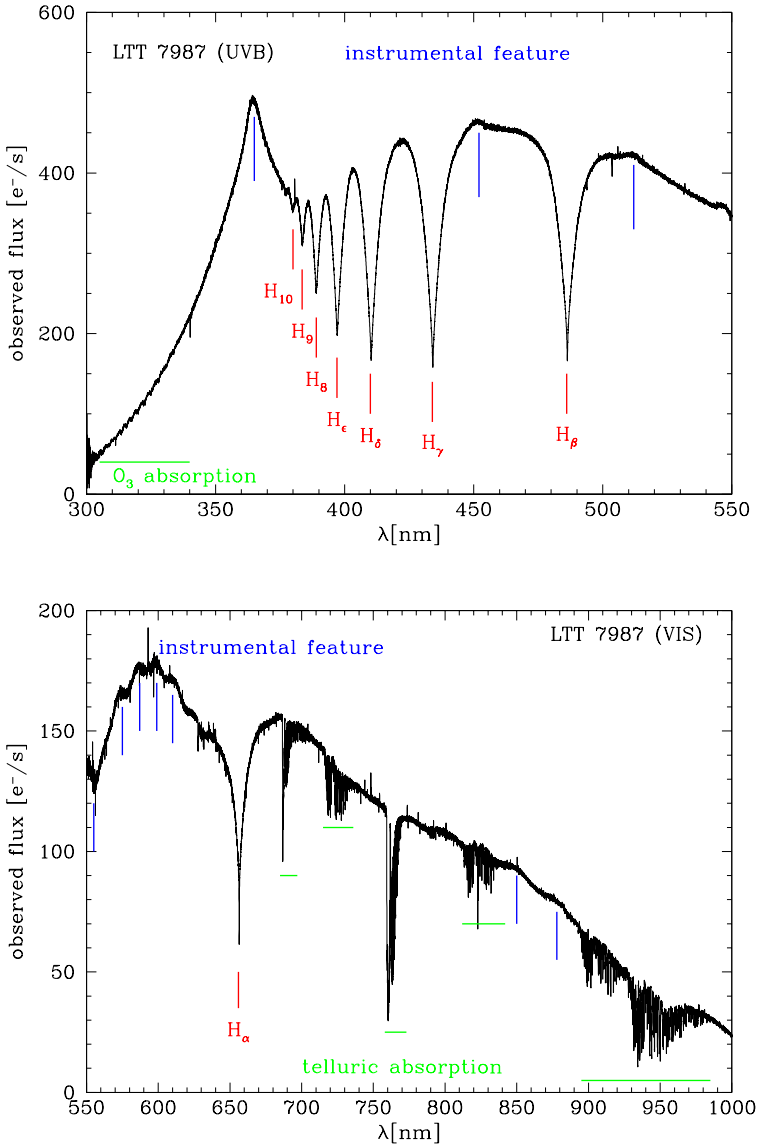

Figure 4.1: Observed X-shooter spectra of LTT 7987, corrected for gain, exposure time, and extinction. The stellar lines (marked in red) are most pronounced in the UVB arm, while the NIR arm and the red part of the VIS arm are strongly affected by telluric absorption (marked in green). All wavelength ranges also show some evidence of instrumental features (marked in blue).

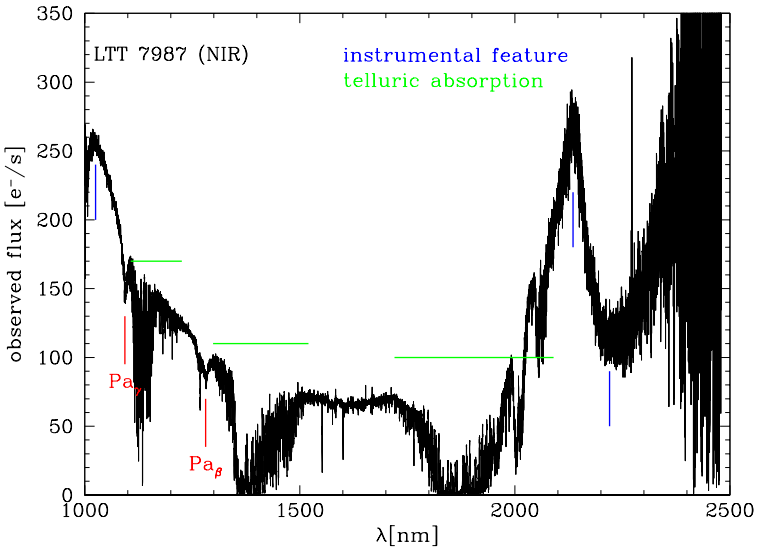

Figure 4.2: As for Figure 4.1.

Figures 4.1 and 4.2 show example X-shooter spectra of the flux standard star LTT 7987, that clearly show the deep and wide stellar lines (marked in red) in the blue (top panel of Figure 4.1), which may extend across more than one échelle order, and the telluric absorption (marked in green) in the redder part of the wavelength range (bottom panel of Figure 4.1 and Figure 4.2).

The DC white dwarf L97-3 was observed on the nights October 1, 2012, October 20, 2012, and December 21, 2012, in the same way as the flux standard stars listed above, i.e. with a slit width of 5″ and in NODDING mode, with total exposure times between 1200 sec and 1360 sec.

4.2.3 Modelling of hot white dwarfs

The spectra of our standard stars include hydrogen lines (in the case of Feige 110 also helium lines) of varying strength (see Fig. 4.1 and 4.2 for an example) that need to be properly modelled if one wants to sample the response of an instrument on scales of some nanometres.

For the past 20 years the physical parameters of hot white dwarfs and other hot, high-gravity stars have been determined by fitting the profiles of the hydrogen (and/or helium) absorption lines in their optical spectra (Bergeron et al. 1992; see Gianninas et al. 2011 and Giammichele et al. 2012 for more recent examples and Koester et al. 2001 for work with high-resolution échelle spectra).

The difficulty of modeling these spectra is illustrated in Fig. 4.3. The top panel shows an example of a parametric fit by Giammichele et al. (2012). The method of fitting the Balmer lines profiles has the advantage that it is sensitive to changes

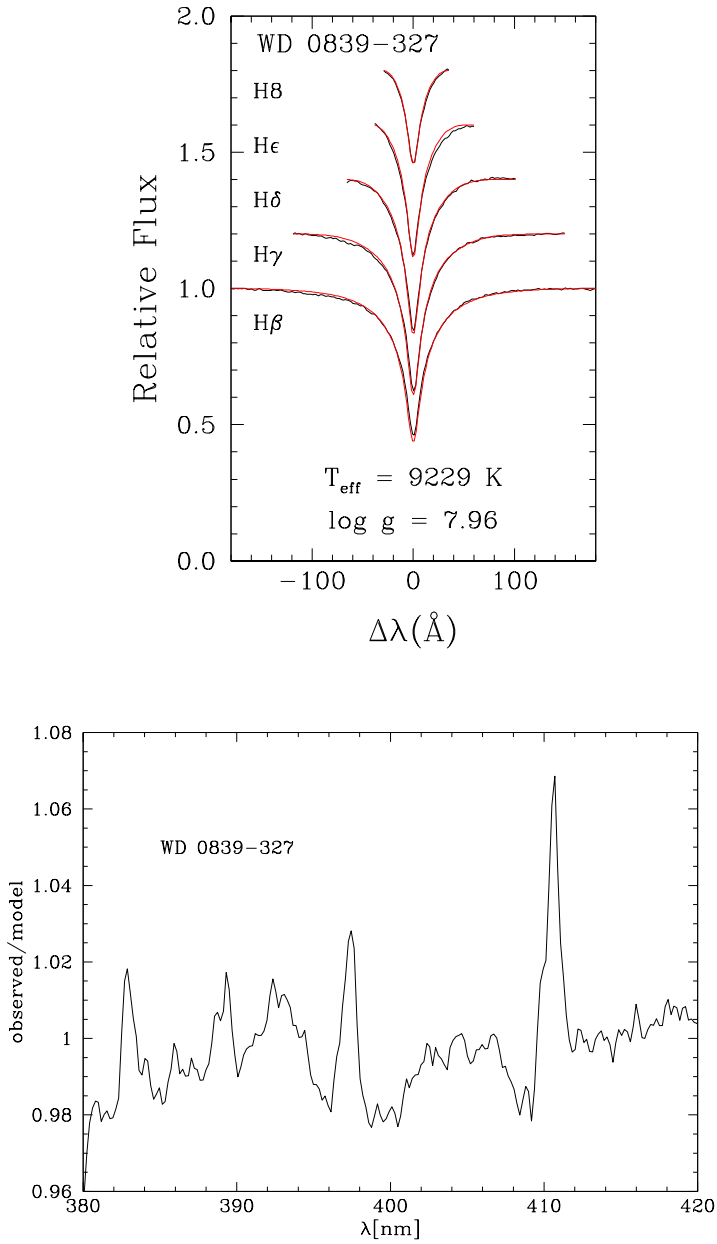

Figure 4.3: Model fit for LTT 3218 (individual lines only) from Giammichele et al. (2012, **top)** and the ratio between their observation and model spectrum (**bottom**). The ratio plot clearly shows residuals in the line cores and also some bumps between the lines.

in temperature and surface gravity at high effective temperature, when optical and near-infrared photometry become insensitive to changes in these parameters. Consequently, this means that model spectra with a wrong effective temperature or surface gravity will not correctly describe the strong hydrogen and/or helium absorption lines in the spectra of these stars. Such a mismatch is most severe at the blue end of the wavelength range studied in this paper, namely between 380 nm and 420 nm, where the lines may overlap with each other, causing a lack of continuum. An example of such a mismatch can be seen in the bottom plot in Fig. 4.3, which shows the ratio of the observed spectrum to the fitted model spectrum for LTT 3218. The bump between 400 nm and 410 nm is caused by an imperfect description of the line overlap region between the Balmer lines Hδ and Hϵ. Compared to the line depths of about 50% the effects are small (at about 2%), but sufficient to introduce artefacts in the resulting response curves. To ensure that no such mismatches exist in the finally selected reference spectra, however, one has to know the true response of the instrument with which the spectra, that are used for the analysis, are observed.

By contrast, the featureless spectra of L97−3 can easily be modelled at the same wavelengths, which was our primary motivation for including it in our sample. This is illustrated in Fig. 4.4, which shows the ratio of model spectrum to observed spectrum from the observed spectra of L97-3 for the regions containing strong lines in the spectra of the flux standard stars discussed here. We used as reference data a stellar model spectrum calculated by Koester (2010) for the parameters reported by Giammichele et al. (2012) for this star. This model spectrum was adjusted to the photometry of the star reported in Simbad[3] using the pseudo-magnitudes described in Sect. 4.2.6. The curves in Fig. 4.4 are rather smooth without significant structure on nanometre scales (as opposed to Fig. 4.3). This suggests that the spectrum has been sucessfully modelled, and the structure in the ratio of observed and modelled spectra reflects the true response curve of the instruments.

4.2.4 Selection of model spectra

We used the X-shooter observations described in Sect. 4.2.2 to verify the quality of the various model spectra available for our standard stars by comparing instrumental res-ponse curves from different standard stars. We concentrated first on the wavelength range 380 nm to 420 nm for the reasons discussed above. Once an acceptable description of the blue range has been achieved we will verify its suitability for the redder wavelength ranges as well.

For our analysis we used one-dimensional extracted and merged X-shooter spectra of the flux standard stars processed with the reflex workflow[4] (Freudling et al. 2013) of X-shooter. These spectra were then corrected for atmospheric extinction using the Paranal extinction curve from Patat et al. (2011, see also Sect. 4.3.1) and normalized by exposure time.

[3] original data from Hauck & Mermilliod (1998, *uvby*); Subasavage et al. (2007, *RI*); Skrutskie et al. (2006, 2MASS point source catalogue, *JHK*).

[4] `http://www.eso.org/sci/software/pipelines/`

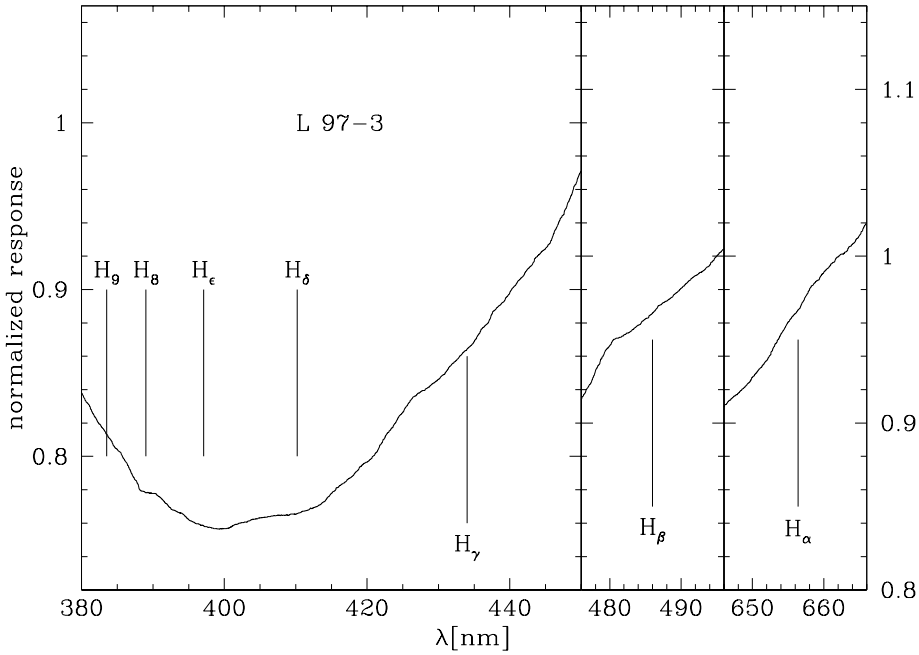

Figure 4.4: Average ratios of observed standard spectrum and shifted reference spectrum for UVB and VIS data of L97-3. The two narrow windows on the right share the same range along the y-axis.

We shifted the model spectrum for a given star to the same radial velocity as the observed spectrum to avoid the introduction of pseudo-P Cygni profiles when the observed spectrum is divided by the model spectrum. We resample the noise-free model spectra instead of the observed spectra because this can be done without loss of information. The radial velocity was obtained from the positions of the line cores of Hδ (UVB), Hα (VIS), and Paγ (NIR). Each observed standard star spectrum was divided by the shifted reference star spectrum. Finally the ratios were averaged per star to achieve a better signal-to-noise ratio. This provided us with raw, i.e. unsmoothed, response curves that allowed us to look for systematic discrepancies between the observed and the model spectra. A response curve is instrument specific and therefore expected to be stable for a long time. Any feature in these ratios that appears only for a particular standard star points strongly towards deficiencies in the reference spectra of these standard stars. Instrumental effects should not depend on which standard star is used. We selected as best description of the UVB spectrum those model spectra that showed the smallest star-specific bumps in the averaged ratio spectra. Section 4.2.5 describes how we adjusted the selected model spectra empirically to remove the remaining small discrepancies.

White dwarfs

For the purpose of this work, we considered the models of EG 274, LTT 3218, and LTT 7987 presented by Giammichele et al. (2012) and the models of GD 71 and GD 153 by Gianninas et al. (2011), hereafter referred to as Montréal spectra, and the model spectra calculated by Koester (2010, in the following referred to as Kiel spectra) for the parameters from Giammichele et al. (2012) and Gianninas et al. (2011).

These model spectra provided good fits to all white dwarfs, but bumps like the one seen in Fig. 4.3 can be seen in the ratios of observed to stellar model spectra, pointing to remaining mismatches. Residuals of this kind (of the order of 2%-3%) are not unexpected for stars with such strong (flux in line core about 40% of continuum level) and overlapping lines (line widths up to 20 nm as can be seen in Fig. 4.3, top plot).

For EG 274, GD 71, and LTT 3218 the Montréal model spectra showed the smallest star-specific bumps in the averaged ratio spectra, while the Kiel model spectra for the Montréal parameters provided the best description for GD 153 and LTT 7987. The parameters are listed in Table 4.1.

Table 4.1: Parameters for the flux standard star reference spectra

Star	Selected Reference Spectrum			
	$T_{\rm eff}$ [K]	$\log g$ [cm s^{-2}]	Reference	Model
EG 274	25985	7.96	2	2
Feige 110	45250	5.8	3	4
LTT 3218	9081	7.71	2	2
LTT 7987	16147	7.98	2	1
GD 71	33590	7.93	5	5
GD 153	40320	7.93	5	1
L97−3	10917	8.15	2	1

(1) Koester (2010); (2) Giammichele et al. (2012); (3) this paper; (4) TMAP; (5) Gianninas et al. (2011).

Feige 110

For Feige 110, we fit FORS2[5] and X-shooter UVB spectra (flux-calibrated with a response curve obtained from GD 71 observations) with TMAP (Tübingen NLTE Model-Atmosphere Package) model spectra (Rauch & Deetjen 2003; Werner et al. 2003) to obtain an appropriate reference spectrum.

[5] ESO's FOcal Reducer/low dispersion Spectrograph 2, which covers the wavelength range 320 nm – 1 100 nm at various resolutions.

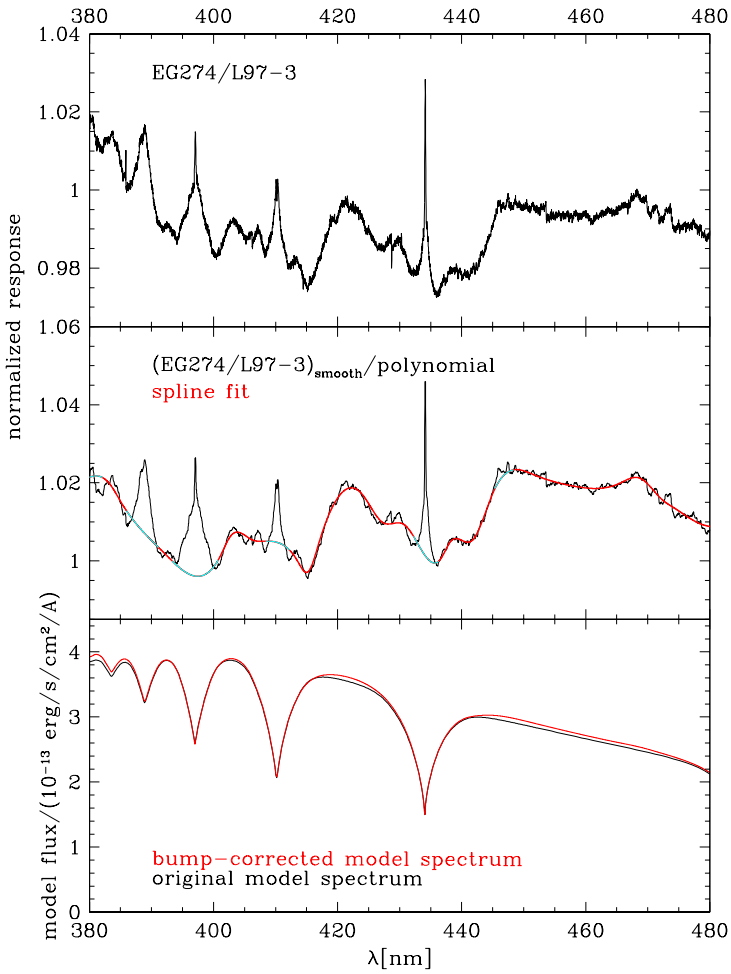

Figure 4.5: Top: Average raw response ((extinction-corrected observation)/(radial-velocity shifted model)), divided by the smoothed response for L97-3, for EG 274. The narrow spikes are due to mismatches in the line cores, while the broad bumps at 405 nm and 420 nm are due to imperfect line broadening, which underestimates the flux between the lines in the model spectra. **Middle:** Raw response from the top plot, with large scale variations removed by a low-order polynomial fit and smoothed (black). The black curve was fit with a spline (red) after masking the regions of the line cores (masked regions in cyan). **Bottom:** Model spectrum before correction (black) and corrected with the fit (red).

4.2.5 Correction of model spectra at short wavelengths

In order to correct the mismatches between model and observed spectra that cause the bumps we reprocessed all flux standard stars observed in NODDING in 2012 with the new model spectra as reference spectra. We first divided each (extinction-corrected) one-dimensional spectrum by the radial-velocity shifted reference spectrum and then by the smoothed response curve derived from L97-3.

The products of this procedure are expected to be equal to 1 in an ideal case, but differences in atmospheric conditions result in residual slopes. The parking of the Atmospheric Dispersion Compensators[6] since August 2012 might also play a role here, as the UVB spectra observed at higher airmass are no longer at a constant position along the slit at all wavelengths, but show instead some curvature at shorter wavelengths, which may in turn affect the extraction.

In addition, remaining mismatches between model spectra and observations cause narrow spikes and bumps that we want to correct (see Fig. 4.5, top). For every star we fitted the shape of this ratio spectrum by a low-order polynomial fit to remove the large-scale variations. Then we smoothed the result and fit the remaining bumpy regions (see Fig. 4.5, middle, for an example). Applying the fit to the model spectrum we obtained the red curve shown in Fig. 4.5 (bottom).

The bump corrections were smallest for GD 71, GD 153, and Feige 110, while EG 274, LTT 7987, and LTT 3218 had significant corrections (increasing in this order). This is expected as the last three stars have the strongest and widest lines and thus present the biggest challenge when it comes to the correct treatment of overlapping lines. Since the mismatches in the line cores were not corrected (as they vary with spectral resolution) some masking is still required when fitting a response (see Sect. 4.4). We also verified that in the spectral range 550 nm to 2 500 nm the only residuals seen are those in the line cores of hydrogen and/or helium lines.

4.2.6 Absolute flux calibration

We have now defined a set of model spectra which adequately reproduce the observed X-shooter spectra of the six flux standard stars, with residuals (outside line cores, that are affected by resolution effects) well below 2%. To allow a proper flux calibration we have to verify that the overall flux distribution of these model spectra reproduces the independently observed (spectro-)photometric data. To do so we convolved the model spectra to a resolution of 1.6 nm for the UVB/VIS spectral range and then binned them to 5 nm steps to reproduce the Hamuy et al. (1992, 1994) data. These reference data are based on absolutely flux calibrated low-resolution spectra, that are tied to the Vega calibration of Hayes (1985) via a recalibration of the secondary standard stars from Taylor (1984). For the NIR range we convolved the data to a resolving power of 2000 (J band) and 1500 ($H + K$ band) and integrated them over the wavelength ranges given in Vernet et al. (2008) for EG 274, Feige 110, LTT 3218, and LTT 7987.

[6] The ADCs in the UVB and VIS arm minimise slit losses, keep the target at the same position, and allow observations at any position angle of the slit on the sky up to zenith distance of 60°.

These flux values were then converted to pseudo-magnitudes

$$mag = -2.5 \cdot \log(flux) \tag{4.1}$$

and aligned to the respective Hamuy and SINFONI (Spectrograph for Integral Field Observations in the Near Infra-red at the ESO VLT; Eisenhauer et al. 2003) data by a constant factor across the full wavelength range.

Figure 4.6 shows the results for EG 274.

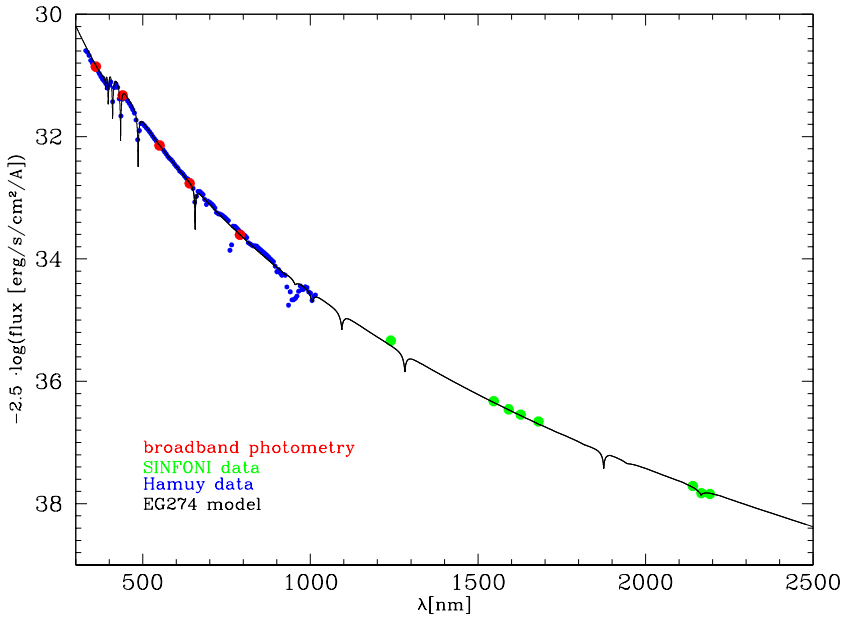

Figure 4.6: Model spectrum for EG 274 (black), aligned to the data from Hamuy et al. (1992, 1994, blue), Vernet et al. (2008, green), and broadband photometry from the SIMBAD database (red).

For GD 71 and GD 153 our new model spectra could also be aligned by a constant factor to the HST model spectra, which are tied to the Vega scale by HST STIS and NICMOS observations (Bohlin et al. 2001). In Fig. 4.7 we compare our aligned model spectrum for Feige 110 to the data from Hamuy and from HST.

Figure 4.8 shows the average ratio of observed and reference spectra for the new model spectra.

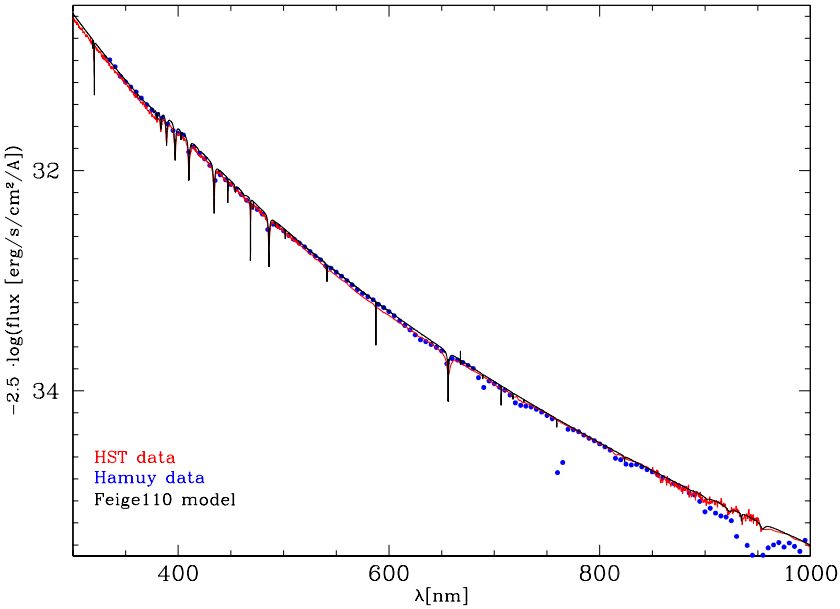

Figure 4.7: Aligned model spectrum for Feige 110 (black) compared to the data from Hamuy et al. (1992, 1994, blue) and from HST (red).

4.3 Correction of atmospheric effects

We have now defined reference spectra that describe the flux standard stars very well. In order to derive a response curve the effects of the Earth's atmosphere have to be removed from the observed spectra. Otherwise the response curve will contain a mixture of instrumental effects and atmospheric effects. The atmospheric effects consist of two major parts: atmospheric extinction (small variation with time in the case of Paranal due to the low aerosol content, which governs the extinction variability) and telluric absorption lines (strong variation with time in the case of water vapour).

The first affects principally the wavelength range 300 nm to 1 000 nm, while the second is important for data above 680 nm (X-shooter NIR arm and the redder part of the VIS arm; see Fig. 4.1, bottom plot, and Fig. 4.2).

4.3.1 Correcting the atmospheric extinction down to 300 nm

Patat et al. (2011) provide an extinction curve for Paranal that is based on FORS2 observations and therefore covers only wavelengths longer than 320 nm. X-shooter data, however, extend down to 300 nm. In order to cover a larger wavelength range

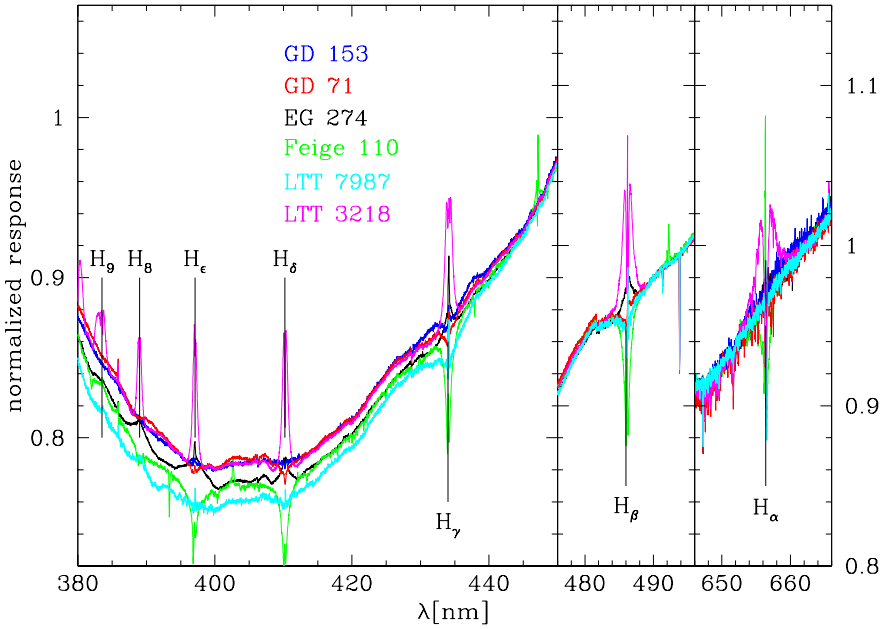

Figure 4.8: Average ratios of observed standard star spectrum (corrected for atmospheric extinction) and shifted reference spectrum for UVB and VIS data for the regions containing Balmer lines, using the bump-corrected model spectra. The curves have been normalized at the red end of the respective plot windows, which show the Balmer lines Hα (right), Hβ (middle), and Hγ to H9 (left). The two narrow windows on the right share the same range along the y-axis.

we obtained from F. Patat a Line-By-Line Radiative Transfer Model (LBLRTM, Clough et al. 2005) spectrum for Paranal, that describes the continuous and line absorption caused by the Earth's atmosphere. As the spectrum was calculated without aerosol contributions, we added the aereosol contribution defined as $k_{\rm aer} = 0.014 \cdot (\lambda[\mu m])^{-1.38}$ (see Patat et al. (2011) for more details). The LBLRTM model spectrum was calculated for the wavelength range 300 nm–1099.4 nm and also contains absorption by telluric lines, which vary rapidly with time and can therefore not be corrected by a static extinction curve (see Sect. 4.3.2 for the correction of telluric lines). To exclude the telluric lines from the extinction curve we interpolated across the regions of strong telluric absorption in the VIS range (585.5 nm–599.2 nm, 626.1 nm–634.9 nm, 643.8 nm–660.0 nm, 682.1 nm–709.4 nm, 712.7 nm–743.4 nm, 756.2 nm–773.1 nm, 780.1 nm–861.3 nm, 879.8 nm–1033.8 nm, above 1050 nm). Figure 4.9 shows the model and our interpolation in comparison to the FORS2 measurements.

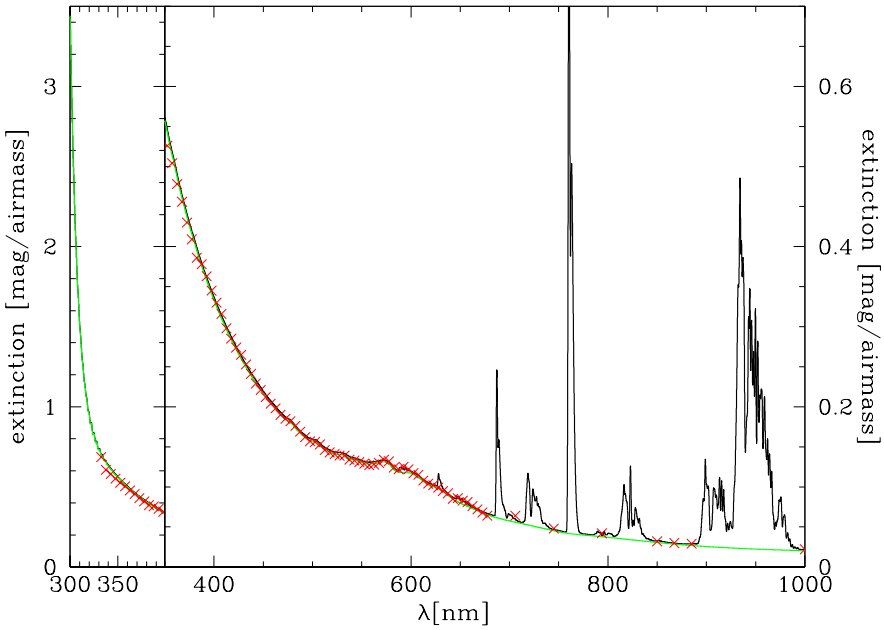

Figure 4.9: LBLRTM model for Paranal (black line) compared to the FORS2 data points from Patat et al. (2011, red crosses) and the interpolated curve (green line).

4.3.2 Telluric absorption

If one does not correct at least those parts of the spectrum that contain low to medium telluric absorption, one has to interpolate the response across very wide wavelength ranges, which results in large systematic uncertainties for the resulting flux calibration. Traditionally such corrections use so-called telluric standard stars, i.e. stars with either no features or extremely well-known features in the regions of telluric absorption, that allow the user to determine the telluric absorption spectrum (see for instance Vacca et al. 2003; Maiolino et al. 1996). This method relies on the assumption that the conditions governing the telluric absorption have not changed between the observation of the science target and the observation of the standard star. Since this assumption is often not fulfilled, we decided instead to use a catalogue of telluric model spectra (Noll et al. 2012; Jones et al. 2013) to correct the telluric absorption lines. Alternatively, a large number of telluric standard star observations can be used to extract the principal components of the telluric transmission (Chen et al. 2014a).

The high-resolution transmission spectra ($R = 60\,000$) were calculated for the wavelength range from 300 nm to 30 μm using the LBLRTM radiative transfer code, the HITRAN molecular line database (see Rothman et al. 2009), and dif-

ferent average atmospheric profiles (pressure, temperature, and molecular abundances) for Cerro Paranal. The atmospheric profiles were derived from the MIPAS equatorial standard profile (J. Remedios 2001; see Seifahrt et al. 2010), profiles for pressure, temperature, and relative humidity from the Global Data Assimilation System (GDAS), Cerro Paranal meteorolo-gical station. The spectra we used cover the airmass values 1.0, 1.5, and 2.0 at six different bimonthly periods (plus an annual mean) and three night-time periods (plus a nocturnal mean). We will refer to this telluric library as the time-dependent library.

To identify the best telluric model spectrum to correct a given observation, the telluric model spectra first have to be aligned to the observed spectrum in both resolution and wavelength. Then the telluric model spectrum that leaves the smallest residuals after applying it to the observation has to be identified. We used the following step-by-step procedure:

1. Convert the wavelength scale (in nm) of the model and observed spectra to natural logarithm.
2. Extract appropriate ranges for cross correlation (NIR: $7.0 \leq \ln \lambda_{\rm nm} \leq 7.1$, H_2O feature; VIS: $6.828 \leq \ln \lambda_{\rm nm} \leq 6.894$, H_2O feature).
3. Cross correlate the extracted telluric model and observed spectra with a maximum shift of 500 sampling units (each of size 10^{-5}) in natural logarithmic space.
4. Fit a Gaussian profile within ± 0.001 in $\ln(\lambda)$ around the cross correlation peak.
5. Shift the logarithmic model wavelength scale by the fitted peak position of the cross-correlation curve.
6. Create a Gaussian with the measured FWHM.
7. Convolve the model spectrum with the Gaussian in $\ln(\lambda)$ space (X-shooter has a constant resolving power R of UVB/VIS/NIR arm, respectively)[7].
8. Convert the shifted and convolved model spectrum to linear wavelength space.
9. Divide the observed spectrum by the convolved and shifted telluric model spectrum (whereby we avoid resampling the observed spectrum).
10. Use predefined continuum points (avoiding regions of strong telluric absorption as well as known lines of the observed star, see Sect. 4.2.3) and fit a cubic spline to the telluric corrected spectrum.
11. Divide the telluric corrected spectrum by the fit of the continuum.
12. Determine mean and rms for regions of moderate telluric absorption in the normalized corrected spectrum.

[7] Since the resolution of the observed spectra is much lower than the resolution of the telluric model spectra, we assume here the resolution of the model spectra to be infinite.

Then, we choose as best fitting model the one for which the average of the residuals computed over regions of moderate telluric absorption is minimal. The telluric corrected spectrum of the flux standard star is then compared to the stellar model spectrum (see Sect. 4.2.3 for details) to determine the response.

Figure 4.10 shows examples for a good telluric correction (bottom) and for undercorrection (top).

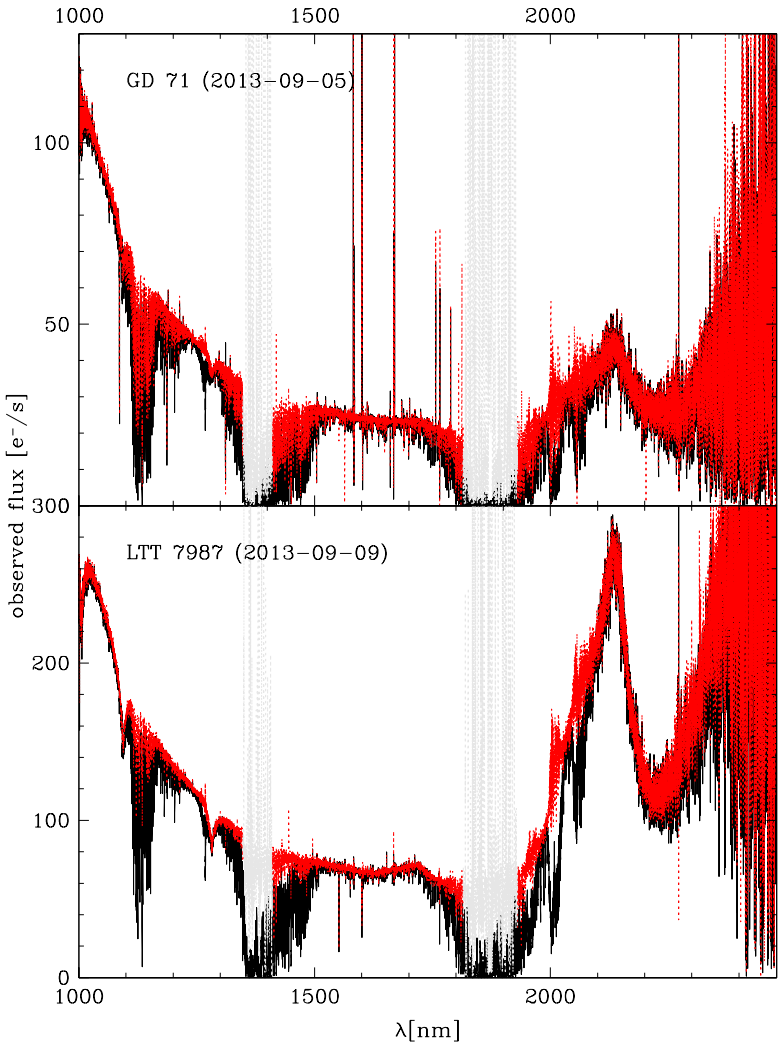

Figure 4.10: Results of the telluric correction (red) for a bad (top) and a good (bottom) case. The grey areas mark regions of extremely high telluric absorption and thus high noise in the corrected data. The lines at 1093.5 nm and 1281.4 nm are stellar lines and the variable peak at about 2100 nm is caused by variations in the flux level and spectral energy distribution of the NIR flat field lamp.

The absorption in the wavelength regions 1985 nm–2030 nm and 2037 nm–2089 nm is caused mainly by CO_2 features, whose abundance is not varied in the telluric model spectra for a given airmass. These regions were therefore ignored when looking for the best fit. We do not restrict the search for the best telluric model spectrum in airmass, as we found that in some cases a telluric model spectrum for an airmass quite different from the observed one can still provide a good fit in the regions that we analyse.

The telluric model spectra discussed so far do not cover high precipitable water vapour (**PWV**) conditions, which result in stronger telluric absorption lines, and therefore spectra taken during such conditions are undercorrected (see Fig. 4.10, top, for an example). This problem is more pronounced in the NIR than in the VIS arm. Therefore we investigated another set of model spectra, which extends to higher PWV conditions (PWV = 0...20 mm) and higher airmass values (PWV-dependent library). Tests with these models showed good corrections for NIR data taken under high PWV conditions (which could not be corrected with the time-dependent grid), but were less successful for data taken during intermediate and low PWV conditions. For the VIS arm the PWV-dependent telluric model catalogue provided good corrections for all of the about 100 flux standard spectra that we tested.

Users who want to employ the telluric model spectra to correct their data can find information about the Cerro Paranal sky model (see Noll et al. 2012) at `http://www.eso.org/sci/software/pipelines/skytools/` together with the following pre-calculated libraries:

1. PWV-dependent library with 45 spectra at airmasses 1.0, 1.5, 2.0, 2.5, 3.0, and PWV (in mm) of 0.5, 1.0, 1.5, 2.5, 3.5, 5.0, 7.5, 10.0, and 20.0.

2. Latest version of time-dependent library with 35 spectra at airmasses 1.0, 1.5, 2.0, 2.5, 3.0, and bi-monthly average PWV values (1=December/January ...6=October/November) as well as a yearly average PWV content (labelled 0). Compared to the time-dependent library used in this paper the airmass coverage has been increased, the night-time periods have been dropped, and the CO_2 content has been updated.

The spectra are provided with resolutions of 60 000 and 300 000 and do not include Rayleigh scattering. The SkyCalc web application can always be used to produce sky radiance and transmission spectra with more specific parameters, including Rayleigh scattering.

The quality of the telluric correction has to be kept in mind when fitting a response to the ratio of such a corrected spectrum to the corresponding stellar model spectrum, as regions with remaining absorption or overcorrected features may distort the fit. For this reason we finally decided to mask the following regions when fitting a response curve to avoid potential telluric residuals: 634 nm–642 nm, 684 nm–696 nm, 714.7 nm–732.3 nm, 757.5 nm–770.5 nm, 813 nm–836.5 nm, 893.9 nm–924 nm, 928 nm–983 nm, 1081 nm–1171 nm, 1267 nm–1271 nm, 1300 nm–1503 nm, 1735 nm–1981 nm, 1995 nm–2035 nm, 2048 nm–2082 nm. We note that this masking rejects far less of the spectrum than would be necessary if no telluric correction had been applied.

4.4 Pipeline implementation

The procedures described in the previous sections have been implemented in ESO's pipeline[8] for the reduction of X-shooter data. Below we provide some more details on the algorithms and reference data used in the pipeline.

4.4.1 Radial velocity correction

As described in Sect. 4.2.4 the model spectra need to be shifted to the same radial velocity as the observed spectra to avoid the generation of pseudo-P Cygni profiles in the response curve. The pipeline uses a robust polynomial fit to the line core to determine the radial velocity. The fit accuracy is limited to 1 pixel (0.02 nm for UVB and VIS, 0.06 nm for NIR). Because of the limited accuracy of the radial velocity correction pseudo-P Cygni profiles are sometimes created when dividing the shifted reference spectrum by the observed one. This effect is taken into account when defining the fit regions for the response curve (see Sect. 4.4.2).

4.4.2 New fitting routine for response determination

The ratio of the shifted reference spectrum to the observed spectrum (telluric corrected for VIS and NIR) shows residuals at the line cores (see Figs. 4.8 and 4.11). At the same time both UVB and VIS spectra show variations on intermediate scales that need to be fit by the response curve because they are instrumental features (see Fig. 4.1; features at 365 nm and 560–620 nm). Therefore, we created for each flux standard star and arm a list of wavelength points at which the response is fit with a cubic spline fit. The pipeline determines at each point the median of the ratio over a predefined range (± 0.04 nm for UVB, ± 1 nm for VIS, and ± 5 nm for NIR). The points are selected so that the wavelength ranges used for the median do not overlap and regions of strong telluric absorption (e.g. between J and H and between H and K) are excluded (see Sect. 4.3.2 for details). Figure 4.11 shows the response curves derived for EG 274 with the pipeline. This new routine has been implemented in the X-shooter pipeline since version 2.2.0.

4.4.3 New reference data

The newly derived reference spectra for the flux standard stars described in Sect. 4.2.3 have been delivered with the X-shooter pipeline since version 2.2.0.

The adjusted LBLRTM model is used to correct the atmospheric extinction of X-shooter UVB and VIS spectra in pipeline version 2.3.0 and higher. For the NIR arm there is no extinction correction.

Since the PWV-dependent grid provides good corrections for NIR data taken during high PWV conditions (which could not be corrected with the time-dependent telluric library), but is less successful for intermediate and low PWV conditions, we decided to use the time-dependent telluric library described in Par. 2 of Sect. 4.3.2 as pipeline default for the NIR arm and provide the PWV-dependent library as possible alternative. For the VIS arm the PWV-dependent telluric library is used.

[8] http://www.eso.org/pipelines

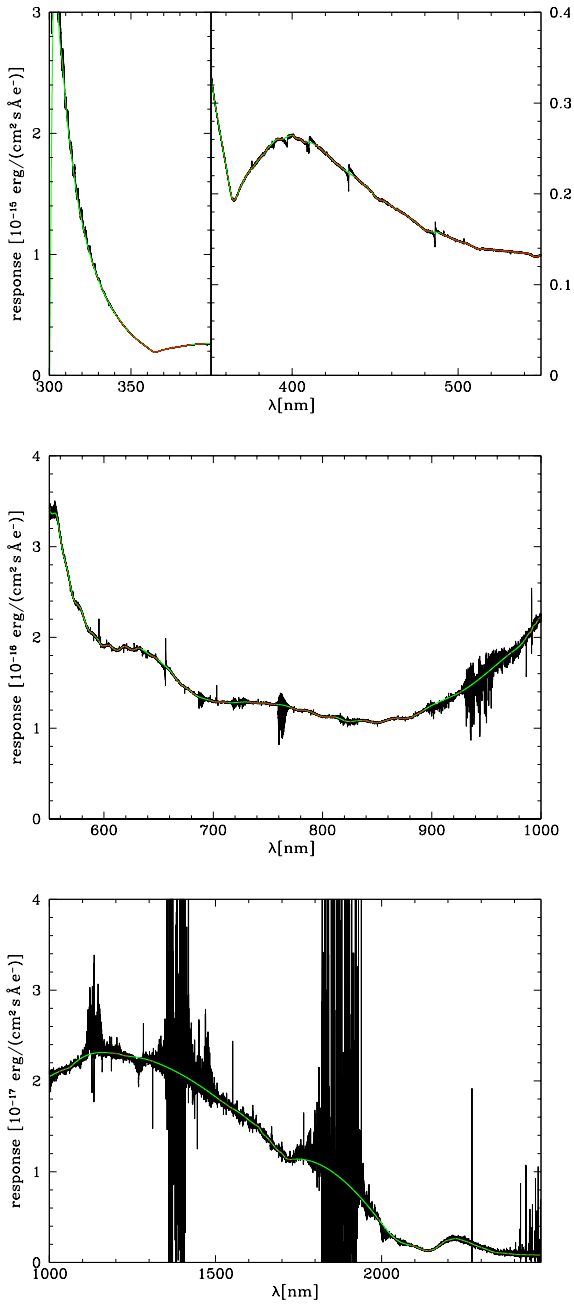

Figure 4.11: X-shooter response curves derived for EG 274. The red dots mark the fit points described in Sect. 4.4.2 and the green line marks the fit through these points.

4.5 Summary

In this paper we have presented flux-calibrated model spectra of southern sky spectral photometric standards in the wavelength range from 300 nm to 2500 nm. The calibrated model spectra are available at the CDS. The consistency of the set of models were verified using X-Shooter observations, and the region of strong line overlap between 380 nm and 450 nm in the model spectra was adjusted taking advantage of X-shooter observations of the featureless spectrum of L97–3. Our analysis shows that the use of stellar model spectra as reference data for flux standard has significant advantages when it comes to calibrating medium-resolution data as they are available on a finely sampled grid. Another significant advantage is the fact that model spectra are not affected by telluric absorption.

Our models are useful to determine the response curve of spectrographs, and the resulting response curve can in turn be used to flux-calibrate spectra of other targets. We have discussed in detail a methodology to carry out such a flux calibration. Beyond the proper choice of stellar model spectra, an appropriate correction of telluric absorption features is essential to flux calibrate data with wavelengths above 680 nm. Our method includes the use of telluric model spectra to correct spectral regions with low to moderate telluric absorption.

To illustrate the quality that can be achieved with the methods and model spectra described in this paper, we show in Fig. 4.12 an example of a standard star (LTT 7987). The spectrum was flux-calibrated with the response curve determined from a different star observed on the same night, namely EG 274. The response curve used for this calibration is shown in Fig. 4.11.

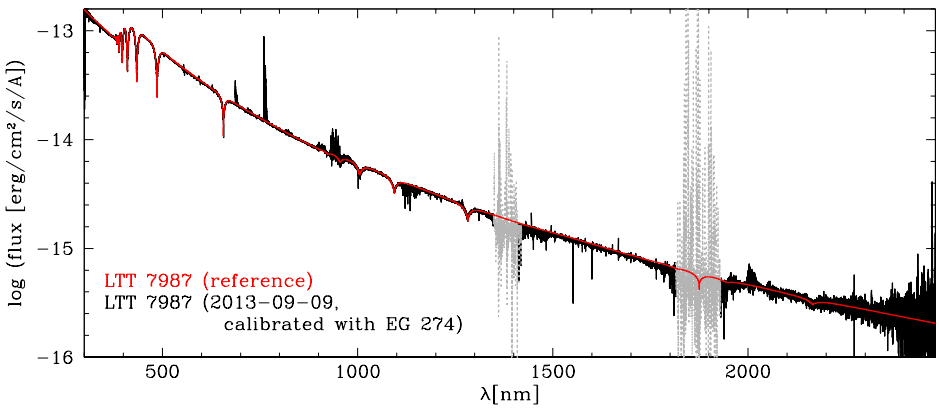

Figure 4.12: Spectrum of LTT 7987, corrected for telluric absorption and flux-calibrated with a response curve derived from observations of EG 274. The red curve is the reference spectrum for LTT 7987. Regions of very high telluric absorption are marked in grey.

While our set of standards is adequate to flux calibrate spectra in the whole southern hemisphere, additional standards would be useful both to enlarge the number of potential calibrators in the south, and to provide a similar set of standards in the northern hemisphere. Our methodology can be used to derive such a set of model spectra. Necessary ingredients for such an endeavour are accurate model spectra[9], availability of flux information (e.g. Hamuy et al. 1994), and observed uncalibrated spectra for both the new calibrators and at least one of the standard stars discussed here to correct for instrumental features.

[9] For hot (pre-) white dwarfs like the flux standard stars discussed here and many others, a good starting point for model spectra would be the TMAP spectral energy distributions at the registered VO service TheoSSA provided by the German Astrophysical Virtual Observatory.

Chapter 5

Database and website

⋆ ⋆ ⋆

This work was done in collaboration with the Centre de Données astronomiques de Strasbourg (CDS) and in particular with F. X. Pineau.

5.1 Introduction

The X-shooter Spectral Library contains the spectra of about 750 stars. They are intended for a variety of purposes, for which a large variety of ancillary data are required. These include information about the data acquisition and reduction, but also about the stars themselves. Pre-existing literature information on the fundamental parameters and the abundances are useful, but measurements of these made within the XSL project using the X-shooter spectra themselves must be made available as well.

Although some of these elements of information can be written into the headers of the frames and files, queries and subset selections become easier with a database. An adequately designed database also makes it possible to keep track of updates and versions. Estimated stellar parameters, for instance, may evolve as available stellar atmosphere models improve.

Once a database is constructed, relatively simple queries produce views of the information that can be displayed to the public. A dedicated website was created to release our data to the community.

5.2 Design of the database

The X-shooter Spectral Library is an ambitious project aiming at covering most of the HR diagram. We observed during six semesters stars from different environment, with various spectral types. Table 5.1 summarizes some informations about our observations.

An "OB" is one star, observed in three wavelength ranges (UVB, VIS, NIR) and in two modes (NODDING and STARE). Thus, one "OB" corresponds in fact $\sim$ to 10 raw frames (this count does not include the calibration files), which gives us a total of $\sim$ 8000 raw frames. This number approaches 10000 if the telluric standard star observations are included (they are useful complements to XSL in the hot star regime).

Period	Associated run	Number of OBs
P84	084.B-0869(A/B)	144
P85	085.B-0751(A/B)	144
P89	189.B-0925(A)	135
P90	189.B-0925(B)	104
P91	189.B-0925(C)	116
P92	189.B-0925(D)	123

Table 5.1: The XSL observing runs.

The needs of the XSL project led to the following list of minimal requirements, regarding the contents and their future evolution.

♣ Contents

- The starting point for the database is all the information used for the PHASE 2 preparation. This includes basic information about the stars, such as names, coordinates, magnitudes, but also selection information, such as the input catalogue from which the star was selected and the host galaxy of the star. Furthermore, the PHASE 2 material also contains an estimation of the fundamental parameters as available in the literature. All these pieces of information should be collected in the database.
- Selected information related to the data acquisition, such as the date of observation, the exposure time, the airmass, the slit width and the name of the output fits file, should be available, even though this duplicates file header information.
- The database should keep track of the data reduction process.
- In addition to the literature values, the database should contain the fundamental parameters derived within the XSL collaboration.

♣ Versions

The database should be able to receive various versions of certain properties. For example, effective temperatures could be derived from optical spectra or from near-infrared spectra, using several methods. A comment holder should allow to save the origin of the various versions.

♣ Current best

If several versions of the same parameter are available, the database should mark with a flag the one considered as “current best” by the collaboration.

5.3 Structure of the database

After discussion with database experts at CDS, it was decided to organize the XSL database into several tables, linked through keys that provide a unique identification of the programme stars. Figure 5.1 shows a schematic of the XSL database structure. The current version of the database only uses 4 of the 7 designed tables.

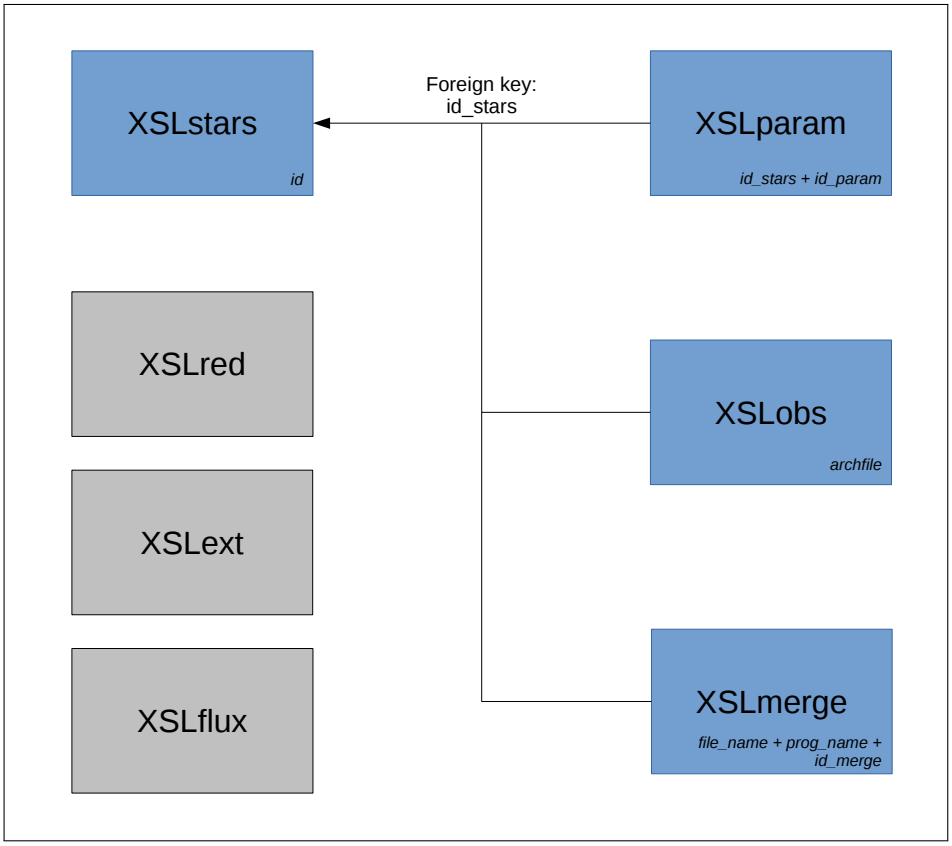

Figure 5.1: Schematic of the XSL database structure. The grey colors indicate the tables which are not used yet.

To create the database, I used PostgreSQL (psql), an open source object-relational database system, together with a number of BASH scripts.

5.4 Individual tables and their primary keys

Once the tables are designed, the next step is to define the primary keys. A primary key consists of a single attribute or multiple attributes in combination that uniquely identifies each record of a table. The primary keys are also used to link the different tables.

5.4.1 Table XSLstars

This table contains most of the information used for the PHASE 2 preparation (coordinates, input catalogue, and so on). The parameters of this table are listed in Table 5.2.

The primary key is the parameter **id**, which is basically a counter of the number of stars.

Parameter	Description
id	id number
name	name of the star
period	period of observations (expected)
identifier	other name of the star
type	type of the star
RA	right ascension of the star : IRCS coordinates
DEC	declination of the star : IRCS coordinates
l	Galactic longitude of the star
b	Galactic latitude of the star
pm_ra	RA proper motion of the star (in mas/yr)
pm_dec	DEC proper motion of the star (in mas/yr)
plx	parallax of the star (in mas)
radvel	radial velocity of the star (in km/s)
magU	magnitude in the U band of the star
magB	magnitude in the B band of the star
magV	magnitude in the V band of the star
magR	magnitude in the R band of the star
magI	magnitude in the I band of the star
magJ	magnitude in the J band of the star
magH	magnitude in the H band of the star
magK	magnitude in the K band of the star
spectype	spectral type of the star
inputCat	input catalogue of the star
population	population of the star (LMC, SMC, Bulge ...)
reference	csv input file
comments	any comments

Table 5.2: Settings for the *XSLstars* table.

5.4.2 Table XSLparam

This table contains all the information about the derived (fundamental) parameters (e.g., temperature, surface gravity, metallicity). This table should contain both the parameters from the literature and the ones derived afterwards. The parameters are listed in Table 5.3.

To define the primary key, we could not use **id_stars**, which corresponds to **id** from table **XSLstars**. Indeed, for a given star, several estimations of the fundamental parameters can be available. Therefore, we use a combination of the parameters **id_stars** and **id_param**, which is basically a counter of the number of estimations made for a given star.

To identify the "best value" for a given parameter, a flag is used. The letter A defines the best value. Of course, per parameter, only one best value is allowed, and the best value can be updated at any time.

Finally, this table can evolve as new parameters are estimated (abundance ratios, rotation velocities, etc).

Parameter	Description
id_stars	id number from XSLstars
id_param	id meter for each id_stars
teff	effective temperature value
meth_teff	method used to determine the effective temperature
comm_teff	any comments
flag_teff	flag for the teff parameter (A,B ...)
logg	surface gravity value
meth_logg	method used to determine the surface gravity
comm_logg	any comments
flag_logg	flag for the logg parameter (A,B ...)
fe_h	metallicity value
meth_feh	method used to determine the metallicity value
comm_feh	any comments
flag_feh	flag for the fe_h parameter (A,B ...)
spec_class	class of the spectrum
comm_class	any comments
flag_class	flag for the spec_class parameter (A,B ...)
spec_type	spectral type of the spectrum
comm_type	any comments
flag_type	flag for the spec_type parameter (A,B ...)

Table 5.3: Settings for the *XSLparam* table.

5.4.3 Table XSLobs

This table contains all the information linked to the observations: when a star was observed, what was the exposure time, etc. The parameters are listed in Table 5.4.

The primary key is the parameter **archfile**, which corresponds to the fits file name of a raw data frame. The filenames are unique contrary to the names of the stars.

Parameter	Description
id_stars	id number from XSLstars
object	name of the observed star
target_ra	right ascension of the star
target_dec	declination of the star
target_l	Galactic longitude of the star
target_b	Galactic latitude of the star
prog_id	observing period
archfile	ARCHive FILEname
obid	identification number of OB
expt	exposure time
tech	observation technique
arm	spectrograph arm
ndit	number of integrations (only NIR arm)
clock	detector read mode
slitu	slit width and length for UVB arm
slitv	slit width and length for VIS arm
slitn	slit width and length for NIR arm
dimm_avg	DIMM seeing average over the exposure
airmass	airmass of the observation
reference	csv input file
comments	any comments

Table 5.4: Settings for the *XSLobs* table.

5.4.4 Tables XSLred, XSLext and XSLflux

In the current version of the database, these tables are not implemented. They should contain respectively:

- information about the reduction done with the pipeline. It should allow one to keep track of repeated pipeline reductions, with version information.
- information about the extraction of the reduced frames, from 2D to 1D.
- information about the steps following the extraction, that lead to the flux calibration. It includes the telluric correction (for example).

5.4.5 Table XSLmerge

This table contains all the information about the final frames, products of the merging of the different wavelength range, after flux calibration. Table 5.5 listed all the parameters (name and description) that we use in the current version of the *XSLmerge* table.

To define the primary key for this table, we use the name of the final frame, **file_name**, and also the observing period, **prog_name**. But this is not sufficient, as the same star can be observed twice in a period. So, we add a counter to the two previous parameters, **id_merge**, to complete the definition of the primary key.

Parameter	Description
id_stars	id number from XSLstars
id_merge	id meter for each file_name
file_name	name of the output file
star_name	name of the observed star
prog_name	observing period
obid	identification number of OB
ra	right ascension of the star
dec	declination of the star
arm	spectrograph arm
mode	observation mode
mjd	modified Julian date
airmass	airmass of the observation
notes	notes (saturated observation
	lost_pair case in nodding observation)
reference	csv input file
author	author of the process
comments	any comments

Table 5.5: Settings for the *XSLmerge* table.

5.5 Design of the XSL website

To provide access to our final spectra as well as information about the XSL project (list of members, related publications), we created a dedicated website: `http://xsl.u-strasbg.fr/` (see Figures 5.2 and 5.3).

This website is in fact an external view of the XSL database, which is meant to be updated at every major new data release. The current version corresponds to Data Release 1, as described in Chen et al. (2014a).

5.5.1 Creation

To create the web pages, I used PHP, a server-side scripting language, together with HTML, the standard language used to create web pages.

For the contents of the pages, we used information taken from the XSL database. We chose not to link the website with the database but to provide a "frozen" database.

In other words, we want the version available on the website to be fixed until the next release. To fulfill all these conditions:

- we create some **views** with the requested parameters.
  A view is a virtual table containing the result of a query made on one or several tables.
- We export the database, to save the version of the database at this date and possibly restore it afterwards.
- We export the **views** as text files to add them to the website.

An example of psql commands used to create the DR1 view is displayed below. In this example, we gather information about the stars themselves (name, coordinates, spectral type), with information about the data acquisition (date of observation, airmass, filename of the output spectra).

```
CREATE VIEW DR1_all AS
SELECT XSLstars.name, XSLmerge.ra, XSLmerge.dec,
XSLmerge.mjd, XSLmerge.airmass, XSLstars.spectype,
XSLmerge.file_name FROM XSLstars, XSLmerge
WHERE XSLmerge.id_stars=XSLstars.id;
```

In addition to visualizing plots of the spectra, the users can download them. To do so, the users need to register. The downloading of spectra is free of charge. We just ask the users to register so that we can have an idea of how many people are using our spectra, and we can send them emails for new data releases. For this purpose, another database was linked to the website.

5.5.2 Further developments

In the near future, the parameters of the carbon stars will be added to the database.

Further improvements of the database can be made. As an example, the interface for the users can be more user-friendly and print their last requests.

Moreover, access to the XSL database could be added for the members of the collaboration.

Last but not least, tools for direct measurements on the XSL data could be made available. Members of the XSL collaboration have actively contributed to the website of the MILES spectroscopy project `http://www.iac.es/proyecto/miles/` and could port these tools to the XSL website.

The X-shooter Spectral Library

- Home
- About the spectra
- All stars
- Stars / spectral type
- People
- Papers

The X-shooter Spectral Library is a collection of 3000–25000 Å all stellar spectra observed at a resolving power of R = λ/Δλ ~ 10 000 with the medium-resolution spectrograph X-shooter at the Very Large Telescope (VLT).

The current release contains more than 200 stars, while the final sample will contain more than 700 stars and cover most of the HR diagram with spectral types between O and M, as well as AGB stars.

Figures 1 and 2, taken from Chen et al. (2014), show the distribution of spectral types in DR1 and the HR diagram of these stars.

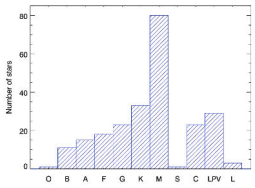

Figure 1: Distribution of the spectral types in XSL observed in Periods 84 and 85 (excluding telluric calibrators). Spectral types were retrieved from SIMBAD or based on educated guesses from the source libraries or atmospheric parameters.

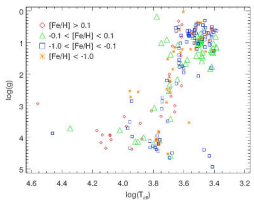

Figure 2: HR diagram of the 219 XSL stars (O–M, LPV, S) with calculated Teff, logg, and [Fe/H], where [Fe/H] is presented in different colors.

Last modified on: September 1, 2014

Maintained by Anaïs Gonneau

Figure 5.2: Screenshot of the XSL website's home page.

All Stars

Home Page Log in Register now

Mark all | Unmark all | Export visible table data into csv | Download marked rows

Filter : Clear

Mark	Name	RA (J2000)	DEC (J2000)	MJD	Airmass	Spec. type
	2MASS J15065441+1321060	15:06:54.41	+13:21:06.0	55438.01492579	1.931	L3
	2MASS J17535707-2931427	17:53:57.05	-29:31:42.8	55438.06879617	1.076	
	2MASS J18024572-3001120	18:02:45.73	-30:01:12.0	55439.19529639	1.994	M7
	2MASS J18024611-3004509	18:02:46.11	-30:04:51.0	55439.20131225	2.11	M6.5
	2MASS J18025277-2954335	18:02:52.78	-29:54:33.6	55439.20945305	2.297	M5
	2MASS J18032525-2959483	18:03:25.25	-29:59:48.3	55397.23553748	1.249	M6
	2MASS J18033716-2954227	18:03:37.16	-29:54:22.7	55393.13866734	1.005	
	2MASS J18040638-3010497	18:04:06.38	-30:10:49.7	55393.17401749	1.032	M5
	2MASS J18042244-3000534	18:04:22.45	-30:00:53.5	55393.18080958	1.042	M6
	2MASS J18042265-2954518	18:04:22.66	-29:54:51.8	55393.18889193	1.056	M9
	2MASS J18080765-3142020	18:08:07.65	-31:42:02.0	55408.1734676	1.112	
	2MASS J18083220-3201531	18:08:32.18	32:01:53.1	55408.19014889	1.167	
	2MASS J18351799-3428093	18:35:17.99	-34:28:09.3	55356.39712438	1.416	
	2MASS J18352206-3429112	18:35:22.06	-34:29:11.2	55356.17421844	1.124	
	2MASS J18352834-3444085	18:35:28.34	-34:44:08.5	55393.05060464	1.204	

Figure 5.3: List of all stars as displayed by the XSL website.

Chapter 6

Conclusions

⋆ ⋆ ⋆

Understanding the formation and the evolution of galaxies was the guideline of this thesis. To tackle this question, we make use of the ESO spectrograph X-shooter to observe stars from the ultra-violet to the near-infrared. We select stars from almost all the Hertzsprung-Russell diagram to build the X-shooter Spectral Library (XSL). This stellar library is unprecedented among the stellar libraries for the following reasons:

- The number of stars: $\sim$ 800 stars (covering a large range of stellar atmospheric parameters).
- The resolution: $7700 \leq R \leq 11000$ (depending on the wavelength range).
- The broad wavelength coverage: from 0.3 to 2.5 μm.
- The simultaneity of the observations.

The X-shooter Spectral Library provides data for years of investigation in various subfields of stellar and extragalactic astrophysics. The contributions of this thesis are the following:

- A data reduction pipeline was developed and used to reduce all the data acquired as part of the ESO Large Programme. In particular, a novel technique was introduced to deal with near-infrared telluric absorption at two steps of the reduction procedure (*Chapter 4*).
- The reduced data were made available on-line via a dedicated XSL website (`http://xsl.u-strasbg.fr/`). The website shows views of an underlying database, that was constructed in order to organize the final data together with a rich variety of metadata regarding the observed stars and the data reduction steps (*Chapter 5*).
- A detailed investigation of the spectra of carbon star spectra in XSL was performed, with the double aim of describing the spectral variety (*Chapter 2*) and of determining fundamental parameters for future usage in galaxy modelling (*Chapter 3*). These spectra more than double the number of C-star spectra available in the literature over the optical and near-infrared wavelength range and increase the available resolution. It is shown that the transition from dust-free to fully obscured carbon stars, i.e. the transition from blue to red colors, occurs along a variety of paths: at a given near-infrared color, the spectrum may have two aspects, depending on the role played by circumstellar dust. Based on a comparison between the XSL

spectra and state-of-the-art theoretical ones, fundamental parameters are estimated when possible, and limitations of current models are discussed.

6.1 Data reduction

Before being able to use the spectra, the first step is the data reduction, starting from the $\sim$ 10 000 raw frames acquired for XSL. This is clearly far more complex than the pressing of a button. It required departures from the reduction procedures available from ESO, a high level of automation, as well as careful book-keeping.

It is worth noting that the need for a good flux calibration and for the removal of telluric absorption features is a specific requirement for spectral libraries meant to be used in population synthesis projects. In the study of individual stars, an alternative is to apply telluric and instrumental transmission curves to theoretical stellar spectra, which can then be matched to the empirical spectra at an earlier stage of reduction.

For the XSL spectra, the ESO pipeline was used only up to the creation of flat-fielded, rectified, wavelength-calibrated two-dimensional (2D) spectra. A weighted extraction of a one-dimensional (1D) spectrum was implemented, based on the principles of Horne (1986), to better remove bad pixels and cosmic rays. In the processing of observations made in nodding mode, at two positions along the slit, the adopted scheme avoids cumulating the bad pixels of the two positions. The tricky part here is to make sure background contributions from the sky and the instrument (thermal emission, scattered light) are properly accounted for.

Innovative procedures were implemented to deal with telluric absorption (contamination from the Earth's atmosphere) in the near-infrared. Instead of dealing with the flux calibration and the correction of telluric absorption bands separately, we implemented a procedure that already accounts for telluric absorption when computing the instrument's response curve. The process avoids poorly constrained interpolations over broad windows in wavelength, over which the raw signal is close to zero and the instrument's response is not flat. Telluric transmission models for Paranal were obtained via ESO, and this led to a collaboration with ESO researchers, who then also implemented a similar procedure in the ESO pipeline. The ESO implementation of the flux calibration procedure resulting from this collaboration is described in *Chapter 4*. The XSL implementation is summarized in the first sections of *Chapter 2*.

The challenge in reproducing the telluric features is to work with a complete list of molecules (e.g. water vapour, molecular oxygen, carbon dioxide and methane for the near-infrared) and to be able to match their relative contributions at the time of observation. Usually people observe telluric standard stars shortly before or after the science targets, and thus derive the underlying telluric transmission spectra by removing the intrinsic stellar spectra. This relies on the assumption that the atmospheric conditions have not changed between the observation of the science target and the observation of the standard star, which of course is not always the case. One solution is to extract the principal components of the telluric transmission of a large number of telluric standard star observations, as described for XSL by Chen et al. (2014a).

Another option is to use models of telluric spectra. In that framework, we can cite the work done by the TAPAS[1] (Transmissions Atmosphériques Personnalisées Pour l'AStronomie) team, which can provide separate transmittances for the different molecules. In *Chapter 4* and in our own analysis, we use the models developed by Noll et al. (2012) and Jones et al. (2013). Our tests show that using the model close in airmass to the science observation does not necessarily provide the best telluric correction. Indeed, it is better to use a set of telluric models and to find the best models among this set or to use a combination of individual models (by doing a principal component analysis for example). Performing the fits over restricted wavelength intervals makes it possible to target different molecules somewhat independently.

Because of the number of stars in the programme, we developed automatic procedures to perform the steps described above. For quality control, many diagnostic plots can be requested from the scripts. A standardized directory tree and file naming scheme makes it possible to trace the various reductions stages from the raw frames to the fully merged, calibrated 1D spectra.

6.2 Carbon stars

Among all the stars available in XSL, I focused for my PhD on the carbon stars, a complex class of objects for which the scarcity of spectra in the literature was well known.

These stars, identified in 1868 by Father Angelo Secchi as type four, struck him by their vivid ruby red colour and also by the complete contrast with the stars of the third type – today known as the M stars. Among the type IV stars, his favorite object is "La Superba" – also known as Y CVn – which is one of the coolest known stars. He described it as follows: "Magnifico oggeto di 4 tipo, e veramente singulare per la sua vivacita" [A splendid object of type 4 which is truly outstanding for its vividness].

To the untrained eye, the forest of lines of (mainly) CN and C_2 that give well resolved C-star spectra a rugged appearance, may look like random noise. But the repeatability of the numerous features is rather amazing. After four years, I agree with Secchi's description and I now see the intrinsic beauty of the carbon stars.

The sample present in the X-shooter Spectral Library is interesting as it displays quite a diversity. We present 35 C-stars with a $(J - K)$ between 1 to 3, taken from the Milky Way and the Magellanic Clouds. Because of its resolution and its wavelength coverage, this collection extends the previous spectral libraries containing carbon stars. A complete description of the collection is provided in *Chapter 2*.

The main result described in that chapter is the bimodality of our sample. Indeed, some of our stars exhibit an absorption feature at $1.53\,\mu$m – usually associated with HCN + C_2H_2. We also found that these stars have a smoother appearance in the near-infrared, which is translated by a lower level of high frequency spectral structure compared to the "classical" carbon stars. We believe that this smooth appearance indicates the presence of a circumstellar shell of dust

[1] `http://www.pole-ether.fr/tapas/`

around the star, with a significant contribution of dust emission to the spectrum. In our sample, all the stars with this feature happen to be in the Large Magellanic Clouds. However, we believe that this is just a selection effect, as others have observed this absorption band for stars located in the Milky Way and in metal-poor dwarf galaxies. The stars with the 1.53 μm feature also happen to be large amplitude pulsators. This property is much more likely to explain the circumstellar dust properties than small differences in metallicity. Indeed, the standard scenario for mass loss on the TP-AGB involves the production of dust grains in compressed cool layers of the pulsating atmospheres, and a subsequent wind driven by the radiation pressure on these particles.

6.3 Comparison with models

The challenge is now to use these spectra in stellar population synthesis codes. For this purpose, we need to relate them to fundamental stellar parameters such as surface gravities, effective temperatures, C/O ratios. One way to do so is to compare the collection of spectra with theoretical models.

In *Chapter 3*, we compare our sample of carbon stars with modern hydrostatic carbon-rich models. These models are dust-free, meaning that they can only be used to reproduce the warmer carbon stars with weak pulsation. We perform a χ^2 minimization (with a multiplicative polynomial) over a four-dimensional parameter space, the parameters being: the effective temperature, the surface gravity, the ratio of carbon over oxygen and the metallicity. We repeat our analysis over two wavelength ranges: the visible (0.4 to 1.0 μm) and the near-infrared (1.0 to 2.4 μm). The idea is to see if the parameters found over the two wavelength ranges agree (which is an ongoing issue).

This exercise is far from being simple. At the nominal resolution of the XSL spectra ($R \sim 10000$), wavelength dependent line offsets indicate that the velocity structure within pulsating stellar atmospheres is significant (velocity differences larger than 10 km/s have been reported both in previous high resolution observations and in pulsating star models). Although this highlights a fundamental limitation of hydrostatic models, we did perform a systematic comparison, but at a reduced spectral resolution ($R \sim 2000$).

The statistical interpretation of χ^2 values relies on good noise spectra and on knowledge of covariance between neighbouring pixels. By allowing for a multiplicative polynomial in the fits, residual flux calibration errors can be accounted for, but covariance on smaller scales remains a strong issue. In an ideal world, a good model would be achieved for a reduced χ^2 equal to 1. In practice, this value is never achieved. But on the other hand the residuals are much smaller than the molecular features themselves: the models explain a large fraction of the spectrum's intrinsic variance. The question is: what should one define as a good fit? Which error bars can one put on the estimated model parameters? We asked ourselves: if the best fit is considered a good fit (i.e. the noise is artificially increased to absorb the difference between the data and the best model, so the corrected reduced χ^2 is 1), what other models should be considered (almost) equally acceptable? This provides error bars consistent with the dispersion observed in

the relationship between parameters determined from UVB+VIS spectra on one hand, and NIR spectra on the other.

Our analysis shows that the temperatures are constrained to $\pm$ 100 K at best. One may easily obtain smaller error bars when using of restricted grids of theoretical spectra, and/or restricted wavelength ranges. It is worth remembering that even our model grid is restricted. For instance, the micro-turbulent velocity is identical in all models. Micro-turbulence is known to affect the relative strengths of molecular bands, leading to additional degeneracies between model parameters.

For the vast majority of spectra, surface gravities typical of AGB stars ($\log(g)$=0) are favored over lower or higher values. This must be considered a success of the models. The spectra also tend to favor slightly subsolar metallicities, which is satisfactory considering the predominance of LMC and SMC stars in the sample. However, the ensemble of acceptable models usually contains both solar and subsolar models.

A high-resolution analysis over specific wavelength regions shows that some of the molecules are not well reproduced in the observations, as for example the C_2 line at 1.77 μm. This emblematic near-infrared C-star feature has a companion bandhead in empirical spectra near 1.75 microns, that is not seen in the models. The forest of lines across the photometric K-band is also difficult to match in cool stars with large C/O ratios. A systematic study, wavelength range by wavelength range, remains to be performed.

For the spectra more obscured by the dust, the static models fail to reproduce them – as expected. The next step is to use dynamical models. It has been suggested that a simple dust-envelope model could be used as an intermediate step, before going into the complexity of dynamical models. But since it is known that the presence of dust around C stars is a consequence of pulsation, and since pulsating C-star models do exist at least at low resolution, it seems more promising to exploit those directly. In particular, a study of their molecular stratification would be useful: the XSL C stars indicate that some CO should be located above dust emission layers, and this hypothesis requires checking. If high resolution versions of the pulsating model spectra can be computed, we could also explore the effects of pulsation on the XSL spectra at $R \sim 10000$ more quantitatively.

6.4 Future perspectives

XSL will provide a benchmark library for stellar population studies in the era of GAIA, the James Webb Space Telescope and the European Extremely Large Telescope. However, XSL is not yet fully complete. It lacks M dwarfs, which are critical for studies of the low-mass region of the initial mass function in galaxies. It also lacks hot massive (young) stars. A search of the ESO archive has shown that M dwarf spectra from other programs have become public, and to address hot stars the numerous telluric absorption standards observed over the years can be harvested.

The stellar analysis of XSL spectra is essential for an efficient usage in population synthesis models. Stellar fundamental parameters for all spectral types will be estimated within the collaboration, by comparison of the optical spectra

with well calibrated libraries such as ELODIE (Prugniel et al. 2007) or MILES (Sánchez-Blázquez et al. 2006). Only theoretical models can be used to assess the observations across the whole range of wavelengths of X-shooter data. An extensive library of high resolution theoretical spectra has been computed for just this purpose by T.-O. Husser, using the PHOENIX models of XSL-collaborator P. Hauschildt (Husser et al. 2013). It contains models for a variety of metallicities and abundance ratios, but not carbon stars.

For carbon stars, as already mentioned, consistent models for the photosphere and the veiling by dust are needed. They will allow us to assess the evolutionary stage of red carbon stars more precisely. For the inclusion of C stars in population synthesis models, we suggest to combine the XSL C star spectra with spectra available in the literature, in order to improve statistics. Standard population synthesis codes assign spectra to locations along a stellar evolution track based on effective temperature and surface gravity. For C stars, at least one extra parameter is required. Tests will need to be performed to compare the relative importance of the C/O ratio and the pulsation properties. We anticipate that pulsation amplitude has a stronger effect than C/O, based on the large proportion of stars with the $1.53\,\mu$m absorption feature among large amplitude variables. Pulsation periods along evolutionary tracks can be predicted by stellar evolution models, and combined with variable star survey data to derive proportions of large amplitude variables (Groenewegen & de Jong 1994; Marigo & Girardi 2007; Wood 2015).

Furthermore, even if the existing sample of carbon stars displays quite a diversity, it will be interesting to expand it with other samples. A collaboration with M. Groenewegen could allow us to include X-shooter spectra of a set of C stars for which mid-infrared observations are available from Spitzer. Also, we can imagine extending the analysis done with the carbon stars to the oxygen-rich giants and LPVs, aiming at improving the contribution of both stars to the thermally pulsing asymptotic giant branch.

While discovering the carbon stars, Secchi acknowledged that “There is a great cosmical law which is about to come forth; but, for the present, we must wait until the review of all the stars has been accomplished.” More than ever, I am convinced that XSL and the new facilities will make this a reality.

Bibliography

⋆ ⋆ ⋆

Aaronson, M., Bothun, G. D., Budge, K. G., et al. 1988, IAUS, 130, 185
Aaronson, M. & Mould, J. 1985, ApJ, 290, 191
Alcock, C., Allsman, R. A., Alves, D., et al. 1996, MNRAS, 280, L49
Ali, B., Carr, J. S., Depoy, D. L., et al. 1995, AJ, 110, 2415
Alksnis, A., Balklavs, A., Dzervitis, U., et al. 2001, BaltA, 10, 461
Allard, F. & Hauschildt, P. H. 1995, ApJ, 445, 433
Alvarez, R., Lançon, A., Plez, B., et al. 2000, A&A, 353, 322
Aringer, B., Girardi, L., Nowotny, W., et al. 2009, A&A, 503, 913
Bacon, R., Accardo, M., Adjali, L., et al. 2010, SPIE, 7735, E08
Bagnulo, S., Jehin, E., Ledoux, C., et al. 2003, Msngr, 114, 10
Ballik, E. A. & Ramsay, D. A. 1963, ApJ, 137, 61
Barnbaum, C., Stone, R. P. S., & Keenan, P. C. 1996, ApJS, 102, 1181
Bergeat, J., Knapik, A., & Rutily, B. 2002, A&A, 390, 967
Bergeron, P., Saffer, R. A., & Liebert, J. 1992, ApJ, 394, 228
Bertelli, G., Bressan, A., Chiosi, C., et al. 1994, A&AS, 106, 275
Bessell, M. S. 1990, PASP, 105, 419
Bessell, M. S., Brett, J. M., Scholz, M., et al. 1991, A&AS, 89, 335
Bessell, M. S., Brett, J. M., Wood, P. R., et al. 1989, A&AS, 77, 1
Bessell, M. S., Scholz, M., & Wood, P. R. 1996, A&A, 307, 481
Bessell, M. S., Wood, P. R., & Evans, T. L. 1983, MNRAS, 202, 59
Blum, R. D., Ramond, T. M., Conti, P. S., et al. 1997, AJ, 113, 1855
Bohlin, R. C., Dickinson, M. E., & Calzetti, D. 2001, AJ, 122, 2118
Boyer, M. L., Girardi, L., Marigo, P., et al. 2013, ApJ, 774, 83
Bruzual, G. & Charlot, S. 2003, MNRAS, 344, 1000
Burstein, D., Faber, S. M., Gaskell, C. M., et al. 1984, ApJ, 287, 586
Cardelli, J., Clayton, G., & Mathis, J. 1989, ApJ, 345, 245
Chabrier, G. 2003, Pub. Astron. Soc. Pac., 115, 763
Chen, Y., Trager, S., Peletier, R., et al. 2014a, A&A, 565, A117
Chen, Y.-P., Trager, S. C., Peletier, R. F., et al. 2014b, The Messenger, 158, 30
Christlieb, N., Green, P. J., Wisotzki, L., & Reimers, D. 2001, A&A, 375, 366
Cioni, M.-R. L., Girardi, L., Marigo, P., et al. 2006, A&A, 448, 77

Cioni, M.-R. L. et al. 2003, A&A, 406, 51

Clough, S. A., Shephard, M. W., Mlawer, E. J., et al. 2005, J. Quant. Spec. Radiat. Transf., 91, 233

Coelho, P., Barbuy, B., Meléndez, J., et al. 2005, A&A, 443, 735

Cohen, M., Walker, R. G., Barlow, M., & Deacon, J. R. 1992, AJ, 104, 1650

Conroy, C. 2013, ARA&A, 51, 393

Cordier, D., Pietrinferni, A., Cassisi, S., et al. 2007, AJ, 133, 468

Cushing, M. C., Rayner, J. T., & Vacca, W. D. 2005, ApJ, 623, 1115

Cutri, R. M., Skrutskie, M. F., van Dyk, S., et al. 2003, VizieR Online Data Catalog, 2246, 0

Dallier, R., Boisson, C., & Joly, M. 1996, A&AS, 116, 239

Davies, B., Kudritzki, R.-P., Plez, B., et al. 2013, ApJ, 767, 3

Egret, D. 1980, BICDS, 18, 82

Eisenhauer, F., Abuter, R., Bickert, K., et al. 2003, in Society of Photo-Optical Instrumentation Engineers (SPIE) Conference Series, Vol. 4841, Instrument Design and Performance for Optical/Infrared Ground-based Telescopes, ed. M. Iye & A. F. M. Moorwood, 1548–1561

Epchtein, N. et al. 1997, ESO Messenger, 87, 27

Eriksson, K., Nowotny, W., Höfner, S., et al. 2014, A&A, 566, A95

Ferraro, F. R., Fusi Pecci, F., Testa, V., et al. 1995, MNRAS, 272, 391

Figer, D. F., McLean, I. S., & Najarro, F. 1997, ApJ, 486, 420

Fluks, M. A., Plez, B., The, P. S., et al. 1994, A&AS, 105, 311

Förster Schreiber, N. M. 2000, AJ, 120, 2089

Freudling, W., Romaniello, M., Bramich, D. M., et al. 2013, A&A, 559, A96

Frogel, J. A., Mould, J., & Blanco, V. M. 1990, ApJ, 352, 96

Frogel, J. A., Persson, S. E., & Cohen, J. G. 1980, ApJ, 239, 495

Frogel, J. A., Stephens, A., Ramírez, S., et al. 2001, AJ, 122, 1896

Gautschy-Loidl, R., Höfner, S., Jørgensen, U. G., et al. 2004, A&AS, 422, 289

Giammichele, N., Bergeron, P., & Dufour, P. 2012, ApJS, 199, 29

Gianninas, A., Bergeron, P., & Ruiz, M. T. 2011, ApJ, 743, 138

Girardi, L. & Bertelli, G. 1998, MNRAS, 300, 533

Girardi, L., Bressan, A., Bertelli, G., et al. 2000, A&AS, 141, 371

Girardi, L., Marigo, P., Bressan, A., et al. 2013, ApJ, 777, 142

Girardi, L., Williams, B. F., Gilbert, K. M., et al. 2010, ApJ, 724, 1030

Glatt, K., Grebel, E. K., Sabbi, E., et al. 2008, AJ, 136, 1703

Goebel, J. H., Bregman, J. D., Witteborn, F. C., et al. 1981, ApJ, 246, 455

Gonneau, A., Lançon, A., Trager, S. C., et al. 2015, A&A, submitted

Goswami, A., Karinkuzhi, D., & Shantikumar, N. S. 2010, MNRAS, 402, 1111

Gregg, M. D., Silva, D., Rayner, J., et al. 2006, in The 2005 HST Calibration

Workshop: Hubble After the Transition to Two-Gyro Mode, ed. A. M. Koekemoer, P. Goudfrooij, & L. L. Dressel, 209

Groenewegen, M. A. T. 2007, astro-ph/0611163

Groenewegen, M. A. T. & de Jong, T. 1994, A&A, 288, 782

Groenewegen, M. A. T., Lançon, A., & Marescaux, M. 2009, A&A, 504, 1031

Gullieuszik, M., Held, E. V., Rizzi, L., et al. 2008, MNRAS, 388, 1185

Hamuy, M., Suntzeff, N. B., Heathcote, S. R., et al. 1994, PASP, 106, 566

Hamuy, M., Walker, A. R., Suntzeff, N. B., et al. 1992, PASP, 104, 533

Hanson, M. M., Conti, P. S., & Rieke, M. J. 1996, ApJS, 107, 281

Hanson, M. M., Kudritzki, R.-P., Kenworthy, M. A., et al. 2005, ApJS, 161, 154

Hauck, B. & Mermilliod, M. 1998, A&AS, 129, 431

Hayes, D. S. 1985, in IAU Symposium, Vol. 111, Calibration of Fundamental Stellar Quantities, ed. D. S. Hayes, L. E. Pasinetti, & A. G. D. Philip, 225

Höfner, S., Jorgensen, U. G., Loidl, R., et al. 1998, A&A, 340, 497

Horne, K. 1986, PASP, 98, 609

Hughes, S. M. G. & Wood, P. R. 1990, A&AS, 99, 784

Husser, T. O., Wende-von Berg, S., Dreizler, S., et al. 2013, A&A, 553A, 6

Ireland, M. J., Scholz, M., & Wood, P. R. 2011, MNRAS, 418, 114

Ivanov, V. D., Rieke, M. J., Engelbracht, C. W., & others. 2004, ApJS, 151, 387

Johnson, H. L. & Méndez, M. E. 1970, AJ, 75, 785

Jones, A., Noll, S., Kausch, W., et al. 2013, A&A, 560A, 91

Jones, H. R. A., Longmore, A. J., Allard, F., et al. 1996, MNRAS, 280, 77

Joyce, R. R. 1998, AJ, 115, 2059

Joyce, R. R., Hinkle, K. H., Wallace, L., et al. 1998, AJ, 116, 2520

Kaeufl, H.-U., Ballester, P., Biereichel, P., et al. 2004, SPIE, 5492, 1218

Kausch, W., Noll, S., Smette, A., et al. 2015, A&A, 576, A78

Keenan, P. C. 1993, PASP, 105, 905

Keenan, P. C. & Morgan, W. W. 1941, ApJ, 94, 501

Kennedy, C. R., Sivarani, T., Beers, T. C., et al. 2011, AJ, 141, 102

Kim, D.-W., Protopapas, P., Bailer-Jones, C. A. L., et al. 2014, A&A, 566, A43

Kleinmann, S. G. & Hall, D. N. B. 1986, ApJS, 62, 501

Koester, D. 2010, Mem. Soc. Astron. Italiana, 81, 921

Koester, D., Napiwotzki, R., Christlieb, N., et al. 2001, A&A, 378, 556

Kriek, M., Labbé, I., Conroy, C., et al. 2010, ApJ, 722L, 64

Kroupa, P. 2001, MNRAS, 322, 231

Kurucz, R. L. 1979, ApJS, 40, 1

Lambert, D. L., Gustafsson, B., Eriksson, K., et al. 1986, ApJS, 62, 373

Lambert, D. L., Smith, V. V., & Hinkle, K. H. 1990, AJ, 99, 1612

Lançon, A. & Wood, P. R. 2000, A&AS, 146, 217

Lançon, A., Gallagher, J. S., I., Mouhcine, M., et al. 2008, A&A, 486, 165
Lançon, A. & Hauschildt, P. H. 2010, ASPC, 425, 61
Lançon, A., Hauschildt, P. H., et al. 2007, A&A, 468, 205
Lançon, A. & Mouhcine, M. 2002, A&A, 393, 167
Lançon, A., Mouhcine, M., Fioc, M., et al. 1999, A&A, 344, 21
Lançon, A. & Wood, P. R. 2000, A&AS, 146, 217
Lancon, A. & Rocca-Volmerange, B. 1992, A&AS, 96, 593
Lanz, T. & Hubeny, I. 2003, ApJS, 146, 417
Lazaro, C., Hammersley, P. L., Clegg, R. E. S., et al. 1994, MNRAS, 269, 365
Le Borgne, J.-F., Bruzual, G., Pelló, R., et al. 2003, A&A, 402, 433
Lebzelter, T., Seifahrt, A., Uttenthaler, S., et al. 2012, A&A, 539, A109
Lee, S.-K., Ferguson, H. C., Somerville, R. S., et al. 2010, ApJS, 184, 100
Lejeune, T., Cuisinier, F., & Buser, R. 1998, A&AS, 125, 229
Lenorzer, A., Vandenbussche, B., Morris, P., et al. 2002, A&A, 384, 473
Lloyd Evans, T. 1980, MNRAS, 193, 97
Lloyd Evans, T. 2010, JApA, 31, 177
Lodieu, N., Scholz, R.-D., McCaughrean, M. J., et al. 2005, A&A, 440, 1061
Loidl, R., Lançon, A., & Jørgensen, U. G. 2001, A&A, 371, 1065
Lyubenova, M., Kuntschner, H., Rejkuba, M., et al. 2010, A&A, 510, A19
Lyubenova, M., Kuntschner, H., Rejkuba, M., et al. 2012, A&A, 543, A75
Maiolino, R., Rieke, G. H., & Rieke, M. J. 1996, AJ, 111, 537
Malkan, M. A., Hicks, E. K., Teplitz, H. I., et al. 2002, ApJS, 142, 79
Maraston, C. 1998, MNRAS, 300, 872
Maraston, C. 2005, MNRAS, 362, 799
Marigo, P., Bressan, A., Nanni, A., et al. 2013, MNRAS, 434, 488
Marigo, P. & Girardi, L. 2001, A&A, 377, 132
Marigo, P. & Girardi, L. 2007, A&A, 469, 239
Marigo, P., Girardi, L., Bressan, A., et al. 2008, A&A, 482, 883
Mármol-Queraltó, E., Cardiel, N., Cenarro, A. J., et al. 2008, A&A, 489, 885
Martins, L. P., González Delgado, R. M., Leitherer, C., et al. 2005, MNRAS, 358, 49
McGregor, P. J., Hyland, A. R., & Hillier, D. J. 1988, ApJ, 324, 1071
Melbourne, J. & Boyer, M. L. 2013, ApJ, 764, 30
Melbourne, J., Williams, B. F., Dalcanton, J. J., et al. 2012, ApJ, 748, 47
Meyer, M. R., Edwards, S., Hinkle, K. H., et al. 1998, ApJ, 508, 397
Meynet, G. & Maeder, A. 2000, A&A, 361, 101
Miner, J., Rose, J. A., & Cecil, G. 2011, ApJ, 727, L15
Modigliani, A., Goldoni, P., Royer, F., et al. 2010, SPIE Conference Series

Moehler, S., Modigliani, A., Freudling, W., et al. 2014, A&A, 568A, 9

Morris, P. W., Eenens, P. R. J., Hanson, M. M., et al. 1996, ApJ, 470, 597

Mouhcine, M. & Lançon, A. 2002, A&A, 393, 149

Mouhcine, M. & Lançon, A. 2003, MNRAS, 338, 752

Mouhcine, M., Lançon, A., Leitherer, C., et al. 2002, A&A, 393, 101

Munari, U., Sordo, R., Castelli, F., et al. 2005, A&A, 442, 1127

Nikolaev, S. & Weinberg, M. D. 2000, ApJ, 542, 804

Noll, S., Kausch, W., Barden, M., et al. 2012, A&A, 543, A92

Nowotny, W., Aringer, B., Höfner, S., et al. 2005, A&A, 437, 273

Nowotny, W., Aringer, B., Höfner, S., et al. 2011, A&A, 529, A129

Nowotny, W., Aringer, B., Höfner, S., et al. 2013, A&A, 552, A20

Oke, J. B. 1990, AJ, 99, 1621

Origlia, L., Ferraro, F. R., & Fusi Pecci, F. o. 1997, A&A, 321, 859

Origlia, L., Moorwood, A. F. M., & Oliva, E. 1993, A&A, 280, 536

Oudmaijer, R. D., Waters, L. B. F. M., van der Veen, W. E. C. J., et al. 1995, A&A, 299, 69

Paladini, C., van Belle, G. T., Aringer, B., et al. 2011, A&A, 533, A27

Patat, F., Moehler, S., O'Brien, K., et al. 2011, A&A, 527, A91

Phillips, J. G. 1948, ApJ, 107, 389

Pickles, A. J. 1998, PASP, 110, 863

Pietrinferni, A., Cassisi, S., Salaris, M., et al. 2004, ApJ, 612, 168

Placco, V. M., Kennedy, C. R., Beers, T. C., et al. 2011, AJ, 142, 188

Pojmanski, G. 2002, Acta Astron., 52, 397

Pols, O. R., Tout, C. A., Lattanzio, J. C., et al. 2001, ASPC, 229, 31

Price, S. D., Smith, B. J., Kuchar, T. A., et al. 2010, ApJS, 190, 203

Prugniel, P. & Soubiran, C. 2001, A&A, 369, 1048

Prugniel, P., Soubiran, C., Koleva, M., et al. 2007, 2007astro.ph..3658P

Raimondo, G., Cioni, M.-R. L., Rejkuba, M., et al. 2005, ApJS, 438, 521

Ramirez, S. V., Depoy, D. L., Frogel, J. A., et al. 1997, AJ, 113, 1411

Ranada, A. C., Singh, H. P., & Gupta, R. o. 2007, Bulletin of the Astronomical Society of India, 35, 87

Ranade, A., Gupta, R., Ashok, N. M., et al. 2004, Bulletin of the Astronomical Society of India, 32, 311

Ranade, A. C., Ashok, N. M., Singh, H. P., et al. 2007, Bulletin of the Astronomical Society of India, 35, 359

Rauch, T. 2003, A&A, 403, 709

Rauch, T. & Deetjen, J. L. 2003, in Astronomical Society of the Pacific Conference Series, Vol. 288, Stellar Atmosphere Modeling, ed. I. Hubeny, D. Mihalas, & K. Werner, 103

Rayner, J. T., Cushing, M. C., & Vacca, W. D. 2009, ApJS, 185, 289

Riffel, R., Pastoriza, M. G., Rodríguez-Ardila, A., et al. 2008, MNRAS, 388, 803

Rosenfield, P., Marigo, P., Girardi, L., et al. 2014, ApJ, 790, 22

Rothman, L. S., Gordon, I. E., Barbe, A., et al. 2009, J. Quant. Spec. Radiat. Transf., 110, 533

Salpeter, E. 1955, ApJ, 121, 161

Samus, N. N., Durlevich, O. V., Kazarovets, E. V., et al. 2007-2012, General Catalogue of Variable Stars, VizieR On-line Data Catalog: B/gcvs

Sánchez-Blázquez, P., Peletier, R. F., Jiménez-Vicente, J., et al. 2006, MNRAS, 371, 703

Sanford, R. F. 1944, ApJ, 99, 145

Schaller, G., Schaerer, D., Meynet, G., et al. 1992, A&AS, 96, 269

Schmidt, M. 1959, ApJ, 129, 243

Secchi, A. 1868, MNRAS, 28, 196

Seifahrt, A., Käufl, H. U., Zängl, G., et al. 2010, A&A, 524, A11

Skrutskie, M. F., Cutri, R. M., Stiening, R., et al. 2006, AJ, 131, 1163

Smith, L. J., Norris, R. P. F., & Crowther, P. A. 2002, MNRAS, 337, 1309

Soszyński, I., Udalski, A., Szymański, M. K., et al. 2009, AcA, 59, 239

Soszyński, I., Udalski, A., Szymański, M. K., et al. 2011, AcA, 61, 217

Spiniello, C., Trager, S. C., Koopmans, L. V. E., et al. 2012, ApJ, 753, L32

Subasavage, J. P., Henry, T. J., Bergeron, P., et al. 2007, AJ, 252

Swan, W. 1857, "On the prismatic spectra of the flames of compounds of carbon and hydrogen", Transactions of the Royal Society of Edinburgh 21, 411

Tanaka, W., Hashimoto, O., Nakada, Y., et al. 1990, Publications of the National Astronomical Observatory of Japan, 1, 259

Taylor, B. J. 1984, ApJS, 259

Taylor, E. N., Hopkins, A. M., Baldry, I. K., et al. 2011, MNRAS, 418, 1587

Tej, A., Lançon, A., & Scholz, M. 2003, A&A, 401, 347

Terndrup, D. M., Frogel, J. A., & Whitford, A. E. 1991, ApJ, 378, 742

Vacca, W. D., Cushing, M. C., & Rayner, J. T. 2003, PASP, 115, 389

Valdes, F., Gupta, R., Rose, J. A., et al. 2004, ApJS, 152, 251

van Belle, G., Paladini, C., Aringer, B., et al. 2013, ApJ, 775, 45

van Loon, J. T., Cioni, M.-R. L., Zijlstra, A. A., et al. 2005, A&A, 438, 273

van Loon, J. T., Cohen, M., Oliveira, J. M., et al. 2008, A&A, 487, 1055

Vandenbussche, B., Beintema, D., de Graauw, T., et al. 2002, A&A, 390, 1033

Venkata Raman, V. & Anandarao, B. G. 2008, MNRAS, 385, 1076

Vernet, J., Dekker, H., D'Odorico, S., et al. 2011, A&A, 536, 105

Vernet, J., Kerber, F., Saitta, F., et al. 2008, in Society of Photo-Optical Instrumentation Engineers (SPIE) Conference Series, Vol. 7016, Society of Photo-Optical Instrumentation Engineers (SPIE) Conference Series, 1

Wallace, L. & Hinkle, K. 1996, ApJS, 107, 312

Wallace, L. & Hinkle, K. 1997, ApJS, 111, 445

Wallace, L. & Hinkle, K. 2002, AJ, 124, 3393

Wallace, L., Meyer, M. R., Hinkle, K., et al. 2000, ApJ, 535, 325

Warner, B. 1972, MNRAS, 159, 95

Weiss, A. & Ferguson, J. W. 2009, A&A, 508, 1343

Werner, K., Deetjen, J. L., Dreizler, S., et al. 2003, in Astronomical Society of the Pacific Conference Series, Vol. 288, Stellar Atmosphere Modeling, ed. I. Hubeny, D. Mihalas, & K. Werner, 31

Westera, P., Lejeune, T., & Buser, R. 2002, A&A, 381, 524

Whitelock, P. A., Feast, M. W., Marang, F., et al. 2006, MNRAS, 369, 751

Wing, R. F. 1971, CoKit, 554, 145

Wood, P. R. 2015, MNRAS, 448, 3829

Wood, P. R., Bessell, M. S., & Fox, M. W. 1983, ApJ, 272, 99

Worthey, G., Faber, S. M., & Gonzalez, J. J. 1992, ApJ, 398, 69

Worthey, G., Faber, S. M., Gonzalez, J. J., et al. 1994, ApJS, 94, 687

Worthey, G. & Ottaviani, D. L. 1997, ApJS, 111, 377

Wright, E. L., Eisenhardt, P. R. M., Mainzer, A. K., et al. 2010, AJ, 140, 1868

Zasowski, G., Johnson, J. A., Frinchaboy, P. M., et al. 2013, AJ, 81

Zibetti, S., Gallazzi, A., & Charlot, S. 2013, MNRAS, 428, 1479

Nederlandse samenvatting

⋆ ⋆ ⋆

Sterrenstelsels bestaan uit verschillende componenten: naast miljarden sterren ook uit de restanten van gestorven sterren, interstellair gas, stof en donkere materie. De rode draad in dit proefschrift is het begrijpen van de vorming en evolutie van deze sterrenstelsels. Dit doel willen we bereiken door te kijken naar alle sterren waaruit een sterrenstelsel is opgebouwd. De kleur van een sterrenstelsel is voornamelijk vanwege de aard van de sterren component. Daarom is door het vergelijken van het spectrum van een sterrenstelsel met die van een ster, is het mogelijk om traceerbaarheid van de soort sterren die overheersend binnen een sterrenstelsel. Hiervoor gebruikt men modellen die de spectrale energie distributie (SED, de hoeveelheid energie uitgestraald als een functie van golflengte) van deze sterrenstelsels proberen te reproduceren. Deze modellen worden ook wel sterpopulatie-modellen genoemd. Eén van de belangrijkste onderdelen in een dergelijk model, is de bibliotheek van stellaire spectra die wordt gebruikt. Door een dergelijke bibliotheek te combineren met de resultaten van sterevolutie-modellen (zoals de effectieve temperatuur en de zwaartekracht aan het oppervlak van de ster), kan het spectrum van een sterrenstelsel gemodelleerd worden.

In dit proefschrift hebben we ervoor gekozen om een nieuwe empirische bibliotheek te creëren. Wanneer we kijken naar de bestaande sterbibliotheken, dan kan gesteld worden dat empirische bibliotheken verbeterd kunnen worden op de volgende punten: betere calibratie, meer sterren, een hogere (spectrale) resolutie en een groter bereik van golflengtes. De technologische vooruitgang van de laatste decennia heeft geleid tot de bouw van nieuwe astronomische instrumenten, waaronder de X-shooter spectrograaf. Deze spectrograaf is gemonteerd op één van de vier telescopen van de Very Large Telescope (VLT) van de Europese Zuidelijke Sterrenwacht (ESO, European Southern Observatory) in Chili. Het unieke aan deze spectrograaf is de mogelijkheid om in één waarneming een compleet spectrum te maken van het ultraviolet tot het nabije-infrarood (van 300 tot 2480 nm), met een gemiddeld oplossend vermogen van 10 000.

Gedurende zes semesters hebben we met X-shooter meer dan 700 sterren in verschillende omgevingen (van de schijf van de Melkweg tot de Magelhaense wolken) en met afwisselende chemische samenstellingen waargenomen. Al deze spectra vormen samen de X-shooter bibliotheek (XSL, X-Shooter Spectral Library P.I. S. C. Trager). Figuur 1 geeft een overzicht van alle sterren die deel uitmaken van XSL in een Hertzsprung-Russel diagram. De symbolen stellen de twee fases van onze waarnemingen voor: een pilotfase (de eerste twee semesters) en de algemene fase (de overige vier semesters).

Een groot deel van mijn proefschrift is gewijd aan datareductie, met andere woorden het transformeren van ruwe data naar één-dimensionale spectra die gebruikt kunnen worden voor wetenschappelijke toepassingen. Voor de datareductie hebben we enerzijds gebruikt gemaakt van de software van ESO en anderzijds van software die we zelf hebben ontwikkeld. Eén aspect in het datareductieproces is de berekening van de instrumentele responscurve voordat de fluxcalibratie is toegepast. Dit wordt beschreven in *Hoofdstuk 4*. X-shooter is een instrument dat zich op aarde bevindt, hetgeen tot gevolg heeft dat de waargenomen spectra beïnvloed worden door de aardatmosfeer. Dit is voornamelijk van belang in het nabijeinfrarood, maar in mindere mate ook in het optische golflengtegebied. Figuur 2 geeft een voorbeeld van het nabij-infraroodspectrum van een flux-standaardster. In dit spectrum zijn de delen die beïnvloed zijn door respectievelijk absorptie in de aardatmosfeer en door instrumentele effecten aangegeven in groen en blauw. Aangezien de twee effecten nauw met elkaar verbonden zijn, hebben we een procedure ontwikkeld om met beide effecten tegelijk af te rekenen.

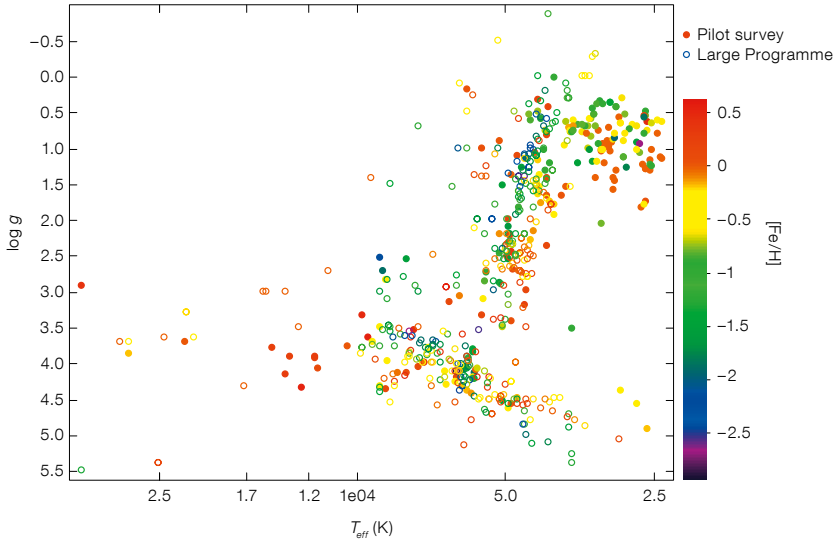

Figure 1: Het Hertzsprung-Russel diagram van XSL sterren, uit Chen et al. (2014b).

De X-shooter bibliotheek is een ambitieus project met uiteindelijke meer dan 700 spectra van sterren. Voor het creëeren van deze spectra zijn bijna 10 000 bestanden gebruikt. Om deze grote hoeveelheid data te verwerken, hebben we een database opgezet, zoals wordt beschreven in *Hoofdstuk 5*. In aanvulling hierop, is er een website in het leven geroepen om onze data voor andere gebruikers beschikbaar te stellen.

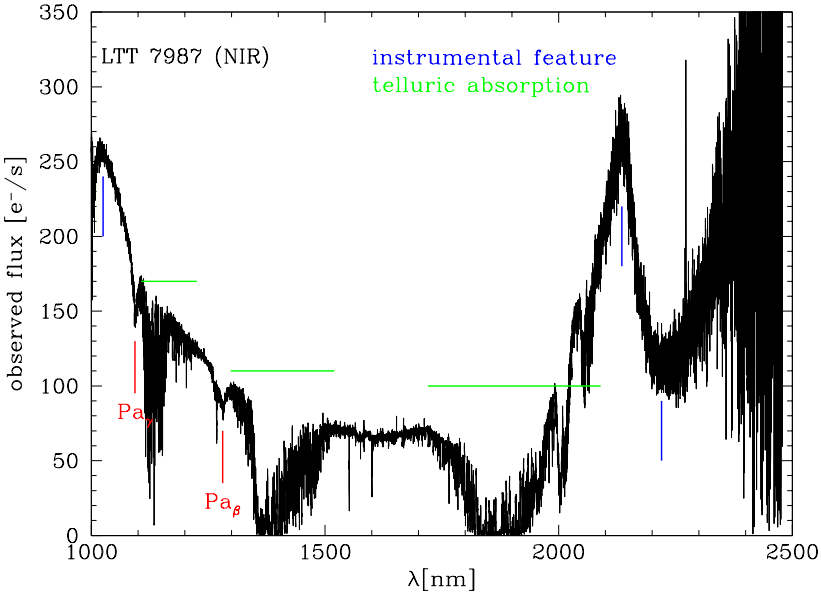

Figure 2: Nabij-infrarood X-shooter spectrum van LTT 7987, uit Moehler et al. (2014).

XSL bevat een significant aantal koele reuzensterren. Dit kunnen zowel sterren van de rode reuzentak (RGB, Red Giant Branch) als van de asymptotische reuzentak (AGB, Asymptotic Giant Branch) zijn. Het opnemen van deze koele reuzensterren in een sterbibliotheek is om twee redenen van belang. Ten eerste hebben deze sterren pulserende atmosferen, waardoor ze periodiek in grootte en lichtkracht variëren. Deze variatie heeft tot gevolg dat twee waarnemingen van dezelfde ster in verschillende golflengtegebieden kan leiden tot verschillende interpretaties wanneer de waarnemingen niet op hetzelfde moment zijn uitgevoerd. Dit veroorzaakt problemen bij het maken van sterpopulatie-modellen. De X-shooter bibliotheek heeft dit probleem echter niet, doordat met X-shooter tegelijkertijd een zeer groot golflengtegebied kan worden waargenomen. Ten tweede is de asymptotische reuzentak een belangrijke fase in de evolutie van sterren, aangezien het voor sterpopulaties met een leeftijd van 1–3 Gjr significant bijdraagt aan de lichtkracht in het nabije-infrarood.

In sterren die zich bevinden op de asymptotische reuzentak vindt kernfusie plaats in twee schillen: de koolstof-zuurstofkern wordt omringd door een schil waarin helium (He) verbrand wordt en een schil waarin waterstof (H) verbrand wordt. Dit is geïllustreerd in Figuur 3. Wanneer de ster verder evolueert op de asymptotische reuzentak, zal de heliumschil op een bepaald moment zonder brandstof komen te zitten. Op dat moment is de energievoorziening van de ster geheel afhankelijk van de verbranding van waterstof. De heliumschil zal op periodieke momenten fel ontbranden waarbij de helium die is geproduceerd door de verbranding van waterstof sinds de laatste fase van heliumverbranding wordt opgebrand.

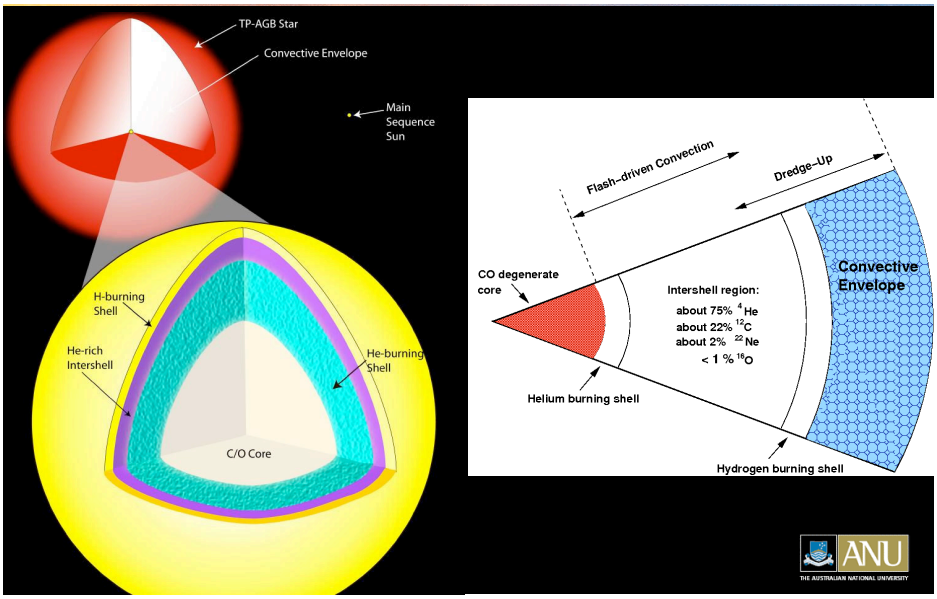

Figure 3: Doorsnede van een thermisch pulserende AGB ster *(van A. Karakas)*.

Dit creëert een convectiezone die zich, gedreven door de flits, kan uitstrekken van de heliumschil tot bijna in de waterstofschil. De verbrandingsproducten van helium (voornamelijk koolstof) zullen hierdoor gemixt worden door de gebieden die zich tussen beide schillen bevinden. Wanneer de flits is uitgedoofd en deze gebieden weer afkoelen, zal de buitenste convectiezone van de ster zich naar binnen verplaatsen voorbij de H/He grens tot in het gebied dat verrijkt is met koolstof. Hierdoor wordt koolstof naar het oppervlak van de ster gebracht, de zogenaamde derde "dredge-up".

De verhouding tussen koolstof en zuurstof (C/O) aan het oppervlak neemt met elke "dredge-up" episode toe. Na een bepaald aantal pulsen kan de ster veranderen van een zuurstofrijke ster (C/O < 1) in een koolstofrijke ster (C/O $>$ 1). Dit betekent dat aan het oppervlak de metaaloxides, zoals TiO en VO, worden vervangen door koolstofmoleculen, zoals CN en C_2.

Hoewel XSL een grote diversiteit aan koele sterren bevat, heb ik in deze thesis de nadruk gelegd op één bepaald type: koolstofsterren. Voordat XSL beschikbaar kwam, was er slecht een kleine verzameling spectra beschikbaar om de diversiteit in koolstofsterren te representeren.

Dankzij XSL hebben we het beschikbare aantal spectra van koolstofsterren in het optische en nabij-infrarode golflengtegebied verdubbeld, zoals beschreven in *Hoofdstuk 2*. De koolstofsterren in XSL zijn zowel sterren uit de Melkweg als uit de Magelhaense wolken. Figuur 4 geeft een aantal voorbeelden van spectra van koolstofsterren in XSL.

De meest opvallende eigenschap van de koolstofsterren in XSL is de bimodale verdeling wanneer $(J - K)$ groter is dan 1.6. Naast de "klassieke" koolstofsterren

blijkt er dan nog een andere familie van spectra te zijn. Deze worden gekenmerkt door een absorptiegebied rond 1.53 μm en een egaler uiterlijk. Een voorbeeld van de twee soorten spectra is te zien wanneer we de twee oranje spectra in Figuur 4 met elkaar vergelijken.

We hebben onze waargenomen spectra vergeleken met modellen om de oorzaak van deze bimodale verdeling te achterhalen en om de fundamentele eigenschappen van onze sterren (zoals temperatuur en metalliciteit) te bepalen. De vergelijking tussen onze spectra en de modellen is daarnaast ook bedoeld ter controle en verbetering van de modellen. Bij het maken van deze vergelijking maken we gebruik van state-of-the-art koolstofrijke hydrostatische modellen. Deze modellen houden echter geen rekening met de effecten van stof en het pulsatiefenomeen. Bij het corrigeren voor de effecten van extinctie hebben we geen standaard extinctiewet gebruikt maar gebruik gemaakt van een polynoom. Dit stelt ons in staat om rekening te houden met de fouten en onzekerheden die inherent zijn aan de fluxcalibratie.

Voor redelijk blauwe koolstofsterren met spectra van gemiddelde resolutie vinden we een goede overeenkomst tussen de modellen en de observaties. In het algemeen komen de fundamentele eigenschappen die zijn afgeleid voor het optische spectrum overeen met de eigenschappen die zijn afgeleid voor het nabije-infrarood. Echter, de onzekerheden voor de geschatte temperaturen blijven hoog (meer dan 100 K) ten gevolge van ontaarding tussen parameters.

Zoals verwacht, werken de hydrostatische modellen niet voor de meest rode sterren. Des te roder een ster is, des te sterker wordt de spectrale energiedistributie beïnvloed door het pulsatie-effect en het effect van circumstellair materiaal. Deze effecten zijn dan ook niet met een simpele extinctiewet te reproduceren. De volgende stap voor deze objecten is dan ook een vergelijking met dynamische modellen.

~ ~ ~ ~ ~

In dit proefschrift hebben we de X-shooter Spectral Library en de hiervoor benodigde ondersteunende software ontwikkeld. In onze analyse hebben we ons gefocust op één bepaald spectraaltype: koolstofsterren. Door het beperkte aantal koolstofsterren dat tot dusver was opgenomen in stellaire bibliotheken, was het niet mogelijk om hun grote verscheidenheid te modelleren in sterpopulatie-modellen. Met XSL gaan we een stap verder: deze verzameling van koolstofsterren breidt niet alleen de voorgaande uit, maar toont zelfs de diversiteit van deze objecten. Als eerste stap hebben we onze observaties vergeleken met hydrostatische modellen. In een volgende stap zal een overstap moeten worden gemaakt naar dynamische modellen die de eigenschappen van de pulsaties van deze sterren meenemen in hun berekening. Voorlopig adviseren we gebruikers om de spectra van onze koolstofsterren te middelen voor het gebruik in sterpopulatie-modellen en geen individuele spectra te gebruiken. De X-shooter bibliotheek staat vol met sterren van verschillende spectrale types. Meer studies zoals gedaan in dit proefschrift zijn nodig om ons begrip van sterrenstelsels verder te vergroten.

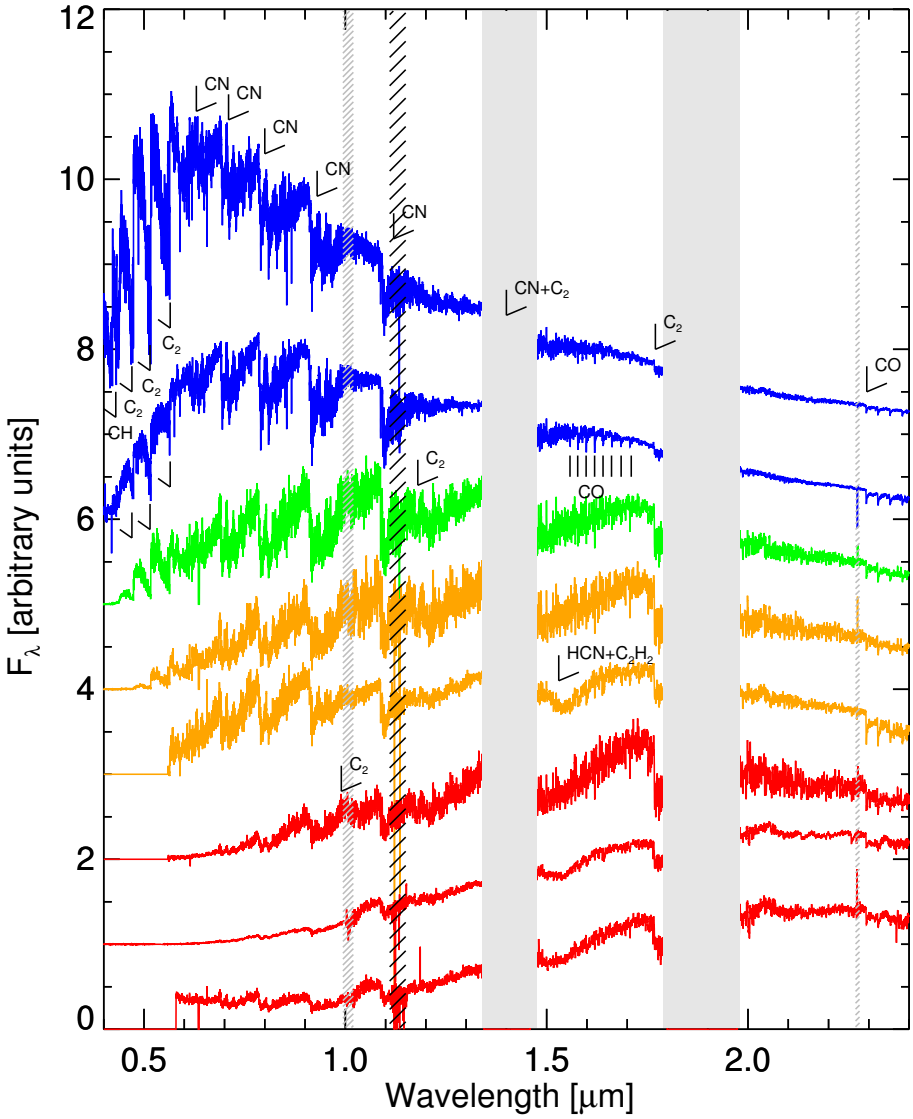

Figure 4: Representatieve spectra voor een selectie van koolstofsterren, uit Gonneau et al. (2015)

English summary

⋆ ⋆ ⋆

The leitmotiv for this thesis has been the understanding of the formation and the evolution of galaxies. To contribute pieces of the puzzle, we tackled this issue from a different point of view: we looked at all the stars that form a galaxy. To be sure, a galaxy is more than just billions of gravitationally-bound stars. It also consists of stellar remnants, interstellar gas and dust, and dark matter. The color of a galaxy is mainly due to the type of stars that compose the galaxy. Therefore, by comparing the spectrum of a galaxy with that of a star, it is possible to trace back the type of stars that prevalent within a galaxy. Recipes are used to model the spectral energy distribution (SED) of galaxies. We call this approach stellar population synthesis (SPS). The key ingredient, according to my – biased – point of view, is a set of libraries of stellar spectra. These libraries, either theoretical or empirical, are used to convert the outputs of stellar evolution calculations, such as surface gravity, effective temperature, into observable SEDs.

In this thesis, we chose to create a new empirical library. Besides the large number of existing libraries, empirical stellar libraries need improvements on the following points: better calibrations, more stars, higher spectral resolution and broader wavelength coverage. The technical progress made over the last decades leads to the emergence of new instruments, including the X-shooter spectrograph. This spectrograph, property of ESO (European Southern Observatory) and mounted at the Very Large Telescope (VLT) in Chile, offers the unique capability to produce in one shot a full spectrum from the ultra-violet wavelength range to the near-infrared (from 300 to 2480 nm), at a mean resolving power of 10 000.

During six semesters, we observed with X-shooter more than 700 stars from a variety of environments (from the nearby disc of the Milky Way to the Magellanic Clouds), with a variety of chemical compositions. All these stars are part of the X-shooter Spectral Library (XSL, P.I. S. C. Trager). Figure 5 shows an overview of our sample in a Hertzsprung-Russell diagram. The symbols represent the two phases of our survey: a Pilot survey (two first semesters) and the Large Programme (four semesters).

A large part of my thesis was devoted to the data reduction, in other words transfor-ming the raw data into final one-dimensional spectra, ready for science application. To do so, we combined the tools provided by ESO with procedures of our own. One aspect of the data reduction process is shown in *Chapter 4*. This concerns the computation of the instrumental response curve, prior to the flux calibration. X-shooter is a ground-based instrument, consequently, the spectra are affected by the Earth's atmosphere (also called telluric features). This is mainly seen in the near-infrared wavelength range, and to a lesser extent in the visible. Figure 6 shows an example of a near-infrared spectrum of a flux standard star, and the parts of the spectrum affected by the telluric absorption (in green) and

the instrumental features (in blue). Because of the intimate relation between these two effects, a procedure was developed to deal with both aspects at the same time.

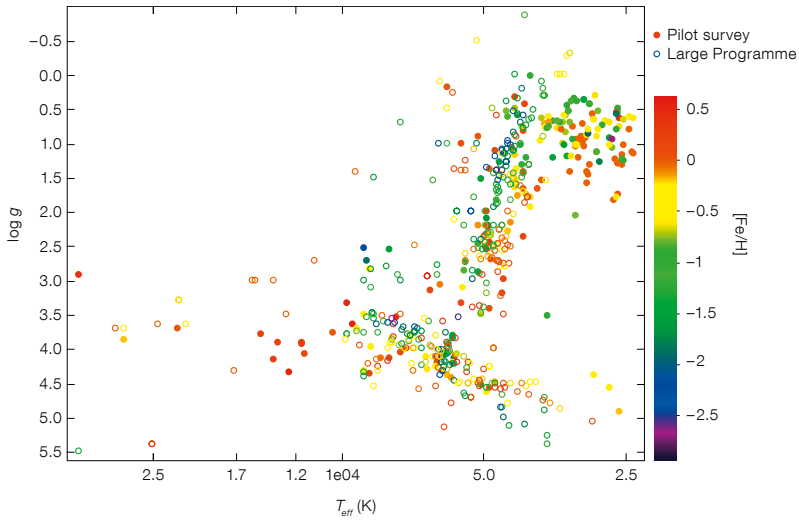

Figure 5: The Hertzsprung-Russell diagram of XSL stars, taken from Chen et al. (2014b).

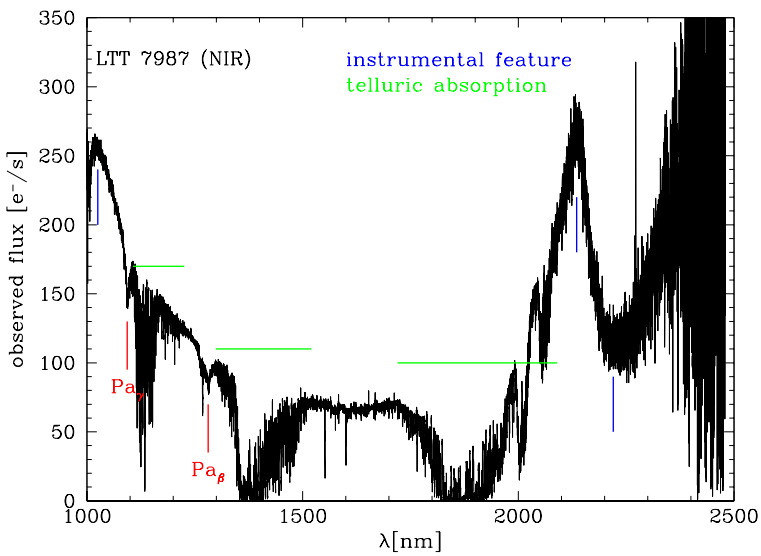

Figure 6: Near-infrared X-shooter spectrum of LTT 7987, taken from Moehler et al. (2014).

The X-shooter Spectral Library is an ambitious project with more than 700 (final) spectra of stars, which represents almost 10000 raw files. To deal with such an amount of data, a database was created, as described in *Chapter 5*. Furthermore, a dedicated website was created to release our data to the community.

A significant part of the stars within XSL are cool giants, either from the red giant branch (RGB) or the asymptotic giant branch (AGB). This is of course not a coincidence. Indeed, these stars have pulsating atmospheres, meaning that the stars actually increase and decrease in size periodically, which leads to changes in the brightness of the stars. This variability implies that two observations of the same star one in the optical wavelength range and the other in the near-infrared might give different results, if the times of observation are different. This issue will affect the construction of stellar population models. Thankfully with X-shooter, simultaneous observations over a broad wavelength range are now available. Furthermore, the (thermally pulsing) AGB is an important phase as stars at this stage are significant contributors to the near-infrared light of intermediate age stellar populations (1–3 Gyr).

Stars on the AGB have a double-shell burning structure: the carbon-oxygen core is surrounding by a helium (He) burning shell and a further hydrogen (H) burning shell, as shown in Figure 7. As the star evolves on the AGB, the helium shell runs out of fuel, and the star derives its energy from fusion of hydrogen. Periodically, the helium burning shell ignites violently (usually refers as helium shell flash or thermal pulse) and burns up the helium produced by the hydrogen shell since the last phase of helium activity. This creates a flash-driven convection zone which extends from the He shell almost up the H burning shell. Therefore, the products of helium burning (mainly carbon) are mixed throughout the intershell region. As the flash dies down, the energy deposited in the intershell causes the outer layers to expand and cool, and the H-burning shell is temporarily extinguished. The base of the convective envelope reaches inward and can penetrate beyond the H/He interface and into the region enriched in carbon. Carbon can thus be mixed to the surface, in the so-called "third dredge-up".

With each dredge-up episode, the surface ratio of carbon over oxygen (C/O) increases. After a certain number of pulses, it may exceed unity and the star will then evolve from an oxygen-rich star (C/O < 1) to a carbon-rich star (C/O > 1). This means a change in the surface envelope: the oxides, such as TiO, VO, are replaced by carbon molecules, such as CN and C_2.

Neglecting the diversity of stars available in XSL, I focused during this thesis on one type of cool stars: carbon stars. Prior to XSL, only small collections of C-star spectra existed to represent their diversity.

Thanks to XSL, we doubled the number of carbon star spectra available across the optical and near-infrared spectral range, as shown in *Chapter 2*. Our sample includes stars from the Milky Way and the Magellanic Clouds. Some representative spectra of our sample are displayed in Figure 8.

The main characteristic of our sample is the bimodal behaviour of our stars when $(J - K)$ is larger than 1.6. At a given near-infrared color, in addition to the "classical" carbon stars, another family of spectra emerge, characterized by the presence of an absorption feature at 1.53 μm and a smoother appearance.

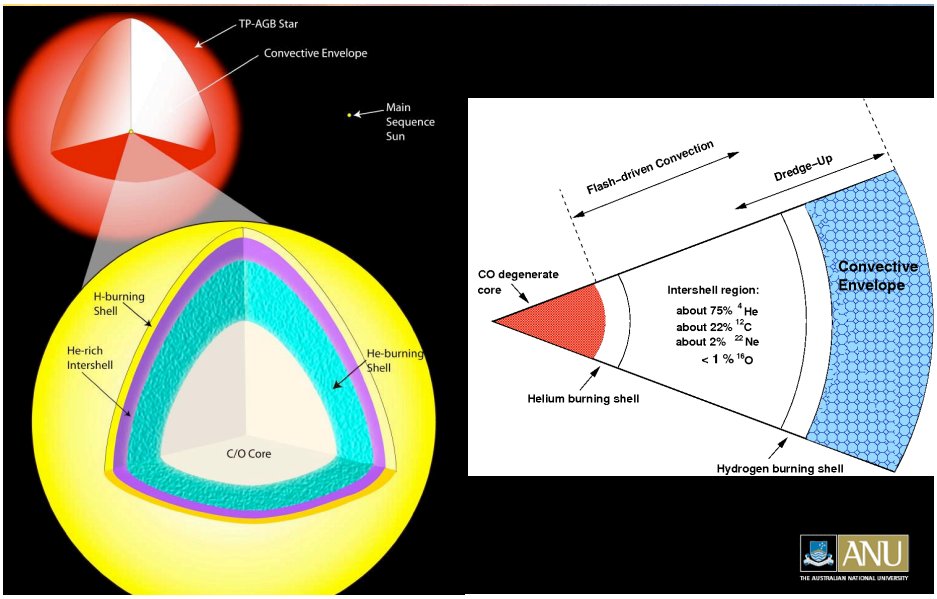

Figure 7: Inside view of a thermally pulsing AGB star *(credit A. Karakas)*.

An example of such behaviour is seen when comparing the two orange spectra from Fig. 8.

To investigate the culprits of this behaviour, and to determine the fundamental parameters of our stars (such as the temperature, the metalliticity), we compared our observed spectra with models. This analysis is summarized in *Chapter 3*. This comparison also aimed at validating and improving the models. We used state-of-the-art hydrostatic carbon-rich models, which means that the pulsation phenomenon and the dust effects are not part of the models. To redden our models, we did not use a standard extinction law, but we chose a polynomial correction, which takes into account the errors related to the flux calibration.

For rather blue carbon stars, we found good fits at intermediate resolution. Overall, the values of the fundamental parameters found in the visible and the near-infrared agree. However, the uncertainties for the estimated temperatures remain still high (more than 100 K) because of degeneracy between the parameters.

For the reddest stars, the hydrostatic models are not good anymore, which is expected. Indeed, those stars are more and more affected by the pulsation effect and by the effects of circumstellar material on the energy distribution (that a simple extinction law cannot reproduce). For those objects, the next step will be to compare them with dynamical models.

~ ~ ~ ~ ~

In this thesis, we have developed the X-shooter Spectral Library and some backstage processes. We have focused our analysis on one spectral type, the carbon stars. Until now, the small number of carbon stars in stellar libraries prevented the reproduction of their diversity in stellar population synthesis. With XSL, we go a step further: this collection extends the previous ones and even shows diversity. A comparison with hydrostatic carbon-rich models was done as a first pass, and the next step is now to turn to dynamical models, which take into account the pulsation properties. For now, we advise users to average our C-star spectra instead of using individual ones for stellar population synthesis applications. The X-shooter Spectral Library is full of stars from various spectral types, and more analysis like that in this thesis need to be done, before reaching for the galaxies.

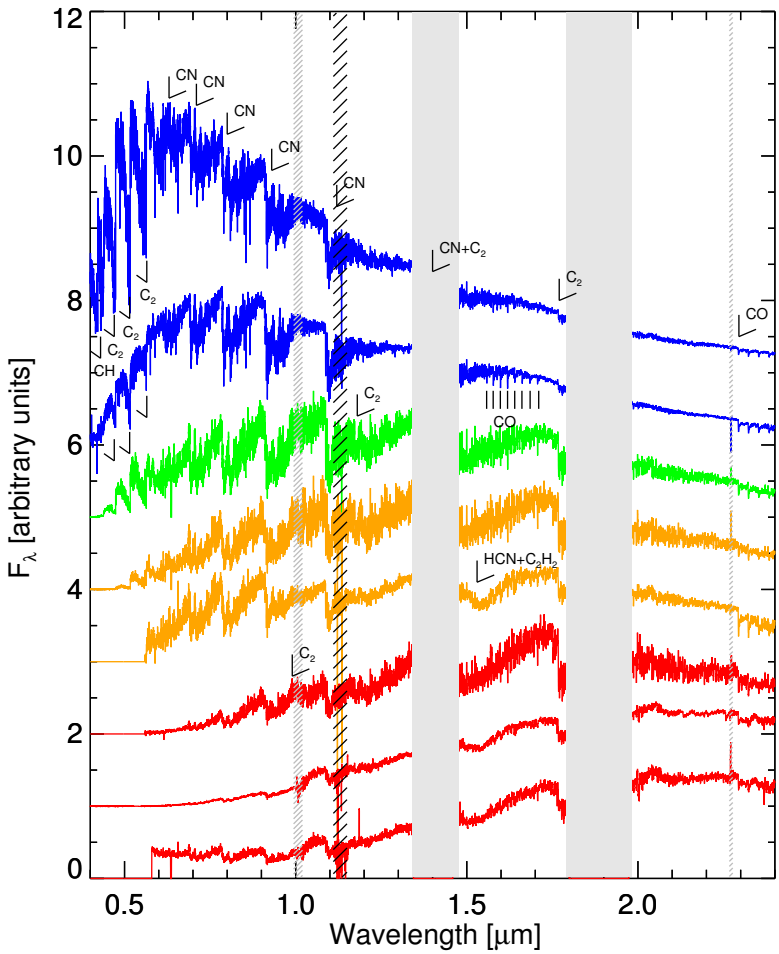

Figure 8: Representative spectra from our sample of carbon stars, from Gonneau et al. (2015).

Résumé

⋆ ⋆ ⋆

Le leitmotiv de cette thèse a été de comprendre la formation et l'évolution des galaxies. Pour apporter des éléments de réponse, nous avons choisi de nous intéresser aux étoiles qui constituent une galaxie plutôt que d'étudier cette dernière dans son ensemble. Bien évidemment, une galaxie ne se résume pas à des milliards d'étoiles liées gravitationnellement. Elle se compose aussi de vestiges stellaires, de gaz, de poussière et de matière noire. La couleur d'une galaxie est essentiellement dûe aux types d'étoiles la composant. Ainsi, en comparant le spectre d'une galaxie à celui d'une étoile, il est possible de trouver le type d'étoile qui la compose majoritairement. Pour modéliser des spectres de distribution d'énergie (en anglais SED, pour Spectral Energy Distribution) de galaxies, on utilise une approche intitulée la synthèse de populations stellaires (SPS). L'élément clé de cette méthode est, selon moi, la collection de bibliothèques de spectres d'étoiles. Ces bibliothèques, qu'elles soient théoriques ou empiriques, vont servir à convertir les produits dérivés de l'évolution stellaire, tels la gravité de surface ou la température effective, en spectres observables.

Dans cette thèse, nous avons choisi de créer une nouvelle bibliothèque empirique. Certes un grand nombre de bibiothèques empiriques existent déjà, mais les améliorations suivantes doivent y être apportées: une meilleure calibration, un plus grand nombre d'étoiles, une plus grande résolution spectrale et une couverture plus grande en terme de longueur d'onde. Les progrès techniques de ces dernières années ont permis l'avènement de nouveaux instruments tel le spectrographe X-shooter. Ce spectrographe, propriété de l'Observatoire Européen Austral (ESO, pour European Southern Observatory) et installé sur le site du Très Grand Telescope au Chili, est le seul à pouvoir produire un spectre simultané de l'ultra-violet à l'infra-rouge proche (de 300 à 2480 nm), pour une résolution moyenne de 10 000.

Pendant six semestres, nous avons observé avec X-shooter plus de 700 étoiles, provenant d'environnements variés (du disque proche de la Voie Lactée aux Nuages de Magellan), et avec des compositions chimiques variées. Toutes ces étoiles font partie de la Bibliothèque Spectrale X-shooter (XSL, pour X-shooter Spectral Library, dont le chef de projet est S. C. Trager). Une vue d'ensemble de notre échantillon d'étoiles est présentée dans la Figure 9. Les symboles correspondent aux deux phases de notre relevé: l'enquête pilote (les deux premiers semestres) et le Large Programme (quatre semestres).

J'ai consacré une grande partie de ma thèse à faire de la réduction de données, c'est-à-dire à transformer les données brutes en spectres finaux, que l'on peut utiliser ensuite pour une étude scientifique. Pour ce faire, nous avons combiné les outils développés par l'ESO et nos propres procédures. Un aspect de la réduction de données est présenté dans le *Chapitre 4*.

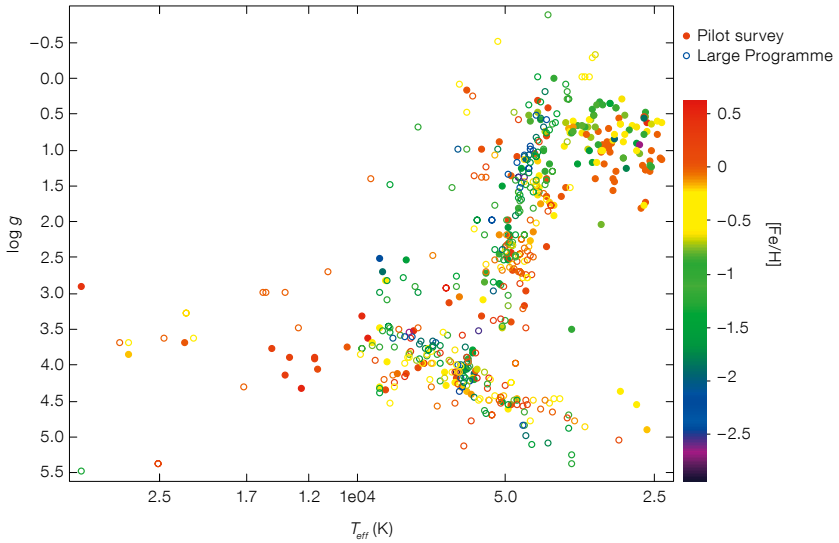

Figure 9: Représentation des étoiles de XSL dans un diagramme de type Hertzsprung-Russel (Chen et al. 2014b).

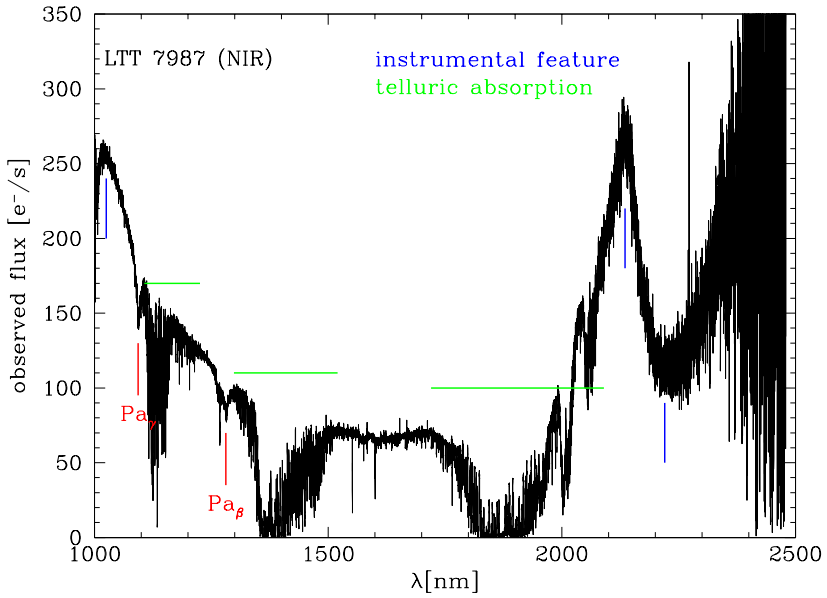

Figure 10: Spectre X-shooter de LTT 7987 dans l'infra-rouge proche (Moehler et al. 2014).

Il s'agit du calcul des courbes de réponse instrumentale, nécessaire pour pouvoir réaliser la calibration en flux. X-shooter étant un instrument basé au sol, nos spectres sont donc affectés par l'atmosphère terrestre. On parle alors de composantes spectrales d'absorption telluriques, ou plus simplement de telluriques. Cela affecte principalement l'infra-rouge proche, et dans une moindre mesure le domaine de longueur d'onde du visible. La Figure 10 montre le spectre d'une étoile standard spectro-photométrique dans l'infra-rouge proche, et les régions affectées par l'absorption tellurique (en vert) et les aspects instrumentaux (en bleu). Les liens étroits qui unissent ces deux aspects nous ont amené à développer une procédure les prenant en compte simultanément.

La bibliothèque spectrale XSL est un projet ambitieux qui nous a permis d'obtenir au final plus de 700 spectres d'étoiles, ce qui représente pas moins de 10000 fichiers bruts. Afin de gérer ce volume de données, nous avons créé une base de données privée. Un accès public est toutefois fourni par le biais d'un site Web (*Chapitre 5*).

Une grande partie des étoiles de XSL sont des géantes froides, de la branche des géantes rouges (Red Giant Branch, RGB) ou de la branche asymptotique des géantes (Asymptotic Giant Branch, AGB). Ce n'est bien sûr pas une coïncidence. En effet, ces étoiles ont des atmosphères pulsantes, ce qui signifie que la taille de ces étoiles va augmenter et diminuer de façon périodique, entraînant un changement de luminosité de l'étoile. Cette variabilité implique que deux observations de la même étoile faites sur deux domaines de longueur d'onde différents, l'une dans l'optique et l'autre dans l'infra-rouge proche, peuvent donner lieu à des interprétations différentes, si les moments d'observation diffèrent. Evidemment, cela pose de sérieux problèmes lorsque l'on construit des modèles de populations stellaires. Fort heureusement, X-shooter permet d'obtenir des observations simultanées sur des grands domaines de longueur d'onde. Outre ces aspects, les étoiles de l'AGB contribuent de façon significative à la lumière infra-rouge proche des populations stellaires d'âge intermédiaire (1–3 milliards d'années).

Dans les étoiles de la branche asympotique, deux couches de fusion coexistent, comme décrit sur la Figure 11. Le coeur de carbone-oxygène est entouré d'une première couche d'hélium (He) en fusion nucléaire, et d'une couche plus lointaine d'hydrogène (H) en fusion. A mesure que l'étoile évolue sur la branche asympotique, la couche d'hélium vient à manquer de combustible, et l'étoile tire son énergie de la fusion de l'hydrogène. Périodiquement, la couche d'hélium s'enflamme violemment (on parle de flash d'hélium ou de pulsation thermique), brûlant l'hélium qui a été produit par la couche d'hydrogène depuis la dernière phase d'activité de l'hélium. Cela crée une zone de convection qui s'étend de la couche d'He à la couche d'H. Ainsi, les produits de la combustion de l'hélium (principalement du carbone) se retrouvent mixés dans toute la région entre les deux couches. Alors que le flash diminue en intensité, l'énergie accumulée dans la région entre les deux couches pousse les couches extérieures de l'étoile à se propager vers l'extérieur et à se refroidir: la couche d'hydrogène va donc temporairement s'éteindre. La base de l'enveloppe convective pénètre au-delà de l'interface H/He et atteint la région enrichie en carbone. Ce processus, que l'on appelle le troisième "dredge-up", permet ainsi de ramener du carbone en surface.

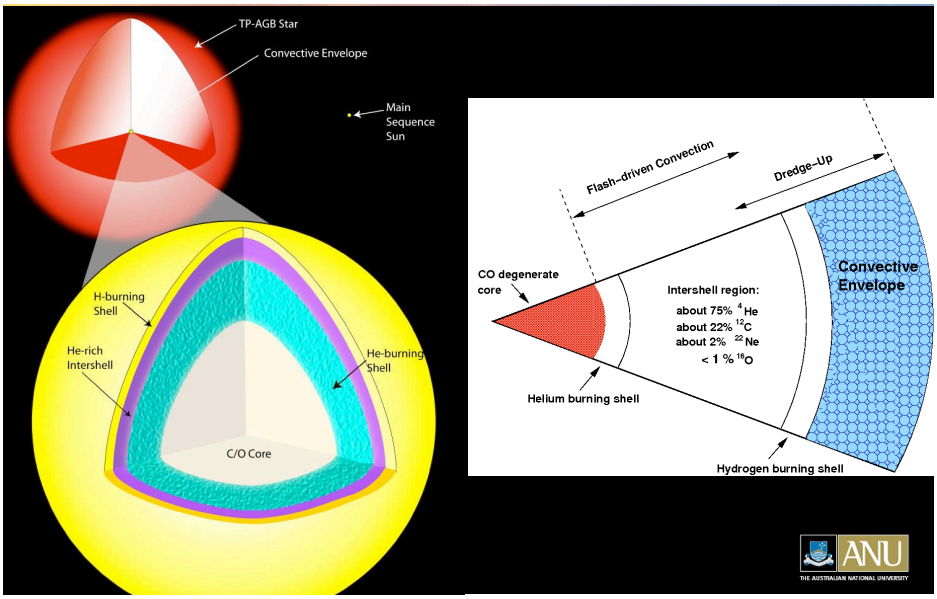

Figure 11: Vue interne d'une étoile de la branche asymptotique des géantes *(crédit A. Karakas)*.

A chaque épisode de "dredge-up", la proportion de carbone par rapport à l'oxygène (C/O) en surface augmente. Après un certain nombre de pulses, ce rapport excède 1, et l'étoile, auparavant oxygénée, devient une étoile carbonée. Cela se traduit par un changement d'enveloppe de surface: les oxides, tels TiO, VO, ont été remplacés par des molécules de carbone, tels CN et C_2.

Parmi tous les types spectraux que compte XSL, je me suis concentrée, dans le cadre de cette thèse, sur les étoiles froides, à savoir les étoiles carbonées. Avant XSL, peu de bibliothèques stellaires contenaient des spectres d'étoiles carbonées, limitant de fait la représentation de leur diversité.

XSL nous a permis de doubler le nombre de spectres d'étoiles carbonées sur les domaines de longueur d'onde de l'optique et de l'infra-rouge proche, comme décrit dans le *Chapitre 2*. Notre échantillon inclut des étoiles de la Voie Lactée et des Nuages de Magellan. La Figure 12 montre des spectres représentatifs de notre collection. La caractéristique principale de notre échantillon est le caractère bimodal de nos étoiles, lorsque l'on s'intéresse à des étoiles qui ont une couleur $(J - K) > 1.6$. Lorsque l'on se place à une couleur infra-rouge proche donnée, en plus des étoiles carbonées classiques, on distingue une autre famille de spectres, caractérisée par la présence d'une bande d'absorption à $1.53\,\mu$m et un spectre à l'apparence plus lissée. On retrouve un exemple de cette dualité en comparant les deux spectres oranges de la Fig. 12.

Afin de comprendre les raisons d'un tel comportement et pour déterminer les paramè-tres fondamentaux de nos étoiles (tels la température, la métallicité), nous avons comparé nos spectres observés avec des modèles. Cette analyse est ré-

sumée dans le *Chapitre 3*. Cette comparaison doit aussi permettre de valider et d'améliorer les modèles. Nous avons utilisé pour cela des modèles d'étoiles carbonées hydrostatiques, ce qui signifie que les phénomènes de pulsation et les effets de poussière ne malheureusement sont pas pris en compte. Pour rougir nos modèles, nous avons choisi de ne pas utiliser une loi d'extinction standard, mais plutôt une correction polynomiale, qui nous permet d'absorber les erreurs liées à la calibration en flux.

Pour des étoiles carbonées relativement bleues, nous obtenons de bons ajustements à moyenne résolution. Dans l'ensemble, les valeurs des paramètres fondamentaux estimés à partir du visible s'accordent avec celles trouvées pour l'infrarouge proche. Cependant, les erreurs que l'on trouve sur les températures restent importantes (plus de 100 K), à cause de dégénérescences entre les paramètres.

Pour les étoiles les plus rouges, comme attendu, les modèles hydrostatiques ne suffisent plus. En effet, ces étoiles sont de plus en plus affectées par les effets de pulsation et les effets de la poussière circumstellaire. Pour ces objets, la prochaine étape est de les comparer à des modèles dynamiques.

~ ~ ~ ~ ~

Cette thèse nous a permis de présenter la bibliothèque spectrale X-shooter (XSL) et quelques aspects de la réduction de données. Nous avons concentré notre analyse sur un type spectral particulier, à savoir les étoiles carbonées. Jusqu'à présent, le faible nombre de bibliothèques stellaires contenant des étoiles carbonées ne permettait pas de reproduire leur diversité dans les modèles de populations stellaires. XSL nous permet de faire un pas en avant car cette collection accroît les précédentes et présente même une diversité. Une première comparaison avec des modèles hydrostatiques d'étoiles carbonées a été réalisée. La prochaine étape est de se tourner vers les modèles dynamiques qui prennent en compte les propriétés de pulsation. Pour le moment, il est mieux de moyenner nos spectres de carbonées plutôt que de les utiliser individuellement pour les applications liées à la synthèse de population. XSL regorge d'étoiles de types spectraux variés, et des analyses du même type que celle menée dans cette thèse devront être faites avant de cerner la formation et l'évolution des galaxies.

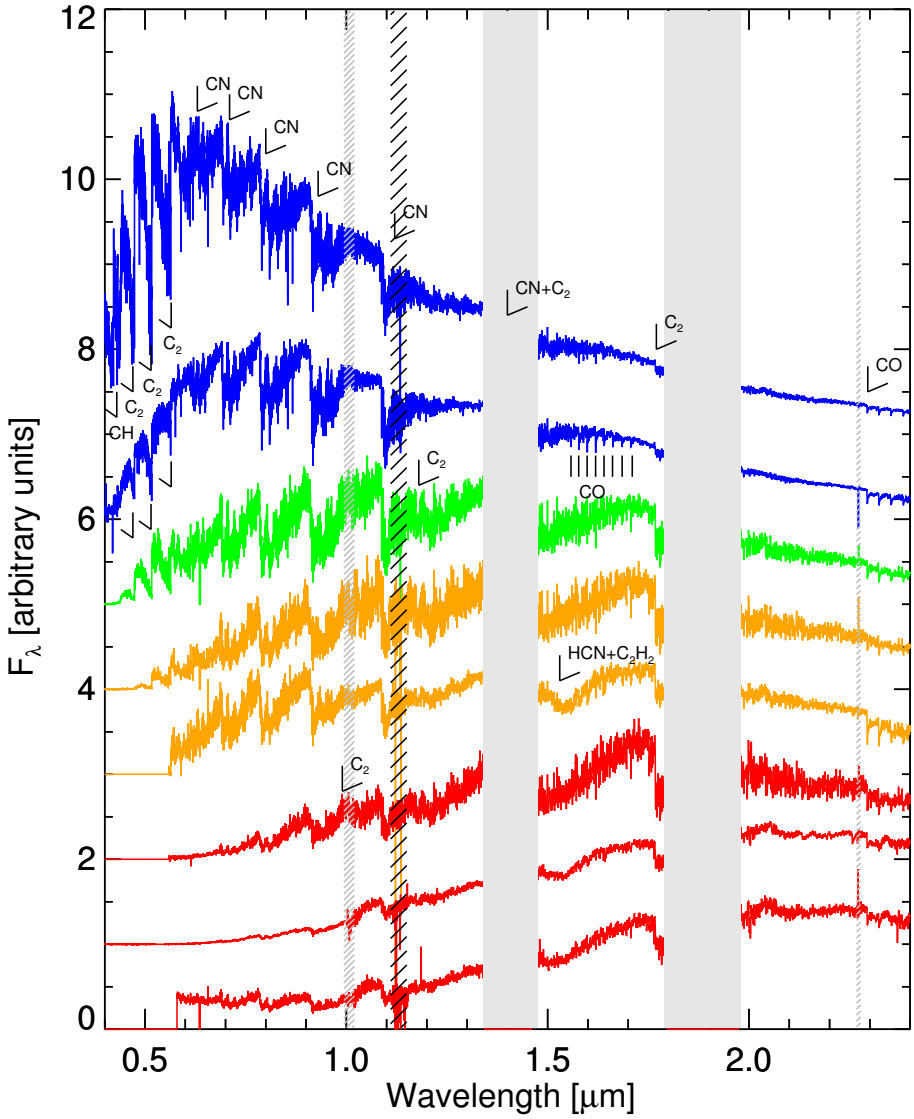

Figure 12: Spectres représentatifs de notre échantillon d'étoiles carbonées (Gonneau et al. 2015).

Acknowledgements / Remerciements

⋆ ⋆ ⋆

Yes. I dit it. I finally completed what I started four years ago. Over the last months (or years ?), it has always been about me, myself and I. Through the following pages, I would like to thank all the people that supported me over the years, and also to apologize for not paying enough attention about their lives. Of course, the following list is not exhaustive, and I will try to keep it short.

~ ~ ~ ~ ~

First of all, a thesis it is not only a subject, deadlines, posters, or trips all over the world (not Hawaï again), it is mostly a relationship with your supervisors. I have been lucky enough to do this thesis with *Ariane and Scott*. Their different personalities contribute to the success of this thesis. Thank you both for everything, and among other things for helping me to grow up and to become a collaborator and not anymore a student.

~ ~ ~ ~ ~

I am grateful to *my reading committee:* Prof. dr. P. Barthel, dr. N. Martin, Prof. dr. J. Th. van Loon and Prof. dr. A. Zijlstra. Thank you for your useful comments, which contributed to improve the quality of this manuscript.

~ ~ ~ ~ ~

As a sandwich PhD student, I spent one year in Groningen, and I became officially a Kapteyner :) The friendly atmosphere that prevails help to make this institute a place to be once in your life. I also really enjoyed all the celebrations with cakes for birthdays, births, projects granted. Thank you my colleagues and friends for this (too short) year.

Reynier, I really enjoyed our collaboration in Groningen and your enthusiasm in the project. I look forward to continue it. Thank you so much.

My dear officemates – Fabian, Sander, Yanan and Nadine –, I could not dream of better officemates before coming to Groningen. I really enjoyed the time we spent together during this year. You tolerated me during the last months of my thesis and we all know that it was not the most peaceful period of my life. Thank you so much. I look forward for your visit in Tenerife. *Fabian*, it was super-duper to meet you :) *Sander*, thank you for your positive attitude, and also for dealing

with my Dutch-related issues. *Yanan*, thank you for being my BOMmen partner ;) *Nadine*, I am glad that you became part of this office. *Myriam*, thank you for all the delicious cakes that you made. I look forward for our next conversation in French.

Judith, Gerjon, Mariya, Matthijs and Wouter, thank you for the stimulating discussions during our group meetings and not only.

Matthijs, thank you (among other things) for reviewing my Dutch summary.

Mariya. As soon as I learnt that you were joining the team, I was looking forward to work with you. And I haven't changed my mind. Thank you for your support and for pushing me sometimes.

Yunhee, I am sorry that we were both too busy finishing our papers / our thesis to be able to spend more time together. I really appreciate the moments we spent together, and especially when we prepared the cake and the decoration for the baking contest. Watching you playing with the train was one of the best moment. Good luck for your new life in Korea.

Sofia, from the time we spent in your office to the diners we had downtown, it has always been a good time. Thank you for your friendship. I wish to Thomas and you all the best for your future.

Niels, thank you for the pleasant conversations we had. You have got a lovely family. I wish you all the best. *Johan*, you are a great singer and I really enjoyed your concerts. Good luck for your new career.

Harish, without you this manuscript won't exist. Thank you for providing me with this latex template.

Among the Kapteyners, I will like to thank particularly *Zheng, Tjitske, Stéphanie, Jorien, Iwona, Asa, Ajinkya* for the nice conversations.

An institute without a good secretariat and a computer group is nothing. Luckily for us, *Christa, Gineke, Hennie, Lucia and Martine* are solving all our (administrative) issues, and *Wim* was also always available to solve my issues with Huygens. Thank you all :)

Yanping, you used to be a Kapteyner, when I was still in Strasbourg. Thank you for sharing all your expertise with me.

I would like also to thank *Scott & Kate & Catriona* for the nice dinners we shared.

~ ~ ~ ~ ~

I am grateful to *Sabine Moehler.* I enjoyed our collaboration about the tellurics correction. Thank you also for providing me with the tex file of your paper.

I also thank the members of *the XSL collaboration.* I look forward to collaborate with you in the future.

Hendrick and Avon, I was really looking forward to meet you. I really enjoyed the conversations we had either about science or other topics. You are definitely a "must do" on my list every time I come to Heidelberg.

J'ai effectué trois de mes quatre années de thèse à l'Observatoire de Strasbourg, et je voudrais par la présente tous et toutes vous remercier. Malheureusement ma soutenance de thèse se fera loin de Strasbourg, mais cela n'est que partie remise avant de célébrer cela avec vous.

Comme dit précédemment, ces derniers mois (dernières années) ont rimé avec "moi je". Merci aux doctorants qui m'ont supporté (dans tous les sens du terme) malgré tout: *Carole, Fréd, John, Julie, François, JB, Julien, Maxime, Nicolas, Ben, Emnanuelle.* Et bienvenue aux nouveaux: *Jérémy, Mathieu, Nicolas, Guillaume.*

Nicolas M., j'ai eu la chance de partager ton (notre :P) bureau. Merci pour ton soutien et ton écoute, nos conversations scientifiques (et pas seulement) me manquent.

Mark, Rémy et Jonathan, merci à vous pour les soirées / week-ends que vous avez dû sacrifier pour que ma thèse avance. Vous êtes évidemment les bienvenus à la Réunion.

On ne le dit pas souvent, donc j'en profite pour dire merci aussi aux documentalistes qui font un travail de titans.

Sans citer tout le monde, je voudrais tout particulièrement remercier *Hervé, Françoise, Rodrigo, Benoît, Christian, Cécile, Evelyne, Patricia, Mireille, Philippe.*

Merci aussi à *Caroline*, pour ta bonne humeur et aussi pour nous avoir permis de continuer à perprétrer la tradition sacrée des mots croisés du midi.

Sans un bon secrétariat et service informatique, un institut n'est rien. Merci donc à *Sandrine, Véronique, Thomas et Jean-Yves*, pour nous simplifier la vie. Merci aussi à l'équipe logistique *Geoffrey et Jean-Luc.*

~ ~ ~ ~ ~

Merci aussi à la petite bande (qui s'agrandit tout doucement): *FX, Elisa, Matteo, Fabien, Brice, Cyril, Aurélie, Olive, Alex, et Cyrielle.* Ca me manque de pouvoir jouer avec vous à Shadow hunters (bien souvent renommé "Tapes FX!").

~ ~ ~ ~ ~

Sandra, nos conversations à la scol', on fait place à des conversations au Bureau pour notre plus grand bonheur à toutes les deux. Merci pour ton soutien au cours de ces années et pardonne moi mon manque de temps.

Claire, on s'est rencontré lors d'un covoiturage, et au bout d'une heure on parlait déjà comme de vieilles copines. Merci pour ta bonne humeur et bon courage pour la fin de ta thèse, tu y es presque.

Clément, nos pauses thé se sont transformées en mails (tout aussi chaleureux). Merci pour tes encouragements et profites bien de ton aventure au Canada.

~ ~ ~ ~ ~

Merci à tous mes amis d'école d'ingé: *Hélène, Camille, Fréd, Rozenn, Rémi, Delphine, Yann, Nathalie, Julien, Itia, Nico, Juju, Jérôme, Damian, Bug, Benoit.* Bon courage à vous tous pour vos carrières respectives.

Merci aussi à *Fanny et Hind*, qui sont l'essence même du mot élégance.

~ ~ ~ ~ ~

Cette thèse a pu se dérouler grâce au soutien matériel que m'ont fourni mes fidèles compagnons: *Oyarsa*, *Huygens* et *Papangue.*

Cette thèse a aussi reçu divers soutiens financiers. Je pense notamment à la Préfecture de la Réunion et notamment à la délégation qui gère le Prix de la Vocation Scientifique et Technique des Filles, au réseau Franco-Néerlandais qui accorde les bourses Eole, et au Programme National de Physique Stellaire. Un grand merci aussi à PPSI sans frontière.

~ ~ ~ ~ ~

J'ai eu beaucoup de chance au cours de ma scolarité car j'ai toujours été encadrée par une équipe pédagogique et administrative qui m'encourageaient dans mes projets. Je tiens tout d'abord à remercier *(Monsieur Moreau) Jean-Yves.* En effet, c'est le voyage culturel que nous avons fait à Paris, Poitiers et Avignon en 4ème qui m'a permis de rencontrer Hubert Reeves et m'a décidé à me lancer dans l'astrophysique. Bien que la liste soit trop longue pour être faite ici, je tiens à remercier les équipes de l'école du Brûlé, du collège Reydellet, du lycée Bellepierre, et aussi de Leconte. Nul doute que les personnes concernées se reconnaîtront.

~ ~ ~ ~ ~

Ma chère *Valérie.* Voilà bien des années que nous nous connaissons, depuis le jour où mes parents ont eu la bonne idée de nous inscrire Pierre et moi au modern jazz. Même si nos routes (physiques) se sont séparées car je suis partie toujours plus loin de toi (Strasbourg, puis Groningen, et qui sait où j'irai encore), nos retrouvailles se passent toujours comme si l'on s'était quitté la veille. Merci pour ton amitié depuis toutes ces années. Et entraîne toi pour notre choré ;)

~ ~ ~ ~ ~

Merci aussi à mes chers voisins du Brûlé, notamment, *Ma tante, Papa, Isa, Eric, Nathalie*, pour leur soutien.

~ ~ ~ ~ ~

Merci aux *familles Feliciano et Prévotat* de m'avoir si souvent ouvert la porte de chez vous. Merci aux *familles Holleville et Mantelet*, pour ces moments en votre compagnie.

~ ~ ~ ~ ~

Toutes ces années d'étude, j'ai pu compter sur le soutien inconditionnel de ma famille. Merci à vous tous.

Je souhaite remercier la famille Raux, et plus particulièrement: *ma Marraine et sese enfants Aurélie, Mathilde et Nicolas*; *Tatie Bernadette, Tonton Guy, Nathan, Rachel*; *Tatie Marie-Pierre, Liam*; *Tatie Françoise, Tonton Jean-François, Julien, Boris et Angéline*; *Tonton Jean-Louis, Morgane, Yann, Kathleen*; et *Papi et Mamie.*

Je remercie aussi la famille Gonneau, et plus particulièrement: *Tatie Lisette, Mimi, Cousin*; *Parrain et Tatie Marie-Claude*; *Valérie, Pascal et leurs familles respectives*; *Gladys, Tante Michette, Tonton Alfred*; *Tonton Christian et famille*; et *Mémé et Pépé.*

Merci à *Corinne, Fabrice et Mathieu* pour vos chaleureux encouragements, et aussi pour l'approvisionnement en Cottin ou en caramel au beurre salé. Merci de faire le déplacement pour ma soutenance. :)

Merci à *mes frères* pour votre amour de loin (voir de très loin). Bien que vous ne pussiez assister à ma soutenance, mes pensées iront vers vous en ce jour. Merci à vous et vos tendres moitiés pour votre soutien depuis toutes ces années.

Merci à *mes parents* sans qui je ne serai pas là où je suis aujourd'hui. Merci à vous pour tout ce que vous avez fait pour moi. Cette thèse est pour vous. Je vous aime :)

"Hello sweetie". Tu es la bonne surprise de cette thèse. Merci de croire en moi, plus que je ne le fais parfois, et pour tout le bonheur que tu m'apportes depuis ces 4 ans.

Because you loved me
Céline Dion

For all those times you stood by me, For all the truth that you made me see
For all the joy you brought to my life, For all the wrong that you made right
For every dream you made come true, For all the love I found in you

I'll be forever thankful baby, You're the one who held me up
Never let me fall, you're the one, Who saw me through, through it all

You were my strength when I was weak, You were my voice when I couldn't speak
You were my eyes when I couldn't see, You saw the best there was in me
Lifted me up when I couldn't reach, You gave me faith 'cause you believed
I'm everything I am, Because you loved me

You gave me wings and made me fly, You touched my hand, I could touch the sky
I lost my faith, you gave it back to me, You said no star was out of reach
You stood by me and I stood tall, I had your love, I had it all

I'm grateful for each day you gave me, Maybe I don't know that much
But I know this much is true, I was blessed because I was loved by you

You were my strength when I was weak, You were my voice when I couldn't speak
You were my eyes when I couldn't see, You saw the best there was in me
Lifted me up when I couldn't reach, You gave me faith 'cause you believed
I'm everything I am, Because you loved me

You were always there for me, the tender wind that carried me
The light in the dark shining your love into my life
You've been my inspiration, through the lies you were the truth
My world is a better place because of you

~ ~ ~ ~ ~

Merci à mes amis et à ma famille pour leur soutien et leur amour.

"When we come to the end, we find that it is only the beginning."

(Secchi, 1878)